ISOSTATICALLY COMPENSATED EXTENSIONAL TECTONICS ON ENCELADUS

by

Scott Stuart McLeod

A thesis submitted in partial fulfillment
of the requirements for the degree

of

Master of Science

in

Earth Sciences

MONTANA STATE UNIVERSITY
Bozeman, Montana

May 2009

©COPYRIGHT

by

Scott Stuart McLeod

2009

All Rights Reserved

APPROVAL

of a thesis submitted by

Scott Stuart McLeod

This thesis has been read by each member of the thesis committee and has been found to be satisfactory regarding content, English usage, format, citation, bibliographic style, and consistency, and is ready for submission to the Division of Graduate Education.

David R. Lageson

Approved for the Department of Earth Sciences

Stephan G. Custer

Approved for the Division of Graduate Education

Dr. Carl A. Fox

STATEMENT OF PERMISSION TO USE

In presenting this thesis in partial fulfillment of the requirements for a master's degree at Montana State University, I agree that the Library shall make it available to borrowers under rules of the Library.

If I have indicated my intention to copyright this thesis by including a copyright notice page, copying is allowable only for scholarly purposes, consistent with "fair use" as prescribed in the U.S. Copyright Law. Requests for permission for extended quotation from or reproduction of this thesis in whole or in parts may be granted only by the copyright holder.

Scott Stuart McLeod

May 2009

DEDICATION

I dedicate this work to my parents, Grace and Rodney McLeod, for their tireless enthusiasm, encouragement and support, and to my friends and colleagues who never stopped believing in me – you know who you are.

ACKNOWLEDGEMENTS

I would like to acknowledge my committee, David R. Lageson, James G. Schmitt and David M. Klumpar for allowing and encouraging me to pursue such an arcane thesis topic; I also wish to thank the following individuals (in alphabetical order): Edward E. Adams, Jeff Banfield, Mike Cavaness, Stuart Challender, Martin Chapman, Tara Chesley-Preston, Mark Greenwood, Trent Hare, Donna Jurdy, Isaac Klapper, Dr. W. Locke, Falene Petrik, Carolyn Porco, Thomas Roatsch, Frank Scholten, Colin Shaw, Alice Stanboli, Michael Sulock, Ismael Talke, Kenneth Tanaka, Peter Thomas, B. William Turner, and Jeannette Wolak. Special thanks go to Monica Bruckner (proofreading) and Beth Helmke (GIS).

Finally, I would like to quote verbatim from the note to the reader from the 1698 English edition of The Celestial Worlds Discover'd:

"'Tis true there are not every where Mathematical Demonstrations; but where they are wanting, you have probable and ingenious Conjectures, which is the most that can reasonably be expected in such matters. What belongs to, or has any thing to do with Astronomy, you will see demonstrated, and rest ingeniously and shrewdly guess'd at, from the affinity and relation of the heavenly Bodies to the Earth. For your farther Satisfaction read on, and farewel."

TABLE OF CONTENTS

1. INTRODUCTION 1

2. GEOLOGIC SETTING 2

Historical background 2
Physical Properties 5
Size, Shape, Mass, and Gravity 6
Size and Mass Comparison with Other Active Bodies 7
Surface Composition and Color 8
Surface Temperature 10
Atmosphere 10
Space environment 12
Orbital Parameters and Resonances 13
Synchronous Rotation 14
Magnetospheric Interaction 15
Generalized Geography 16
Sulci Explained 19

3. METHODS 21

Data Source 22
Reference Grid Construction 23
Accuracy and Scale 27
Distortion 28
Terrain Types and Visual Interpretation 29
Kinematic Analysis 31
Dynamic Analysis 32
Crater Counting 32
Geophysical Modeling 34

4. RESULTS 40

Surface Features: Descriptive Analysis 40
Craters, Cratered Plains and Crater Counting 40
Impact Craters 41
Crater Counting 48
Ridged Plains 51
Srp Regions 52
Crp Regions 54

TABLE OF CONTENTS – CONTINUED

The South Polar Terrain 56
Dorsa 57
Faults, Fractures and Sulci 58
Kinematic Analysis 59
The Tiger Stripes as Possible Spreading Centers 62
Tectonic Features Outside the South Polar Terrain 67
Dynamic and Geophysical Analysis 67
Enceladus Thermal Anomaly 68
Properties of Water 70
Formation of a South Polar Basin 72
Ice, Subduction and Spreading 80

5. DISCUSSION 81

A Subsurface Ocean 81
Other Geologic Issues 82
Downslope Transportation on Low-mass Bodies 82
Cryovolcanism as a Resurfacing Mechanism 83
Enceladus' Internal Heat Source 85
Ohmic Heating 85
Serpentinization 86
Diapir-induced Reorientation 87
Ammonia 88
Comparison with Miranda 88
A Possible "Ancestral Antapical Venting System" (AAVS) 90

6. CONCLUSIONS 91

REFERENCES CITED 93

APPENDICES 93

APPENDIX A: Tabulated Planet and Small Body Properties 102
APPENDIX B: RGB False-Color Image Construction 106
APPENDIX C: Geophysical Model Formulas, Output and Data 115
APPENDIX D: Reference Grid Construction 125
APPENDIX E: Crater Counting Data 129
APPENDIX F: Named Features on Enceladus 166
APPENDIX G: Additional Structural Interpretations 170

LIST OF TABLES

Table Page

1. Scale variation across DLR photomosaics 27

LIST OF FIGURES

Figure Page

1. Voyager 2 color image of Enceladus 4

2. False-color image of Enceladus' south polar region 9

3. Enhanced false-color view of SPT jets 11

4. Enhanced false-color view of jet interaction with E-ring 12

5. Scale diagram of Saturn and inner moons 14

6. Sulci compared 20

7. Ali Baba region with oblique orthographic grid 26

8. Comparison of sharp vs. gradual terrain boundaries 29

9. Effect of lighting angle on low-contrast features 30

10. Graphical representation of geophysical model of Enceladus' interior 35

11. Comparison of Enceladus, Mimas, Tethys and Hyperion 43

12. Ali Baba and Aladdin craters 44

13. Fractured craters 46

14. Possible crater chain 47

15. Craters dissected by Samarkand Sulci 48

16. Crater counting plots 50

17. Sarandib Planitia 53

18. Coarse subparallel-ridged plain near Otbah crater 54

19. Extreme close-up of ridges within SPT 55

LIST OF FIGURES – CONTINUED

Figure Page

20. Oblique view of the SPT and Labtayt Sulci 57

21. Close-up of central grooves in Ebony – Cufa Dorsa 58

22. Large faults and fractured craters 59

23. Comparison of Enceladan features to spreading ridges and transforms 63

24. Asymmetric spreading reconstruction, PIA11140 64

25. Enceladus thermal anomaly, July 2005 69

26. South polar hot-spot remains stable over 16 months 69

27. Phase diagram for water with Enceladus pressure regime overlay 71

28. Temperature – density chart for water and ice 72

29. Subsidence rates for various initial crustal thicknesses 75

30. Initiation of the thermal subsidence – equilibration cycle 76

31. Further development of the thermal subsidence – equilibration cycle 77

32. Cashmere Sulci 78

33. Cross-section through Cashmere Sulci 78

34. Overhead and oblique views of icefall structures in Jackson glacier, MT 79

35. Accumulation of material in Psyche crater, 433 Eros 82

36. Cryovolcanic flows on Ariel 83

37. Samarkand Sulci in enhanced false-color 84

38. Miranda southern hemisphere mosaic 88

LIST OF PLATES

Plate

1. Annotated photomosaic of Enceladus..... CD-ROM

2. Annotated southern hemisphere mosaic PIA11126..... CD-ROM

Unless otherwise credited, illustrations are by the author.

GLOSSARY

Albedo	The reflectivity of a planetary surface, expressed as a ratio
AMU	Atomic Mass Unit (1.660,538,86 x 10^{-27} kg)
Apoapsis	The most distant point in an orbit from the orbited body's center
Atm	Standard Atmosphere, a unit of pressure (101,325 Pa exactly)
AU	Astronomical Unit, a unit of distance (≈1.496 x 10^{11} m)
B	The Blue channel in an additive tri-color image
CICLOPS	Cassini Imaging Central Laboratory for Operations
CIRS	Cassini Infra-red Spectrometer
cp	Cratered plains geologic region
Crp	Complexly-ridged plains geologic region
DLR	Deutsches Zentrum für Luft- und Raumfahrt
Dorsa	An isolated ridge-like feature
Eccentricity	A measure of the deviation of an orbit from a circle: $e = (r_a - r_p) / (r_a + r_p)$ where r_a = radius at apoapsis and r_p = radius at periapsis
Fossa	A long, narrow furrow (literally, Latin for ditch)
G	The Green channel in an additive tri-color image
GSFC	Goddard Space Flight Center
IAU	International Astronomical Union
INMS	Ion and Neutral Mass Spectrometer (Cassini instrument)
IR	Infrared electromagnetic radiation

ISS	Imaging Science Subsystem (Cassini instrument suite)
JHUAPL	Johns Hopkins University Applied Physics Laboratory
Macula	A dark spot
MORB	Mid-ocean Ridge Basalt
NAC	Narrow-angle camera (Cassini ISS instrument)
Periapsis	The closest point in an orbit to the orbited body's center
Period	The time taken for a body to complete an orbit
PIA	Planetary Image Atlas (NASA – JPL online resource)
Planitia	Plains
R	The Red channel in an additive tri-color image
Rp	Ridged plains geologic region
RGB	An acronym for the three channels in an additive-color image
Semimajor axis	Half the distance between the apoapsis and periapsis of an orbit
SPT	South Polar Terrain (on Enceladus)
Srp	Subparallel-ridged plains geologic region
Sulci/sulcus	Any set of subparallel grooves or ridges
Terminator	The demarcation between the sunlit and night hemisphere
UV	Ultraviolet electromagnetic radiation
UVIS	Ultraviolet Imaging Spectrometer (Cassini instrument)
WAC	Wide-angle Camera (Cassini ISS instrument)

ABSTRACT

Saturn's moon Enceladus is the smallest body in the solar system known to be geologically active. Extensive, energetic resurfacing processes are ongoing and it possesses a system of geysers at the South Pole that supply material to the E-ring. The South Polar Terrain (SPT) is the youngest region on Enceladus and its contacts with the older cratered and grooved plains to the north are delineated by a variety of complex geologic features including mountain ranges and massive grabens. Many of the geologic features seen on Enceladus bear superficial resemblance to terrestrial structures associated with plate tectonics. A detailed structural geologic analysis, supported by crater counting studies, was used to determine whether the features seen on Enceladus are compatible with terrestrial-style plate tectonics. On Earth, new lithosphere is created at spreading centers and consumed at subduction zones, enabled by the compositional dichotomy between oceanic and continental crust. Enceladus's lithosphere appears to be made entirely of pure water ice, so any newly formed crust will have the same composition, but lower density due to higher temperature, making subduction and consequently spreading, as we understand it on Earth, impossible. Geometrically, the absence of fold-thrust belts and transform faults in the presence of normal faults and basin and range-style features implies extension without corresponding shortening elsewhere. This is not possible in a conventional (terrestrial) plate tectonic regime as surface area is not conserved; therefore, an alternate explanation is required. Topographic features associated with density contrasts between old and new terrain that are diagnostic of terrestrial spreading centers are also not observed on Enceladus. I conclude that features observed on Enceladus are inconsistent with terrestrial-style plate tectonic spreading, and represent a style of tectonism peculiar to bodies with icy lithospheres. I present an interpretation in which the cordillera surrounding the SPT is a broadly developed extensional regime, and describe a model for its formation that is consistent with the known physical properties of Enceladus, dependent on the presence of a water-ice phase transition below the south polar terrain.

INTRODUCTION

The plate tectonics paradigm revolutionized the Earth sciences in the 1960s-70s by providing a unified framework on which to interweave the observations of many different sub-disciplines, allowing them to be viewed as complementary scenes within the same grand tapestry. It is reasonable to ask, does this "living planet" paradigm operate on other worlds?

Though broadly similar in size and composition to a pantheon of cold, dead, frigid worlds beyond the asteroid belt, Enceladus is further from being a moribund ice-ball than could have been imagined prior to the arrival of the Cassini spacecraft and the gradual unveiling of its remarkable secrets. For on the startling, snow-white surface of this tiny world, surrounded by its battered lifeless cousins orbiting the ringed giant Saturn, we see an improbable, stunning array of youthful geologic complexity without parallel elsewhere in the solar system. Even more compelling is the resemblance of many of these features to structures associated with terrestrial plate tectonics – could this be the unlikely place where we discover a world so different from our own, yet recycling its outer lithosphere in much the same way as Earth? This project attempts to unravel the unique geology of Enceladus and synthesize a coherent picture of its tectonic continuum.

GEOLOGIC SETTING

Historical Background

While recorded observations of Saturn go back to at least the 7th century B.C.E. (Alexander, 1962), its satellites remained unknown until some decades after Galileo popularized the use of the telescope for astronomical observations in January 1610 with his epochal discovery of Jupiter's moons Io, Europa, Ganymede and Callisto. Galileo turned his telescope to Saturn only a few months afterward, marking the first observation of its rings and the beginning of the modern era of scientific study of that planet (Galilei, 1610). Unfortunately, a combination of factors, among them the poor quality of early instruments and the unique appearance of the planet, meant that the true nature of the rings was not discovered until almost half a century later, by the famous Dutch astronomer, mathematician and inventor Christiaan Huygens (Alexander, 1962).

In 1655 Huygens correctly deduced the existence of a thin, flat ring surrounding the planet and discovered Titan, second largest moon in the solar system (Huygens, 1668). The great distance of the Saturn system from Earth prevented discovery of more satellites until better telescopes allowed Jean-Dominique Cassini to observe Iapetus in 1671, Rhea in 1672, and Dione and Tethys in 1684 (Bakich, 2000). More than a century would pass before Sir William Herschel discovered Mimas and Enceladus during the ring-plane crossing of 1789 (idem).

Early attempts to measure the diameter of Enceladus showed only that it was very small; a very high albedo was required to account for its observed brightness. Later, more precise astrometry showed Enceladus to be only about 500 km in diameter, with an albedo of ~1.38 (Verbiscer et al., 2007), making it by far the most reflective known object in the solar system. The albedo remains almost constant throughout each orbit, a very unusual condition for solid bodies whose surface features typically exhibit significant brightness variations.

Approximately every 15 years, Saturn's rings appear edge-on as viewed from Earth. Since the rings are exceedingly thin (10-100m) these ring-plane crossings render the main rings virtually invisible, and more than a dozen moons have been discovered by careful observation at these times (Van Helden, 1984). During the 1966 event, the existence of a tenuous, "fluffy" ring outside the main ring system (the E ring) was finally confirmed after decades of controversial visual sightings (Feibelman, 1967). Its diffuse nature is very different to the main rings and its maximum density coincides with Enceladus's orbit; the implication of these discoveries was that Enceladus may somehow be supplying material to the E-ring (Batson et al., 1984; Mendis et al., 1984).

The first spacecraft to visit the Saturn system was Pioneer 11 in 1979, but no useful images of Enceladus were returned. The far more capable Voyager 1 and 2 explored Saturn in November 1980 and August 1981, but the timing and approach geometry of the two spacecraft meant that only Voyager 2 returned images of Enceladus suitable for mapping purposes (Figure 1).

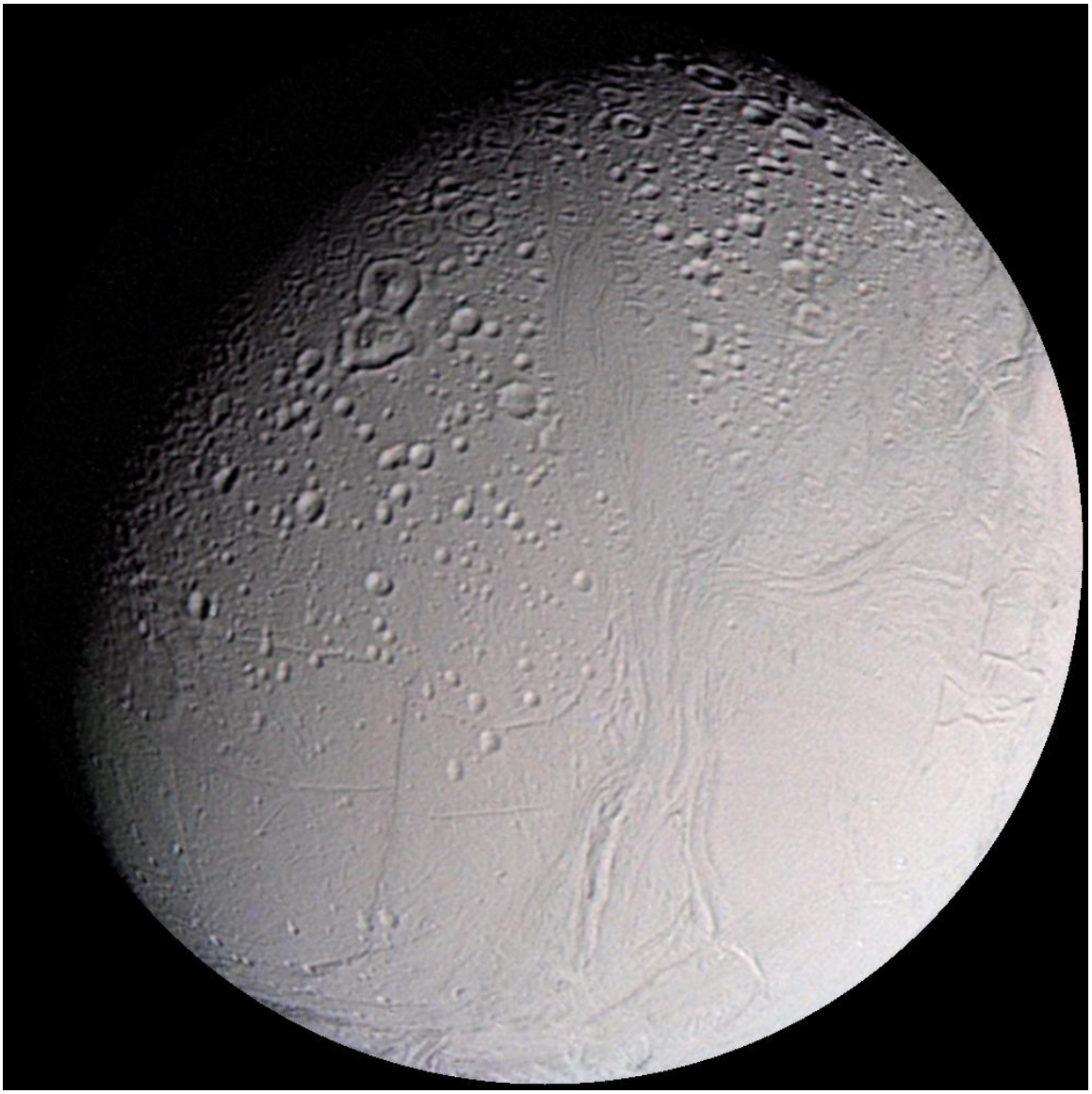


Figure 1. This color image of Enceladus was acquired by Voyager 2 during its August 1981 flyby. It is centered at approximately 38°N, 341°W; north is up and rotated ~2° to the right. The largest impact structures in the northern cratered plains show evidence of viscous relaxation in the form of softened rims and bulging floors, while unmodified complex craters (i.e. with flat floors and central peaks) are conspicuously absent. The contrast between the cratered plains and the smooth (at this scale of observation) Samarkand Sulci – Anbar Fossa region (running north-south and bisecting this hemisphere) is particularly striking. What is not visible here is the dramatic transition further south into the Cashmere Sulci – South Polar Terrain, whose existence was unknown at the time. NASA/JPL/USGS image PIA00347, courtesy NASA/JPL/Caltech.

It was immediately apparent that large portions of Enceladus had undergone resurfacing in geologically recent time (Batson et al., 1984). Surface relief was low and generally muted, with large areas exhibiting curvilinear grooves vaguely similar in appearance to those seen on Jupiter's moon, Ganymede; a more extreme manifestation of grooved terrain would be discovered by Voyager 2 on Uranus's moon Miranda in 1986 (Pappalardo and Greeley, 1995; Schenk and Moore, 1995).

The Voyager missions were flybys, and further detailed exploration of the Saturn system did not occur until the arrival of the Cassini-Huygens orbiter/lander spacecraft in June 2004.

Physical Properties

No robotic spacecraft has landed on Enceladus as of this writing, so knowledge of its physical properties is entirely derived from remote sensing, except for the atmosphere, which has been sampled directly by the Cassini orbiter (Waite et al., 2006). Compared to other satellites, Enceladus' most striking characteristics are its small size combined with a remarkable degree of geologic activity, lack of surface color and compositional variations, and the likely presence of liquid water beneath the surface. Early estimates of its density were somewhat vague, and even after the Voyager 2 flyby, values around 1,200 ± 500 kgm^{-3} were the norm (Morrison et al., 1984). Doppler tracking of the Cassini orbiter has revised this value to 1,608.3 kgm^{-3} (Porco et al., 2006), with concomitant implications for its interior structure and evolution.

Size, Shape, Mass, and Gravity

The figure of Enceladus is a triaxial ellipsoid with radii: 256.6 ± 0.5 km (sub-Saturn), 251.4 ± 0.2 km (along-orbit) and 248.3 ± 0.2 km (polar) (Porco et al., 2006). The volume of a triaxial ellipsoid is given by

$V = 4/3\ \pi\ a\ b\ c$

$= 67{,}094{,}552\ km^3$

A sphere of equivalent volume has a radius of 252.08 km; unless otherwise noted, a radius value of 252.1 km is adopted for the remainder of this work. While an exact solution exists for volume, there is no closed analytical solution for the surface area of a triaxial ellipsoid (e.g. Keller, 1979); the area of a sphere of radius 252.1 km is

$S = 798{,}648.3\ km^2$

For terrestrial comparison, the surface area of Enceladus is approximately the same as that of New South Wales, Australia (800,642 km^2), or the Dakotas, Nebraska and Kansas combined (796,284 km^2).

Enceladus' density of 1,608.3 ± 4.5 kgm^{-3} yields a mass range of 1.076×10^{20} kg – 1.082×10^{20} kg. The average value of 1.079×10^{20} kg is used here. This mass gives a surface gravity of (e.g. Zeilik and Gregory, 1998):

$g = GM / r^2$

$= (6.6742 \times 10^{-11}\ m^3 kg^{-1} s^{-2} \times 1.079 \times 10^{20}\ kg) / (252{,}100\ m)^2$

$= 0.11332\ ms^{-2}$

which is about 1/86 of the acceleration due to gravity on Earth. Enceladus' escape velocity is given by (idem):

$$v_e = \sqrt{(2GM/r)}$$

$$= \sqrt{((2\ (6.6742 \times 10^{-11}\ m^3 kg^{-1} s^{-2} \times 1.079 \times 10^{20}\ kg)) / 252{,}100\ m)}$$

$$= 239\ ms^{-1}$$

This is a very low velocity; for comparison, the speed of sound at STP is 331.5 ms^{-1} (Lide, 2006). The mean orbital velocity of Enceladus is approximately:

$$v = 2\pi r / P$$

$$= 12{,}633\ ms^{-1}$$

where r = 2.3802×10^8 m, and P = 118,386 s (Bakich, 2000); therefore, it is much easier for ice and dust particles to be ejected from the surface (by whatever mechanism) than it is for them to depart the general vicinity, due to Saturn's immense gravity well.

Size and Mass Comparison with Other Active Bodies

Besides Earth, there are only 3 other bodies in the solar system known to be geologically active at present: Jupiter's moon Io, Neptune's moon Triton, and Enceladus (Kargel, 2006). The extraordinary nature of Enceladus' activity becomes apparent in comparison to Io and Triton: Io is 3,630 km in diameter (slightly larger than the Moon, at 3,476 km), with a mass of 8.94×10^{22} kg (25% more massive than the Moon, and more than *800 times* that of Enceladus), while Triton is 2,705 km in diameter and has a mass of 2.147×10^{22} kg, 199 times that of Enceladus (Bakich, 2000). Io's internal heat is believed to be supplied primarily by tidal flexing due to gravitational interaction with

Jupiter and the other Galilean moons, Europa, Ganymede and Callisto (Rothery, 1992; Harland, 2001). Triton circles Neptune in a highly inclined, retrograde orbit, indicating it is a captured body; tidal stresses imposed by the gradual circularization of Triton's initially eccentric orbit would have supplied the necessary heat to initiate and maintain geologic activity (idem). Appendix A contains a tabulated comparison of basic physical parameters of the terrestrial planets, major satellites and small bodies.

Surface Composition and Color

Enceladus' surface is unique among known solar system bodies by virtue of its extreme whiteness, reflectivity and uniform composition. The surface is composed of water ice in either crystalline or amorphous form, and is almost devoid of contaminants, with only trace absorption features at 3.44-µm and 3.53-µm attributed to low molecular weight organics, and highly localized to areas in the immediate vicinity of the active SPT sulci (Brown et al., 2006). This is in stark contrast to other icy moons in the Saturn system (and elsewhere), all of which display varying degrees of rocky or organic surface deposits. A consequence of this heterogeneity is the lack of colorimetric stratigraphic indicators, such as ejecta deposits and rays from impact craters (though the low escape velocity may also be partly responsible for the absence of these features).

Cassini's Imaging Sub-System (ISS) has detectors that are sensitive to a wide range of wavelengths and narrow-pass or broadband filters are used to tune the spectral response for specific imaging purposes (Porco et al., 2004). In the case of Enceladus, false-color images using the combination of IR3 (930 nm) = R, G (568 nm) = G

and UV3 (338 nm) = B, greatly enhance the extremely subtle color variations of the surface ice. Amorphous ice appears whiter, and crystalline ice appears bluish-green (idem). The gradual destruction of the ice crystal lattice by charged particle radiation on direct exposure to the local space environment (and other mechanisms that produce amorphous ice) allows the color of the surface to be used as a rough proxy for relative age (Brown et al., 2006; Harland, 2007).

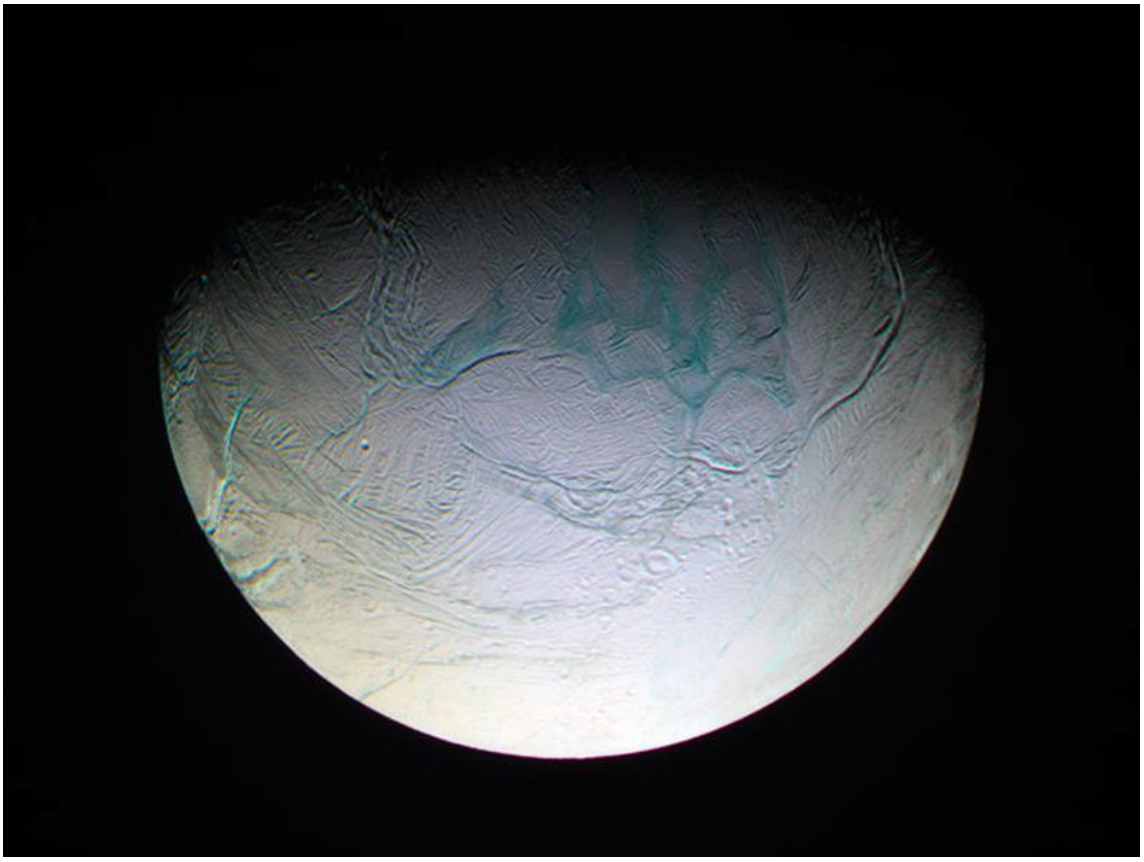


Figure 2. This false-color composite image of the south polar terrain of Enceladus was created from Cassini-ISS Narrow-Angle Camera (NAC) frames N00103783 (IR3-R), N00103781 (G) and N00103780 (UV3-B), acquired on March 12 2008 at a range of ~144,000 km. Note the color variations, which are not apparent at visible wavelengths. The large graben at 8 o'clock also shows greenish walls, indicating it is a relatively recent feature. Courtesy NASA/JPL/Space Science Institute; composite image by the author.

Numerous IR3-GRN-UV3 composites were prepared from Cassini-ISS raw images by the author, not only of Enceladus (e.g. Figure 2), but also of other moons in the Saturn system for comparison purposes. The method used to produce these images is described in Appendix B.

Surface Temperature

The extremely high albedo contributes to very low average surface temperature. Observed temperatures in the high 70s K (e.g. Spencer et al., 2006) are slightly lower than the equilibrium temperature given by (Zeilik and Gregory, 1998):

$$T_p \approx 279\,(1 - A)^{1/4}\,(r_p)^{-1/2} \approx 90\ \text{K}$$

Where r_p = 9.555 AU (the mean orbital distance from Saturn to the Sun) and the albedo term is disregarded since it is >1. However, much higher temperatures are measured at actively venting locations along the "tiger-stripe" sulci within the south polar terrain (Brown et al., 2006; Spencer et al., 2006; Spitale and Porco, 2007).

Atmosphere

Enceladus possesses a tenuous and highly unusual "atmosphere", derived from emissions from the geysers within the SPT (Figure 3, 4). It is localized around the SPT, as Enceladus' gravity is too low to retain a conventional atmosphere, and extends several hundred kilometers above the surface (e.g. Baker, 2006; Dougherty et al., 2006; Porco et al., 2006; Tokar et al., 2006). The gaseous (as opposed to particulate) composition of the atmosphere (or plumes) is primarily water vapor (91 ± 3%), with N_2 (4 ± 1%), CO_2 (3.2 ±

0.6%), CH_4 (1.6 ± 0.4%), and trace amounts of acetylene, propane and ammonia (Waite et al., 2006).

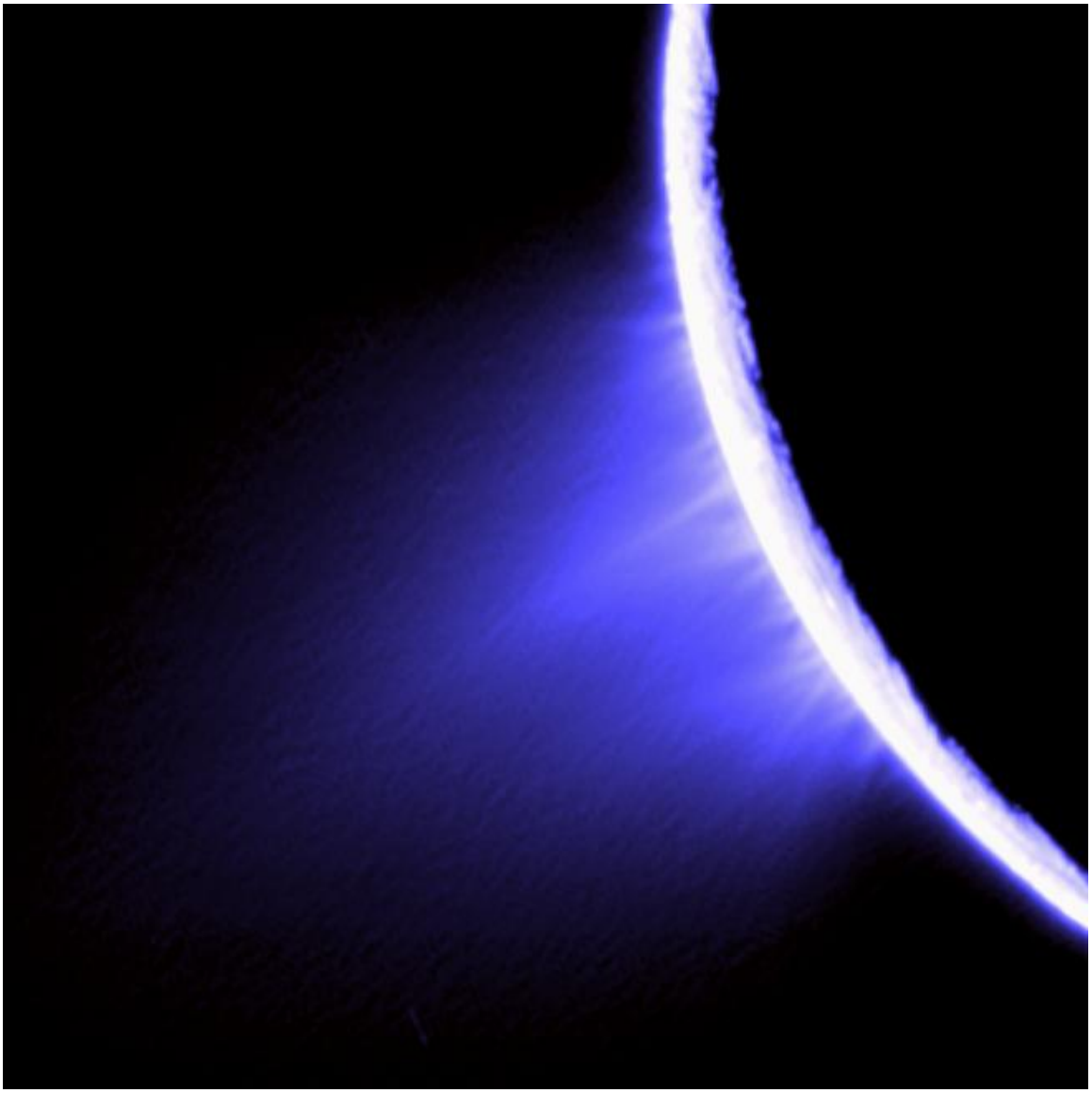


Figure 3. The complex structure of the SPT jets is visible in this enhanced false-color view; their actual radial extent is considerably greater than shown here, and they blend into the E-ring as shown in Figure 4. The jets are visible without enhancement when backlit. Note that there are many individual vents and they are not all emitting perpendicular to the surface. 656 x 656 pixel crop from PIA08386, courtesy NASA/JPL/Space Science Institute.

The CO molecule has the same mass as N_2 (28 AMU) and is indistinguishable to the Cassini Ion and Neutral Mass Spectrometer (INMS), but its UV absorption was not detected during a stellar occultation[1], so if carbon monoxide is present, it is at levels below 3% (Hansen et al., 2006; Hansen et al., 2008).

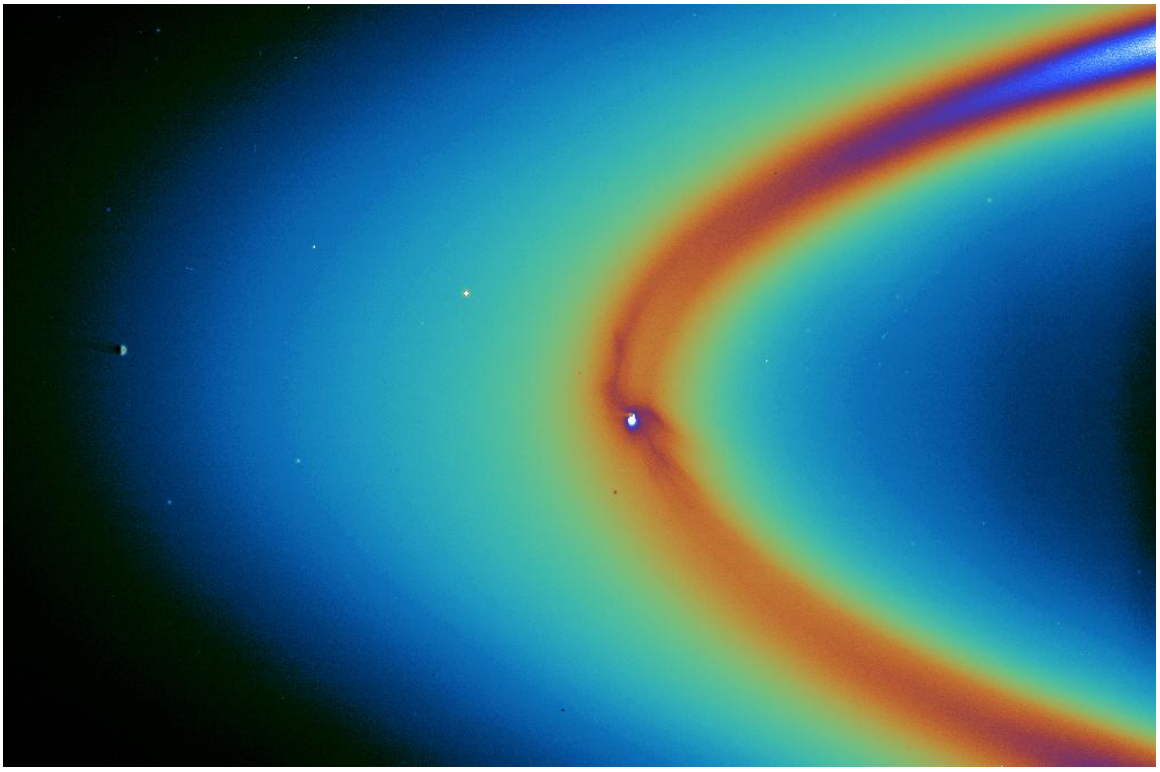


Figure 4. An enhanced, colorized version of PIA08321, showing the complex interaction of Enceladus's jets (center) with the E-ring. Note the extent of the E-ring is such that Tethys (far left) actually casts a shadow. Some of the radial brightness variations are posterization effects. Base image courtesy NASA/JPL/Space Science Institute.

Space Environment

Since this thesis research is concerned with an entire extraterrestrial body instead of a specific region on Earth, a brief description of its location and surroundings

[1] The spectrum of a star is monitored while the target passes between it and the observing instrument/s

is in order. As the broader contextual geologic history and present-day environs are relevant to a more traditional field area, so the environment in which Enceladus exists has a definite bearing on its geologic history and present-day characteristics.

Orbital Parameters and Resonances

Enceladus circles Saturn in a prograde orbit with the following major parameters (Bakich, 2000):

- Semimajor axis *a* 238,020 km
- Eccentricity *e* 0.0045
- Inclination *i* 0.02°
- Period P 118,386 s (32 h 53.1 min)

The *e* and *i* values describe a very nearly circular orbit (the Moon's *e* = 0.0549, more than twelve times greater) that barely deviates from Saturn's equatorial plane.

Unlike the Galilean moons of Jupiter, whose orbital periods are commensurate in an approximately 1 : 2 : 4 : 8 relationship, the only major Saturnian moon involved in a present-day resonance with Enceladus is Dione[2] (1 : 2), though other resonances may have existed in the past (Greenberg, 1984; Porco et al., 2006). The low eccentricity and inclination of Enceladus' orbit suggests significant tidal dissipation has occurred (idem). With a limited core mass to supply radiogenic heating, the source of Enceladus' internal heat remains contentious (e.g. Morrison et al., 1984).

[2] Enceladus makes almost exactly 2 orbits for every one orbit of Dione (P = 236,472 s)

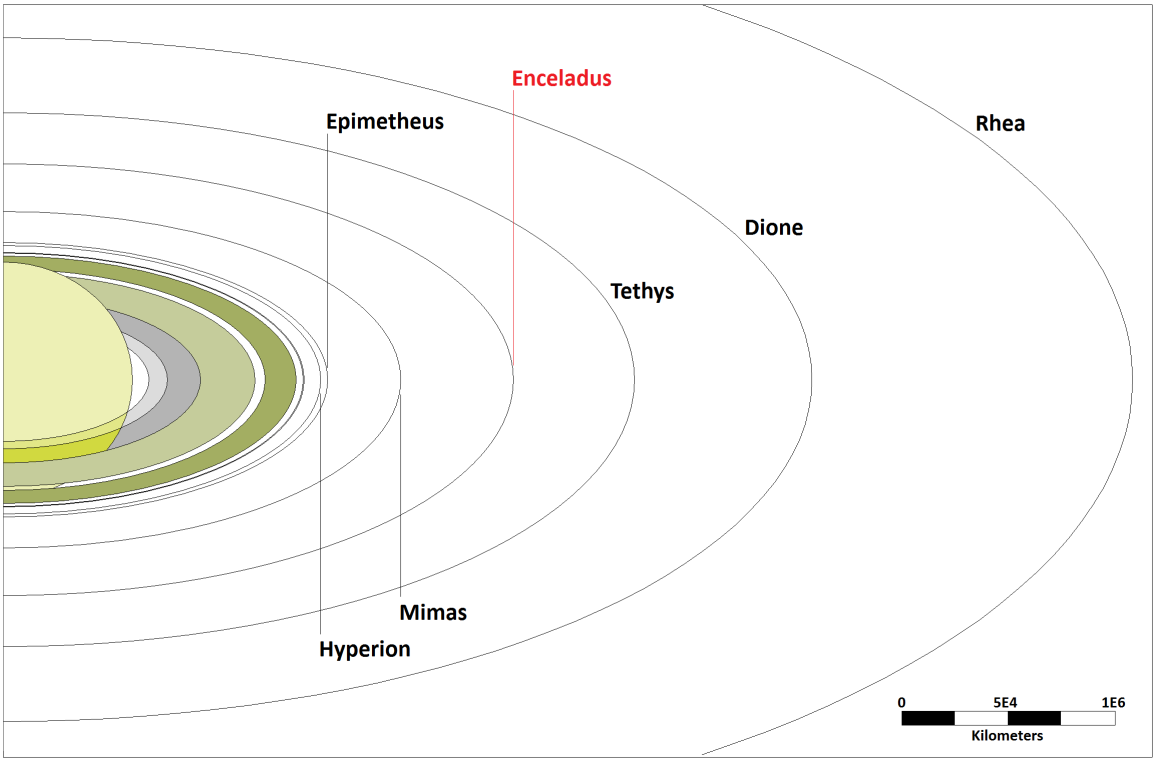


Figure 5. A scale diagram showing the orbits of the innermost major moons of Saturn and the main ring system; Saturn's equatorial plane is inclined at 65° to the page. The E-ring (omitted for clarity) extends from approximately the orbit of Mimas to just beyond the orbit of Tethys, with its maximum density occurring at Enceladus' orbit. Titan orbits at 1,221,870 km (~20.25 Saturn radii) and is not visible here. Iapetus orbits at 3.56 million km and Phoebe at 12.95 million km (Scott McLeod)

Synchronous Rotation

With very few exceptions, major planetary satellites rotate synchronously in prograde orbits (i.e., counterclockwise when viewed from above the ecliptic plane), a condition which (in principle, and again, with exceptions) leads to a hemispheric brightness dichotomy, the leading hemisphere being more reflective than the trailing. This process, referred to as "impact gardening" by analogy with turning up fresh soil (Shoemaker and Wolfe, 1982**;** Melosh, 1989), generally occurs as follows: outer planet

satellites have lithospheres primarily composed of water ice or other frozen volatiles, contaminated with varying amounts of organic materials. Lacking significant atmospheres, prolonged exposure to the space environment causes a gradual darkening of the surface by ultraviolet radiation-induced polymerization, sometimes leading to the formation of high-molecular-weight hydrocarbons collectively referred to as "tholins" (Sagan and Khare, 1979; Sagan, Khare and Lewis, 1984). Moons orbiting within the magnetosphere are bombarded more heavily by trapped charged particles on their *trailing* hemisphere since the gas giants have rotation periods which are shorter than the satellites' orbital periods (at least in the case of the major moons).

Synchronous rotation causes the leading hemisphere to present a higher true space velocity (on average) relative to interplanetary debris, since the orbital velocity of the satellite is added to that of the primary. Thus, the greater number of impacts on the leading hemisphere excavates relatively more, fresh, undarkened material, leading to a slightly higher albedo. However, there are enough exceptions to this generalized process (e.g. Pollack and Consolmagno, 1984) that implications drawn from it must be regarded with caution and, in any case, neither the cratering record nor the albedo distribution of Enceladus are suggestive of any such phenomena being significant with respect to its present-day appearance (Plescia and Boyce, 1983).

Magnetospheric Interaction

Enceladus orbits entirely within Saturn's magnetosphere (Van Allen, 1984), and it has recently been found to be the solution to a long-standing mystery regarding that

planet's magnetic field inclination. All other planets with geodynamos exhibit a significant angular offset between the dipole and the rotational axis, except in the case of Saturn where they are aligned within 1° (Connerney et al., 1984). Cassini revealed the interaction between Enceladus' atmosphere, the E-ring, and Saturn's magnetosphere to be unexpectedly powerful, and responsible for a torquing effect on the overall field geometry that masks the underlying asymmetry (Jones et al., 2006; Kivelson, 2006; Tokar et al., 2006).

Generalized Geography

Unlike many icy satellites, Enceladus can be broadly divided into a series of physiographically distinct regions; despite its uniform surface composition and color, these regions are easily recognized due to their dissimilar morphologies, and in most cases they are sharply delineated from each other. Furthermore, they are not randomly distributed, but follow a recognizable pattern. See Plate 1 for an annotated photomosaic, with stereographic projections of the north and south polar regions from 55° - 90°, and a Mercator projection from ± 57°. Appendix F lists the names, locations and principal dimensions of the features shown in Plate 1. Plate 2 is a stereographically projected photomosaic of the entire southern hemisphere, with overlays and annotations by the author. Appendix F and Plates 1 and 2 should be referred to wherever the actual location of a feature named in this thesis is in question.

The northern hemisphere is dominated by cratered terrain (e.g., Figures 7, 8, 13 and 22), extending from about 30° to the pole, with a southern extension about 60-70° wide, centered on the anti-Saturn hemisphere (180°W) and extending to about 50°S. Craters within these regions are often highly modified, with bulging, fractured floors and collapsed rims (Figure 12). In some cases, the original impact has been flattened and infilled to the point where it attains a pancake-like profile with no trace of the original bowl remaining (e.g. Figure 14, north of Harran and Hamah Sulci). Overall, though, cratering is relatively sparse compared to other Saturnian moons (Morrison et al., 1984).

The mid-latitudes are primarily covered by ridged terrain of varying sub-types. The leading hemisphere is particularly bland, and between about 30°-150°W is virtually devoid of impact craters (with one notable exception – a fresh-looking simple crater ~10.3 km in diameter, located at about 12°N, 63°W). The ridges vary from very fine and subparallel (for example, Sarandib Planitia, Figure 17) to quite coarse and irregularly oriented (as seen over a large part of the leading hemisphere). In some locations further south, the terrain would more properly be described as grooved rather than ridged, for example, the region between Labtayt Sulci and Khorasan Fossa (about 30°S, 270°W). In general, the ridged (and grooved) terrain becomes coarser moving farther south. The ridged plains include the only significant non-impact related positive-relief features anywhere on the globe, the Ebony-Cufa Dorsa, a polygonal complex of isolated ridges which are coincident with the northern terminus of the Labtayt Sulci graben, very close to the center of the trailing hemisphere.

Finally, the SPT forms the last major geographic subdivision, a remarkably symmetrical region centered on the pole and commencing at about 50°S. The SPT is completely devoid of craters to the limit of available image resolution (e.g. Porco et al., 2006) and consequently is the youngest surface on Enceladus (and probably one of the youngest in the solar system). Its border with the plains to the north is very distinct and marked in most places by a scarp, with the SPT being topographically lower (Figure 2). The south side of the contact contains very coarse, arcuate ridges and grooves, which rapidly smooth and flatten out toward the pole. Near the center of the SPT are the Arabian Sulci or "tiger stripes", a series of four or five very narrow fracture-like features with raised rims, striking about 45° to the orbital direction (Figure 6 (Damascus), 18 and 19). The vents of the south polar geysers or jets (Figure 3 and 4) are located along these sulci, making them uniquely different from similar fracture-like features elsewhere. The border of the SPT is not straight (i.e. a small circle) but wavy, and in some locations, the convex-north segments transition into north-south trending grabens of varying width and depth. These grabens are especially well-developed on the trailing hemisphere (Figure 20), subdued or absent on the (admittedly poorly-imaged) leading hemisphere (Figure 2), and are among the most striking formations on Enceladus.

Taken as a whole, the geography of Enceladus is indicative of a history of pervasive yet probably individually relatively brief resurfacing events, separated by periods of quiescence, of which the geologically active SPT and its northern extensions into the trailing hemisphere is the current expression. This conclusion is suggested by

the division of the surface into numerous large, physiographically distinct regions of varying ages (indicated by the cratering record), while the usually very sharp boundaries or contacts between these regions are evidence that the resurfacing processes are temporally distinct i.e., they did not grade into one another (Plescia and Boyce, 1983). Note also that surface types are classified by a slightly different scheme in this thesis compared to the system based on Voyager imagery (e.g. Morrison et al., 1984).

Sulci Explained

The reader will have no doubt wondered about the use of the term "sulci" throughout this work to refer to such a wide variety of features as to speculate about its definition (Figure 6). However, there is a historical rationale for the application of deliberately vague terminology to extraterrestrial geologic features. In the early days of planetary exploration, most missions were brief flybys and images were acquired at high speed and great distances with relatively primitive equipment, so details were often sketchy at best. Furthermore, in order to avoid using terrestrial geologic nomenclature that carries genetic implications and may well be proven incorrect in the future, Latin terms such as sulci (groove), fossa (ditch), dorsa (ridge), planitia (plain), regio (region) and terra (land) are used to "classify" extraterrestrial surface features, but as seen for example in Figure 6, some of these terms are used only in the most general sense imaginable.

Therefore the reader should not impute a relationship between Enceladan features based on their IAU generic designation. However, where an actual geologic term is used in this work, such as describing Labtayt Sulci as a "graben", it should be

understood that this usage is an interpretation by the author based on geometric comparisons to terrestrial analogs.

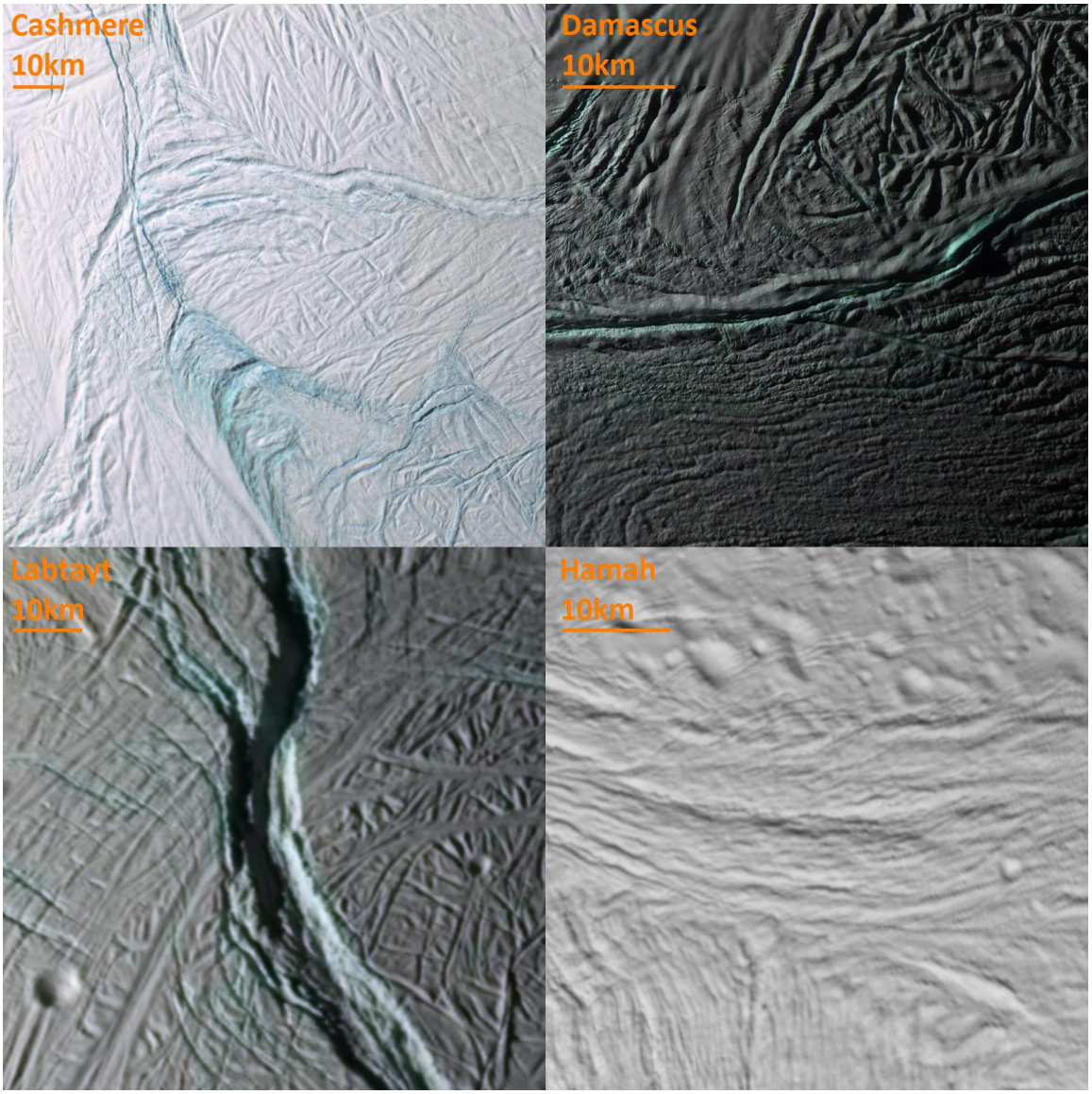


Figure 6. Comparison of four different feature types all referred to as sulci; clockwise from top left: Cashmere (800 x 800 pixel crop from PIA06254), Damascus (800 x 800 pixel crop from PIA11112), Hamah (800 x 800 pixel crop from PIA08353), and Labtayt (400 x 400 pixel crop from PIA11133). Due to the variable obliquity of the views, scale bars are approximate. Base images courtesy NASA/JPL/Space Science Institute; annotated by the author.

METHODS

The approach to understanding the tectonic continuum of Enceladus was to apply the three-part "detailed structural analysis" employed by structural geologists and those engaged in regional tectonic analysis (Davis, 1984; Davis and Reynolds 1996):

- Descriptive analysis
    - Recognize and identify geologic structures; measure their size and orientation; describe their physical and geometric components
    - Crater counting was performed over selected regions to attempt to determine relative ages; the results were inconclusive and unexpected
- Kinematic analysis
    - Based on geometry, reconstruct displacement patterns that took place during the formation of regional tectonic features
- Dynamic analysis
    - Interpret the forces, stresses and processes that create structures and regional tectonic features

In addition, a simplified geophysical model was created, with the aim of better understanding conditions within Enceladus that may have a bearing on material properties and behavior under distinctly extraterrestrial circumstances. The geophysical model proved to be unexpectedly valuable, as it provided the pivotal insight into understanding the apparently contradictory surface geology revealed by the structural analysis. The following sections explain these methods in detail.

Data Source

The primary data source for this project was high-resolution imagery returned by the Cassini orbiter, launched from Cape Canaveral Air Station on October 15, 1997. It is part of a binary spacecraft, the NASA/ESA/ASI Cassini-Huygens mission to Saturn and Titan. The ESA-built Huygens lander touched down on the surface of Titan on January 14, 2005. It fulfilled its mission and is no longer operational. The orbiter's main mission was completed in June 2008, and it is now in an extended operational phase known as the Cassini Equinox Mission, in reference to the approach of the Saturnian vernal equinox in August 2009. This is a significant event, as it will expose the far northern latitudes of most of the major satellites to direct sunlight, and therefore optical observation, for the first time since the spacecraft arrived.

In addition to the raw and "press" images used for geologic interpretation, where dimensional and positional accuracy was required (for example, for crater counting) a series of controlled photomosaics of Enceladus produced by the DLR (Deutsches Zentrum für Luft- und Raumfahrt – German Center for Air and Space Travel) from Cassini and Voyager 2 images were utilized (Roatsch et al., 2008). Global coverage is provided by fifteen mosaics in three projections: polar stereographic (90° - 65°), Lambert conformal conic (66° - 21°, secant at 58° and 30°) and Mercator (± 22°, secant at ± 13°), projected onto a sphere of radius 252.1km (idem). The availability of the DLR photomosaics greatly facilitated mapping and contextual realization. The unannotated base images from which the DLR 1:500,000 scale mosaics were created are

approximately 20% larger and therefore these were used instead of the finished Adobe® Portable Document Format (PDF) products to provide higher resolution and greater accuracy. They were downloaded from the NASA PDS node.

Saturn's equatorial plane is tilted at 26.73° to its orbital plane, causing it to experience a northern-hemisphere winter since the autumnal equinox in 1995, and therefore, only low-resolution Voyager 2 images of the north pole of Enceladus were available for preparation of the DLR mosaics (Roatsch et al., 2008). However, the March 2008 Enceladus flyby provided the best resolution images of the northern cratered plains yet, allowing crater counting over a limited area not covered by the DLR maps. For this region, a special 10°x10° oblique orthographic grid was generated and fitted to the image (see Figure 4; crater counting and the technique used to produce the grids will be discussed in detail in a later section).

Reference Grid Construction

Since the unannotated base images lacked any form of reference grid to accurately locate features and calculate areas, it was necessary to create them. All grids were generated using IMSIDesign TurboCAD 15 Computer Aided Design (CAD) software at a scale of 1mm = 1km with precision set to three digits for angles and lengths. The stereographic projection has the property that it is the only map projection that is both conformal and a true geometric projection (Snyder, 1993), so grid construction was straightforward. Grid spacing for all projections was set at 2 x 2°, except within 10° of the pole where 2 x 6° was used for clarity. The location of the grid lines were defined by

the intersections of the generators with the stereographic image plane, as radial distances in mm/km. The outer diameter of the plot, 223.556 space units (in this case, mm) was then divided by the mean diameter of the DLR raw mosaic bitmap, 2030 pixels, to obtain a scale factor for plotting the grid. The finished grid was converted from a vector to a bitmap image, converted again to a format that supports transparency (Portable Network Graphics, or PNG), overlaid on the photomosaic and then saved as a lossless bitmap (Tagged Image File Format, or TIF) in Adobe® Photoshop CS3 Extended for analysis.

Reference grids for Lambert conformal conic and secant Mercator projections cannot be created entirely graphically. The method used for latitudinal grids in both cases employed the graticule on the DLR PDFs as reference points to obtain a set of coordinates of pixel values (x) against latitude (y). These data were entered into a spreadsheet (Microsoft Excel) and the trendline function was used to derive a formula that would output a latitude in decimal degrees for any given pixel value. Third-order polynomial functions were found to give an excellent fit ($R^2 \geq 0.999999$) for both projections (Appendix D). As stated by Yang et al. (2000), this is an acceptable method where "the relation between two projections… [is] difficult to obtain or the analytic expression of the original map is undetermined".

Longitudinal grids were trivial for the Mercator projection (as the grid is orthogonal and there is no east-west variation), but were graphically constructed for the Lambert conformal conic projection. The Lambert conformal conic projection presents

the appearance of an unrolled section of a conical frustum, but the property of conformality imposes distortions that cannot be geometrically derived by projecting a sphere onto an actual secant cone (Snyder, 1993). The graphical procedure was as follows: the exact dimensions of the fan-shaped raw mosaics were recreated in CAD software at a scale of 10 pixels = 1 mm (for reasons related to the on-screen display of the CAD drawing grid) at triple-digit precision for both angles and lengths. The inner and outer radii and the included angle between the edges of the mosaic were determined by direct measurement from this construction using the appropriate CAD tools. The included angle was divided by 45 to obtain a 2° step size, and appropriately spaced lines were added. The inverse function from the spreadsheet trendline referred to above was used to determine the radii for the latitudinal grid arcs (rounded to the nearest pixel). Once trimmed of construction lines, the completed vector grid was exported, converted and overlaid on the photomosaics in an identical procedure to that described above, with the additional step of creating a horizontally mirrored version for the southern hemisphere mosaics. See Appendix D for more details.

The image used for crater counting in the Ali Baba region presented a special challenge. Reference points approximately equidistantly spaced along the horizon were chosen to represent a segment of a circular arc (which close inspection shows they are not, but since the DLR mosaics are based on an entirely fictitious sphere it was definitely not worth the effort to create an elliptical grid for this purpose) and the center and radius were derived from these in CAD. Fortunately, several prominent features are

visible in this image and they were used in conjunction with the DLR mosaics to locate a few control points with known latitude-longitude values. It was then relatively straightforward (if tedious – see Appendix D) to manually create a tilted and rotated orthographic grid, and overlay it on the image (Figure 7).

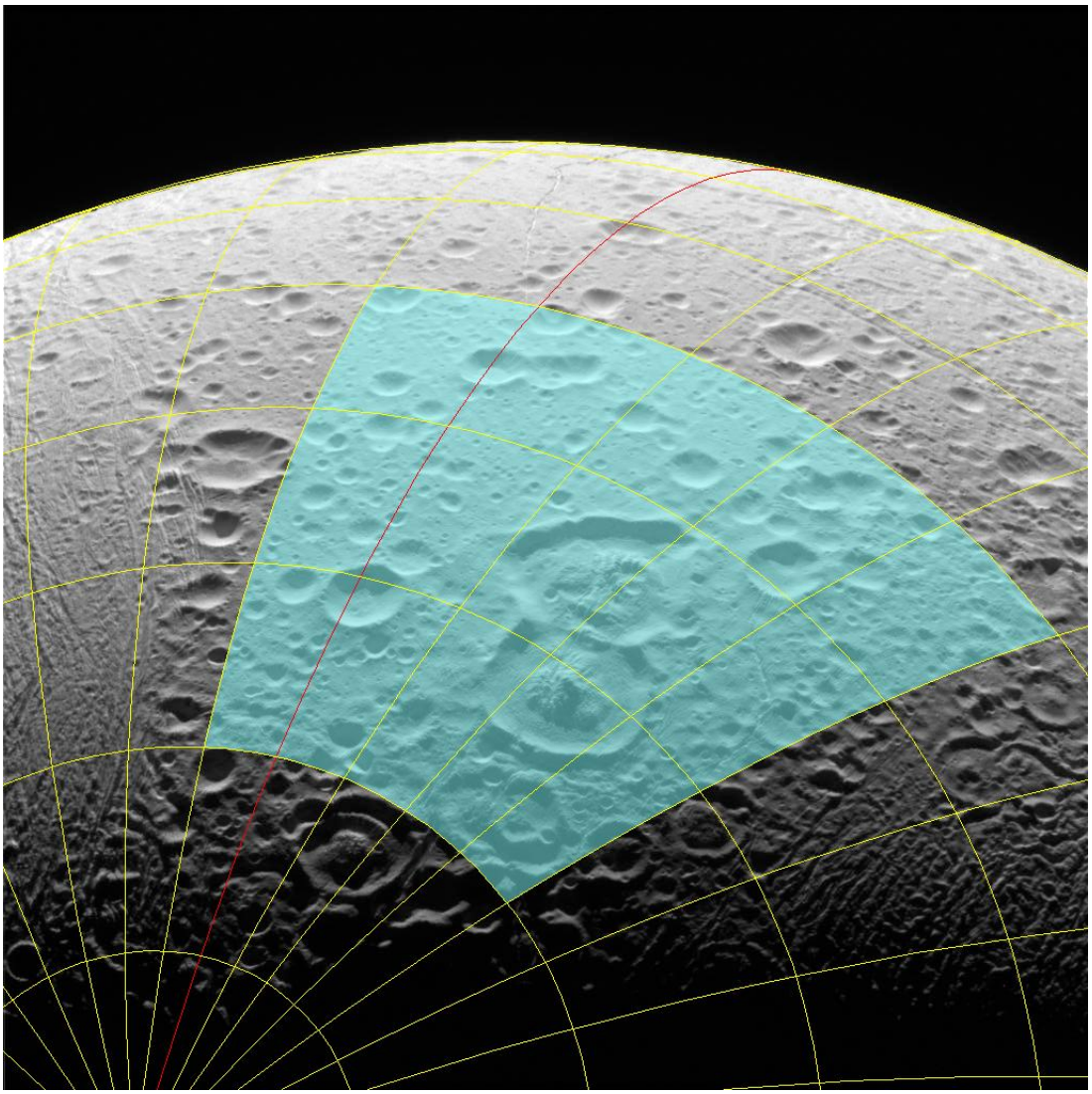


Figure 7. Raw image N00103768, acquired during the March 2008 flyby through the CL1 and CL2 filters (i.e. it is panchromatic) at a range of 31,856 km. 10° x 10° grid added by the author; the counted area is highlighted and the prime meridian is indicated in red. Base image courtesy NASA/JPL/Space Science Institute.

Accuracy and Scale

The stated positional accuracy of the DLR photomosaics is given as: 736m (*x*), 335m (*y*), and 608m (*z*) (Roatsch et al., 2008). One degree on the surface of the reference sphere = 4400 m. Surface features officially named and ratified by the International Astronomical Union (IAU) are located to an accuracy of 0.01° (44 m) and sized to an accuracy of 100m for craters only (see Appendix F). Due to the lack of a sufficiently accurate control network at this time, neither the DLR mosaics nor the data presented here conform to US National Mapping Accuracy Standards. At the dimensions of the base images used here, the following scale factors (rounded to the nearest meter) apply:

Table 1. Scale variation across each mosaic (from Appendix D).

Projection	Maximum	Secant/tangent	Minimum
Polar stereographic	110 m/pixel @ 65°	108 m/pixel @ 90°	n/a
Lambert conformal	104 m/pixel @ 66°	110 m/pixel @ 30/58°	113 m/pixel @ 21°
Secant Mercator	113 m/pixel @ 0°	110 m/pixel @ 13°	105 m/pixel @ 22°
Oblique orthographic	190 m/pixel	n/a	n/a

The Ali Baba region used a raw Cassini image (i.e. not calibrated or validated) with a scale of approximately 190 m/pixel, calculated by multiplying the range to the target by the field of view of a single pixel (Porco et al., 2004) as follows:

Scale (m / pixel) = range (m) x 5.9907×10^{-6} (radians, Narrow Angle Camera)

Since this image was not reprojected onto the control network, the absolute accuracy of the crater count is probably somewhat lower than that achieved using the DLR mosaics;

however, the low-angle illumination was very helpful in enhancing the contrast of low-relief features. The $\log_{10}$ - $\log_{10}$ scale of the crater counting plots makes them fairly robust against small systematic errors so the results are unlikely to have suffered unduly (however, see the disclaimer in Appendix E). Other raw images that were used throughout this work employed the same method to determine scale, where necessary.

Distortion

Linear distortion was calculated from the spreadsheet data (Appendix D). The following values were obtained:

- Polar stereographic distortion varies from 0% at the pole to a maximum of negative 1.62% at 65° (that is, the image scale must be increased to represent the object scale)
- Lambert conformal conic distortion has three maxima: negative 5.85% at 66°, positive 3.03% at 44° and negative 2.63% at 21° with minima of 0% occurring at the secant intercepts of 58° and 30°
- Secant Mercator distortion has three maxima: negative 5.09% at 22°, positive 2.63% at 0° and negative 5.09% at -22° with minima of 0% occurring at the secant intercepts of 13° and -13°

Linear distortion of this magnitude (≤~5%) is irrelevant for the purposes of this work; where accurate areas were required (e.g. crater counts) the reference grids were used.

Terrain Types and Visual Interpretation

Enceladus presents special problems for geologic interpretation. It is effectively devoid of color and/or albedo variations that make for a straightforward, first-order distinction between terrain types on other bodies (such as the Moon, Io, Ganymede, Titan, Miranda, and Triton, for example), so they must be distinguished by geomorphology alone. In some cases, the difference is obvious, in others it is difficult to state with confidence whether there is a gradual transition between two adjacent terrains, of if the transitional terrain itself represents a geologically distinct region (Figure 8).

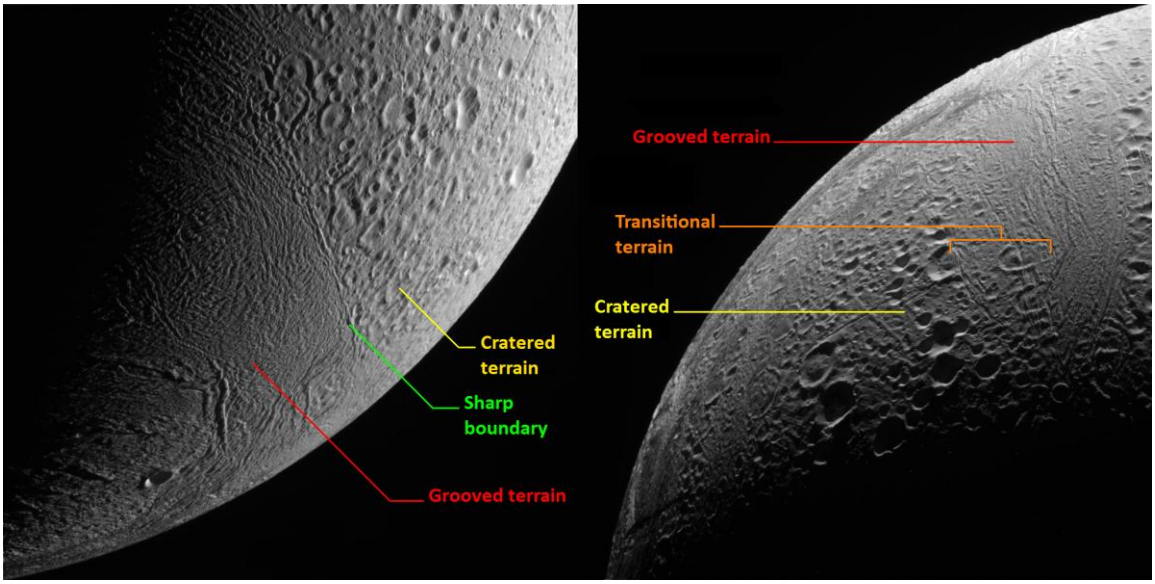


Figure 8. This composite shows a comparison between sharp (left) and gradual (right) boundaries between terrain types on Enceladus. Both panchromatic (CL1-CL2 filter) frames are from the northern hemisphere. Note the apparent increase in surface roughness near the terminator; this effect is enhanced on airless bodies by the lack atmospheric scattering. Raw images N00103769 (L) and N00103767 (R) courtesy NASA/JPL/Space Science Institute; annotation by the author.

The appearance of low-contrast surface features is also critically dependent on lighting angle. This effect is clearly seen on the Moon as the phase changes during each lunation; a terrestrial example is shown in Figure 9.

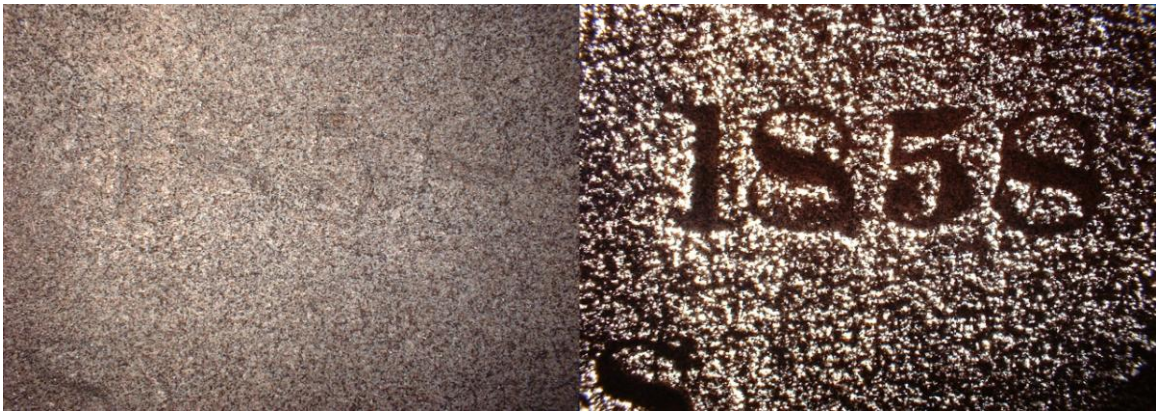


Figure 9. A comparison showing the effect of lighting angle on the visibility of low-contrast surface features, from the 1858 grave marker of Catherine Rowley, Liverpool Pioneer's Memorial Park, New South Wales. The left image was acquired with a perpendicular light source, the right with a grazing incidence source while shaded from ambient light. The appearance of this surface under more typical lighting conditions lies somewhere between these two extremes. (Photos: Scott McLeod)

Resurfacing processes have modified some impact craters almost beyond recognition; whether some crater-like features are in fact derived from impacts or have an endogenic origin, and the possible implications of their modification, will be discussed in more detail under Results. One consequence of the low gravity and uniform near-surface lithology is the conspicuous absence of ejecta blankets and rayed craters, which can often be used to deduce stratigraphic relationships. Since almost all impact structures are circular when first created (Melosh, 1989), even these unadorned craters can still be useful as kinematic indicators when deformed.

False-color RGB composite images (see Figure 2 and Appendix B) were useful in accentuating otherwise obscure relationships between terrain types that in some cases did not appear substantially different at visible wavelengths. Specific examples appear in the Results section, with comparisons to other Saturnian moons imaged at the same wavelengths. Lacking not only color and brightness variations, but erosion (as we experience it) and drainage patterns to reveal topography, careful examination of shadows and limb geometry proved crucial in interpreting the relationships between surface features, and the nature of contacts between geologic units.

Kinematic Analysis

Like descriptive analysis, kinematic analysis of Enceladan surface features must rely entirely on images obtained from thousands (occasionally, hundreds) of kilometers away, without ground truth data for verification. Unfortunately, kinematic analysis in geology often relies on mesoscopic or microscopic motion indicators that are not apparent in aerial photography, let alone satellite imagery. With most images having scales of over 100 m per pixel, correctly interpreting features much less than a few kilometers in size becomes dubious and it is preferable to use the largest motion indicators available, such as deformed craters and careful analysis of shadows to infer regional topography. In the latter case, the uniformity of the Enceladan surface is beneficial since in visible light there are virtually no color variations to misinterpret;

brightness variations are due to illumination angle and surface roughness, with rougher surfaces appearing somewhat darker.

Dynamic Analysis

Reconstructing the forces that produced the observed structures was the most difficult and counter-intuitive part of the entire project. Much of what is seen on the surface of Enceladus, particularly within and around the SPT, at first appears reassuringly familiar, but close inspection shows serious flaws in interpreting these as analogs of terrestrial-style tectonic activity.

Crater Counting

Crater counting is an accepted method for assigning relative ages to planetary surfaces based on the assumption that when averaged over geologic time, impact cratering occurs at a more or less constant rate, and the rate at which craters of any given diameter are produced is dependent on the size distribution of impactors in interplanetary space (Arvidson et al., 1978). It has been found that this size distribution follows an approximately inverse-power relationship, so that large craters are formed much less frequently than small ones (as common sense suggests). Where the absolute age of a particular surface is known, such as on regions of the Moon visited by Apollo and Luna sample-return missions, the crater counts for those areas can be used to calibrate the relative age series obtained for other locations. Unfortunately, for the

outer solar system (beyond the main asteroid belt) absolute ages are unknown and the impactor population distribution is controversial, so at best only relative ages can be determined by this method (McKinnon et al., 1984). When an area is resurfaced by some geologic process, it erases the existing cratering record and "resets the clock"; partial erasure is also possible, which complicates the procedure, especially if the mechanism is not well characterized. It is the timing of these resurfacing processes that is of interest here, rather than their actual ages.

The population of interest is impact craters within a geologically contiguous region on the body under study; while Enceladus is the target of interest, a count was also performed on Epimetheus to provide a comparison with an apparently unmodified surface (this did not work out as anticipated, as Epimetheus appears severely depleted in small craters relative to Enceladus, implying some selective resurfacing process may be at work, or an abnormality in the impactor population). Once a region is selected as suitable for counting, its area is determined from the reference grid and all craters that lie within it are counted, regardless of degradation. The only variable measured is crater diameter. Crater sizes are geometrically binned on a √2 scale, with one bin boundary at 1 km. Due to the scale of the base images it was impractical to attempt to measure craters much smaller than this so 1 km was chosen as the lower bound. The crater counts were plotted on both a cumulative frequency distribution and a relative frequency distribution or "R plot" as described in Arvidson et al. (1978) (Appendix E).

Geophysical Modeling

In order to better understand the conditions within Enceladus, a simplified geophysical model was created using Microsoft Excel (see Appendix C for the formulas used and tabulated values obtained). It was based on the known physical parameters of size, mass, and density, and the assumption that the interior is fully differentiated into a water ice lithosphere/mantle, with an estimated average density of 1000 kgm^{-3} (since the depth to any solid-liquid phase transition is unknown), an outer core composed of silicate rock with an estimated average density of 3,000 kgm^{-3} (similar to terrestrial basalt), and a metallic inner core with an estimated average density of 8,000 kgm^{-3} (similar to iron). The combined density of the inner and outer core is assumed to be 3,300 kgm^{-3}, the same as the Moon and slightly less than Io (3,530 kgm^{-3}). Densities within each layer are assumed to remain constant with depth.

One of the main purposes of this model was to determine the upper limits of pressure within the icy mantle. Water ice can exist in at least 10 polymorphs, most of which, unlike the terrestrially common and ubiquitous hexagonal form ice Ih, are denser than liquid water (Eisenberg and Kauzmann, 1969; Franks, 1972; La Plata 1973), and the presence of high-pressure ice would have a fundamental bearing on the behavior of material at any liquid-solid interface that might exist below the surface. The rationale for choosing a reasonably high value for the combined inner/outer core density was that it would provide a (slightly) more extreme maximum pressure at the core-mantle

boundary. However, the solution (Figure 10) indicated that the difference in terms of suitable environments for high-pressure polymorphs was insignificant (see Results).

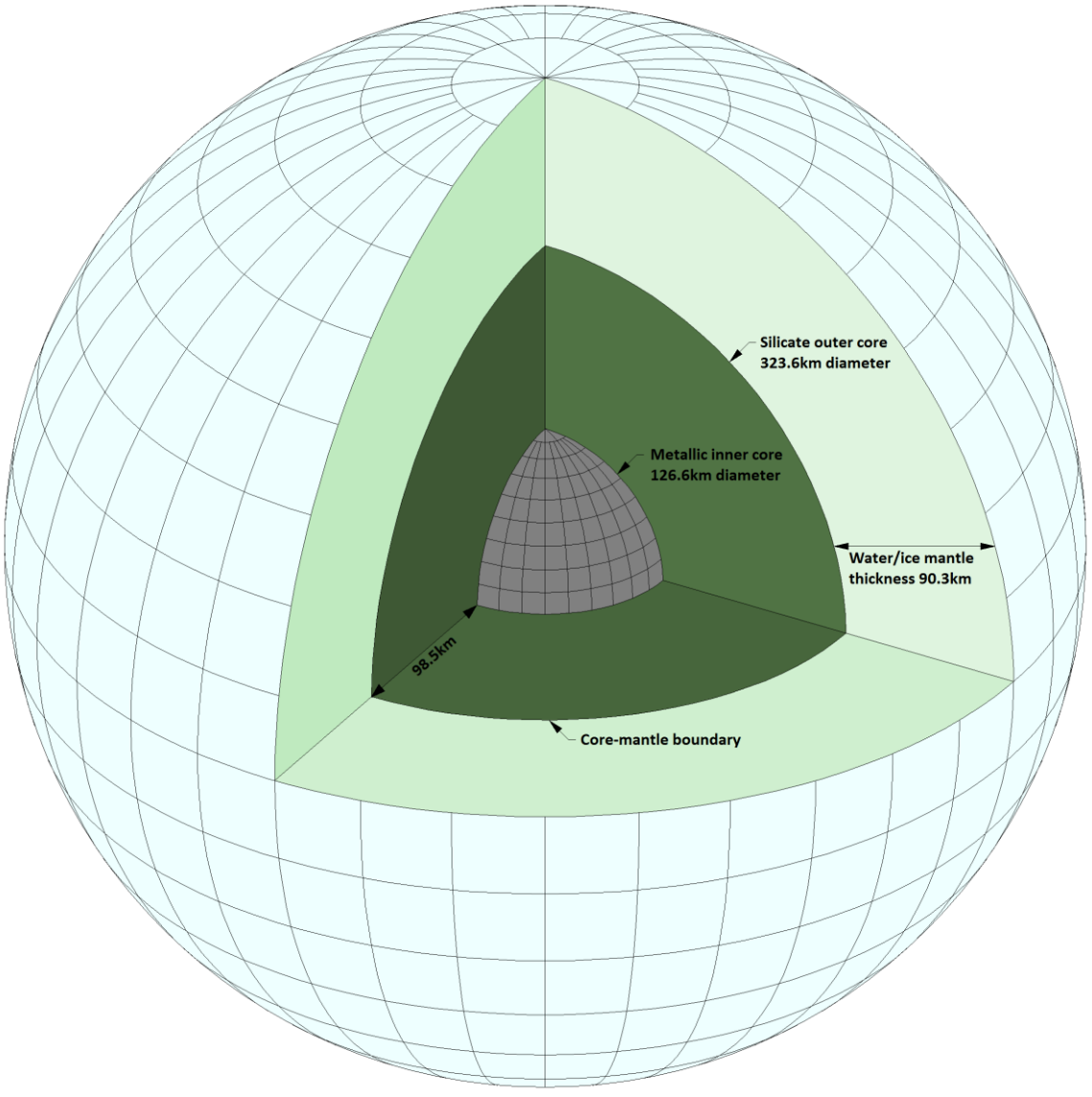


Figure 10. A scale drawing showing the thickness of the water/ice mantle and silicate outer core, and the size of the metallic inner core derived from the results of the spreadsheet model described in the text. Depth to the core-mantle boundary is 90.3 km; the solid-liquid mantle phase transition is not shown (Scott McLeod)

The apparently high levels of available internal heat and the uncontaminated surface are consistent with a fully-differentiated body (in the sense that no silicates are seen to be mixed with the ice, even in excavated crater interiors), though the exact state of the interior will remain unknown until a moment of inertia is obtained.

Once the basic parameters of individual and combined densities were selected, the model was constructed in two phases, the first for the thickness of the layers and core diameter, using the following method:

- The first step was to calculate the thickness of the mantle, by treating the combined inner/outer core as a homogenous body of density 3,300 kgm^{-3}
- The radius of the inner core was increased in 300 meter increments, and the volume of the overlying spherical shell was reduced by a commensurate amount at each step
- The combined mass was calculated at each step
- The diameter of the combined inner/outer core (and therefore the depth to the core-mantle boundary) was set at the value giving the closest approximation to the known mass of Enceladus for the remainder of the calculations
- The radius of the inner core (density 8,000 kgm^{-3}) was increased in 300 meter increments, and the volume of the spherical shell comprising the outer core (density 3,000 kgm^{-3}) was reduced by a commensurate amount
- The combined mass was calculated at each step

- The diameter of the inner core was set at the value that produced an equal mass to that obtained previously for the combined inner/outer core

This procedure gave the following results:

- Depth to core-mantle boundary: 90.3 km
- Outer core radius: 161.8 km
- Inner core radius: 63.3 km

The values obtained by this method are consistent with those of Kargel (2006), who used a model with a homogenous "rock [sic] core" of 3,000 kgm^{-3} and a "volatile crust" of 1,010 kgm^{-3} to derive a core radius of 169.04 km and a depth to the core-mantle boundary of 83.26 km.

The next phase was to calculate pressure at depth within the mantle. The common formula for pressure under a column is

$$p = \rho g h$$

Where ρ = density, g = acceleration due to gravity, and h = column height. However, expanding gives

$$p = \rho (GM / r^2) h$$

where r is the body radius to the base of the column; therefore it is only valid in this form if the height (or depth) of the column is small relative to r. It can also be seen that it implies the column is not self-gravitating, i.e. the part of the column below some point does not exert a gravitational force on the part above that point (and vice-versa). This is

a reasonable assumption in the case of surface atmospheric pressure calculations (because the mass and therefore gravitation of the atmosphere is small), but not here.

An additional complication arises in the case of thick spherical shells. Consider a 1 m^2 area on the surface on Enceladus. Since the pressure force due to gravity is directed radially inward everywhere, at the depth of the core-mantle boundary the area "under" 1 m^2 measured at the surface is only

$$A = A\,((161.8)^2 / (252.1)^2)$$

$$\approx 0.412\ m^2$$

So the column can no longer be treated as a prism, it is a frustum. There are various ways of approaching this problem, but since the spreadsheet already existed it was modified appropriately and reused. The problem of self-gravitation is simplified considerably by Newton's First Theorem (e.g. Zeilik and Gregory, 1998) which states that no gravitational field gradient exists within a hollow, spherically symmetrical shell. Therefore, only the weight of the overlying shell (again, calculated numerically in 300 meter thick increments) needs to be considered as it exerts no gravitational force on the spherical volume within it. A consequence of this, and the large stepwise increase in density at the outer core, is that the value of *g* increases with depth, reaching 0.1493 ms^{-2} at the core-mantle boundary, about 32% higher than at the surface.

With these caveats accounted for, the revised spreadsheet gave a pressure of ~18.4 MPa at the core-mantle boundary. Lastly, the spreadsheets were reused again to calculate moments of inertia for various degrees of differentiation. An undifferentiated

(completely homogenous) model, considered as an end-member, has a moment of inertia 31.6% higher than the fully-differentiated version described above (see Appendix C for details).

Enceladus's mass is sufficient to determine an accurate value for the dynamic potential Love number k2 by Doppler tracking of the Cassini orbiter, but whether an adequate number of close flybys devoted exclusively to gravity studies are actually scheduled remains to be seen (P. Thomas, pers. comm., March 7, 2008). During a gravity study, the spacecraft must remain absolutely passive, so it cannot use thrusters or reaction wheels to pitch, yaw, roll, or translate. This requirement, combined with the need to have the high-gain antenna pointed in the right direction for the duration of the tracking, means that other remote-sensing opportunities must be sacrificed. In the case of Titan, a prime target of the original mission, many flybys were planned (more than 50 having been executed at the time of writing) and obtaining gravity measurements was a known objective. Enceladus has proved to be an unexpected boon for planetary science, but orbiting so close to Saturn (compared to Titan) makes scheduling flybys difficult and infrequent, and exploring its surface and determining the composition of the geyser plumes are likely to take precedence over gravity studies.

RESULTS

For the sake of clarity and to avoid repetition, the descriptive, kinematic and dynamic analyses (where possible) are grouped by analysis type rather than feature type; within each section the feature types follow an approximate chronological sequence from oldest to youngest. Due to the impracticality of describing an area of almost 800,000 km^2 at a uniformly meaningful level of detail, a broad overview of the major morphological characteristics is given, accompanied by images of typical examples of the features in question. The final section of this chapter includes geophysical modeling results and their implications with respect to understanding Enceladan tectonics.

Surface Features: Descriptive Analysis

Cratered Plains, Craters and Crater Counting

There are two major terrain types on Enceladus: ridged plains and cratered plains (herein abbreviated as rp and cp, respectively). Under low-angle illumination, the cp regions also reveal muted, low-relief ridges, but visually the difference is obvious, with the rp regions being mostly or entirely devoid of impacts and with the ridges being clearly visible under all lighting conditions, while the cp regions are more-or-less dominated by impact features. While as stated this is a purely subjective distinction, it is useful to note the difference in crater counting statistics (see below) which indicate that even a fairly old rp region (i.e. one that has a usefully countable number of impacts),

such as the Ebony Dorsum region, is nevertheless approximately $10^{-1.5}$ or $1/30^{th}$ the age of the typical cp units. Very young rp units have so few (or no) impacts as to make determining relative age accurately by this method alone a fraught proposition.

Cratered plains cover at least ~40% of the surface of Enceladus, calculated by measuring from the DLR photomosaics. There is some uncertainty as to the exact value due to poor lighting and low resolution over parts of the leading hemisphere, but 40% (or ~324,000 km^2) is a reasonable minimum. They dominate the northern hemisphere, though with significant incursions of ridged terrain (see for example Figures 7 & 8). Overall, though, the degree of cratering is notably low compared to other moons in the Saturn system (Figure 11).

Impact Craters Impact craters are endogenous structural features produced on solid surfaces by high-speed collision of interplanetary debris of all sizes from microscopic dust to asteroids. To produce a true impact crater (as opposed to a "pit" which lacks the geological characteristics of a true crater), the speed of the impactor must be in excess of about 5 kms^{-1}. Beyond that speed, the kinetic energy exceeds about 12 kJ/g, the energy released is sufficient to dissociate the molecules of any solid material, and the explosive result is termed a hypervelocity impact (Dietz, 1959). The vast majority of impact craters are approximately circular in outline, as may be clearly seen on the Moon, Mars, Mercury and indeed throughout the solar system, with only extremely shallow impacts producing elliptical features (e.g. Melosh, 1989). This allows

ovalized or otherwise deformed craters to be used as strain indicators. Morphologically, there are basically two types of crater, simple and complex (e.g. Melosh, 1989):

- Simple craters are characterized by raised, circular rims and bowl-shaped floors
- Complex craters possess raised rims, though often less circular than those of simple craters as their size makes them more likely to interact with pre-existing structural fabric in the country rock, (more or less) flat floors, terraced rims, and central peaks or, if they are large enough, one or more interior rings (not all features are necessarily present in a single crater)

The size at which the relatively abrupt transition from simple to complex craters occurs is dependent on both surface gravity and composition; for silicate bodies such as Earth, Mars and the Moon it scales approximately to the function $1/g$; for icy surfaces the transition occurs below this line (Melosh, 1989). Extremely large impacts take on the form of a multiring basin, with Mare Orientale on the Moon (e.g. PIA00120), the Caloris Basin on Mercury (e.g. PIA11077) and Valhalla on Callisto (e.g. PIA01649) being excellent examples (Melosh, 1989). The largest craters on Enceladus are Ali Baba, 39.2 km diameter, and the immediately adjacent Aladdin, 37.4 km; both are visible within the highlighted region in Figure 4. While they are definitely not simple craters, their morphology suggests they are highly modified, with bulging central domes that are distinct from the flat floors and sharply defined peaks of unmodified complex craters (see Figures 11 and B1 for comparison).

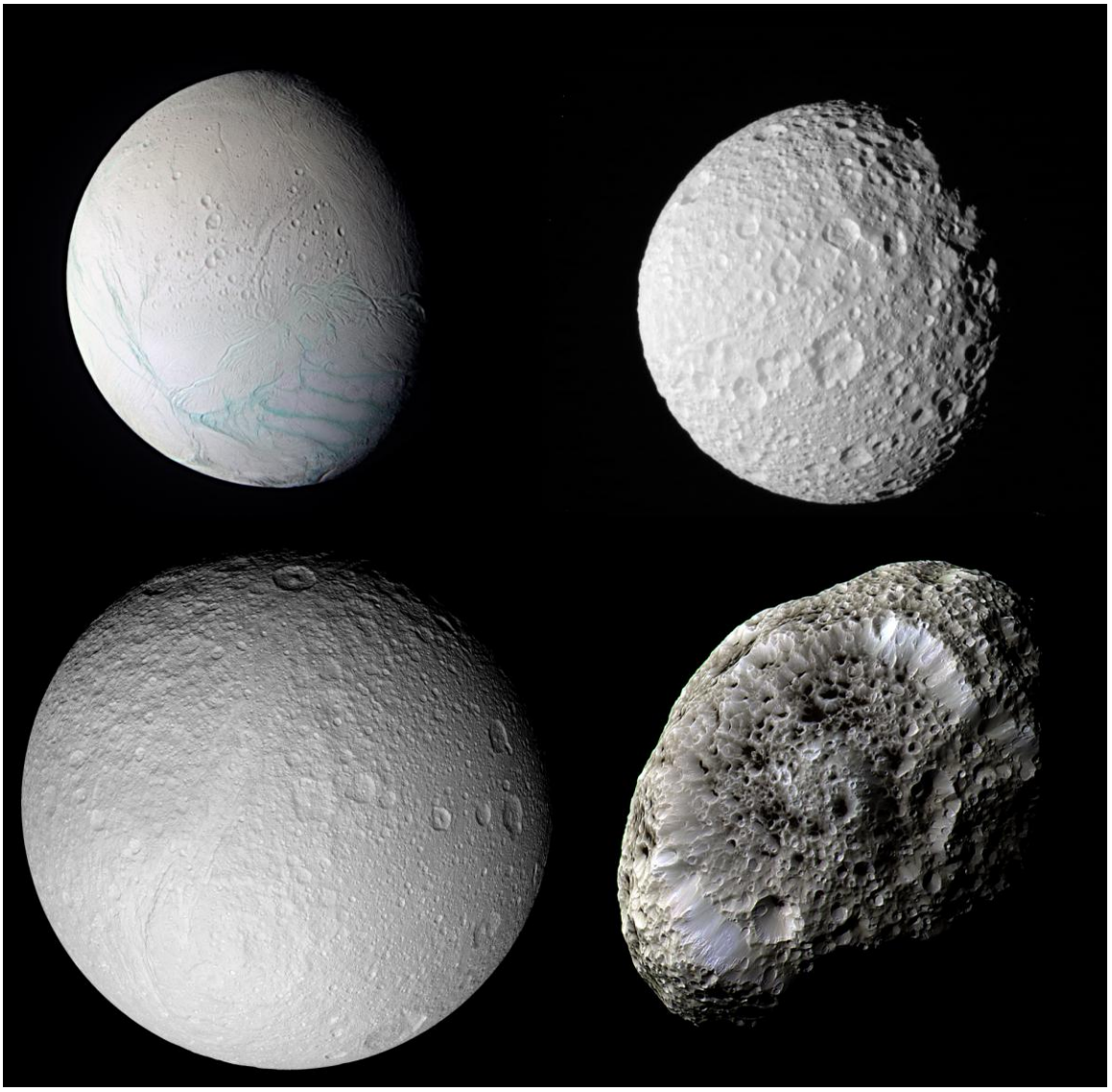


Figure 11. A visual comparison (not to scale) of cratering densities and morphologies on four Saturnian moons; see Figure 5 for their relative locations. Clockwise from top left: Enceladus, 504 km (PIA06249); Mimas, 398 km (N00037625); Hyperion, 370 km (PIA07740); Tethys, 1,060 km (PIA07738). Numerous complex craters are visible on both Mimas and Tethys even in this reduced-scale view, and the very smooth limb of Enceladus compared to Mimas is also apparent, an indicator of its generally subdued topographic relief (especially notable for such a small body). The peculiar, "sponge-like" appearance of Hyperion is unique but the high density of impact cratering is obvious. Note also that Enceladus orbits between Mimas and Tethys. Images courtesy NASA/JPL/Space Science Institute; montage by the author.

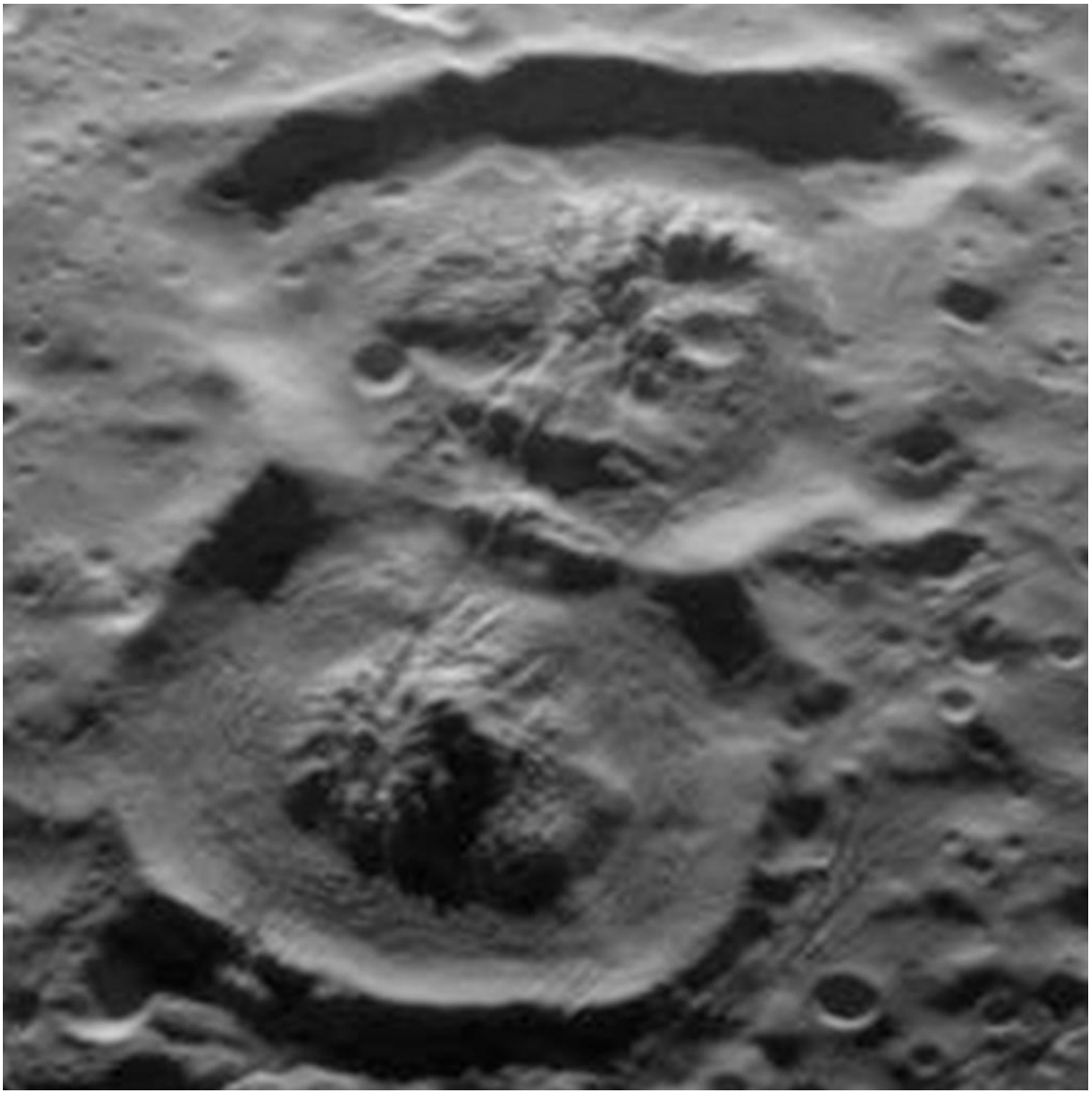


Figure 12. An enlarged (4x bicubic upsampled) 1024 x 1024 pixel crop from N00103768, acquired through the CL1 – CL2 filters at a range of approximately 31,856 km. It shows the two largest impact structures on Enceladus, Ali Baba (top) and Aladdin. They are evidently fairly old, having suffered subsequent smaller impacts, and show signs of considerable post-impact modification. The rims are degraded and irregular, and a lineation (possibly a fracture but difficult to be certain at this resolution) can be seen connecting the central uplifts, which are not the sharply concentrated, well-defined peaks seen in complex craters elsewhere (e.g. Figure 11) but are broad, convex, roughly cabochon-shaped features. Terracing is absent, but traces of wrinkle-like features are just visible on the floor surrounding the central dome of Aladdin. Base image courtesy NASA/JPL/Caltech.

There are no obviously pristine complex craters anywhere on Enceladus, suggesting that the modification processes that affect craters above some critical diameter act rapidly and more or less uniformly across the surface.

An unusual feature of large impact craters on Enceladus is that many of them are connected by networks of closely-spaced, subparallel tensional fractures, almost like "star-cracks" connecting stone chips on an automobile windshield (Figure 13). Note that the fracture patterns indicate stresses in the lithosphere are anisotropic as some almost adjacent craters are not connected.

Crater chains are relatively common throughout the solar system, and are formed by two distinct processes: they can result from "streamers" of material ejected from a larger impact (and are therefore secondary craters) or they can form as primary craters from the nearly simultaneous impact of fragments of a disrupted object. On bodies with significant atmospheres, the disruption can occur due to aerodynamic forces, but in the case of gas giants and their moons it is usually a result of gravitational tidal stress; the impact of comet Shoemaker-Levy 9 with Jupiter in 1994 is probably the most famous example of this phenomenon. The Galilean moons bear ample evidence that this is not an especially isolated occurrence (for example, see NASA/JPL/Caltech image PIA00581). The cratered plains of Enceladus do not bear clear evidence of crater chains, though secondary cratering is extremely unlikely to occur due to the very low escape velocity. There are suspicious alignments of craters (particularly in the northern plains), but these particular features are unusual and difficult to classify (Figure 14).

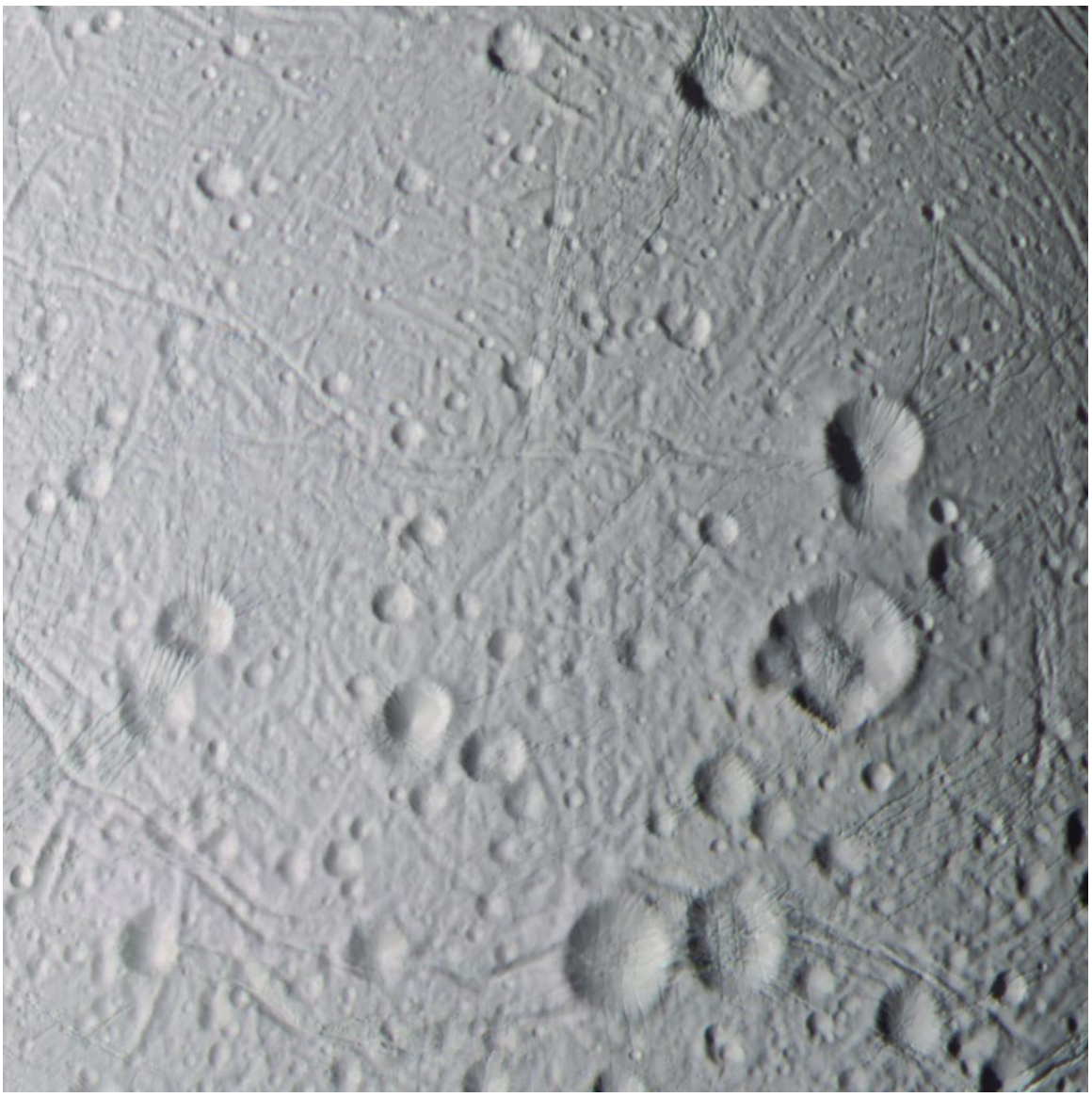


Figure 13. A 1024 x 1024 pixel crop from the enhanced-color mosaic PIA06254, showing fracture networks connecting craters in the southern part of the anti-Saturn hemisphere. The largest crater just to the right of bottom center is Hassan (14.5 km diameter); the large crater with the bulging floor to its upper right is Zumurrud (21 km diameter). This image was acquired under favorably oblique lighting conditions, and it is apparent that except for the very smallest impacts, all the craters have a rather “soft” appearance with rounded rim crests, in contrast to the features seen on other moons in Figure 11. Also visible is the subtly ridged (or grooved) nature of the cratered plains when viewed appropriately. The degraded, low-relief ridges seen here are typical of those seen throughout the cp regions. Courtesy NASA/JPL/Space Science Institute.

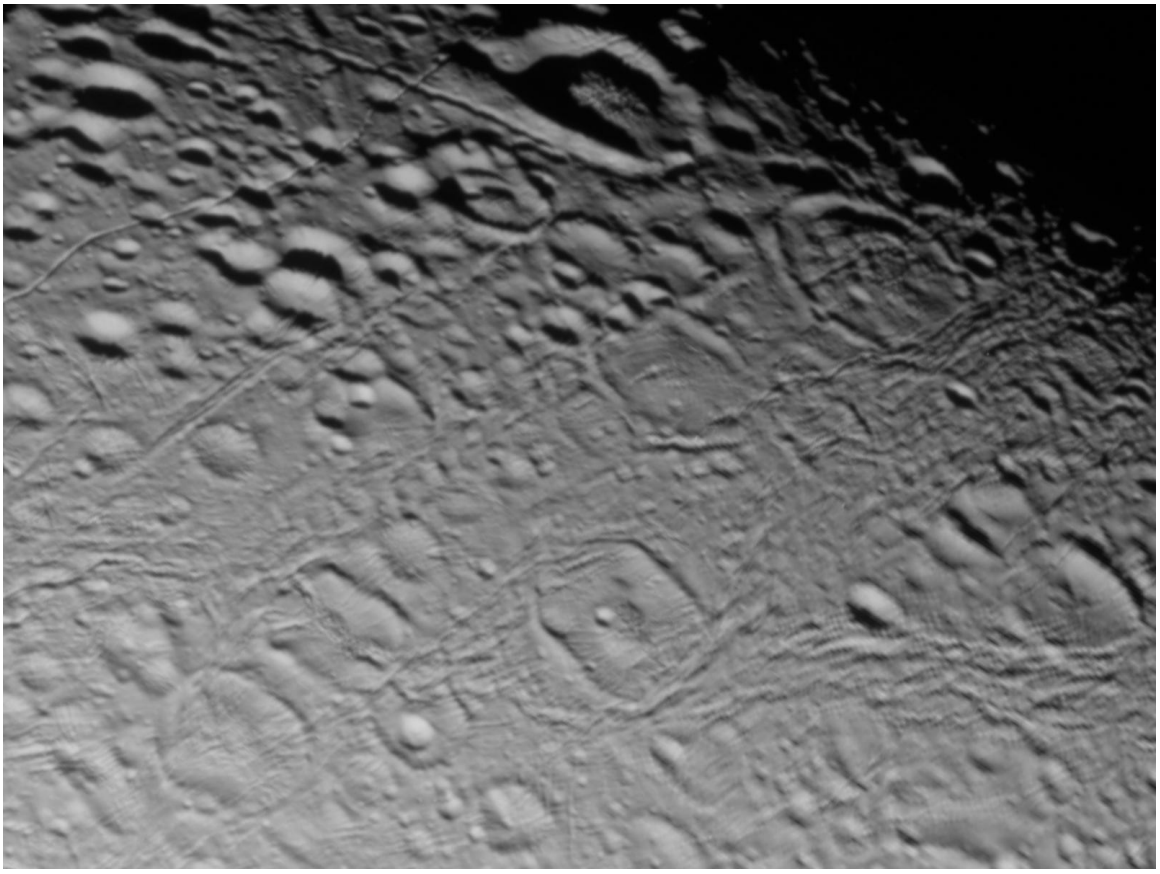


Figure 14. 1600 x 1200 pixel crop from PIA08353. Several unusual features are visible in this image, the most striking being the linear alignment of very low-relief craters (or, possibly, crater-like structures) running diagonally across the frame. Note the numerous subparallel lineations that follow the chain. Craters along this chain range from almost circular at lower left and upper right to almost square and lozenge-shaped (like Ayyub, immediately below the chain). Evidently the geothermal gradient in this region is both very high and laterally discontinuous as evidenced by the highly localized viscoelastic relaxation along the chain, while impact structures nearby remain largely unaffected. This is a common occurrence on Enceladus and is seen even more dramatically elsewhere. Compare the large crater at top center with an asymmetrically bulging floor to the last crater in the chain at upper right. They are virtually the same diameter but the one in the chain has not only been infilled, its rim has collapsed or sunk to a fraction of its original elevation. Courtesy NASA/JPL/Space Science Institute.

Strained craters often occur immediately adjacent to circular ones, as seen in Figure 14. Elsewhere, craters are seen to be elongated, but instead of ovalization by tectonic distortion they are dissected by normal faults at the edges of sulci (Figure 15).

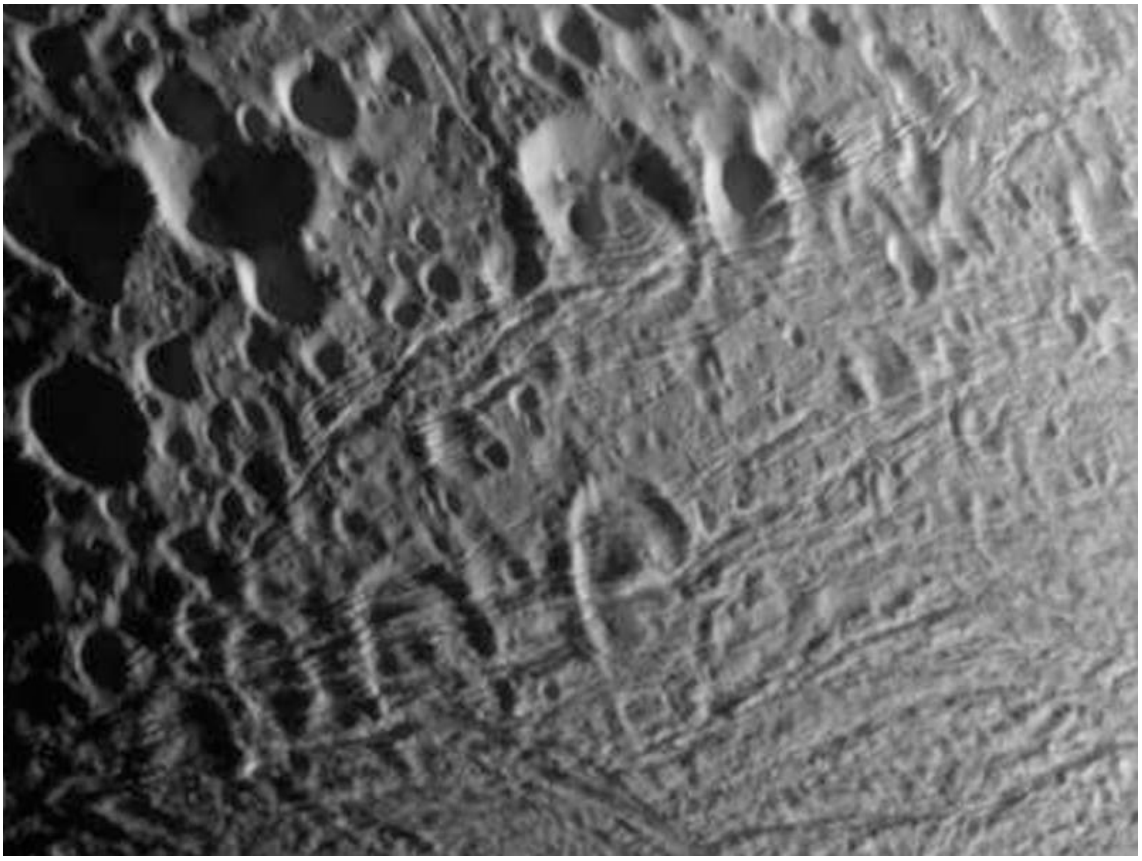


Figure 15. An 800 x 600 pixel crop from a 2x upsample of N00103767, showing dissected craters at the eastern border of Samarkand Sulci. Note the asymmetrically bulging floor of the large crater above center, and the closely-spaced normal faults that have stretched the craters out with their long axes perpendicular to the trend of the faults. The topographic expression of these craters (both positive and negative) has in some cases been completely destroyed proximal to the sulci. Courtesy NASA/JPL/Caltech.

Crater Counting The results of this exercise were quite unexpected. Despite the widely varying appearance of the ridged plains, it appears that all the cratered plains on Enceladus, or at least the ones counted here, are about the same age; the Ebony Dorsum region is not classed as a cratered plain. Fitnah shows a relative excess of impacts in the 4-8km range (bins 5 and 6) and a deficiency in larger craters, but the lower end of the plot is similar to other areas. The curve for Epimetheus provided an

interesting result: it is significantly depleted in craters below about 2.5-3km, an anomalous observation for a geologically "dead" body, and particularly troubling as it was originally selected to provide an unmodified baseline for comparison. Its close proximity to the outer edge of the F ring (<11,000 km) probably allows stray ring material to be drawn onto the surface at a relative velocity too low to cause hypervelocity cratering (~600 ms^{-1}), effectively blanketing small impacts in a layer of dust. This mantle of dust is visible in NASA/JPL/Caltech image PIA09813 (Figure E3), but equally apparent are upslope areas devoid of dust that also bear few small craters. No doubt other processes are involved – which raises questions about the validity of crater counting when applied within a system that apparently possesses the ability to "sort" impactors (the organizational structure of the rings being the best example of this) and possibly to erase, or at least conceal, impacts within a specific size range. More research on these and other moons in the Saturn system will be required to attempt to answer these questions. Perhaps the most important result obtained here is that the northern cratered plains, represented by the Ali Baba count, appear indistinguishable in age (on the basis of this data and analysis) from the southernmost cratered plains represented by the almost antipodal Zumurrud region. This was highly unexpected as the northern plains have long been considered by far the oldest terrain on Enceladus (e.g. Morrison et al., 1984). It is my contention that the northern plains appear much more heavily cratered because the currently highly oblique lighting renders surface roughness far more apparent (and the craters easier to count) on such a low-contrast surface, and

until recently high-resolution imagery of the region was unavailable to settle the issue.

See Appendix E for more details on the procedure and the actual data collected.

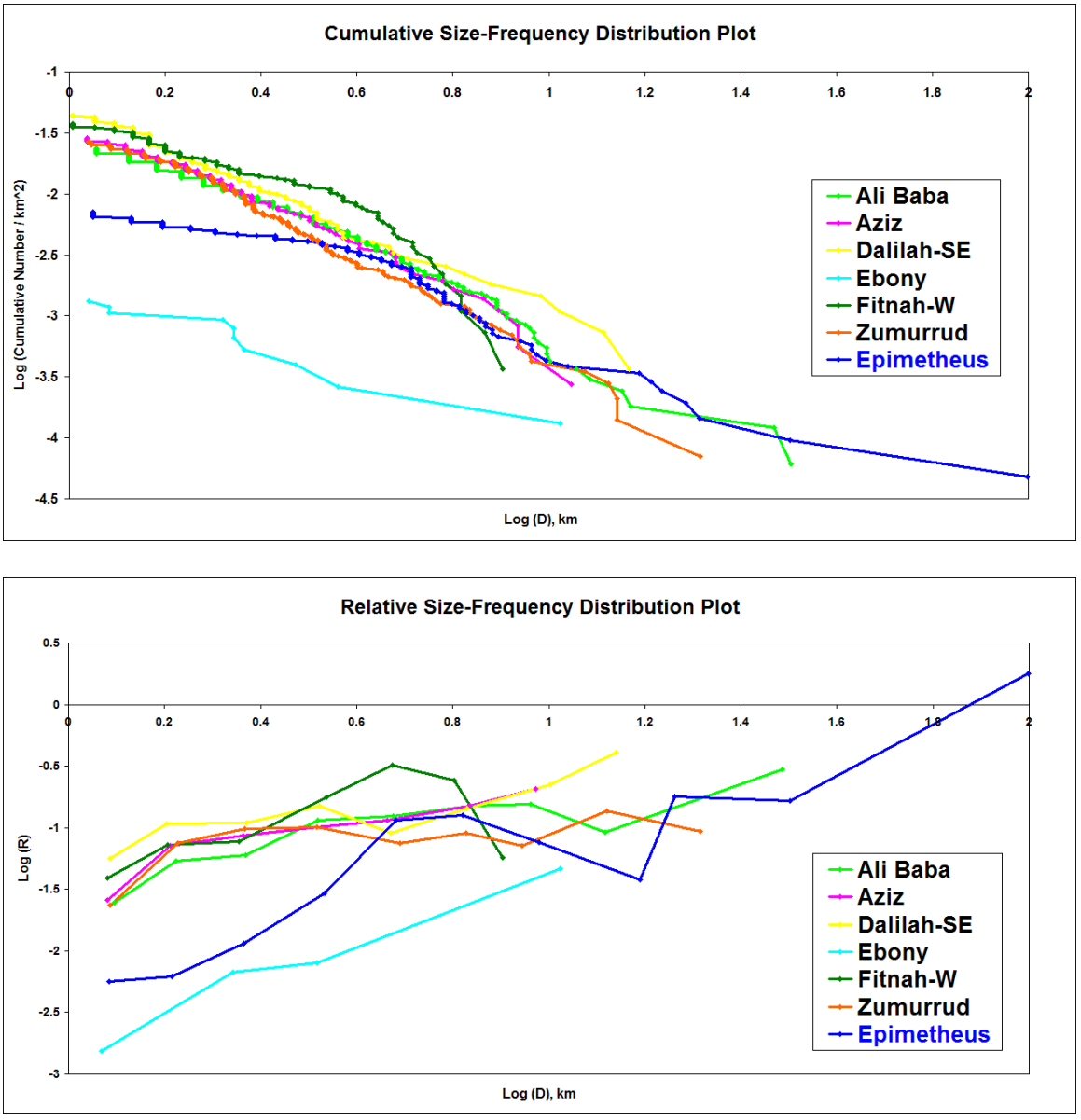


Figure 16. Cumulative and "R" plots for six regions of Enceladus and a partial hemisphere of Epimetheus. Younger surfaces plot lower. $R = (D^{bar})^3 n / A (D_b - D_a)$, where D^{bar} is the geometric mean of the craters counted in a particular bin, D_b and D_a are the upper and lower limits of the bin, A is the area over which the count was performed, and n is the number of craters in the bin. Note that R is dimensionless.

Ridged Plains

Overall, including the SPT, ridged plains cover the remaining ~60% of the surface. Voyager 2 images were of relatively low resolution and some ridged plains appeared featureless, which led to contemporary geologic sketch maps describing these regions as “smooth plains” (Morrison et al., 1984). While they are indeed smooth, they are also covered in low-relief, closely-spaced ridges, and this nomenclature is not used here. These regions can be further subdivided according to whether the ridges are subparallel (Srp) or complex/chaotic (Crp):

- Srp regions often terminate abruptly, with the boundary running parallel to the ridge direction (sulci are considered here to be a subset of Srp units)
- Crp regions often occur far from any borders with cratered plains and grade into subparallel-ridged plains, and may be darker in color than the surrounding Srp units. For example, the ~40 km diameter macula-like feature located at 10°S, 80°W is seen at high resolution to be a concentration of complexly-oriented ridges within an Srp region

The morphology of the ridges varies widely beyond the first-order distinction of their relative alignment. However, thorough examination of the available imagery reveals that some general observations about the relationships between Srp, Crp and cp regions are possible:

- Whenever an rp meets a cp, features on the cp region are always truncated (not the ridges)

- Whenever an rp meets a cp, the rp is always topographically equivalent or, more often, lower – never higher (Figure 18)
- The boundary between rp and cp regions is often extremely abrupt but is not always marked by a visible fracture or fault
- When viewed in UV3-GRN-IR3 false color, rp regions are greener than cp regions, implying they have been exposed to the space environment for less time (solar/cosmic radiation converts crystalline ice to an amorphous form)

Srp Regions These geologic units form the majority of the ridged plains outside the SPT (Figure 17), and some of those within it, notably the terrain immediately south of the grabens that delineate the borders of the SPT.

The overall appearance of most of the smooth Srp units outside the SPT is that of low-relief, very closely spaced ridges that over distances of a few tens of kilometers also exhibit “waviness”; due to shadowing effects this gives a false impression of undulating topographic relief. As seen in Figure 17, they are generally bland but at also contain the Ebony and Cufa dorsa positive-relief features which are described separately below. Within the SPT, Srp terrains of noticeably different character appear. These are coarser, less uniform, often strongly arcuate, and generally show much greater topographic relief (but are still lower than the cratered plains). In most cases they are strikingly green compared to the surrounding terrain and closely follow the border of the SPT with the northern cp and rp regions (Figures 2, 18 and 20).

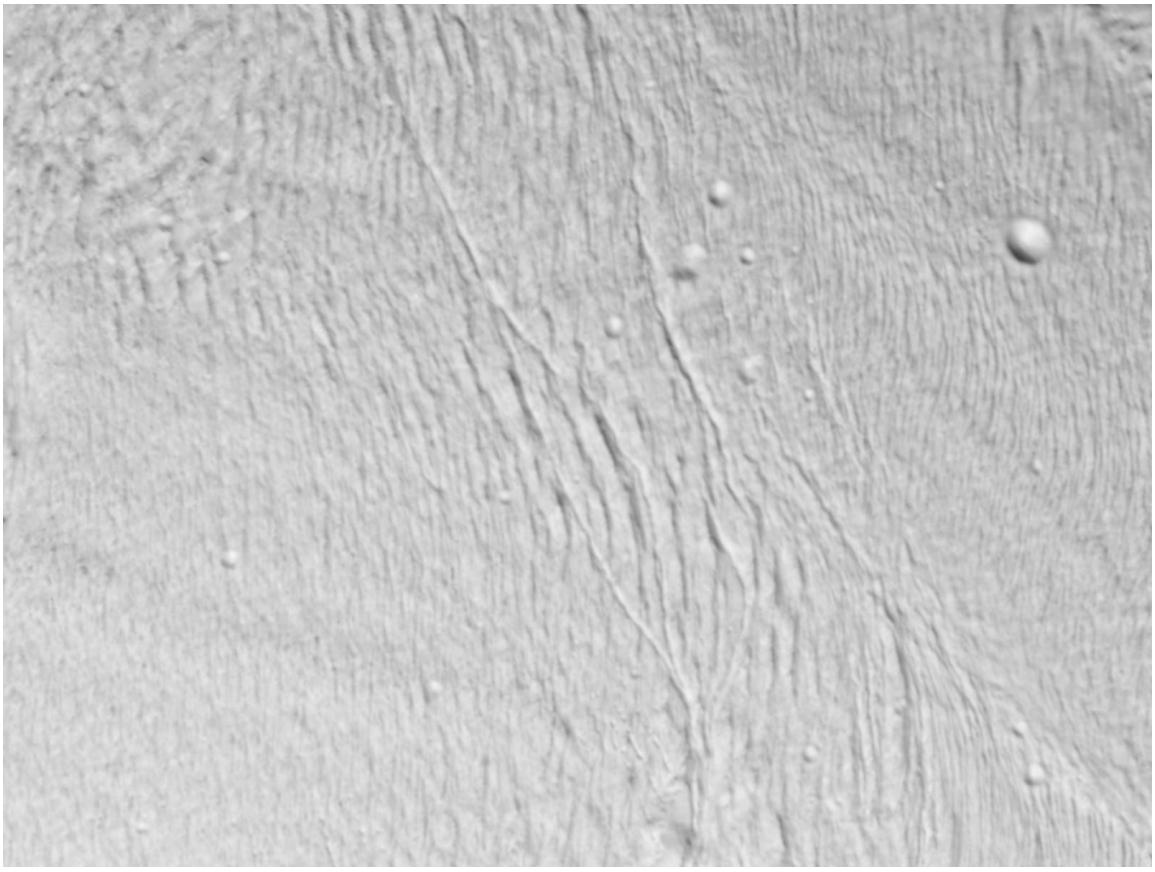


Figure 17. A typical “smooth" Srp region, Sarandib Planitia, just to the west of Cufa Dorsa. The largest crater, Sharrkan, is 3.7 km in diameter. 1600 x 1200 pixel crop from PIA08353; courtesy NASA/JPL/Space Science Institute.

The smooth Srp region shown in Figure 17 bears a striking resemblance to an NSC (normal-slip crenulation) shear zone displaying composite foliations (both C- and S-surfaces); as noted by Hatcher (1994), these features are extensional, and scale-independent (p. 186-197, Figure 10-26). In this case, the shape and orientation of the foliations indicates that right-lateral shear has occurred (when viewed normal to the trend of the ridges).

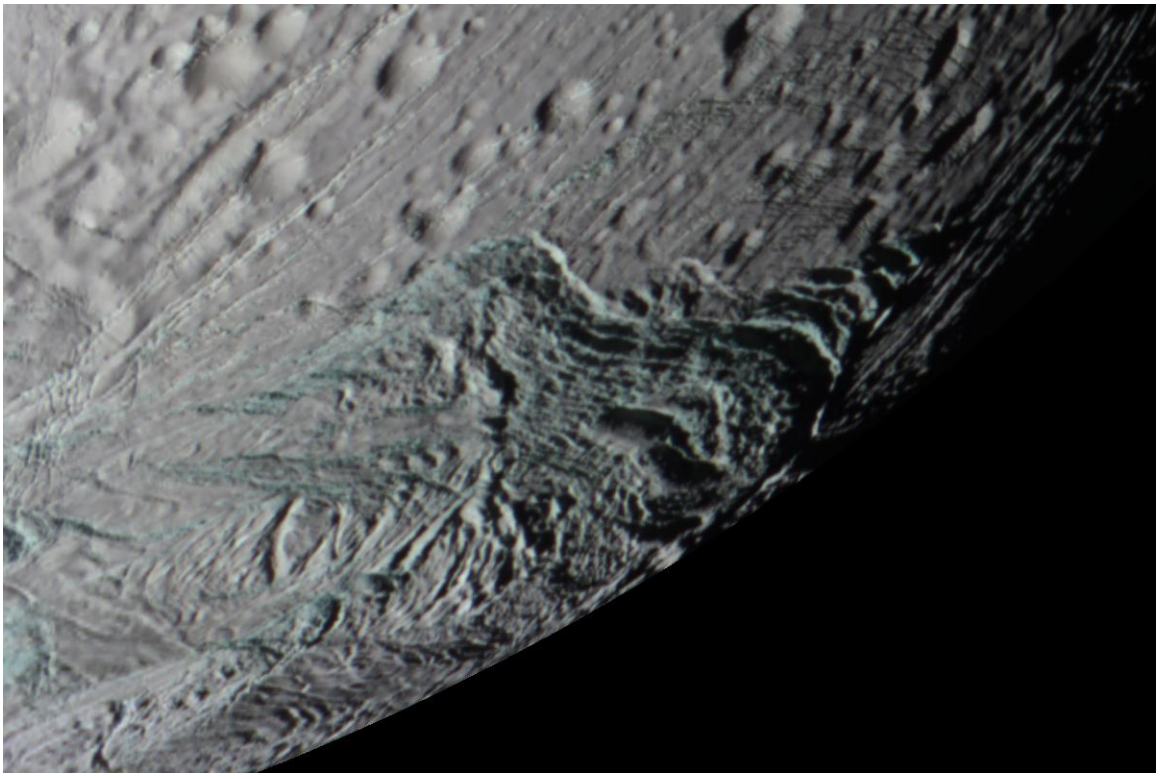


Figure 18. Coarse Srp terrain, seen bordering the SPT at ~160°, near the crater Otbah. This particular image (1200 x 800 pixel crop from PIA08354; courtesy NASA/JPL/Space Science Institute) was chosen for its oblique angle and shallow illumination showing the higher elevation of the cp units. Note also the old, NW-trending grooves visible in the cratered plain.

Crp Regions Crp units are associated with highly active regions such as the terrain between and around the vents in the SPT sulci. The ridges in these units are oriented essentially chaotically; though they may contain small, highly localized subparallel groups, the defining characteristic is the presence of prominent cross-cutting and often tightly arcuate ridges (Figure 19). In some areas sets of grooves (as opposed to ridges) at different orientations have been tectonically overprinted, forming a pseudo-Crp unit such as the region immediately to the east of junction of Khorasan

Fossa with Cashmere Sulci (see Plates 1 and 2). Very high-resolution imagery would be required to say anything more definitive about these formations.

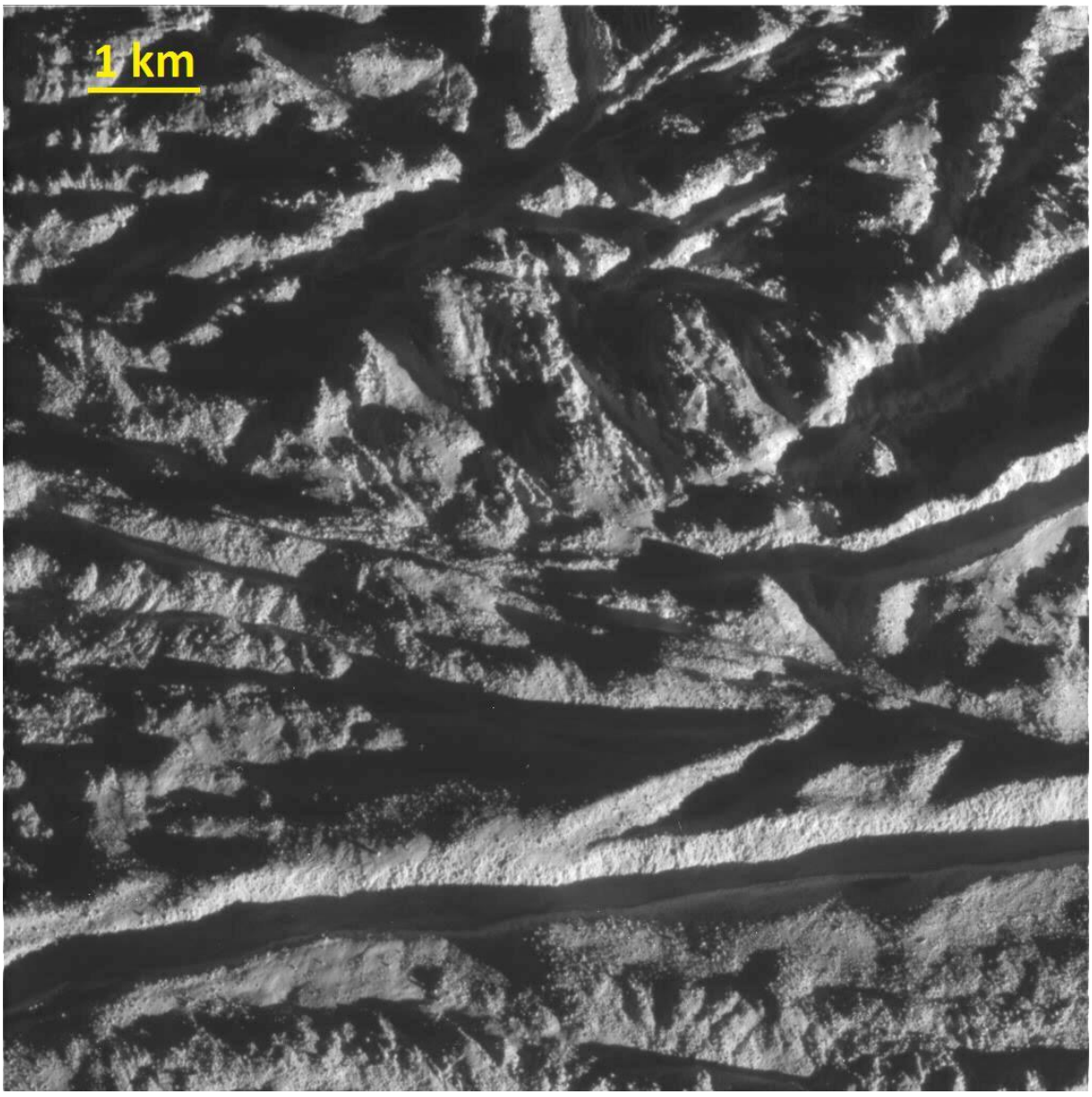


Figure 19. An extremely close view of Crp terrain adjacent to an active sulcus within the SPT. At this scale the ridges on either side of the sulci are seen to have steep, planar inner sides and sharp peaks; their surface texture is extremely granular and no layering is apparent on the exposed faces. The distal ridges are rounded, but also granular or detrital. The largest boulders in this image are approximately house-sized, i.e. 10 – 30 m in diameter. Note that fines are distributed more on the outer faces of the ridges. N00118363, courtesy NASA/JPL/Caltech; annotated by the author.

The South Polar Terrain The SPT is the youngest region on Enceladus, being devoid of impact craters and, except at its borders, generally having a very smooth appearance; it covers an area of slightly more than 60,000 km^2. It contains a series of four or five large subparallel sulci, the now-famous Arabian Sulci or "tiger stripes", that contain (or closely involve) the active jets or geysers that produce Enceladus' atmosphere and supply icy material to the E-ring. It is surrounded by coarse, almost mountainous Srp units whose arcuate shapes are superficially reminiscent of fold-thrust belt salients but as seen in Figure 18 and 20, they are topographically lower than the cratered plains they abut, so this resemblance is completely spurious. In many places the border of the SPT is marked by a prominent graben-like feature that extends periodically into the northern plains in massive inverted-Y-shaped structures, with Labtayt Sulci, located at about 280° being the deepest and broadest example (Figure 19). Both the coarse terrain near the borders and the regions immediately surrounding the Arabian Sulci are noticeably greener and therefore more recently exposed; the morphology of some sections of the coarse border terrains is suggestive of basin-and-range block faulting or ice-fall topography on a glacier. They also bear a strong resemblance to the topographic expression of any of a number of extensional terrain models shown diagrammatically in Hatcher (1995, p. 264), Faulds and Varga (1998), and Van der Pluijm and Marshak (2004, p. 387-395), and in map view are analogous to a series of interconnected C-shaped half graben (Van der Pluijm and Marshak, 2004, Figure 16.14); see also Figures 32 and 33.

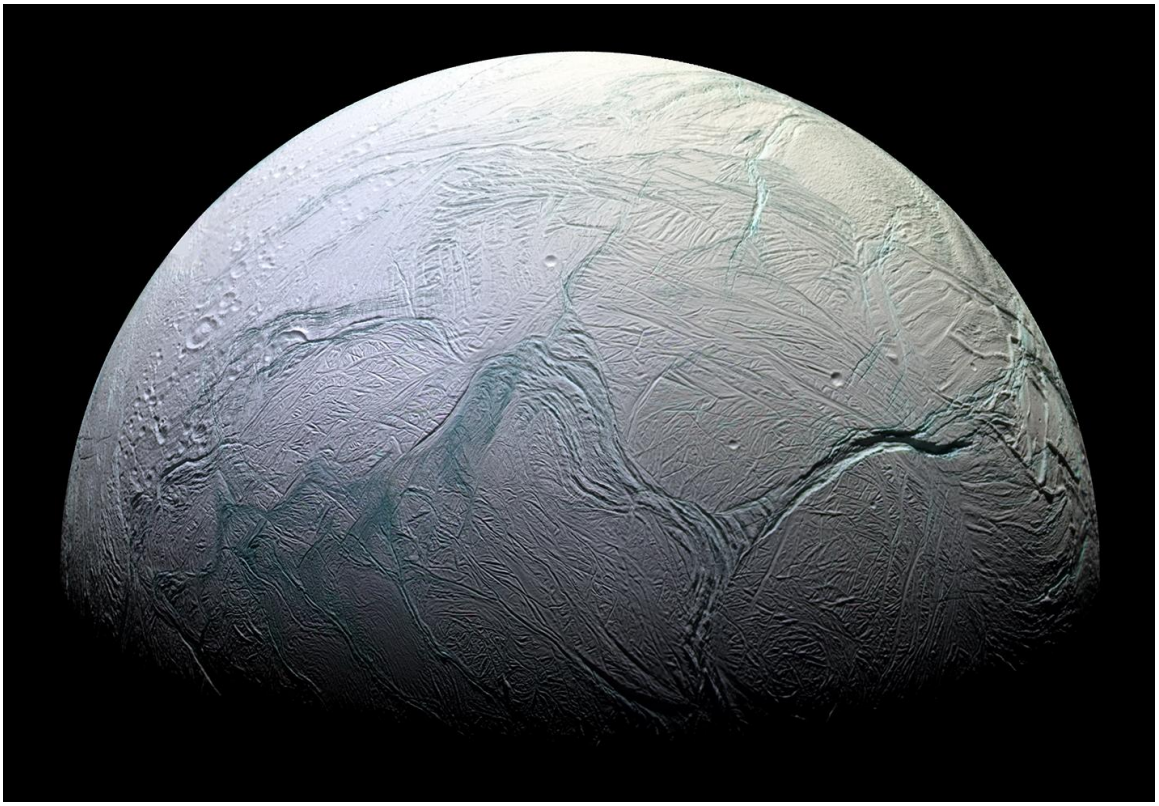


Figure 20. A partial view of the SPT (lower left) and its border with the plains to the north. The massive graben Labtayt Sulci can be seen on the right, extending into the ridged plains that contain the Ebony and Cufa Dorsa (the prominent polygonal ridge network near the limb at 2 o'clock). Shadows (or the lack thereof) indicate that the salient-like features are topographically lower than the plains to the north. The very flat terrain between the tiger stripes, and the raised ridges delineating them, are apparent under these lighting conditions. PIA11133, courtesy NASA/JPL/Space Science Institute.

Dorsa The dorsa (isolated ridges) are confined to a limited equatorial region between about 270° - 290° W (the center of the trailing hemisphere, or antapex). They form a unique network of polygonal shapes at the northernmost extent of the prominent and deep graben, Labtayt Sulci. When examined closely, some of these ridges show a central groove (Figure 21), suggesting a possible genetic relationship with the isolated double ridges associated with the active SPT sulci (Figure 19).

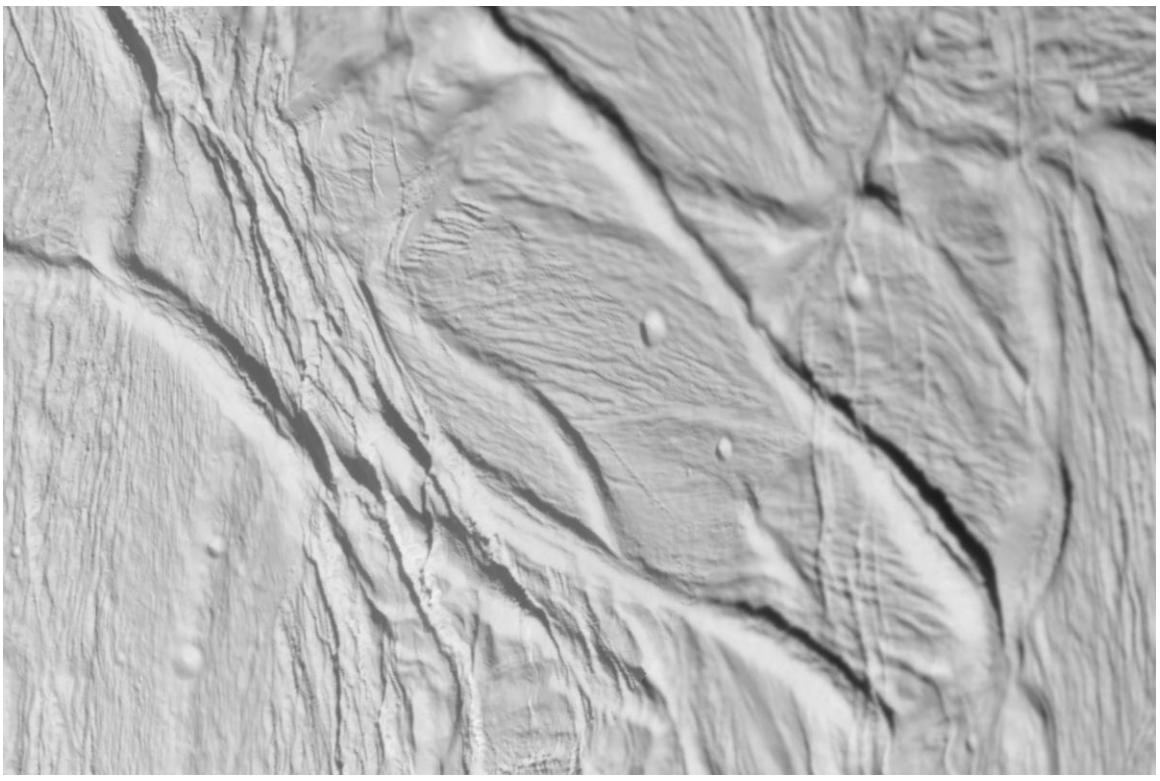


Figure 21. An oblique view of the central grooves associated with some of the dorsa. Note that their alignment does not appear to be determined by the pre-existing fabric of the surrounding ridged plains. The small crater near the center of the image is ~2.6 km in diameter. 1200 x 800 pixel crop from PIA08353; courtesy NASA/JPL/Space Science Institute.

Faults, Fractures and Sulci

The surface of Enceladus is replete with disruptions of all sizes, from massive grabens to miniscule, meter-scale fractures at the very limit of resolution. Fracture geometry varies widely: some are long, narrow and straight; some are long, broad and branching; some abruptly bend through ~90; and a few are short, wide and deep. It is striking that while a vast number of surface features such as craters, ridges and grooves

are cut by faults and fractures, convincing evidence of significant lateral offset is conspicuously absent.

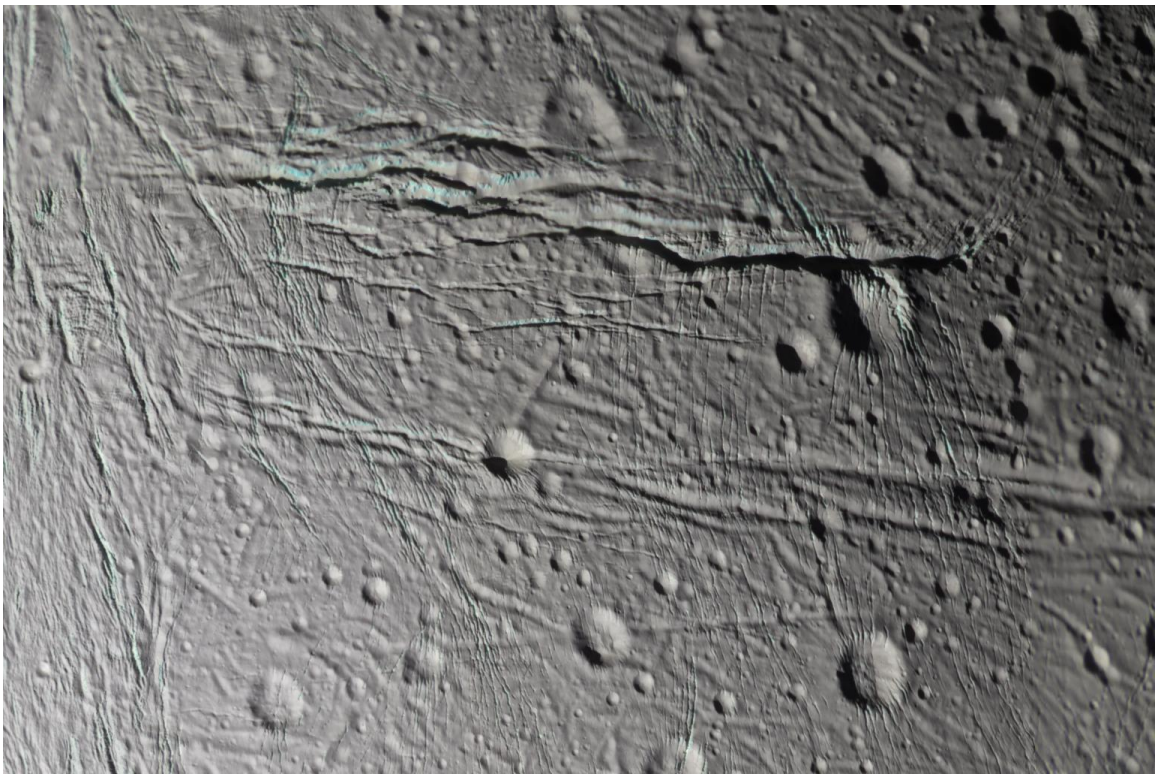


Figure 22. Faulted and fractured cratered plains about 110 km south of the Al-Haddar – Shahrazad – Dunyazad crater complex. The large dissected crater lies at 20° N, 195° W. Note that walls of the complex east-west trending graben are distinctly greenish, indicating this is a relatively young feature. While the dissected crater suggests a minor amount of left-lateral offset, careful examination of its shape (especially the northern half, and the very tight radius of what remains to the south) raises the possibility it may have originally been an elliptical structure caused by a very low-angle impact. 1536 x 1024 pixel crop from PIA08354, courtesy NASA/JPL/Space Science Institute.

Kinematic Analysis

It is obvious that Enceladus experiences extensive, energetic resurfacing with new terrain being created at present (indicated by the lack of craters within the SPT). On

Earth, which possesses an organized system of plate tectonics, resurfacing occurs by several interrelated processes: oceanic crust is continuously created at spreading centers and consumed at subduction zones (remarkably quickly, with only small fragments of oceanic crust being older than ~180 Ma); continental crust grows slowly by microplate accretion over time; weathering and erosion produces sediment that is transported and deposited in basins to eventually become new rock units; and extrusive volcanic activity can blanket preexisting landforms. Thus, the overall surface area of the Earth remains constant except for variations due to topography. The driving force in all of these processes is the in-plane motion of tectonic plates, responsible for, among other things, mountain ranges, volcanoes, and subduction-zone trenches.

Given the degree of activity displayed on Enceladus, including the spectacular geyser system, it is tempting to speculate on whether some analog of terrestrial plate tectonics is at work, creating new terrain and reworking the existing surface. Indeed, there are certainly features that superficially resemble those associated with terrestrial plate tectonics: in particular, the “tiger stripe” sulci look somewhat like spreading ridges (Figures 23 & 24) and the mountainous sulci bordering the SPT look somewhat like fold-thrust belts (except under close inspection). However, one must also consider the eventual fate of any newly created terrain, and this is where serious problems with this simplistic interpretation occur, for if spreading is occurring within the SPT, subduction must occur elsewhere to conserve surface area. With plate motion on Earth driven primarily by the consumption of oceanic lithosphere at subduction zones while being

simultaneously accommodated by seafloor spreading, it is difficult to visualize an analogous plate-tectonic cycle where either process could exist without the other.

The nature of the contacts between the SPT and the plains to the north are crucial to an understanding of the geologic processes occurring within the SPT. For example, an illustration in Porco (2008) interpreted this boundary as a "Himalaya"-like mountain range, which is one type of structural feature that might reasonably be expected to exist where tectonic plates converge. However, the detailed geometry of this boundary is inconsistent with any kind of convergent boundary – it is marked in many locations by a very prominent, deep graben (or half-graben; see Figures 2 and 20), with *the ranges on the south side*. If terrain created by spreading within the SPT is being subducted under the cratered plains to the north (with the graben-like feature representing a trench), there should be a surficial expression on those plains in the form of mountains, or at least hills, but the area immediately to the north of the graben is conspicuously flat and undeformed right to the very edge of the scarp (e.g. Figures 18 and 20). On Earth, an ocean-continent or ocean-ocean subduction zone would have the mountains on the overriding plate, the exact opposite of what is seen on Enceladus. Alternately, if the relatively younger SPT crust is being thrust over the old terrain to the north, it would have to be topographically higher, but it is actually lower, so the interpretation of convergence and collision is even more implausible. In the case of Himalayan-style continent-continent convergence, the overall topography of the range should be higher than on either side (it is not), there should be obvious fold-thrust

structures (also absent), and it is difficult to visualize how such a boundary could create an extensional feature (graben or half-graben) at the contact. To the author, the closest morphological terrestrial analog to the SPT-plains contact is basin-and-range topography or glacial icefalls (Paterson, 1994; Benn and Evans, 1998), both of which are produced by extension. The accordion-like stretching of impact craters at the border of Samarkand Sulcus (Figure 15) is a more subtle example; a hypothesis for the formation of such features is described in the following section.

The Tiger Stripes as Possible Spreading Centers

It is worthwhile to examine the evidence for and against identifying the Arabian Sulci as spreading centers in some detail. The region shown in Figure 23 superficially resembles a transform, but the similarity is limited to an orthogonal alignment of a fracture/ridge set lacking many of the features of a true transform. In a genuine transform, new lithosphere is created parallel to the spreading ridge, as clearly shown by the closely spaced striations in the terrestrial bathymetric image. As noted by the CICLOPS team in the accompanying press release, the Enceladan version has no such related structures. Note also the subtle topography in the oceanic transform: the seafloor immediately proximal to the spreading centers is thinner, hotter, and therefore higher than its surroundings. This ridge-and-trough topography is characteristic of terrestrial spreading ridges and transforms (Moores and Twiss, 1995, p. 32-33, Fig. 3.5). Even accounting for the anomalous behavior of water ice compared to silicate rock (see

Dynamics and Geophysics), there should be some topographic expression, either positive or negative, either side of an active spreading center.

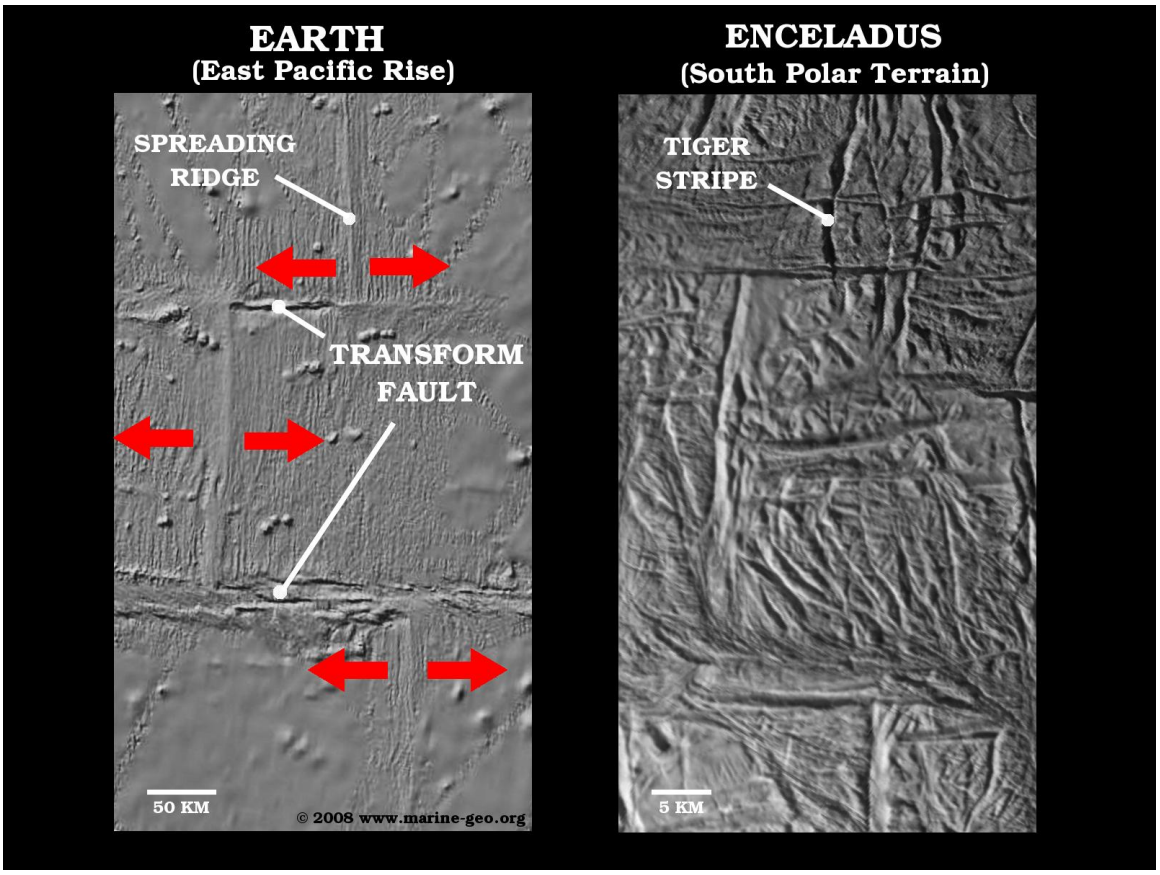


Figure 23. Comparison of SPT features at 72°S, 5°W, with a terrestrial spreading ridge and transform complex on the East Pacific Rise at 9.5°N, 104°W. The tiger stripe indicated in the image is the distal end of the southern branch of Damascus Sulcus. Note the 10x scale difference. PIA11138, courtesy NASA/JPL/Space Science Institute.

Helfenstein et al. suggest (2008) that the tiger stripes are not "exact analogs to classic terrestrial oceanic rifts", but nevertheless imply that spreading does occur, perhaps fragmentally and asymmetrically (see Figure 24).

If the tiger stripes really are spreading centers, they should also terminate in prominent transforms – which they do not; instead they hook dextrally at either end. If

more than one is actively spreading, then the terrain outboard of the terminations should show evidence of differential extension, which is also not observed.

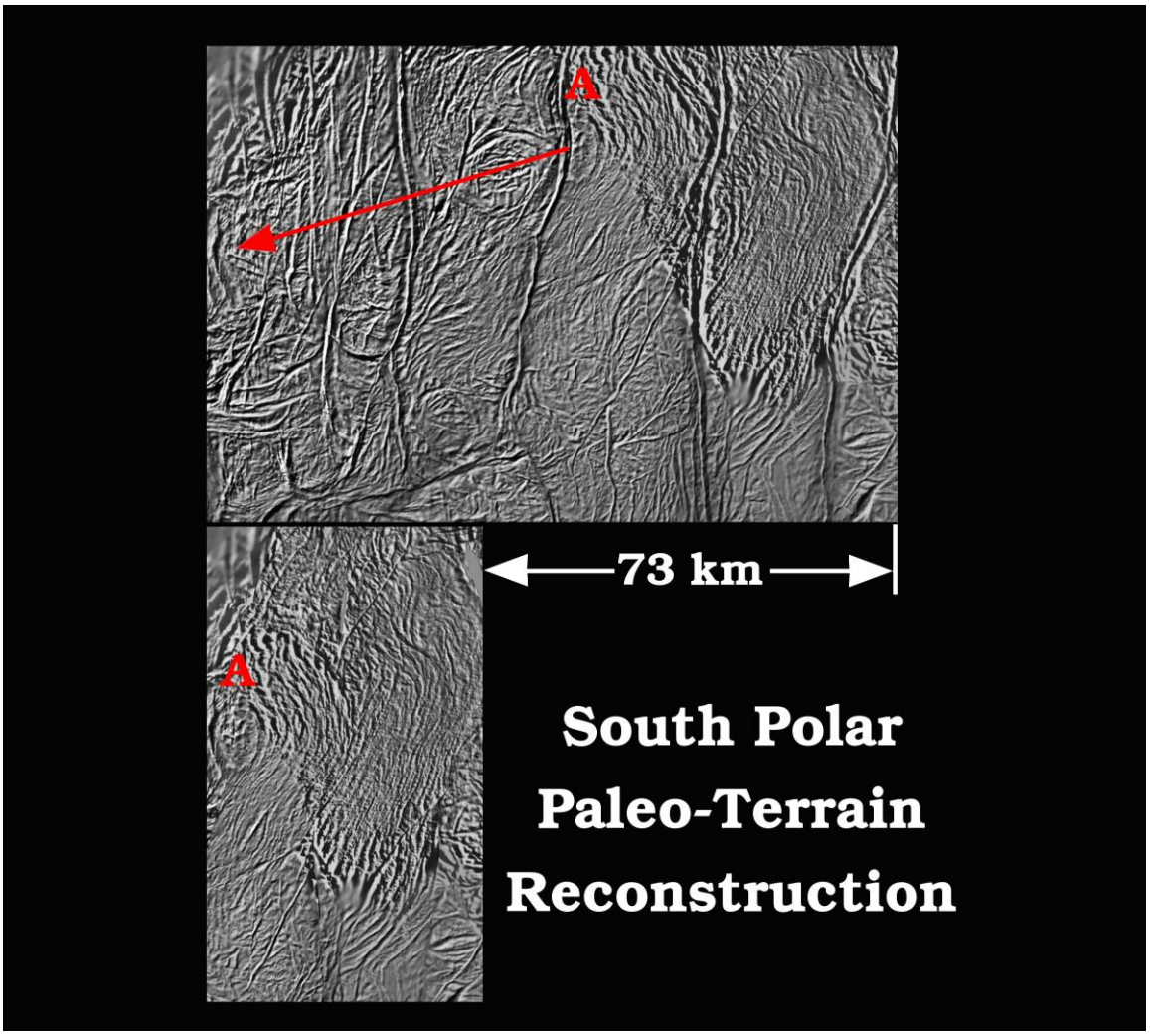


Figure 24. A paleo-terrain reconstruction purporting to show asymmetric spreading in the SPT. PIA11140, courtesy NASA/JPL/Space Science Institute.

More importantly, transforms do not exist in isolation, but form part of an extended network of structures accommodating the geometric requirements of seafloor spreading on a spherical surface i.e. plate motion about an Euler pole (e.g. Moores and

Twiss, 1995, p. 50-55, Figs 4.2-4.6). The Enceladan “transforms” cannot be traced for any great distance and are most likely chance alignments of regionally distributed fractures. There is an additional, related geometric objection to the tiger stripes as spreading centers: they should follow great circles (e.g. Moores and Twiss, 1995, p. 51, 54, 55, Fig 4.3, 4.5), and it is evident from the excellent available imagery of the SPT that they more closely resemble the tidally-induced cycloidal fracture patterns seen on Europa (Hoppa et al., 1999).

When examining the SPT in false-color RGB, the tiger stripes are conspicuously green on *both* sides of their central grooves, which is not what one would expect with “asymmetric spreading”, since terrain on one side should be much older. One possible explanation for this is that venting from the geysers (which are coincident with the stripes) proximally deposits crystalline fines that are radiatively degraded at a much faster rate than any extension caused by spreading. However, very distinct regions of crystalline ice are seen within the SPT far from any known vents (e.g. Figures 2 and 20), so presumably there are other processes involved in exposing fresh ice besides cryovolcanism (e.g., normal faulting, as proposed herein). The similar shapes of the fractures on either side of the “new” terrain is superficially attractive, but as noted above, fracture patterns produced by tidal flexing may be a better analog (note the active sulci are not really straight but display cusp-like shapes; see Hoppa et al., 1999 for illustrative examples of this phenomena). In the example shown in Figure 24, a second

tiger stripe (Alexandria Sulci) has appeared within the alleged region of spreading. Indistinguishable from the first, its morphology raises some problematic questions:

- What is the relative timing of the appearance of Alexandria and Cairo sulci?
- Is Alexandria Sulci a static structure, without spreading? If so, why does it look exactly like the purported asymmetric spreading center?
- If it does experience spreading, is it symmetric or asymmetric? If asymmetric, which side is creating new terrain?
- Finally, note the complex orientation of features within the "new" terrain – very different to the parallel striations one would see in an analogous terrestrial setting (e.g. Figure 23)

The morphology of the terrain on either side of the stripes should be distinctly different if the spreading is asymmetric, but this is not observed here; both sides display similar relief, in the sense that one side is not softer and more subdued than the other. Furthermore, the SPT between and around the tiger stripes is replete with quasi-circular features of indeterminate origin (several are visible in PIA11140), so the matching features of the paleo reconstruction are by themselves not very convincing.

Close-up imagery acquired during the most recent flybys strongly suggests the ridges associated with the tiger stripes are cryovolcaniclastic in origin (see Figure 18; for further examples, see N00118361, N00118362 & N00118364). This raises the possibility that the low-profile ridges seen throughout the SPT are cryovolcaniclastic levees, tracing

the past activity of fractures that for the most part are now dormant. If so they represent secondary expressions of underlying tectonic forces.

Tectonic Features Outside the South Polar Terrain

Outside the SPT, faulting is universally seen to be extensional, with no features that could readily be classified as regionally contractile (though there may be very subtle high-angle reverse faults, see Dynamics and Geophysics). Lateral offsets along faults are similarly absent, as are subduction zones (which may be physically impossible in this environment, also discussed below). Combined with the presence of extensional features bordering the south polar terrain, this leads to a potentially disturbing conclusion: extension is apparently ubiquitous, but without corresponding shortening available to accommodate it. In a conventional (terrestrial) plate-tectonic regime, such a situation cannot occur as area is not conserved, so an alternate explanation is required to account for these observations.

Dynamic and Geophysical Analysis

As stated earlier, the most difficult and counterintuitive facet of this project was creating a plausible dynamic framework within which to integrate the descriptive and kinematic analyses when observed over the surface of Enceladus as a whole. Indeed, without such a framework, the usefulness of the entire exercise would be questionable, and the closer the imagery was examined, the more intractable the situation appeared.

It transpired that the geophysical analysis, though simplified, provided the cipher with which to decode the seemingly contradictory observations.

Enceladus Thermal Anomaly

The intense geologic activity associated with the south polar terrain is not only manifest in the extremely youthful surface and the geyser-like jets, but is visible to the Cassini Composite Infrared Spectrometer (CIRS) as a pronounced and temporally stable hot-spot (Figure 25 and 26), one of the most striking geophysical features of this tiny body (Spencer et al., 2006).

On Earth and other bodies with silicate lithospheres, a positive thermal anomaly would normally be associated with topographic uplift due to the higher temperatures causing a reduction in density of the rock. The Enceladan observations, conversely, suggest *downslope* movement toward the center of the south polar terrain as seen in the basin-and-range and/or icefall-like features.

At first this contradiction appeared irreconcilable until the unique physical behavior of water was taken into account, as the most important geophysical fact about Enceladus is that its lithosphere is made of water ice – and almost certainly involves liquid water at some depth below the surface.

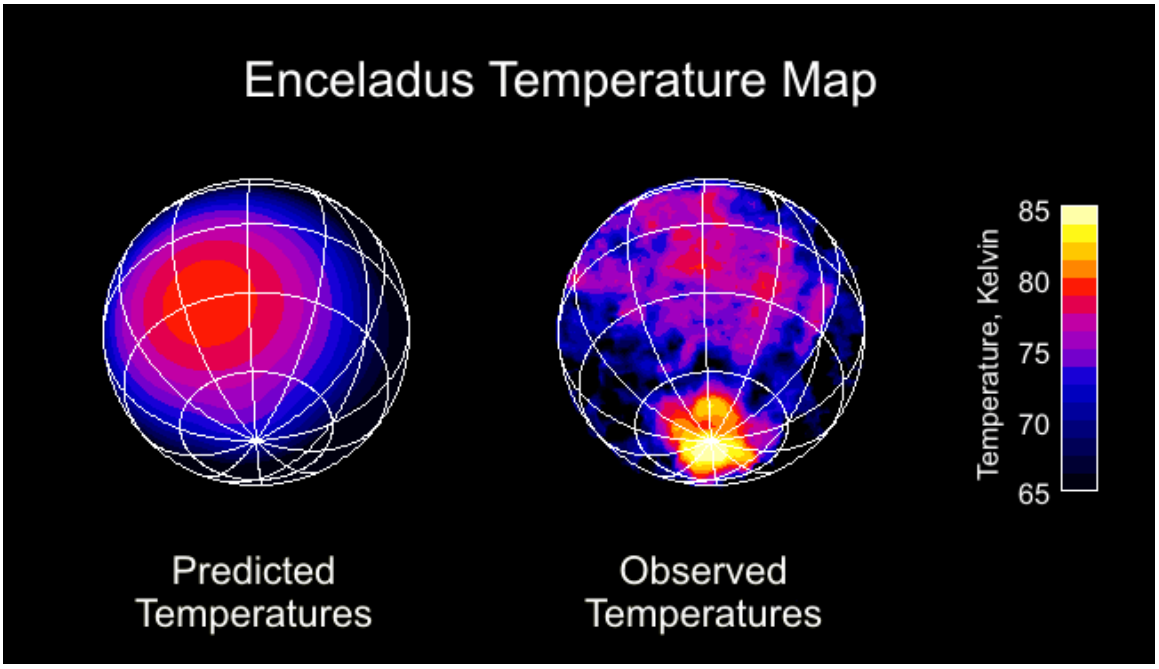


Figure 25. Predicted equilibrium versus observed temperatures on Enceladus in July 2005, prior to the discovery of the south polar jets. PIA06432, courtesy NASA/JPL/GSFC.

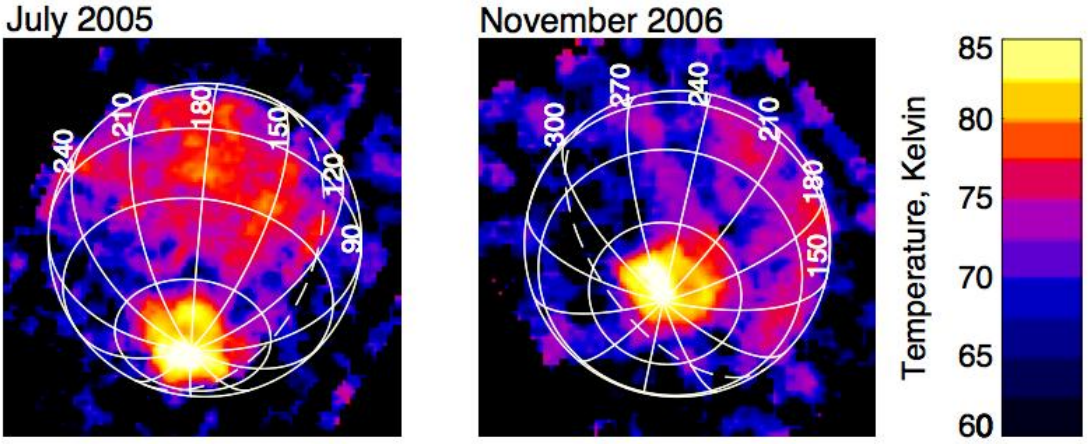


Figure 26. The south polar hot spot remained active and highly visible throughout this observation period. At restricted locations near the vents, temperatures are much higher than indicated in these low-resolution images. The dashed line indicates the terminator; 180° is the center of the anti-Saturn hemisphere. PIA09037, courtesy NASA/JPL/GSFC/Southwest Research Institute.

Properties of Water

Water is an extremely common substance, not only Earth, the outer planets and their moons, but also in deep space (Zeilik and Gregory, 1998). As the surface of Earth is very close to the triple point of water, we are intimately familiar with it in its solid, liquid and gaseous forms. The surface of Enceladus is extraordinarily cold compared to Earth, similar to the temperature at which liquid nitrogen boils (77.2 K; Lide, 2006), so it is relevant to investigate the properties of water, or more specifically ice, under these conditions.

As stated in the Methods section, the pressure calculated at the core-mantle boundary depth of 90.3 km is ~18.4 MPa:

- 18.4 MPa ≈ 182 atm → equivalent to terrestrial pressure ~700 m underground or ~1900 m underwater
- at this pressure and any reasonable temperature, ice can only exist in the Ih form (ordinary hexagonal ice) (Figure 27), and regardless of temperature, ice Ih is *always* less dense than water (Figure 28)
- As seen in Figure 27, conditions at the core-mantle boundary of Enceladus are inadequate by an order of magnitude to allow the formation of high-pressure ice polymorphs
- Temperatures at depth could be as high as ~375° C before boiling occurs
- Furthermore, the temperature-density plot in Figure 28 indicates that while the density of liquid water falls by over 4% as it approaches boiling, and the

density of ice increases by about 1% as its temperature drops from 0° C to -180° C, the curves never cross, i.e. even extremely cold ice Ih will (temporarily) float in very hot water

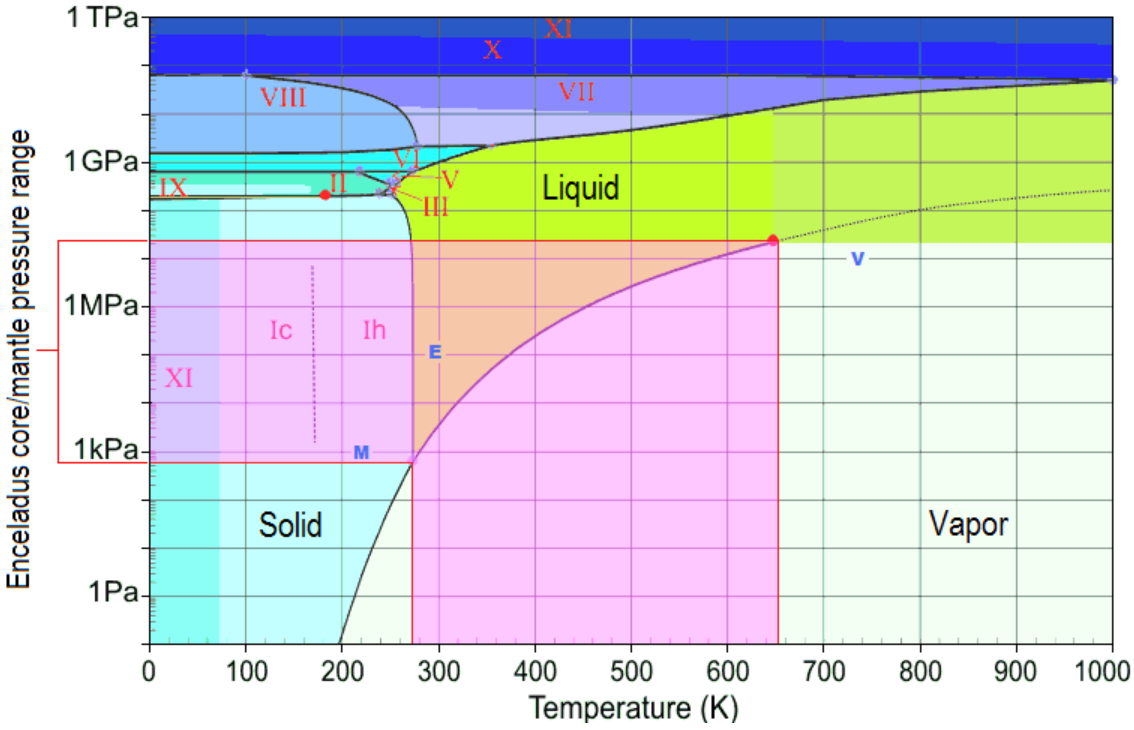


Figure 27. Phase diagram for water. The pressure range from the surface of Enceladus to the core-mantle boundary at -90.3 km is indicated on the y-axis by the pink overlay and is extended to the boiling curve to indicate the stable temperature range on the x-axis. The blue letters E, M and V indicate surface conditions on Earth, Mars and Venus respectively. Original diagram by Martin Chapman, London South Bank University; retrieved 16/07/2008 from http://www.lsbu.ac.uk/water/images/phase.gif. Triple points verified with Eisenberg and Kauzmann, 1969; modified by the author and used with permission. See Appendix C for a table of triple points.

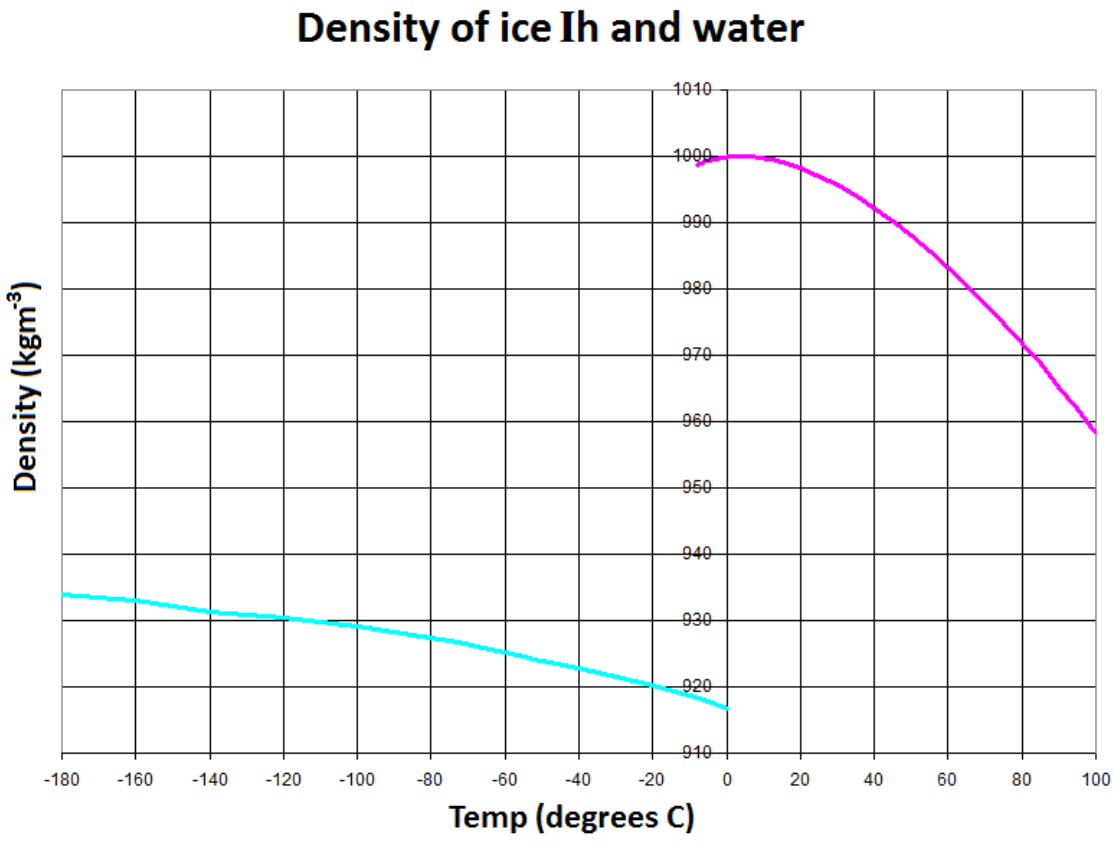


Figure 28. Density of ice Ih (cyan) and water (pink) from -180° C to 100° C. Data from Lide (2006) includes density values for water supercooled to -9° C.

Formation of a South Polar Basin

The expansion of water on freezing leads to some interesting behavior, and provides an explanation for the apparent contradiction of a positive thermal anomaly causing topographic subsidence instead of uplift. The following simple model (some stages of which are shown in Figures 30 & 31) assumes that, instead of the thermal anomaly merely warming the ice, it results in a subsurface phase change between an icy crust (density 917 kgm^{-3}) and a watery mantle (density 1,000 kgm^{-3}, i.e. ~273 K); changes in the exact values will not change the nature of the results, just the numbers. As stated

in the Generalized Geography section, the resurfacing process is interpreted to be a discontinuous cycle that has occurred numerous times, and at varying scales, over the history of Enceladus. The exact mechanism that causes repeated resurfacing events, interspersed by periods of quiescence, is unknown; the following ten stages represent one possible sequence from initiation to cessation:

1) As the crust is thinned by heating from below, a given mass of low-density ice is displaced by the same mass of high-density water, therefore the surface *must subside* to preserve isostatic equilibrium in the column
2) Subsidence occurs at a constant rate with respect to thinning, affected only by the *density contrast* between crust and mantle (Figure 29)
    - in this case, the ratio of subsidence/thinning = 83 m/km
3) Initial crustal thickness and mantle depth have no effect on this relationship (except when correcting for sphericity)
4) Flexurally-induced collapse features (like the seracs in a glacial icefall) occur at the edge of the subsidence zone, creating jagged, ridged terrain juxtaposed with cratered terrain (Figures 18 & 32)
5) The collapsed blocks slowly move a short distance downslope, away from the unaffected crust, leaving a trench-like, break-away scarp at the edge of the subsidence zone

6) As the heat spreads outward at the surface, the edge of the subsidence zone expands into the older cratered terrain and more distal extensional structures are developed
7) The already collapsed blocks gradually soften with heat transfer from below and topographic relief is reduced (leading to the flatter terrain close to the center of the SPT)
8) When the mantle heat source shuts off, heat is slowly lost to space and the crust begins to thicken by re-freezing from below
9) The thickening crust then rises to preserve isostasy, virtually eliminating pre-existing topography, though traces may remain as low-relief features
10) Normal faults produced during the collapse phase may be reactivated as high-angle reverse faults during isostatic adjustments, producing remnant low-profile ridges and/or grooves

Various stages in this complete cycle are interpreted as responsible for the flat, subparallel-ridged terrain seen across Enceladus, the fault-block features south of the contact of the SPT with the plains to the north, and the formation of the south polar basin; the result of the reactivation of normal faults produced by flexure and limited downslope motion of semi-detached blocks during a thermal event as high-angle reverse faults on re-equilibration is shown by the differentially stretched and flattened craters at the border of Samarkand Sulci (Figure 15), which is interpreted as an example of a highly localized, miniature version of the SPT processes described above.

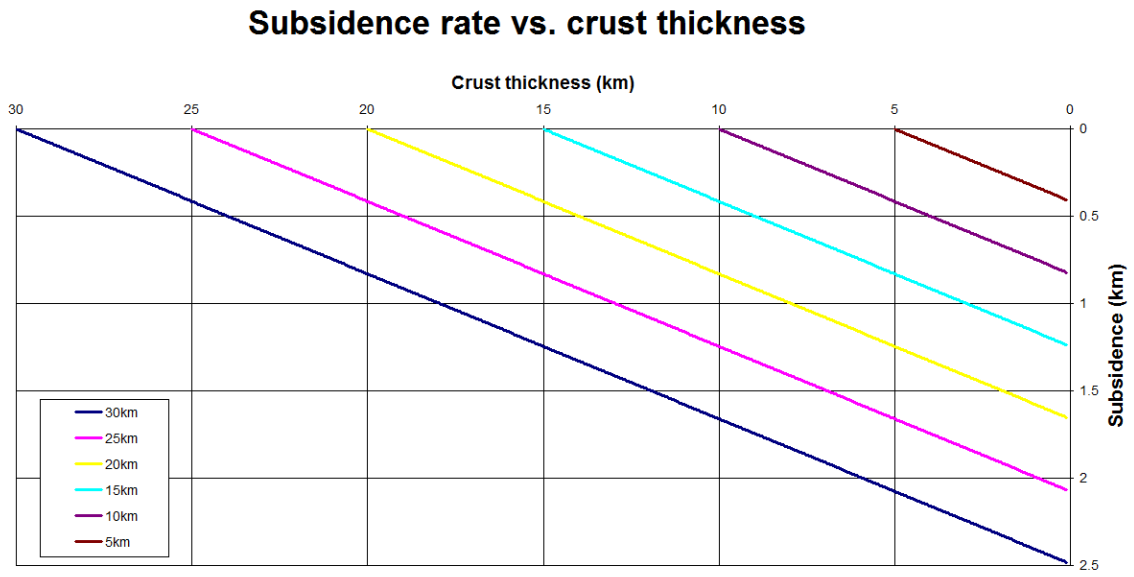


Figure 29. Subsidence rates as a function of thinning for various initial crustal thicknesses. The rate of subsidence is indicated by the slope; when thinned from initial thicknesses of 30, 25, 20, 15, 10 and 5 km to zero, the rate remains constant at about 83m of subsidence per km of thinning to maintain a constant column mass. Note that this chart is not corrected for sphericity, but the effect is minor.

During a thermal event, the crust may be thinned enough for venting to occur directly to space, which we see today at the tiger stripes (Hurford et al., 2007). These eruptions eject large (up to >20m) blocks of ice and vast amounts of finer particles, forming cryovolcaniclastic levee deposits around the vents (Figure 18, 19, 20 and 22). On Enceladus, a 20 m block of ice would weigh about the same as a 3.3 m boulder of granite on Earth (even assuming the ice has zero porosity, which it probably does not), so ejecta deposits of this coarseness should not be ruled out a priori. These deposits also form the chaotic ridges seen in various locations, and interference between eruptive plumes may create isolated ridges far from any active vents. Venting ceases when the crust re-thickens.

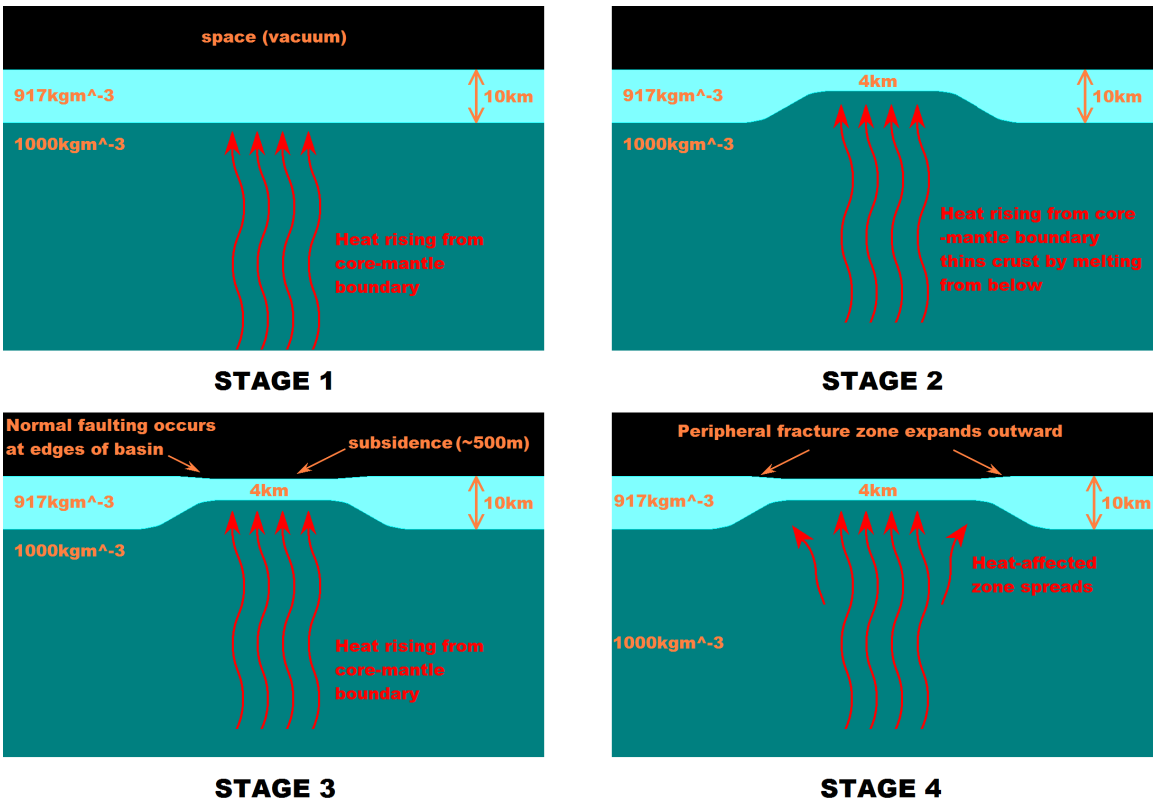


Figure 30. Cartoon representation of the initial stages in the formation of a basin over a positive thermal anomaly, as predicted for the south polar terrain in the model.

Small-scale details such as the formation of normal faults at the peripheral zone of flexure and the resulting topography are not shown in Figures 30 and 31, but are best illustrated by photographs of an Enceladan example with an interpretive cross-section (Figures 32 and 33) and an approximate terrestrial analog: overhead and oblique views of seracs in an icefall formation in Jackson glacier, Montana (Figure 34). In the Cashmere Sulci example, basin-and-range like architecture develops over a limited lateral extent at the contact; the high local geotherm causes viscoelastic relaxation and the topography rapidly flattens out on moving south into the SPT basin proper. These features strongly resemble the accommodation zones described by Faulds and Varga (1998).

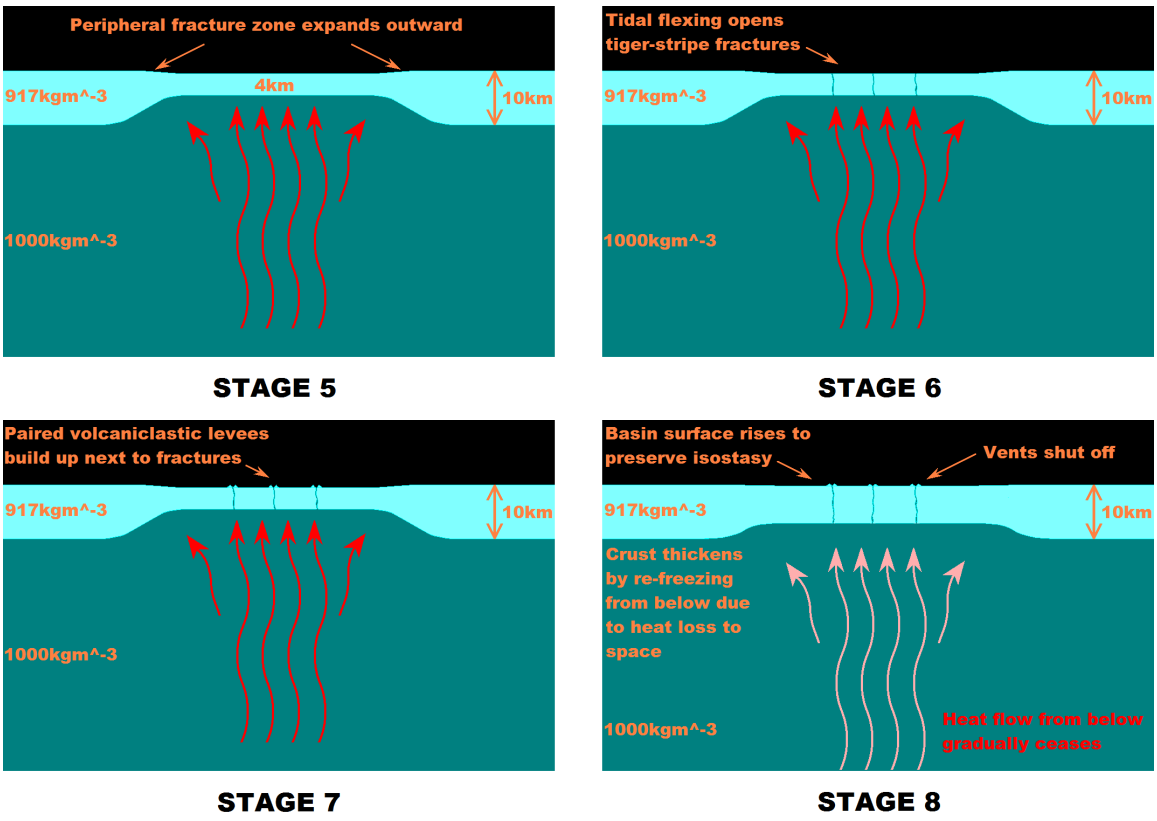


Figure 31. Later stages in the development and cessation of the system shown above. The thicknesses shown in these illustrations are not necessarily accurate for Enceladus, but the proportionality between thinning and surface subsidence is correct for these density values.

The thermal-isostatically driven resurfacing processes described above have presumably occurred cyclically many times since the formation of the solar system; the ancient cratered plains, seen under favorable lighting to be imprinted with ridges and grooves, are interpreted as the highly degraded remnants of rp regions created in earlier episodes. While sea ice on Earth is effectively unrestrained, frost heave in frozen soil could be considered an approximate (but inverse) terrestrial analog: as water trapped in the soil freezes, it expands and the surface rises (and cracks); when the ice thaws, the volume decreases and the surface subsides.

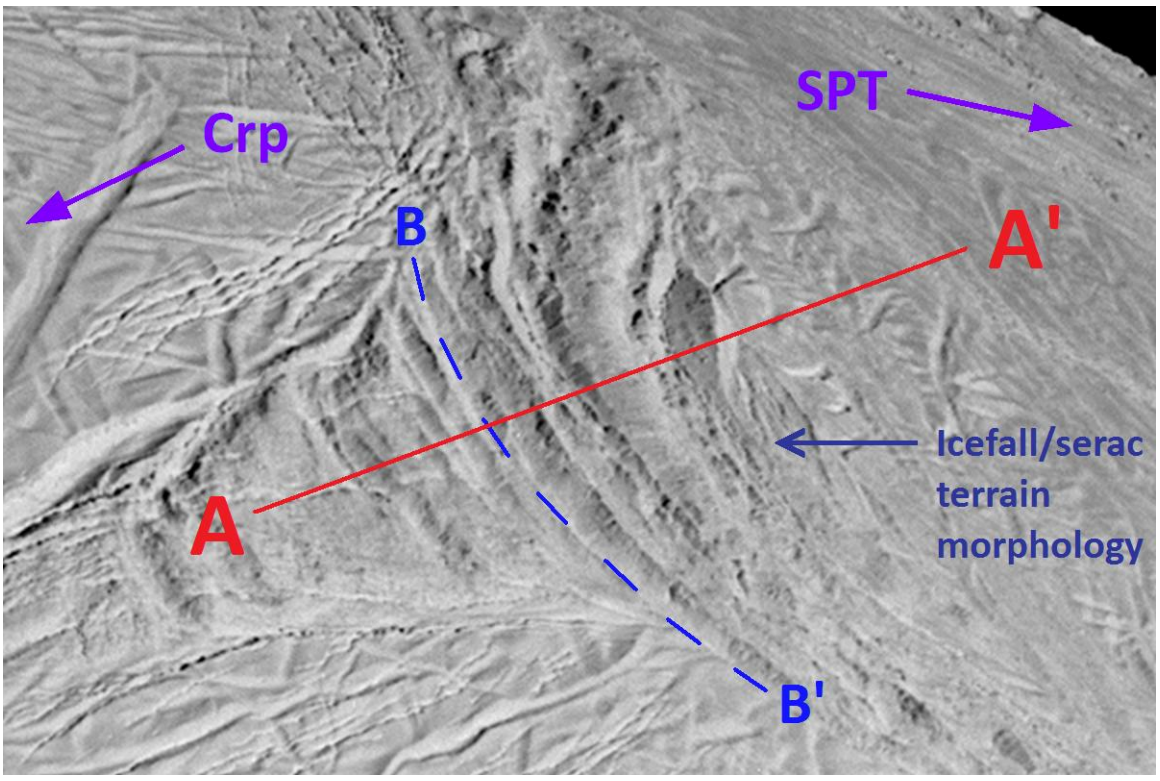


Figure 32. Extensional topography in Cashmere Sulci, produced at the flexurally loaded contact between the thinned basin crust (right) and the cold, thick, rigid plains to the north (left). 600 x 400 crop from PIA06191, courtesy NASA/JPL/Space Science Institute.

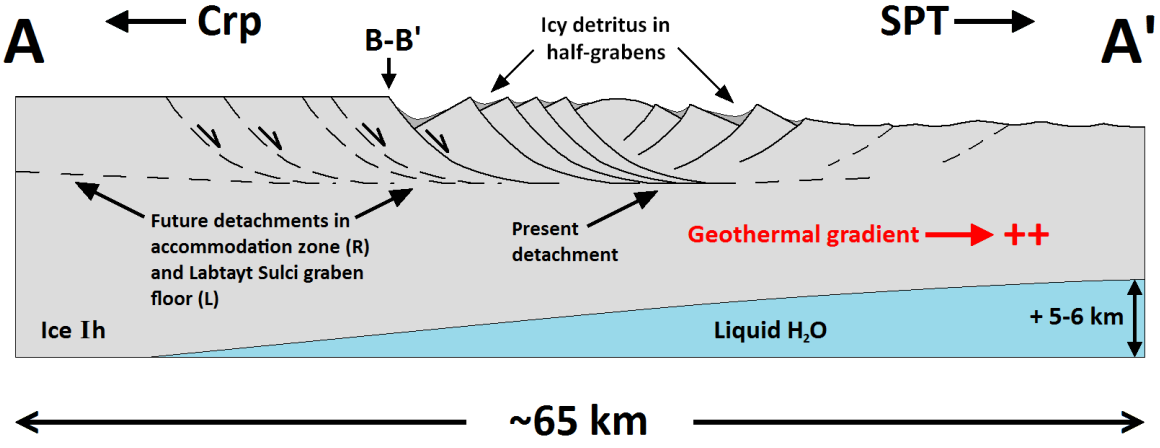


Figure 33. An interpretive cross-section through A-A', at a time when B-B' marked the edge of the SPT and the interior of the Labtayt Sulci graben (seen under the letter “A” in Figure 32) had not yet started to collapse (depths not to scale). Dashed lines to the left (north) of B-B' indicate future listric normal faults. The water depth indicated would create a basin ~400-500m deep, consistent with observation (Porco et al., 2006).

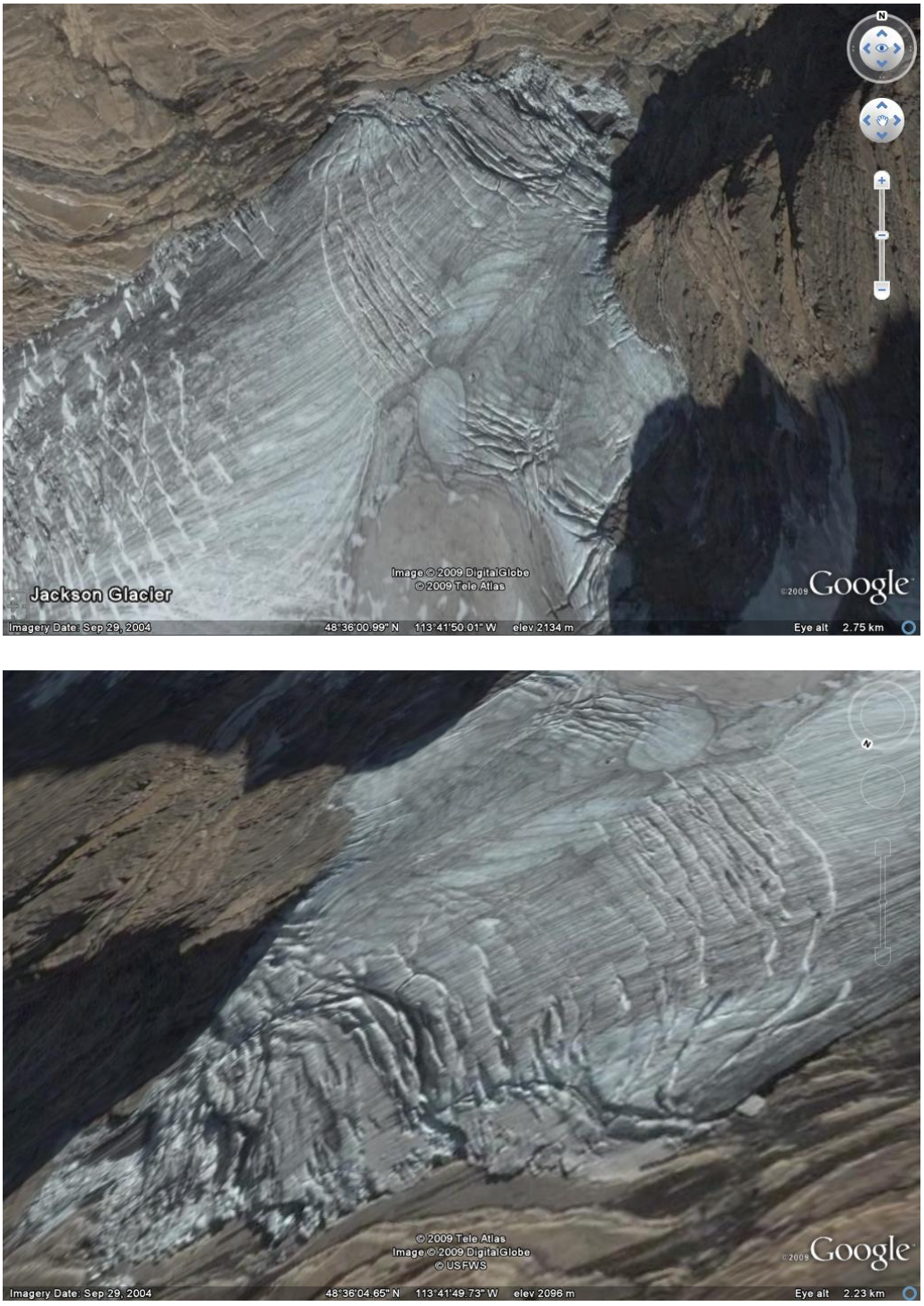


Figure 34. Overhead (top) and oblique (bottom) views of arcuate icefall structure with jagged seracs in Jackson glacier, Montana, 48°36'N, 113°42'W. Note that these structures are concave downslope, whereas ogives are convex. Google Earth images.

Ice, Subduction and Spreading

The previous sections have described geometric and phase-density arguments against an Earth-like style of plate tectonics operating on Enceladus, but there is a potentially even more fundamental objection based on geophysics. Seafloor spreading on Earth is driven primarily by slab pull, with a minor component supplied by ridge push (e.g. Forsyth and Uyeda, 1975; Spence, 1987; Bott, 1993; Conrad and Lithgow-Bertelloni, 2002; Conrad et al., 2003; Conrad, and Lithgow-Bertelloni, 2004; Schellart, 2004; Faccenna et al., 2007; Schellart, 2008; and in all cases, references therein). While the terrestrial mantle certainly experiences convection, this does not drive spreading. On Earth, spreading is enabled by the dichotomy of MORB/continental crust, with the difference in composition and density between mafic seafloor and felsic continental rocks allowing (and encouraging) subduction to occur. However, with the Enceladan lithosphere made entirely of water ice, any newly created lithosphere will have the same composition but *lower density* due to higher temperature (being more recently solidified), making subduction and consequently spreading, as we understand it on Earth, mechanically implausible.

DISCUSSION

A Subsurface Ocean

In the previous chapter, the existence of a water-ice phase transition below the south polar terrain was invoked to explain the existence of a basin, which in turn was required to account for apparent extension/downslope motion (based on geometric and kinematic analyses of high-resolution images) toward a known positive thermal anomaly, a process upon which the entire tectonic hypothesis hinges. When distilled in this way, the argument acquires a somewhat contrived, if not ad hoc, character that may give the critical reader pause. However, the unique properties of water proved to be more than just a deus ex machina for the author's geologic interpretation; numerous other workers were simultaneously hypothesizing a subsurface ocean for a variety of reasons, mostly related to the geyser-like plume composition and velocity (e.g. Hurford et al., 2007; Spencer and Grinspoon, 2007; Hansen et al., 2008; Schmidt et al., 2008) but also due to considerations of shear heating (Nimmo et al., 2007) and topographic deviation from the spheroid (Collins and Goodman, 2007). The existence of a basin at the south pole of Enceladus is now well established (idem), and it is encouraging that this conclusion was arrived at via completely independent lines of evidence – image-based analysis of map-scale geologic structures combined with geophysical modeling.

Other Geologic Issues

Downslope Transportation on Low-mass Bodies

While the gravity of Enceladus is very low compared to Earth, the other terrestrial planets, and even the larger moons, downslope movement of material as required in the author's tectonic interpretation can definitely occur in the absence of a transporting medium as shown on much smaller bodies such as Epimetheus (Figure E3) and asteroids such as 433 Eros (33 x 13 x 13 km) (Figure 35).

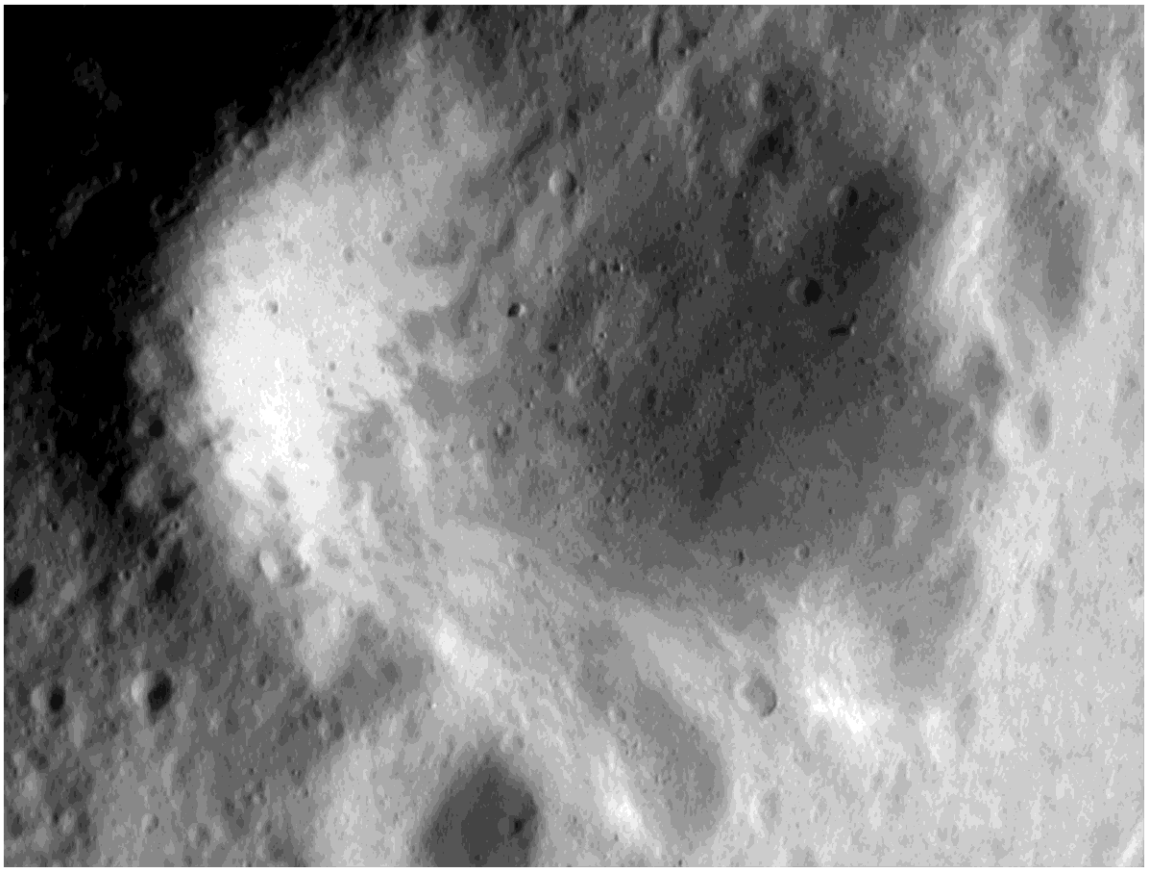


Figure 35. Dark, coarse material has accumulated downslope in the 5.3km crater Psyche on asteroid 433 Eros. Due to Eros's highly irregular shape, "down" is not toward the topographically lowest point in the crater, but is offset to the right, hence the exposure of bright material only on the left wall. PIA03121, courtesy NASA/JPL/JHUAPL.

Cryovolcanic Flows as a Resurfacing Mechanism

The high levels of interior heat that are apparently available within Enceladus raise the question of whether extrusive cryovolcanism may at some time also played a part as a resurfacing mechanism. Fortunately there is a precedent for such activity on an icy moon of Uranus, Ariel (Croft and Soderblom, 1991), so the morphology of the flows can be compared with features seen on the surface of Enceladus.



Figure 36. The southern hemisphere of Ariel (1,162 km diameter) as seen in false-color by Voyager 2 in 1986 from a distance of 170,000 km. Note the prominent and extensive grabens that have been infilled with viscous, convex-surfaced flows. PIA00041, courtesy NASA/JPL (color balance applied by the author).

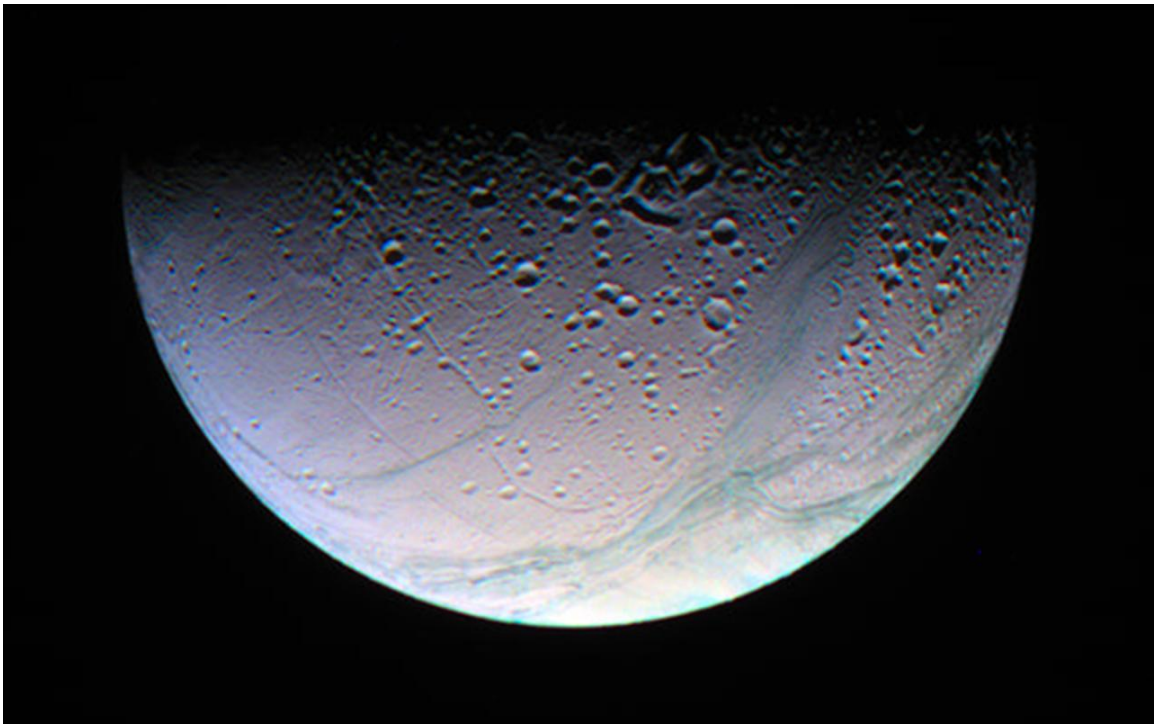


Figure 37. Perhaps the only feature on Enceladus to have a vaguely flow-like appearance is Samarkand Sulci (a small section of which was shown previously in Figure 15). In this enhanced false-color composite by the author, it can be seen as the greenish flame-shaped zone cutting through the cratered plains of the northern hemisphere Ali Baba region. Unlike the convex graben-filling flows on Ariel, Samarkand Sulci is remarkably flat, does not occupy a pre-existing channel, and as indicated by the close-up of the dissected craters, it has clearly not experienced longitudinal flow (the craters having been stretched normal to the long axis of the sulci). Raw images N00114738 (IR3 – Red), N00114737 (GRN – Green), N00114736 (UV3 – Blue) courtesy NASA/JPL/Caltech.

Despite the intense and ongoing geologic activity seen on Enceladus, at this time there is no convincing evidence for extrusive cryovolcanic flows acting as a resurfacing agent. Possibly the closest related phenomenon might be the unusual infilling of large impact craters; the morphology of these features when viewed at high resolution is suggestive of the extrusion of a shallow dome of extremely viscous material whose upper surface is intensely fractured (e.g., Figure 12).

Enceladus' Internal Heat Source

The remarkable (though long-suspected) discovery that Enceladus is currently geologically active and supplying material to the E-ring poses serious questions about its internal heat engine, for it is two orders of magnitude less massive than the next largest active body, Neptune's moon Triton – a captured object whose energy is derived from the gradual circularization of its retrograde orbit. Enceladus is somewhat denser than the average for icy Saturnian moons at ~1,608 kgm^{-3}, but this may be an evolved rather than being an inherent property, caused by continuous, gradual mass loss over geologic time (via the geysers) due to its low escape velocity, though the rate would have to be orders of magnitude greater than that observed today (e.g. Porco et al., 2006) to be significant.. An entirely water-ice crust and a substantial heat source combine in Enceladus to present a moon where various processes such as dynamic resurfacing, viscous relaxation and possible cryovolcanic infilling have destroyed any craters larger than about 40km and covered large areas with a bewildering variety of ridged and grooved landforms. It appears that neither tidal flexing nor radiogenic heating are entirely adequate to explain the observed levels of geologic activity (Hubbard, 1984; Morrison et al., 1984). In addition to these, there are at least two other possible (highly speculative) sources – electromagnetic, and chemical:

Ohmic Heating Enceladus and its partially ionized atmosphere orbit Saturn with a period of 118,386 seconds, while Saturn and its magnetic field rotate in approximately 38,745 seconds, ~3x faster (assuming co-rotation). The resulting electromagnetically

coupled dynamo produces a current in the order of 10,000 Amps (Dougherty et al., 2006). This is only about 10% of the equivalent current that flows in the Jovian magnetosphere due to the volcanic activity of Io (idem), but Io is much more massive, so the relative current flow at Enceladus is ~80 times greater per unit mass. However, Khurana et al. (1998) concluded that induced currents in the Jupiter system were unlikely to be significant sources of heat for either Europa or Callisto, both of which display strong evidence for electrically conductive subsurface oceans. Hubbard (1984) came to a similar conclusion for the general case of a satellite coupled to the interplanetary magnetic field, which is on average faster by about an order of magnitude, but much weaker, ~1/3,500 in the case of the Saturnian 0.21 gauss dipole field (Connerney et al., 1984). While this appears to imply that ohmic dissipation can be ruled out as ever having been a substantial heat source for Enceladus, if the current flow were confined to a very limited volume, such as a shallow, briny layer adjacent to the core-mantle boundary, the effect could be significant over geologic time (note that pure water is a very poor conductor). Further investigation into such a form of “thin-film” ohmic heating could prove worthwhile.

Serpentinization It is noteworthy that the pressure-temperature range calculated here for Enceladus’ core-mantle boundary is in the prograde regime for serpentinization (Minshull et al., 1998), a low-temperature, exothermic metamorphic process that is also known to have occurred on asteroids due to the widespread presence of serpentine minerals in certain classes of meteorites (chondrites and ureilites) (Brearley and Jones,

1998; Mittlefehldt et al., 1998). With a large, primitive (i.e. ultramafic) silicate core and an apparently ample supply of liquid water, there is no a priori reason to assume Enceladus' interior could not support this process. Evidence of water-rock interaction in the form of neutral sodium chloride, sodium bicarbonate, and ionized potassium entrained in the geyser plumes has recently been announced (Postberg et al., 2009), lending credence to the possibility of chemical heat sources within Enceladus. Ion-rich, electrically conductive brine could encourage thin-film ohmic heating in spatially restricted zones within the mantle, further increasing localized temperatures and creating dissolved-ionic gradients (as the current flow is direct) within a complex subsurface plumbing system. Such an environment, with warm, chemical-laden and compositionally stratified water, could well prove an amenable habitable for extraterrestrial extremophiles (though the conditions may be no more extreme than some terrestrial environments).

Diapir-induced Reorientation

The concentration of heat at Enceladus' south pole, the moon's polar-flattened shape (indicative that it is not in hydrostatic equilibrium), and evidence for a series of past resurfacing events has led to the hypothesis that warm, low-density ice diapirs rising through an icy mantle during a thermal event may have resulted in sufficient distortion to its moment of inertia to cause true (and significant) polar wander (e.g. Nimmo and Pappalardo, 2006). The effect of the entire body tipping through some large angle would be considerable, as tidal forces would dissipate considerable energy in re-

equilibrating the ellipsoid to its minimum-inertia configuration, and would provide additional heat to drive resurfacing (idem; Ojakangas and Stevenson, 1989). The issue of what triggers the diapirism, and exactly where in the interior it originates, remains unresolved. Nimmo and Pappalardo also note that diapir-induced reorientation does not preclude the existence of a global subsurface ocean, provided that the diapir occurs in the icy mantle and not the silicate core.

Ammonia

Ammonia is extremely soluble in water and forms a variety of compounds including "exotic" water-ammonia ice that melts at ~176 K, almost 100 K lower than pure water (Greenberg et al., 1984), and had often been invoked as a possible causative agent to explain anomalous geologic activity in small icy bodies such as Enceladus and Miranda (e.g. idem; Pollack and Consolmagno, 1984; Squyres et al., 1983). However, the continued failure to detect substantial quantities of ammonia on or around Enceladus suggests that it is not present in sufficient amounts to be a significant factor, especially if the measured atmospheric concentration of <<0.2% (Waite et al., 2006) is a true representation of Enceladus' water-ice mantle composition.

Comparison with Miranda

Uranus's moon Miranda is the only known object in the solar system that remotely bears comparison with Enceladus. Its surface appearance was the most unexpected revelation of Voyager 2's 1986 encounter with the planet and its moons.

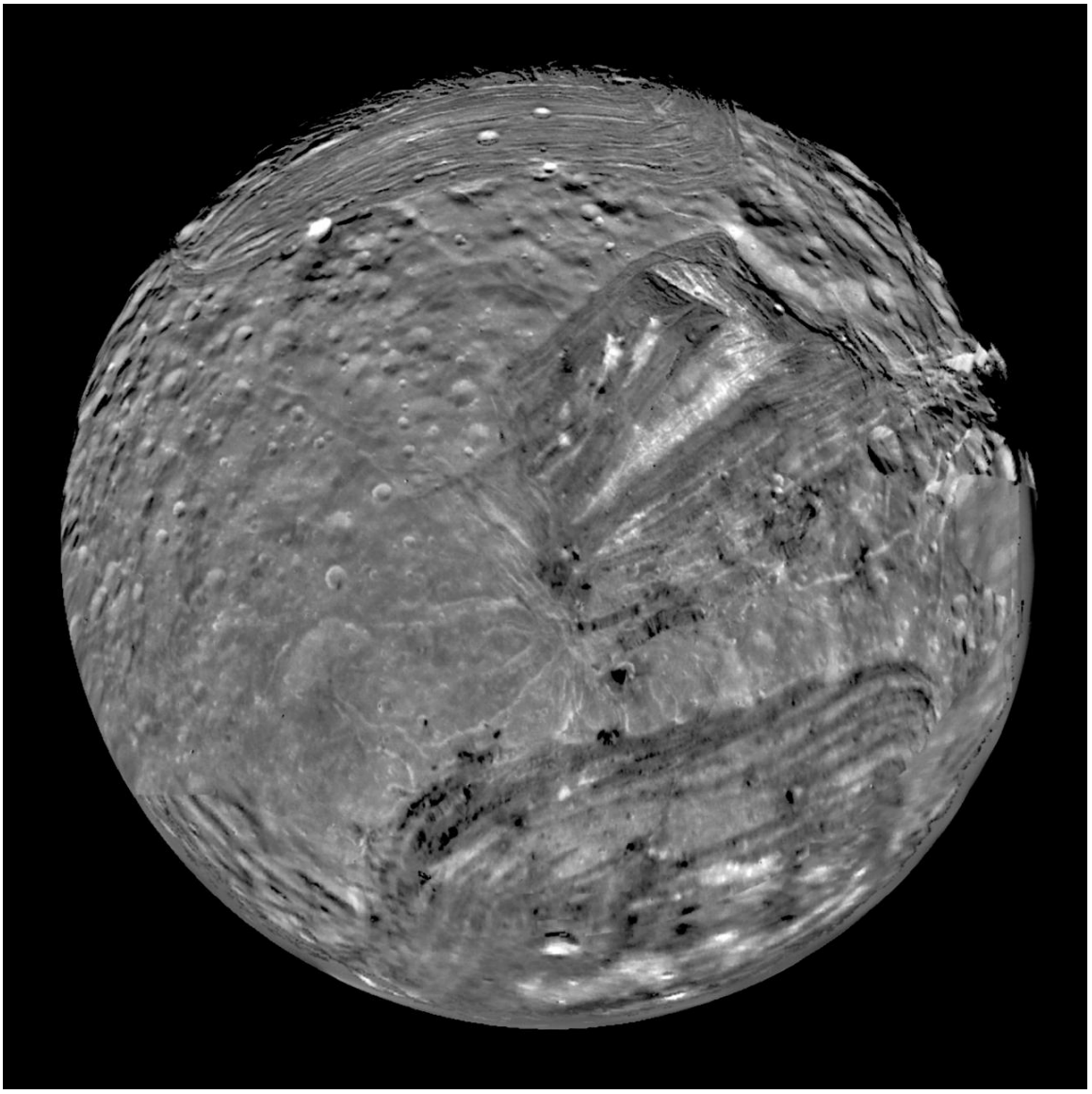


Figure 38. Voyager 2 mosaic of Miranda's southern hemisphere, showing moderately cratered terrain, oval (or "racetrack") and chevron-shaped "coronae" of unknown origin, and a massive canyon system from which fractures radiate near the center of the disk. Note the overall fairly dark surface with distinct brightness variations, and a relatively much "rougher" texture to the cratered plains than seen on Enceladus. Miranda exhibits spectacular evidence of widespread resurfacing, and provides the next-best example that small, icy moons can have wildly varied histories, but there are no indications that it is currently geologically active (Greenberg et al., 1984). 1280 x 1280 pixel crop from PIA01490; courtesy NASA/JPL/USGS.

Miranda is similar to Enceladus in size, with a mean radius of 235.8 ± 0.7 km (Greenberg et al., 1984), but considerably less dense at 1,150 ± 150 kgm^{-3} (idem), though it is worth recalling that the Voyager-era density value for Enceladus was revised upward considerably with the benefit of Cassini data, so it is possible that Miranda is also denser than these figures would suggest. Like Enceladus, it orbits entirely within its primary's magnetosphere (Ness et al., 1984). However, its differential velocity is slower (about 2x) and the magnetospheric interactions are complicated by Uranus's uniquely tilted and axially offset field geometry (idem). Significantly, Miranda is not associated with any known rings in the Uranus system; the U1 ring of Uranus is the only known ring of any planet to be as blue as the E ring of Saturn, but it is associated with the miniscule (~24km diameter) satellite Mab, so despite its spectral characteristics is not believed to be a product of cryovolcanism but derived from impacts (de Pater et al., 2006).

A Possible "Ancestral Antapical Venting System" (AAVS)

As noted previously, the antapical Ebony-Cufa Dorsa may be genetically related to the presently active tiger stripes. It is unlikely to be a coincidence that they occur at the terminus of the largest and deepest north-trending graben extending from the periphery of the SPT (Figure 20). While different in configuration (somewhat resembling a cracked eggshell) the dorsa, Diyar and Sarandib Planitia, and the surrounding sulci (Harran to the east and north; Hamah to the north-west, and Samarkand and Lahej to the west and south, respectively) may represent an extinct, relatively ancient formation analogous to the SPT; the central part of this region is indicated in the Plates.

CONCLUSIONS

Enceladus is in many ways one of the most extreme objects in the solar system, being by far the smallest body known to be geologically active at present – a highly exclusive group consisting of only Earth, Io and Triton. It is denser than any other Saturnian moon except giant Titan, and extremely reflective, having the brightest surface of any satellite of any planet. It possesses a unique south polar hot-spot powering an extraordinary system of geyser-like jets, which spew water vapor, ice, dust and gas into orbit around Saturn to produce the broad, diffuse E-ring. The jets themselves have provided evidence for a subsurface ocean of liquid water, making it a prime future target in the search for extraterrestrial life (e.g. Kargel, 2006). Vast tracts of its surface are nearly or completely devoid of impact craters, indicating ongoing resurfacing processes. Furthermore, some of its surface features appear strikingly familiar, resembling terrestrial structures associated with crustal extension. Could this strange, tiny world be in some way a distant cousin to our own living planet?

A detailed structural geologic analysis was performed (after Davis, 1984, and Davis and Reynolds, 1996), combining descriptive, kinematic and dynamic analyses using high-resolution Cassini-ISS imagery and DLR controlled photomosaics. The results were seemingly counterintuitive until integrated with a geophysical model to account for the alien size, composition and material properties, at which point a solution appeared in the form of a subsurface phase transition – an ocean.

While large scale resurfacing is ongoing, terrestrial-style tectonic plate motion does not occur, and surface features on Enceladus are formed by a set of processes peculiar to bodies with icy lithospheres and are unlike those that occur on Earth. In contrast to Earth where new lithosphere is created at spreading centers and consumed at subduction zones, a process enabled by differences in composition, density, thickness and mineral properties between continental and oceanic crust, resurfacing processes on Enceladus are driven by thermal subsidence, flexure, isostatic compensation, and viscoelastic relaxation. Unlike its neighbors in the Saturn system, large areas of Enceladus' surface have been raised so close to the melting point they are incapable of preserving any pre-existing topography, and the crust is incapable of supporting high-relief features anywhere over geologic time. This fascinating object will no doubt be the subject of intense scrutiny for the foreseeable future.

The term "idemtectonics" is suggested to encompass the processes at work on Enceladus. It is derived from the Latin root "idem" for "same", as in same materials, same level, same location, to indicate the lack of a crustal dichotomy, the importance of isostasy, and the absence of plate motion.

REFERENCES CITED

Alexander, A.F.O'D., 1962, The Planet Saturn: A History of Observation, Theory and Discovery: New York, The Macmillan Company, 474 p.

Arvidson, R., Boyce, J., Chapman, C., Cintala, M., Fulchignoni, M., Moore, H., Neukum, G., Schultz, P., Soderblom, L., Strom, R., Woronow, A., and Young, R., 1978, NASA-TM-79730 Standard Techniques for Presentation and Analysis of Crater Size-Frequency Data: Washington, D.C., Scientific and Technical Information Office, 24 p.

Baker, J., 2006, Tiger, Tiger, Burning Bright: Science, v. 311, p. 1388.

Bakich, M.E., 2000, The Cambridge Planetary Handbook: Cambridge, Cambridge University Press, 336 p.

Batson, R.M., Lee, E.M., Mullins, K.F., Skiff, B.A., Bridges, P.M., Inge, J.L., Masursky, H. and Strobel, M.E., 1984, Voyager 1 and 2 Atlas of Six Saturnian Satellites: Washington, D.C., Scientific and Technical Information Branch, National Aeronautics and Space Administration.

Benn, D.I., and Evans, D.J.A., 1998, Glaciers and Glaciation: London, Hodder Arnold, 734 p.

Bland, M.T., Beyer, R.A., and Showman, A.P., 2007, Unstable extension in Enceladus' lithosphere: Icarus, 192, p. 92-105.

Bott, M.H.P., 1993, Modelling the plate-driving mechanism: Journal of the Geological Society, v. 150, p. 941-951.

Brearley, A.J., and Jones, R.H., 1998, Chondritic Meteorites, *in* Papike, J.J., ed., Reviews in Mineralogy, Volume 36: Planetary Materials: Washington, D.C., Mineralogical Society of America, 1059 p.

Brown, R.H., Clark, R.N., Buratti, B.J., Cruikshank, D.P., Barnes, J.W., Mastrapa, R.M.E., Bauer, J., Newman, S., Momary, T., Baines, K.H., Bellucci, G., Cappaccioni, F., Cerroni, P., Combes, M., Coradini, A., Drossart, P., Formisano, V., Jaumann, R., Langevin, Y., Matson, D.L., McCord, T.B., Nelson, R.M., Nicholson, P.D., Sicardy, B., and Sotin, C., 2006, Composition and Physical Properties of Enceladus' Surface: Science, v. 311, p. 1425-1428.

Collins, G.C., and Goodman, J.C., 2007, A south polar sea on Enceladus?: Lunar and Planetary Science, XXXVIII.

Connerney, J.E.P., Davis Jr., L., and Chenette, D.L., 1984, Magnetic field models, *in* Gehrels, T., and Matthews, M.S., eds., Saturn: Tucson, The University of Arizona Press, 968 p.

Conrad, C.P., Bilek, S., and Lithgow-Bertelloni, C., 2003, Great earthquakes and slab pull: interaction between seismic coupling and plate-slab coupling: Earth and Planetary Science Letters, 218, p. 109-122.

Conrad, C.P., and Lithgow-Bertelloni, C., 2002, How Mantle Slabs Drive Plate Tectonics: Science, v. 298, p. 207-209.

Conrad, C.P., and Lithgow-Bertelloni, C., 2004, The temporal evolution of plate driving forces: Importance of "slab suction" versus "slab pull" during the Cenozoic: Journal of Geophysical Research, v. 109, B10407.

Croft, S.K., and Soderblom, L.A., 1991, Geology of the Uranian Satellites: *in* Bergstrahl, J.T., Miner, E.D., and Matthews, M.S., eds., Uranus: Tucson, The University of Arizona Press, 1076 p.

Davis, G.H., 1984, Structural geology of rocks and regions: New York, John Wiley & Sons, 492 p.

Davis, G.H., and Reynolds, S.J., 1996, Structural geology of rocks and regions, second edition: Hoboken, John Wiley & Sons, 776 p.

Dietz, R.S., 1959, Shatter cones in cryptoexplosion structures (meteorite impact?): Journal of Geology, v. 67, no. 5, p. 496-505.

Dougherty, M.K., Khurana, K.K., Neubauer, F.M., Russell, C.T., Saur, J., Leisner, J.S., and Burton, M.E., 2006, Identification of a Dynamic Atmosphere at Enceladus with the Cassini Magnetometer: Science, v. 311, p. 1406-1409.

Eisenberg, D., and Kauzmann, W., 1969, The Structure and Properties of Water: New York, Oxford University Press, 296 p.

Faccenna, C., Heuret, A., Funiciello, F., Lallemand, S., and Becker, T.W., 2007, Predicting trench and plate motion from the dynamics of a strong slab: Earth and Planetary Science Letters, 257, p. 29-36.

Faulds, J.E. and Varga, R.J., 1998, The role of accommodation and transfer zones in the regional segmentation of extended terranes, *in* Faulds, J.E., and Stewart, J.H., eds., Accommodation Zones and Transfer Zones: The Regional Segmentation of the Basin and Range Province: GSA Special Paper 323, 257 p.

Feibelman, W.A., 1967, Concerning the "*D*" Ring of Saturn: Nature, v. 214, p. 793-794.

Forsyth, D., and Uyeda, S., 1975, On the Relative Importance of the Driving Forces of Plate Motion: Geophysical Journal International, v. 43, Issue 1, p. 163-200.

Franks, F., 1972, The Properties of Ice, *in* Franks, F., ed., Water: a Comprehensive Treatise, Volume 1, The Physics and Physical Chemistry of Water: New York, Plenum Press, 596 p.

Galilei, G., 1610, Sidereus Nuncius: Venice, 60 p.

Greenberg, R., 1984, Orbital resonances among Saturn's satellites: *in* Gehrels, T., and Matthews, M.S., eds., Saturn: Tucson, The University of Arizona Press, 968 p.

Greenberg, R., Croft, S.K., Janes, D.M., Kargel, J.S., Lebofsky, L.A., Lunine, J.I., Marcialis, H.J., Melosh, H.J., Ojakangas, G.W., and Strom, R.G., 1984, Miranda: *in* Bergstrahl, J.T., Miner, E.D., and Matthews, M.S., eds., Uranus: Tucson, The University of Arizona Press, 1076 p.

Hansen, C.J., Esposito, L., Stewart, A.I.F., Colwell, J., Hendrix, A., Pryor, W., Shemansky, D., and West, R., 2006, Encleadus' Water Vapor Plume: Science, v. 311, p. 1422-1425.

Hansen, C.J., Esposito, L.W., Stewart, A.I.F., Meinke, B., Wallis, B., Colwell, J.E., Hendrix, A.R., Larsen, K., Pryor, W., and Tian, F., 2008, Water vapour jets inside the plume of gas leaving Enceladus: Nature, v. 456, p. 477-479.

Harland, D.M., 2007, Cassini at Saturn – Huygens Results: Chichester, Praxis Publishing, 403 p.

Hatcher Jr., R.D., 1995, Structural Geology: Principles, Concepts and Problems, Second Edition: New Jersey, Prentice Hall, 525 p.

Helfenstein, P., Denk, T., Giese, B., Ingersoll, A., Johnson, T. V., McEwen, A. S., Neukum, G., Perry, J., Porco, C., Roatsch, T., Thomas, P. C., Turtle, E., Verbiscer, A., and Veverka, J., 2008, Enceladus' South Polar Terrain Geology: New Details from Cassini ISS High Resolution Imaging: Eos Transactions, American Geophysical

Union, 89 (53) Fall Meeting Supplement, Abstract P13D-02.

Hoppa, G.V., Tufts, B.R., Greeenberg, R., and Geissler, P.E., 1999, Formation of Cycloidal Features on Europa: Science, v. 285, p. 1899-1902.

Hubbard, W.B., 1984, Planetary Interiors: New York, Van Nostrand Reinhold Company, Inc., 334 p.

Waite J.H. Jr., Combi, M.R., Wing-Huen, I., Cravens, T.E., McNutt Jr., R.L., Kasprzak, W., Yelle, R., Luhmann, J., Niemann, H., Gell, D., Magee, B., Fletcher, G., Lunine, J., and Wei-Ling, T., 2006, Cassini Ion and Neutral Mass Spectrometer: Enceladus Plume Composition and Structure: Science, v. 311, p. 1419-1422.

Hurford, T.A., Helfenstein, P., Hoppa, G.V., Greenburg, R., and Bills, B.G., 2007, Eruptions arising from tidally controlled periodic openings of rifts on Enceladus: Nature, v. 477, p. 292-294.

Huygens, C., 1668, The Celestial Worlds Discover'd: London, Timothy Childe, 160 p.

Jones, G.H., Roussos, E., Krupp, N., Paranicas, C., Woch, J., Lagg, A., Mitchell, D.G., Krimigis, S.M., and Dougherty, M.K., 2006, Enceladus' Varying Imprint on the Magnetosphere of Saturn: Science, v. 311, p. 1412-1415.

Kargel, J.S., 2006, Enceladus: Cosmic Gymnast, Volatile Miniworld: Science, v. 311, p. 1389-1391.

Keller, S.R., 1979, On the Surface Area of the Ellipsoid: Mathematics of Computation, v. 33, no. 145, p. 310-314.

Kieffer, S.W., Xinli, L., Bethke, C.M., Spencer, J.R., Marshak, S., Navrotsky, A., 2006, A Clathrate Reservoir Hypothesis for Enceladus' South Polar Plume: Science, v. 314, p. 1764-1766.

Kivelson, M.G., 2006, Does Enceladus Govern Magnetospheric Dynamics at Saturn?: Science, v. 311, p. 1391-1392.

Khurana, K.K., Kivelson, M.G., Stevenson, D.J., Schubert, G., Russell, C.T., Walker, R.J., and Polanskey, C., 1998, Induced magnetic fields as evidence for subsurface oceans in Europa and Callisto: Nature, v. 395, p. 777-780.

La Placa, S.J., Hamilton, W.C., Kamb, B., and Prakash, A., 1973, On a nearly proton-ordered structure for ice IX: Journal of Chemical Physics, v. 58, no. 2, p. 567-580.

Lide, D.R., ed., 2006, CRC Handbook of Chemistry and Physics, 87th edition: Boca Raton, Taylor & Francis Group, 2608 p.

Melosh, H.J., 1989, Impact Cratering: A Geologic Process: Oxford, Oxford University Press, 245 p.

Mendis, D.A., Hill, J.R., Ip, W.-H., Goertz, C.K., and Grün, E., 1984, Electrodynamic Processes in the Ring System of Saturn: *in* Gehrels, T., and Matthews, M.S., eds., Saturn: Tucson, The University of Arizona Press, 968 p.

Mittlefehldt, D.W., McCoy, T.J., Goodrich, C.A., and Kracher, A., 1998, Non-Chondritic Meteorites from Asteroidal Bodies, *in* Papike, J.J., ed., Reviews in Mineralogy, Volume 36: Planetary Materials: Washington, D.C., Mineralogical Society of America, 1059 p.

Moores, E.M., and Twiss, R.J., 1995, Tectonics: New York, W.H. Freeman and Company, 415 p.

Morrison, D., Johnson, T.V., Shoemaker, E.M., Soderblom, L.A., Thomas, P., Ververka, J., and Smith, B., 1984, Satellites of Saturn: Geological Perspective, *in* Gehrels, T., and Matthews, M.S., eds., Saturn: Tucson, The University of Arizona Press, 968 p.

Ness, N.F., Connerney, J.E.P., Lepping, R.P., Schulz, M., and Voigt, G-H., 1984, The magnetic field and magnetospheric configuration of Uranus: *in* Bergstrahl, J.T., Miner, E.D., and Matthews, M.S., eds., Uranus: Tucson, The University of Arizona Press, 1076 p.

Nimmo. F., and Pappalardo, R.T., 2006, Diapir-induced reorientation of Saturn's moon Enceladus: Nature, v. 441, p. 614-616.

Nimmo, F., Spencer, J.R., Pappalardo, R.T., and Mullen, M.E., 2007, Shear heating as the origin of the plumes and heat flux on Enceladus: Nature, v. 447, p. 289-291.

Ojakangas, G.W., and Stevenson, D.J., 1989, Polar wander of an ice shell on Europa: Icarus, 81, p. 242-270.

Pappalardo, R.T. and Greeley, R., 1995, A review of the origins of subparallel ridges and troughs: Generalized morphological predictions from terrestrial models: Journal of Geophysical Research, v.100, p. 18985-19007.

Paterson, W.S.B., 1994, The Physics of Glaciers, Third Edition: Oxford, Butterworth-Heinemann, 481 p.

Plescia, J.B., and Boyce, J.M., 1983, Crater numbers and geological histories of Iapetus, Enceladus, Tethys and Hyperion: Nature, v. 301, p. 666-670.

Pollack, J.B., and Consolmagno, G., 1984, Origin and Evolution of the Saturn System, *in* Gehrels, T., and Matthews, M.S., eds., Saturn: Tucson, The University of Arizona Press, 968 p.

Porco, C.C., West, R.A., Squyres, S., McEwen, A., Thomas, P., Murray, C.D., Delgenio, A., Ingersoll, A.P., Johnson, T.V., Neukum, G., Ververka, J., Dones, L., Brahic, A., Burns, J.A., Haemmerle, V., Knowles, B., Dawson, D., Roatsch, T., Beurle, K., and Owen, W., 2004, Cassini imaging science: instrument characteristics and anticipated scientific investigations at Saturn: Space Science Reviews, v. 115, p. 363-497.

Porco, C.C., Helfenstein, P., Thomas, P.C., Ingersoll, A.P., Wisdom, J., West, R., Neukum, G., Denk, T., Wagner, R., Roatsch, T., Kieffer, S., Turtle, E., McEwan, A., Johnson, T.V., Rathbun, J., Ververka, J., Wilson, D., Perry, J., Spitale, J., Brahic, A., Burns, J.A., DelGenio, A.D., Dones, L., Murray, C.D. and Squyres, S., 2006, Cassini Observes the Active South Pole of Enceladus: Science, v. 311, p. 1393-1401.

Porco, C.C., 2008, Enceladus: Secrets of Saturn's Strangest Moon: Scientific American, December, p. 52-63.

Postberg, F., Kempf, S., Schmidt, J., Brillantov, N., Abel, B., Beinsen, A., Buck, U., and Srama, R., 2009, Sodium Salts in Ice Grains from Enceladus' Plumes: Probes of a Subsurface Ocean: Geophysical Research Abstracts, v. 11, EGU2009-12013.

Roatsch, T., Wählisch, M., Giese, B., Hoffmeister, A., Matz, K.-D., Scholten, F., Kuhn, A., Wagner, R., Neukum, G., Helfenstein, P., and Porco, C.C., 2008, High-resolution Enceladus atlas derived from Cassini-ISS images: Planetary and Space Science, v. 56, p. 109-116.

Roberts, J.H., and Nimmo, F., 2008, Near-surface heating on Enceladus and the south polar thermal anomaly: Geophysical Research Letters, v. 35, L09201.

Rothery, D.A., 1992, Satellites of the Outer Planets: Worlds in their own right: Oxford, Oxford University Press, 208 p.

Sagan, C., and Khare, B.N., 1979, Tholins: organic chemistry of interstellar grains and gas: Nature, v. 277, p. 102-107.

Sagan, C., Khare, B.N., and Lewis, J.S., 1984, Organic Matter in the Saturn System, *in* Gehrels, T., and Matthews, M.S., eds., Saturn: Tucson, The University of Arizona Press, 968 p.

Schellart, W. P., 2004, Quantifying the net slab pull force as a driving mechanism for plate tectonics: Geophysical Research Letters, v. 31, L07611.

Schellart, W.P., 2008, Subduction zone trench migration; slab driven or overriding plate-driven?: Physics of the Earth and Planetary Interiors, v. 170, p. 73-88.

Spence, W., 1987, Slab Pull and the Seismotectonics of Subducting Lithosphere: Reviews of Geophysics, v. 25, no. 1, p. 55-69.

Schenk, P.M. and Moore, J.M., 1995, Volcanic constructs on Ganymede and Enceladus: Topographic evidence from stereo images and photoclinometry: Journal of Geophysical Research, v. 100, no. E9, p. 19009-19022.

Schmidt, J., Brilliantov, N., Spahn, F., and Kempf, S., 2008, Slow dust in Enceladus' plume from condensation and wall collision in tiger stripe fractures: Nature, v. 451, p. 685-688.

Shoemaker, E.M., and Wolfe, R.F., 1982, Cratering time scales for the Galilean satellites, *in* Morrison, D. and Matthews, M.S., eds., Satellites of Jupiter: Tucson, The University of Arizona Press, 972 p.

Snyder, J.P., 1993, Flattening the Earth: Two Thousand Years of Map Projections: Chicago, The University of Chicago Press, 365 p.

Spencer, J., and Grinspoon, D., 2007, Inside Enceladus: Nature, v. 445, p. 376-377.

Spencer, J.R., Pearl, J.C., Segura, M., Flasar, F.M., Mamoutkine, A., Romani, P., Buratti, B.J., Hendrix, A.R., Spilker, L.J. and Lopes, R.M.C., 2006, Cassini Encounters Enceladus: Background and the Discovery of a South Polar Hot Spot: Science, v. 311, p. 1401-1405.

Spitale, J.N., and Porco, C.P., 2007, Association of the jets of Enceladus with the warmest regions on its south-polar fractures: Nature, v. 449, p. 695-697.

Squyres, S.W., Reynolds, R.T., Cassen, P.M., and Peale, S.J., 1983, The evolution of Enceladus: Icarus, 53, p. 319-331.

Thomas, Peter, pers. comm. 2008, Cornell University, Department of Radiophysics and Space Research, pthomas@astro.cornell.edu

Tokar, R.L., Johnson, R.E., Hill, T.W., Pontius, D.H., Kurth, W.S., Crary, F.J., Young, D.T., Thomsen, M.F., Reisenfeld, D.B., Coates, A.J., Lewis, G.R., Sittler, E.C., and Gurnett, D.A., 2006, The Interaction of the Atmosphere of Enceladus with Saturn's Plasma: Science, v. 311, p. 1409-1412.

Van Allen, J.A., 1984, Energetic particles in the inner magnetosphere of Saturn, *in* Gehrels, T., and Matthews, M.S., eds., Saturn: Tucson, The University of Arizona Press, 968 p.

Van der Pluijm, B.A., and Marshak, S., 2004, Earth structure: an introduction to structural geology and tectonics: New York, W.W. Norton & Company, 656 p.

Van Helden, A., 1984, Saturn through the telescope: a brief historical survey, *in* Gehrels, T., and Matthews, M.S., eds., Saturn: Tucson, The University of Arizona Press, 968 p.

Verbischer, A., French, R., Showalter, M. and Helfenstein, P., 2007, Enceladus: Cosmic Graffiti Artist Caught in the Act: Science, v. 315, p. 815.

Yang, Q., Snyder, J.P., and Tobler, W.R., 2000, Map Projection Transformation: Principles and Applications: London, Taylor & Francis, 367 p.

Zeilik, M., and Gregory, S.A., 1998, Introductory Astronomy and Astrophysics, fourth edition: Fort Worth, Saunders College Publishing, 672 p.

APPENDICES

APPENDIX A

TABULATED PLANET AND SMALL BODY PROPERTIES

Tabulated Planet and Small Body Properties

The following table lists 40 solar system solid bodies in order of decreasing size. Note that while numerous Trans-Neptunian Objects, Kuiper Belt Objects and other small bodies have recently been discovered that would occupy extra space in this table, most of these have been excluded in favor of major planetary satellites, most of which also have better defined physical parameters. Bodies known to be geologically active *at present* are indicated in bold. Except for planets, where the equatorial diameter is given, the average diameter is quoted.

Table A1. Planet and small body properties; note the somewhat improbable occurrence of a geologically active body so far down this list.

NAME	CATEGORY	Ø (km)	AREA (km^2)	MASS (kg)	DENSITY (kgm^{-3})
Earth	**planet**	**12,756**	**511,185,501**	**5.976E+24**	**5.499E+03**
Venus	planet	12,104	460,264,348	4.869E+24	5.244E+03
Mars	planet	6,794	145,010,881	6.42E+23	3.910E+03
Ganymede	moon of Jupiter	5,268	87,184,853	1.482E+23	1.936E+03
Titan	moon of Saturn	5,150	83,322,821	1.346E+23	1.881E+03
Mercury	planet	4,879	74,784,422	3.303E+23	5.431E+03
Callisto	moon of Jupiter	4,806	72,563,302	1.076E+23	1.851E+03
Io	**moon of Jupiter**	**3,630**	**41,396,417**	**8.940E+22**	**3.570E+03**
Moon	moon of Earth	3,476	37,958,532	7.150E+22	3.251E+03
Europa	moon of Jupiter	3,120	30,581,494	4.799E+22	3.018E+03
Triton	**moon of Neptune**	**2,707**	**23,021,097**	**2.147E+22**	**2.067E+03**
Eris	Trans-Neptunian Object	2,600	21,237,148	1.67E+22	1.815E+03
Pluto	Kuiper Belt Object	2,322	16,938,461	1.305E+22	1.991E+03
Sedna	Trans-Neptunian Object	1,700	9,079,195	5.100E+21	1.983E+03
Titania	moon of Uranus	1,578	7,822,823	3.527E+21	1.714E+03
Rhea	moon of Saturn	1,530	7,354,148	2.310E+21	1.232E+03
Oberon	moon of Uranus	1,523	7,287,009	3.014E+21	1.629E+03
Makemake	Kuiper Belt Object	1,500	7,068,578	4.000E+21	2.264E+03
Iapetus	moon of Saturn	1,436	6,478,260	1.590E+21	1.025E+03
Haumea	Trans-Neptunian Object	1,436	6,478,260	4.20E+21	2.709E+03
Charon	moon of Pluto	1,207	4,576,822	1.520E+21	1.651E+03
Umbriel	moon of Uranus	1,169	4,293,174	1.172E+21	1.401E+03
Ariel	moon of Uranus	1,162	4,241,913	1.353E+21	1.647E+03
TC302	Trans-Neptunian Object	1,150	4,154,753	1.60E+21	2.009E+03
Dione	moon of Saturn	1,120	3,940,811	1.052E+21	1.430E+03

Tethys	moon of Saturn	1,060	3,529,891	6.220E+20	9.974E+02
Orcus	Trans-Neptunian Object	946	2,811,459	7.500E+20	1.692E+03
Ceres	main belt asteroid 1	941	2,781,818	9.430E+20	2.161E+03
Varuna	Kuiper Belt Object	900	2,544,688	3.700E+20	9.693E+02
Quaoar	Kuiper Belt Object	844	2,237,868	1.800E+20	5.718E+02
AW197	Kuiper Belt Object	734	1,692,550	4.100E+20	1.980E+03
Ixion	Trans-Neptunian Object	650	1,327,322	3.000E+20	2.086E+03
Pallas	main belt asteroid 2	545	933,131	2.110E+20	2.489E+03
Vesta	main belt asteroid 4	530	882,473	2.670E+20	3.425E+03
Huya	Trans-Neptunian Object	530	882,473	6.50E+19	8.338E+02
Enceladus	**moon of Saturn**	**504**	**798,648**	**1.079E+20**	**1.610E+03**
Miranda	moon of Uranus	480	723,822	6.590E+19	1.138E+03
Hygeia	main belt asteroid 10	430	580,880	8.850E+19	2.126E+03
Proteus	moon of Neptune	416	543,671	5.000E+19	1.326E+03
Mimas	moon of Saturn	398	497,640	3.750E+19	1.136E+03

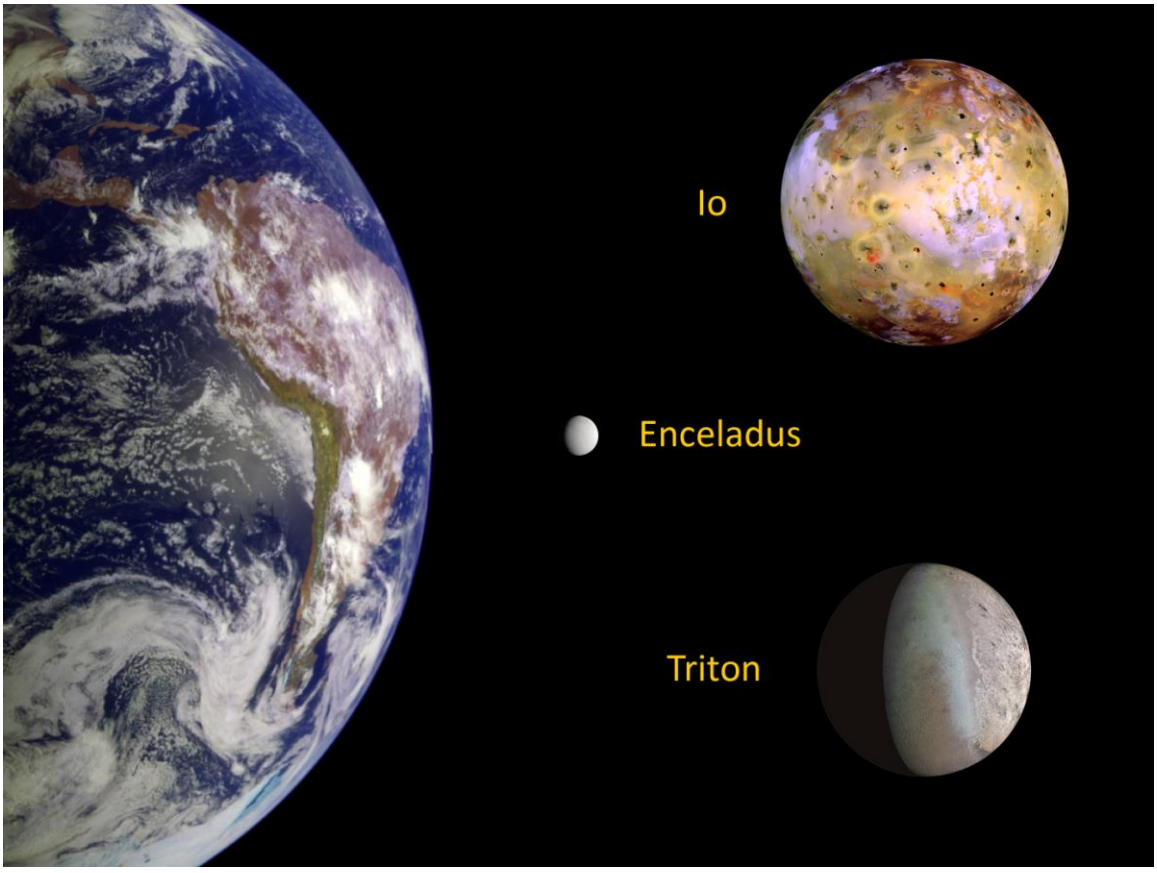


Figure A1. Scale size comparison of Earth, Io, Triton and Enceladus. Clockwise from Earth: PIA00342, PIA02309, PIA00317, PIA00347; editing and montage by the author.

Table A2. Size and densities of the major Saturnian satellites. Enceladus is significantly denser than any other moon except Titan, which is 1,247 times more massive. While probably coincidental, it is interesting to note that Dione, the only satellite with which Enceladus shares a resonance, is also significantly denser than the other icy satellites (Titan excluded).

NAME	Ø (km)	AREA (km^2)	MASS (kg)	DENSITY (kgm^{-3})
Titan	5,150	83,322,821	1.346E+23	1.881E+03
Rhea	1,530	7,354,148	2.310E+21	1.232E+03
Iapetus	1,436	6,478,260	1.590E+21	1.025E+03
Dione	1,120	3,940,811	1.052E+21	1.430E+03
Tethys	1,060	3,529,891	6.220E+20	9.974E+02
Enceladus	**504**	**798,648**	**1.079E+20**	**1.610E+03**
Mimas	398	497,640	3.750E+19	1.136E+03

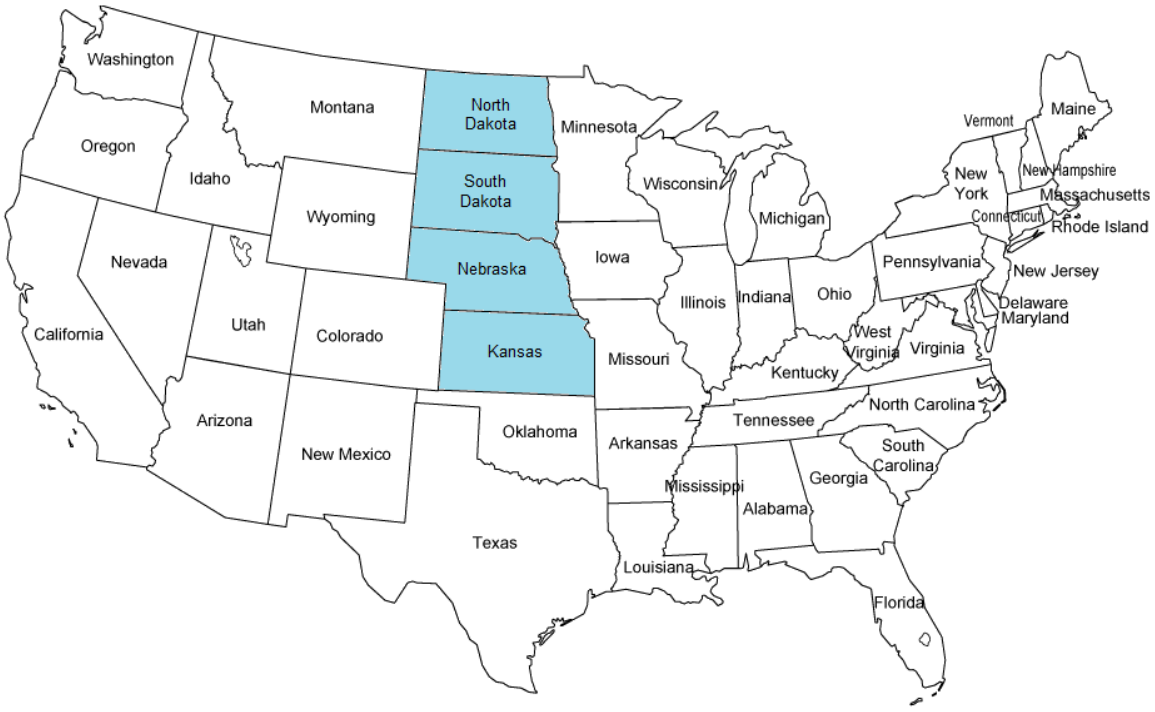


Figure A2.Enceladus' surface area compared. Adapted from http://www.united-states-map.com/usa7241z.htm.

APPENDIX B

RGB FALSE-COLOR IMAGE CONSTRUCTION

Assembling RGB False-Color Images from Cassini-ISS Raw Frames

The Cassini Imaging Subsystem (ISS) comprises two cameras, a narrow-angle (NAC) and a wide-angle (WAC). NAC images were generally found to be more useful for this project. Each camera has a 1024 x 1024 (i.e. 2^{10} or 1MP) pixel sensor sensitive to a wide range of wavelengths, and each is equipped with two filter wheels that can selectively adjust the desired sensitivity to emphasize different features on planetary surfaces or in atmospheres (Porco et al., 2004). In addition to the broadband (i.e. clear-filter) images, which were often the sharpest and clearest due to shorter integration times, the combination of IR3 (930 nm) = R, G (568 nm) = G and UV3 (338 nm) = B (each with a clear filter in the other wheel), greatly enhanced the extremely subtle color variations of surface ice on Enceladus. Amorphous ice appears whiter, and crystalline ice appears bluish-green (idem.). Assigning the channels this way, with near-infrared = red, green = green and ultraviolet = blue maintains the relative color balance of the scene, effectively compressing the sensed wavelengths into the human visual range. While the Cassini-ISS team produced many RGB composites of Enceladus and other targets in the Jupiter and Saturn systems, there were times when it was felt worthwhile to create images of Enceladus (and other moons) from views that were not officially released as composites. The general procedure used to create RGB false-color composites was as follows (these instructions pertain to Adobe® Photoshop CS3 but most imaging software capable of these operations should work similarly):

- Select a suite of images containing raw frames acquired through the desired filters
- Save the frames and record additional pertinent data (filter pack and range to target) in the file name, for example: raw frame N00117202 could be saved as N00117202_CL1-IR3_412750km.jpg. (Note: while an 8-bit (i.e. monochrome) JPG is not the ideal format to work with, the uncompressed, calibrated and validated images typically take months to be posted on the NASA Planetary Data System website http://pds.nasa.gov and they are only (as of this writing) made available in a JPL-specific IMG format. These factors, combined with the tedious procedure required to locate and download the image metadata, label and tag, and convert them to a format usable by commercially available software makes any benefit possible from using the "official" versions a dubious proposition – and the conversion options provided by NASAView 3.3.0 are limited to 8-bit formats (GIF and JPG))
- Because the spacecraft moves between each frame, it is necessary to convert each image to a common scale. Select the image acquired at the *closest* range and resample (*not* resize) from 1024 x 1024 pixels to 4096 x 4096 using the Bicubic Smoother algorithm; this algorithm helps to ameliorate the appearance of JPG compression artifacts found in the raw images. Use the closest range to target as the denominator of the scaling factor to determine the resize of the remaining two frames; they will be *larger* than 4096 x 4096 (sometimes only by

a pixel or two). Zoom as necessary to enable fitting them on-screen. 4096 x 4096 was chosen as it is large enough to enable accurate repositioning and alignment at the sub-pixel level, while manageable enough (16MP) to be manipulated in reasonable time by an average computer

- Create a new blank image of dimensions 4224 x 4224 in RGB color mode at a bit depth of 8 bits per pixel. This image is deliberately made larger than the original to provide sufficient white space to facilitate repositioning (alignment and/or rotation) the individual frames without running into the borders, which can cause the images to "stick" if they get too close (an effect designed to allow accurate registration against the edge, but undesirable in this application. It is similar in intent to the "snaps" found in CAD and similar applications)
- Select one of the resized images (it does not matter which one) and copy to the clipboard, taking note of the filter used to acquire it
- Select the blank image and open the channels palette. Select the appropriate channel to match the filter of the first selected frame (using the mouse, or the shortcut Ctrl+1 → Red, Ctrl+2 → Green, Ctrl+3 → Blue) and then paste the frame from the clipboard into the new image. It should appear (as grayscale) centered in the new image. Repeat for the remaining two frames, making sure to assign them to the appropriate channel in the new image. Depending on how this is done, the result may temporarily appear cyan, magenta or yellow. When all

three are loaded into the new image, select RGB in the channels palette (or Ctrl+~) to see them overlaid

- It will be immediately obvious that the images need to be aligned (but see below in case this is not possible due to target rotation). Maximize the new image and zoom to at least 100%. Ensure the layer is not locked, select one channel (it must be highlighted in the palette or this will not work) and use the move tool (shortcut "v") to grab the layer with the pointing device and move it into alignment. The best way to do this is to leave one layer alone (for example, Green), make one channel invisible by deselecting the respective "eye" in the palette (say, Red), and move the remaining channel (Blue) into alignment. In this example, you will see a cyan image with green and blue fringes where the individual channels don't match up. Position the Blue channel so that the entire image is cyan and devoid of colored fringes. It may be that it is impossible to achieve a perfect result. In this case, first check your calculations in case the scaling is wrong (this problem will usually be immediately obvious). Or, the image may need to be rotated as well as translated. Finally, the *target* may have rotated significantly relative to the spacecraft between frames in which case the composite may not be salvageable as such (though it may be possible to use two of the frames from the sequence to create a 3-D anaglyph – an exercise left to the reader; see Figure B2 for an example)

- When the first two channels are satisfactorily aligned, uncheck the eye next to the *channel you just moved* and the image will once again appear grayscale as you are only seeing the Green channel (in this case). Repeat the above procedure, this time moving the Red channel. Where Red and Green are aligned the image will appear yellow; where they are not there will be red and green fringes
- Select RGB to see the completed (but not finished) composite. Examine it closely (still at 100% or higher) to see if further adjustments can improve its appearance. With icy satellites that are basically some shade of gray, any misalignment will be very obvious as color fringes and the image will appear to "snap" into chromatic neutrality when alignment is achieved
- When the alignment is determined to be satisfactory (often a compromise in one way or another), resample it down to 1056 x 1056 pixels using a suitable algorithm (not all Cassini-ISS raw images are of equal quality but if they will stand it, use the Bicubic Sharper to add some crispness to the finished product). 1056 pixels is exactly 1/4 the size of the original composite (including the white space); using an exact binary multiplier like 2^{-2} ensures the best possible results by eliminating artifacts that would result from non-integral resampling
- Crop the image as desired but note that it is always preferable to crop to a dimension that is divisible by 8 on each side. This ensures the best possible

conversion if the crop is later saved in a compressed format like JPG or subsequently resized (e.g. for inclusion in a document or e-mail)

- Save in a lossless format like TIF or PNG at 8 bits per channel; PNG is useful as it is one of the very few formats that support transparency as seen for example in the overlays used in Figure 7
- Finally, enhancing the image (brightness, contrast, saturation, etc.) can usefully improve the visibility of surface color and brightness variations. The saturation control in PS3 seems to produce very poor results with these images; the "color booster" tool in Nikon Capture NX (for example) is capable of providing a much smoother, more saturated output without channel clipping or posterization effects (Figure B1). Other image manipulation software packages may also produce better or worse results

In some cases, where significant relative rotation has occurred during an imaging sequence, it may still be possible to salvage an RGB composite by dividing it into smaller sections, aligning the sections separately and then merging them together using automated software. This may also be the only option for images acquired at very close range (so that small regions of the surface fill the entire field of view). In either case, the use of an automated process to recombine the aligned images is highly recommended to achieve an acceptable result as operations such as matching and blending can be carried out virtually seamlessly, which is not possible when assembling photomosaics manually.



Figure B1. An RGB false-color composite of Dione created from Cassini-ISS raw frames N00081700 (IR3-Red), N00081698 (GRN-Green), and N00081697 (UV3-Blue). Range to target: 197,932 km; scale: 1.19 km per pixel (1020 x 1020 pixels; this image was not cropped to a divisible-by-8 size due to insufficient channel overlap that would have left colored fringes along one or more edges at 1024 x 1024 pixels). Note the color variation across the surface, the reddish-brown ejecta blanket around the small crater above center, well-developed complex craters and tectonic fractures. The 350 km diameter multiring basin Evander is visible across the terminator at the top of the image. The dark gray annulus near the right limb is the shadow of a dust particle on one of the filters as rendered by the Ritchey-Chretien (Cassegrainian) optics of the narrow-angle camera. Raw images courtesy NASA/JPL/Caltech.

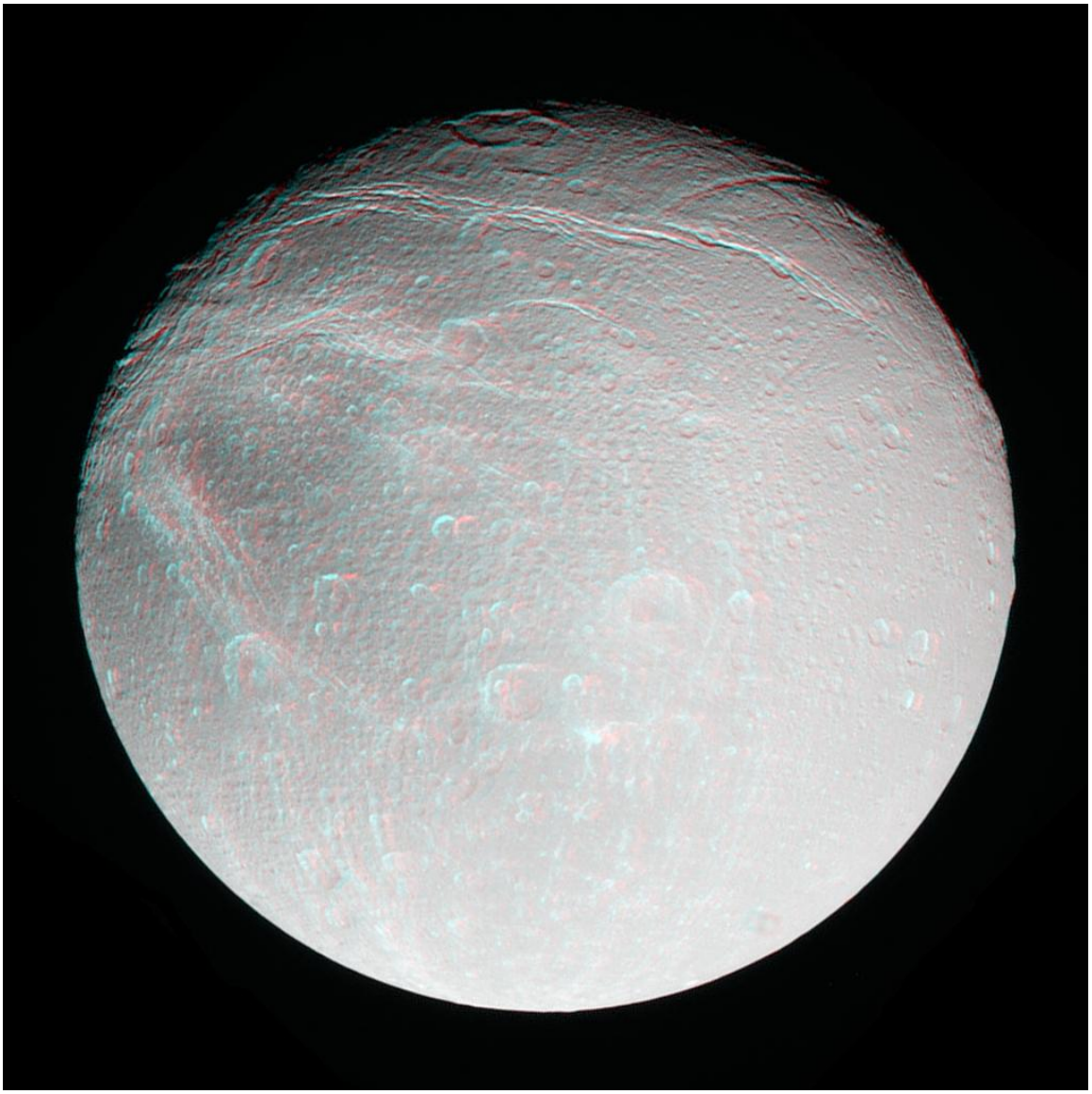


Figure B2. A 3-D anaglyph created from a pair of images where the target (Dione) had rotated sufficiently between frames to make a false-color composite impossible. In this case the two frames were N00101799 (CL1-CL2) and N00101802 (CL1-GRN), acquired from distances of 209,771 km and 211,429 km respectively. These particular frames were chosen to minimize contrast differences that would have occurred using other filter combinations. To render the composite viewable with red-cyan 3-D glasses, the stacked, aligned images had to be rotated through about a 45° (CW) angle, the resulting white space had to be filled in with black, and then another crop was applied (to 1024 x 1024 pixels). When viewed correctly the surface of Dione should appear to bulge out of the page, but the unusual lighting angle can make this difficult to visualize. Raw images courtesy NASA/JPL/Caltech.

APPENDIX C

GEOPHYSICAL MODEL FORMULAS, OUTPUT AND DATA

Geophysical Model Formulas and Output

Values of *g* and pressure at depth were calculated from the spreadsheet using the following formulas (Column 1 increments the radius in 300 m steps from 161.8 km):

1. Column 2 = $3{,}907{,}844{,}892 / (r \times 1000)^2$ [GM/r^2]
    - Value of *g* at the given distance from the outer core
2. Column 3 = $4/3\ \pi\ r^3$
    - Volume enclosed by the radius in column 1
3. Column 4 = (Column 3) – 1.77428×10^{16}
    - Volume of mantle (m^3)
4. Column 5 = (Column 5) x 1000
    - Mass of mantle (kg)
5. Column 6 = $(5.85515 \times 10^{19} + ((\text{Column 5}) \times 6.6742 \times 10^{-11})) / (r \times 1000)^2$
    - Value of *g* at the incremental radius due to core + mantle mass
6. Column 7 = $(r / 161.8)^2$
    - Area at incremental radius / surface area of outer core
7. Column 8 = (Column 7) x 300
    - Volume of the 300 m thick shell (m^3)
8. Column 9 = (Column 6) x (Column 7) x 1000 [Sum of Column 9 = total P]
    - Pressure P exerted due to shell (Pa)

Table C1. Pressure at depth from surface to core-mantle boundary. Values shown below have been truncated for space reasons.

r (km)	g (core)	vol at r (km^3)	vol – core vol	m (kg) (mantle)	g at r (mantle)	area	vol (shell)	rho*g*h
161.8	0.14927	1.77E+16	3.75E+10	3.8E+13	0.14927	1	300	44781.8
162.1	0.14872	1.78E+16	9.89E+13	9.9E+16	0.14897	1.00371	301.114	44857.4
162.4	0.14817	1.79E+16	1.98E+14	2E+17	0.14867	1.00743	302.229	44933.3
162.7	0.14763	1.8E+16	2.98E+14	3E+17	0.14838	1.01116	303.347	45009.5
163	0.14708	1.81E+16	3.98E+14	4E+17	0.14808	1.01489	304.466	45086
163.3	0.14654	1.82E+16	4.98E+14	5E+17	0.14779	1.01863	305.588	45162.7
163.6	0.14601	1.83E+16	5.99E+14	6E+17	0.1475	1.02237	306.712	45239.8
163.9	0.14547	1.84E+16	7E+14	7E+17	0.14721	1.02613	307.838	45317.1
164.2	0.14494	1.85E+16	8.01E+14	8E+17	0.14692	1.02989	308.966	45394.7
164.5	0.14441	1.86E+16	9.03E+14	9E+17	0.14664	1.03365	310.096	45472.6
164.8	0.14389	1.87E+16	1.01E+15	1E+18	0.14636	1.03743	311.228	45550.7
165.1	0.14337	1.89E+16	1.11E+15	1.1E+18	0.14608	1.04121	312.362	45629.2
165.4	0.14285	1.9E+16	1.21E+15	1.2E+18	0.1458	1.04499	313.498	45707.9
165.7	0.14233	1.91E+16	1.31E+15	1.3E+18	0.14552	1.04879	314.637	45786.9
166	0.14181	1.92E+16	1.42E+15	1.4E+18	0.14525	1.05259	315.777	45866.3
166.3	0.1413	1.93E+16	1.52E+15	1.5E+18	0.14498	1.0564	316.919	45945.9
166.6	0.1408	1.94E+16	1.63E+15	1.6E+18	0.14471	1.06021	318.064	46025.7
166.9	0.14029	1.95E+16	1.73E+15	1.7E+18	0.14444	1.06403	319.21	46105.9
167.2	0.13979	1.96E+16	1.84E+15	1.8E+18	0.14417	1.06786	320.359	46186.4
167.5	0.13929	1.97E+16	1.94E+15	1.9E+18	0.14391	1.0717	321.51	46267.1
167.8	0.13879	1.98E+16	2.05E+15	2E+18	0.14364	1.07554	322.662	46348.2
168.1	0.13829	1.99E+16	2.15E+15	2.2E+18	0.14338	1.07939	323.817	46429.5
168.4	0.1378	2E+16	2.26E+15	2.3E+18	0.14312	1.08325	324.974	46511.1
168.7	0.13731	2.01E+16	2.37E+15	2.4E+18	0.14287	1.08711	326.133	46593
169	0.13682	2.02E+16	2.48E+15	2.5E+18	0.14261	1.09098	327.294	46675.2
169.3	0.13634	2.03E+16	2.58E+15	2.6E+18	0.14236	1.09486	328.457	46757.7
169.6	0.13586	2.04E+16	2.69E+15	2.7E+18	0.1421	1.09874	329.622	46840.5
169.9	0.13538	2.05E+16	2.8E+15	2.8E+18	0.14185	1.10263	330.789	46923.6
170.2	0.1349	2.07E+16	2.91E+15	2.9E+18	0.14161	1.10653	331.958	47007
170.5	0.13443	2.08E+16	3.02E+15	3E+18	0.14136	1.11043	333.129	47090.6
170.8	0.13396	2.09E+16	3.13E+15	3.1E+18	0.14111	1.11434	334.303	47174.6
171.1	0.13349	2.1E+16	3.24E+15	3.2E+18	0.14087	1.11826	335.478	47258.9
171.4	0.13302	2.11E+16	3.35E+15	3.3E+18	0.14063	1.12219	336.656	47343.4
171.7	0.13256	2.12E+16	3.46E+15	3.5E+18	0.14039	1.12612	337.835	47428.3
172	0.13209	2.13E+16	3.57E+15	3.6E+18	0.14015	1.13006	339.017	47513.4
172.3	0.13163	2.14E+16	3.68E+15	3.7E+18	0.13991	1.134	340.2	47598.9
172.6	0.13118	2.15E+16	3.8E+15	3.8E+18	0.13968	1.13795	341.386	47684.6
172.9	0.13072	2.17E+16	3.91E+15	3.9E+18	0.13945	1.14191	342.574	47770.7
173.2	0.13027	2.18E+16	4.02E+15	4E+18	0.13921	1.14588	343.764	47857
173.5	0.12982	2.19E+16	4.13E+15	4.1E+18	0.13899	1.14985	344.956	47943.7
173.8	0.12937	2.2E+16	4.25E+15	4.2E+18	0.13876	1.15383	346.15	48030.6
174.1	0.12893	2.21E+16	4.36E+15	4.4E+18	0.13853	1.15782	347.346	48117.9
174.4	0.12848	2.22E+16	4.48E+15	4.5E+18	0.13831	1.16181	348.544	48205.4

174.7	0.12804	2.23E+16	4.59E+15	4.6E+18	0.13808	1.16581	349.744	48293.3
175	0.1276	2.24E+16	4.71E+15	4.7E+18	0.13786	1.16982	350.946	48381.4
175.3	0.12717	2.26E+16	4.82E+15	4.8E+18	0.13764	1.17383	352.15	48469.9
175.6	0.12673	2.27E+16	4.94E+15	4.9E+18	0.13742	1.17786	353.357	48558.6
175.9	0.1263	2.28E+16	5.05E+15	5.1E+18	0.1372	1.18188	354.565	48647.7
176.2	0.12587	2.29E+16	5.17E+15	5.2E+18	0.13699	1.18592	355.775	48737
176.5	0.12544	2.3E+16	5.29E+15	5.3E+18	0.13677	1.18996	356.988	48826.7
176.8	0.12502	2.31E+16	5.41E+15	5.4E+18	0.13656	1.19401	358.203	48916.7
177.1	0.12459	2.33E+16	5.52E+15	5.5E+18	0.13635	1.19806	359.419	49007
177.4	0.12417	2.34E+16	5.64E+15	5.6E+18	0.13614	1.20213	360.638	49097.6
177.7	0.12375	2.35E+16	5.76E+15	5.8E+18	0.13593	1.2062	361.859	49188.4
178	0.12334	2.36E+16	5.88E+15	5.9E+18	0.13573	1.21027	363.082	49279.6
178.3	0.12292	2.37E+16	6E+15	6E+18	0.13552	1.21435	364.306	49371.2
178.6	0.12251	2.39E+16	6.12E+15	6.1E+18	0.13532	1.21844	365.533	49463
178.9	0.1221	2.4E+16	6.24E+15	6.2E+18	0.13511	1.22254	366.762	49555.1
179.2	0.12169	2.41E+16	6.36E+15	6.4E+18	0.13491	1.22665	367.994	49647.5
179.5	0.12129	2.42E+16	6.48E+15	6.5E+18	0.13471	1.23076	369.227	49740.3
179.8	0.12088	2.43E+16	6.6E+15	6.6E+18	0.13452	1.23487	370.462	49833.3
180.1	0.12048	2.45E+16	6.73E+15	6.7E+18	0.13432	1.239	371.699	49926.7
180.4	0.12008	2.46E+16	6.85E+15	6.8E+18	0.13413	1.24313	372.939	50020.4
180.7	0.11968	2.47E+16	6.97E+15	7E+18	0.13393	1.24727	374.18	50114.4
181	0.11928	2.48E+16	7.1E+15	7.1E+18	0.13374	1.25141	375.423	50208.7
181.3	0.11889	2.5E+16	7.22E+15	7.2E+18	0.13355	1.25556	376.669	50303.3
181.6	0.1185	2.51E+16	7.34E+15	7.3E+18	0.13336	1.25972	377.917	50398.2
181.9	0.11811	2.52E+16	7.47E+15	7.5E+18	0.13317	1.26389	379.166	50493.5
182.2	0.11772	2.53E+16	7.59E+15	7.6E+18	0.13298	1.26806	380.418	50589
182.5	0.11733	2.55E+16	7.72E+15	7.7E+18	0.1328	1.27224	381.672	50684.9
182.8	0.11695	2.56E+16	7.84E+15	7.8E+18	0.13261	1.27643	382.928	50781.1
183.1	0.11656	2.57E+16	7.97E+15	8E+18	0.13243	1.28062	384.185	50877.6
183.4	0.11618	2.58E+16	8.1E+15	8.1E+18	0.13225	1.28482	385.445	50974.4
183.7	0.1158	2.6E+16	8.22E+15	8.2E+18	0.13207	1.28902	386.707	51071.6
184	0.11543	2.61E+16	8.35E+15	8.4E+18	0.13189	1.29324	387.972	51169
184.3	0.11505	2.62E+16	8.48E+15	8.5E+18	0.13171	1.29746	389.238	51266.8
184.6	0.11468	2.64E+16	8.61E+15	8.6E+18	0.13153	1.30169	390.506	51364.9
184.9	0.1143	2.65E+16	8.74E+15	8.7E+18	0.13136	1.30592	391.776	51463.3
185.2	0.11393	2.66E+16	8.87E+15	8.9E+18	0.13118	1.31016	393.049	51562.1
185.5	0.11357	2.67E+16	8.99E+15	9E+18	0.13101	1.31441	394.323	51661.1
185.8	0.1132	2.69E+16	9.12E+15	9.1E+18	0.13084	1.31866	395.599	51760.5
186.1	0.11284	2.7E+16	9.25E+15	9.3E+18	0.13067	1.32293	396.878	51860.2
186.4	0.11247	2.71E+16	9.39E+15	9.4E+18	0.1305	1.3272	398.159	51960.2
186.7	0.11211	2.73E+16	9.52E+15	9.5E+18	0.13033	1.33147	399.441	52060.5
187	0.11175	2.74E+16	9.65E+15	9.6E+18	0.13017	1.33575	400.726	52161.2
187.3	0.11139	2.75E+16	9.78E+15	9.8E+18	0.13	1.34004	402.013	52262.2
187.6	0.11104	2.77E+16	9.91E+15	9.9E+18	0.12984	1.34434	403.302	52363.5
187.9	0.11068	2.78E+16	1E+16	1E+19	0.12967	1.34864	404.592	52465.2
188.2	0.11033	2.79E+16	1.02E+16	1E+19	0.12951	1.35295	405.885	52567.1
188.5	0.10998	2.81E+16	1.03E+16	1E+19	0.12935	1.35727	407.18	52669.4
188.8	0.10963	2.82E+16	1.04E+16	1E+19	0.12919	1.36159	408.478	52772

189.1	0.10928	2.83E+16	1.06E+16	1.1E+19	0.12903	1.36592	409.777	52875
189.4	0.10894	2.85E+16	1.07E+16	1.1E+19	0.12888	1.37026	411.078	52978.2
189.7	0.10859	2.86E+16	1.09E+16	1.1E+19	0.12872	1.3746	412.381	53081.8
190	0.10825	2.87E+16	1.1E+16	1.1E+19	0.12857	1.37896	413.687	53185.7
190.3	0.10791	2.89E+16	1.11E+16	1.1E+19	0.12841	1.38331	414.994	53290
190.6	0.10757	2.9E+16	1.13E+16	1.1E+19	0.12826	1.38768	416.303	53394.6
190.9	0.10723	2.91E+16	1.14E+16	1.1E+19	0.12811	1.39205	417.615	53499.5
191.2	0.1069	2.93E+16	1.15E+16	1.2E+19	0.12796	1.39643	418.929	53604.7
191.5	0.10656	2.94E+16	1.17E+16	1.2E+19	0.12781	1.40081	420.244	53710.3
191.8	0.10623	2.96E+16	1.18E+16	1.2E+19	0.12766	1.40521	421.562	53816.2
192.1	0.1059	2.97E+16	1.2E+16	1.2E+19	0.12751	1.40961	422.882	53922.4
192.4	0.10557	2.98E+16	1.21E+16	1.2E+19	0.12737	1.41401	424.204	54029
192.7	0.10524	3E+16	1.22E+16	1.2E+19	0.12722	1.41843	425.528	54135.9
193	0.10491	3.01E+16	1.24E+16	1.2E+19	0.12708	1.42284	426.853	54243.1
193.3	0.10459	3.03E+16	1.25E+16	1.3E+19	0.12693	1.42727	428.182	54350.7
193.6	0.10426	3.04E+16	1.27E+16	1.3E+19	0.12679	1.43171	429.512	54458.6
193.9	0.10394	3.05E+16	1.28E+16	1.3E+19	0.12665	1.43615	430.844	54566.9
194.2	0.10362	3.07E+16	1.29E+16	1.3E+19	0.12651	1.44059	432.178	54675.4
194.5	0.1033	3.08E+16	1.31E+16	1.3E+19	0.12637	1.44505	433.514	54784.3
194.8	0.10298	3.1E+16	1.32E+16	1.3E+19	0.12623	1.44951	434.853	54893.6
195.1	0.10267	3.11E+16	1.34E+16	1.3E+19	0.1261	1.45398	436.193	55003.2
195.4	0.10235	3.13E+16	1.35E+16	1.4E+19	0.12596	1.45845	437.536	55113.1
195.7	0.10204	3.14E+16	1.37E+16	1.4E+19	0.12583	1.46293	438.88	55223.3
196	0.10172	3.15E+16	1.38E+16	1.4E+19	0.12569	1.46742	440.227	55333.9
196.3	0.10141	3.17E+16	1.39E+16	1.4E+19	0.12556	1.47192	441.575	55444.9
196.6	0.1011	3.18E+16	1.41E+16	1.4E+19	0.12543	1.47642	442.926	55556.1
196.9	0.1008	3.2E+16	1.42E+16	1.4E+19	0.1253	1.48093	444.279	55667.8
197.2	0.10049	3.21E+16	1.44E+16	1.4E+19	0.12517	1.48545	445.634	55779.7
197.5	0.10019	3.23E+16	1.45E+16	1.5E+19	0.12504	1.48997	446.991	55892
197.8	0.09988	3.24E+16	1.47E+16	1.5E+19	0.12491	1.4945	448.35	56004.7
198.1	0.09958	3.26E+16	1.48E+16	1.5E+19	0.12479	1.49904	449.711	56117.6
198.4	0.09928	3.27E+16	1.5E+16	1.5E+19	0.12466	1.50358	451.074	56231
198.7	0.09898	3.29E+16	1.51E+16	1.5E+19	0.12454	1.50813	452.439	56344.6
199	0.09868	3.3E+16	1.53E+16	1.5E+19	0.12441	1.51269	453.806	56458.6
199.3	0.09838	3.32E+16	1.54E+16	1.5E+19	0.12429	1.51725	455.175	56573
199.6	0.09809	3.33E+16	1.56E+16	1.6E+19	0.12417	1.52182	456.547	56687.7
199.9	0.09779	3.35E+16	1.57E+16	1.6E+19	0.12405	1.5264	457.92	56802.7
200.2	0.0975	3.36E+16	1.59E+16	1.6E+19	0.12392	1.53099	459.296	56918.1
200.5	0.09721	3.38E+16	1.6E+16	1.6E+19	0.12381	1.53558	460.673	57033.9
200.8	0.09692	3.39E+16	1.62E+16	1.6E+19	0.12369	1.54018	462.053	57149.9
201.1	0.09663	3.41E+16	1.63E+16	1.6E+19	0.12357	1.54478	463.435	57266.4
201.4	0.09634	3.42E+16	1.65E+16	1.6E+19	0.12345	1.54939	464.818	57383.2
201.7	0.09606	3.44E+16	1.66E+16	1.7E+19	0.12334	1.55401	466.204	57500.3
202	0.09577	3.45E+16	1.68E+16	1.7E+19	0.12322	1.55864	467.592	57617.8
202.3	0.09549	3.47E+16	1.69E+16	1.7E+19	0.12311	1.56327	468.982	57735.6
202.6	0.0952	3.48E+16	1.71E+16	1.7E+19	0.123	1.56791	470.374	57853.8
202.9	0.09492	3.5E+16	1.72E+16	1.7E+19	0.12288	1.57256	471.768	57972.3
203.2	0.09464	3.51E+16	1.74E+16	1.7E+19	0.12277	1.57721	473.164	58091.2

203.5	0.09436	3.53E+16	1.76E+16	1.8E+19	0.12266	1.58187	474.562	58210.4
203.8	0.09409	3.55E+16	1.77E+16	1.8E+19	0.12255	1.58654	475.962	58330
204.1	0.09381	3.56E+16	1.79E+16	1.8E+19	0.12244	1.59122	477.365	58449.9
204.4	0.09354	3.58E+16	1.8E+16	1.8E+19	0.12233	1.5959	478.769	58570.2
204.7	0.09326	3.59E+16	1.82E+16	1.8E+19	0.12223	1.60058	480.175	58690.8
205	0.09299	3.61E+16	1.83E+16	1.8E+19	0.12212	1.60528	481.584	58811.8
205.3	0.09272	3.62E+16	1.85E+16	1.9E+19	0.12202	1.60998	482.994	58933.2
205.6	0.09245	3.64E+16	1.87E+16	1.9E+19	0.12191	1.61469	484.407	59054.9
205.9	0.09218	3.66E+16	1.88E+16	1.9E+19	0.12181	1.61941	485.822	59176.9
206.2	0.09191	3.67E+16	1.9E+16	1.9E+19	0.12171	1.62413	487.238	59299.4
206.5	0.09164	3.69E+16	1.91E+16	1.9E+19	0.1216	1.62886	488.657	59422.1
206.8	0.09138	3.7E+16	1.93E+16	1.9E+19	0.1215	1.63359	490.078	59545.3
207.1	0.09111	3.72E+16	1.95E+16	1.9E+19	0.1214	1.63834	491.501	59668.8
207.4	0.09085	3.74E+16	1.96E+16	2E+19	0.1213	1.64309	492.926	59792.6
207.7	0.09059	3.75E+16	1.98E+16	2E+19	0.1212	1.64784	494.353	59916.8
208	0.09033	3.77E+16	2E+16	2E+19	0.1211	1.65261	495.782	60041.4
208.3	0.09007	3.79E+16	2.01E+16	2E+19	0.12101	1.65738	497.213	60166.3
208.6	0.08981	3.8E+16	2.03E+16	2E+19	0.12091	1.66216	498.647	60291.6
208.9	0.08955	3.82E+16	2.04E+16	2E+19	0.12081	1.66694	500.082	60417.2
209.2	0.08929	3.84E+16	2.06E+16	2.1E+19	0.12072	1.67173	501.519	60543.2
209.5	0.08904	3.85E+16	2.08E+16	2.1E+19	0.12063	1.67653	502.959	60669.6
209.8	0.08878	3.87E+16	2.09E+16	2.1E+19	0.12053	1.68133	504.4	60796.3
210.1	0.08853	3.88E+16	2.11E+16	2.1E+19	0.12044	1.68615	505.844	60923.4
210.4	0.08828	3.9E+16	2.13E+16	2.1E+19	0.12035	1.69096	507.289	61050.9
210.7	0.08803	3.92E+16	2.14E+16	2.1E+19	0.12026	1.69579	508.737	61178.7
211	0.08778	3.93E+16	2.16E+16	2.2E+19	0.12017	1.70062	510.187	61306.9
211.3	0.08753	3.95E+16	2.18E+16	2.2E+19	0.12008	1.70546	511.638	61435.4
211.6	0.08728	3.97E+16	2.19E+16	2.2E+19	0.11999	1.71031	513.092	61564.4
211.9	0.08703	3.99E+16	2.21E+16	2.2E+19	0.1199	1.71516	514.548	61693.6
212.2	0.08679	4E+16	2.23E+16	2.2E+19	0.11981	1.72002	516.006	61823.3
212.5	0.08654	4.02E+16	2.25E+16	2.2E+19	0.11972	1.72489	517.466	61953.3
212.8	0.0863	4.04E+16	2.26E+16	2.3E+19	0.11964	1.72976	518.928	62083.7
213.1	0.08605	4.05E+16	2.28E+16	2.3E+19	0.11955	1.73464	520.393	62214.4
213.4	0.08581	4.07E+16	2.3E+16	2.3E+19	0.11947	1.73953	521.859	62345.6
213.7	0.08557	4.09E+16	2.31E+16	2.3E+19	0.11938	1.74442	523.327	62477.1
214	0.08533	4.11E+16	2.33E+16	2.3E+19	0.1193	1.74933	524.798	62608.9
214.3	0.08509	4.12E+16	2.35E+16	2.3E+19	0.11922	1.75423	526.27	62741.1
214.6	0.08486	4.14E+16	2.37E+16	2.4E+19	0.11914	1.75915	527.744	62873.7
214.9	0.08462	4.16E+16	2.38E+16	2.4E+19	0.11906	1.76407	529.221	63006.7
215.2	0.08438	4.17E+16	2.4E+16	2.4E+19	0.11898	1.769	530.7	63140.1
215.5	0.08415	4.19E+16	2.42E+16	2.4E+19	0.1189	1.77393	532.18	63273.8
215.8	0.08391	4.21E+16	2.44E+16	2.4E+19	0.11882	1.77888	533.663	63407.9
216.1	0.08368	4.23E+16	2.45E+16	2.5E+19	0.11874	1.78383	535.148	63542.3
216.4	0.08345	4.24E+16	2.47E+16	2.5E+19	0.11866	1.78878	536.635	63677.2
216.7	0.08322	4.26E+16	2.49E+16	2.5E+19	0.11858	1.79375	538.124	63812.4
217	0.08299	4.28E+16	2.51E+16	2.5E+19	0.11851	1.79872	539.615	63948
217.3	0.08276	4.3E+16	2.52E+16	2.5E+19	0.11843	1.80369	541.108	64083.9
217.6	0.08253	4.32E+16	2.54E+16	2.5E+19	0.11836	1.80868	542.603	64220.3

217.9	0.0823	4.33E+16	2.56E+16	2.6E+19	0.11828	1.81367	544.1	64357
218.2	0.08208	4.35E+16	2.58E+16	2.6E+19	0.11821	1.81866	545.599	64494.1
218.5	0.08185	4.37E+16	2.6E+16	2.6E+19	0.11813	1.82367	547.1	64631.5
218.8	0.08163	4.39E+16	2.61E+16	2.6E+19	0.11806	1.82868	548.604	64769.4
219.1	0.08141	4.41E+16	2.63E+16	2.6E+19	0.11799	1.8337	550.109	64907.6
219.4	0.08118	4.42E+16	2.65E+16	2.6E+19	0.11792	1.83872	551.617	65046.2
219.7	0.08096	4.44E+16	2.67E+16	2.7E+19	0.11785	1.84375	553.126	65185.2
220	0.08074	4.46E+16	2.69E+16	2.7E+19	0.11778	1.84879	554.638	65324.5
220.3	0.08052	4.48E+16	2.7E+16	2.7E+19	0.11771	1.85384	556.152	65464.3
220.6	0.0803	4.5E+16	2.72E+16	2.7E+19	0.11764	1.85889	557.667	65604.4
220.9	0.08008	4.52E+16	2.74E+16	2.7E+19	0.11757	1.86395	559.185	65744.9
221.2	0.07987	4.53E+16	2.76E+16	2.8E+19	0.11751	1.86902	560.705	65885.8
221.5	0.07965	4.55E+16	2.78E+16	2.8E+19	0.11744	1.87409	562.227	66027.1
221.8	0.07944	4.57E+16	2.8E+16	2.8E+19	0.11737	1.87917	563.751	66168.7
222.1	0.07922	4.59E+16	2.81E+16	2.8E+19	0.11731	1.88426	565.277	66310.8
222.4	0.07901	4.61E+16	2.83E+16	2.8E+19	0.11724	1.88935	566.805	66453.2
222.7	0.07879	4.63E+16	2.85E+16	2.9E+19	0.11718	1.89445	568.335	66596
223	0.07858	4.65E+16	2.87E+16	2.9E+19	0.11711	1.89956	569.868	66739.2
223.3	0.07837	4.66E+16	2.89E+16	2.9E+19	0.11705	1.90467	571.402	66882.8
223.6	0.07816	4.68E+16	2.91E+16	2.9E+19	0.11699	1.90979	572.938	67026.7
223.9	0.07795	4.7E+16	2.93E+16	2.9E+19	0.11693	1.91492	574.477	67171.1
224.2	0.07774	4.72E+16	2.95E+16	2.9E+19	0.11686	1.92006	576.017	67315.8
224.5	0.07754	4.74E+16	2.97E+16	3E+19	0.1168	1.9252	577.56	67460.9
224.8	0.07733	4.76E+16	2.98E+16	3E+19	0.11674	1.93035	579.104	67606.5
225.1	0.07712	4.78E+16	3E+16	3E+19	0.11668	1.9355	580.651	67752.4
225.4	0.07692	4.8E+16	3.02E+16	3E+19	0.11662	1.94067	582.2	67898.7
225.7	0.07671	4.82E+16	3.04E+16	3E+19	0.11657	1.94584	583.751	68045.3
226	0.07651	4.84E+16	3.06E+16	3.1E+19	0.11651	1.95101	585.303	68192.4
226.3	0.07631	4.85E+16	3.08E+16	3.1E+19	0.11645	1.95619	586.858	68339.9
226.6	0.07611	4.87E+16	3.1E+16	3.1E+19	0.11639	1.96138	588.415	68487.7
226.9	0.0759	4.89E+16	3.12E+16	3.1E+19	0.11634	1.96658	589.974	68636
227.2	0.0757	4.91E+16	3.14E+16	3.1E+19	0.11628	1.97179	591.536	68784.6
227.5	0.0755	4.93E+16	3.16E+16	3.2E+19	0.11623	1.977	593.099	68933.7
227.8	0.07531	4.95E+16	3.18E+16	3.2E+19	0.11617	1.98221	594.664	69083.1
228.1	0.07511	4.97E+16	3.2E+16	3.2E+19	0.11612	1.98744	596.231	69232.9
228.4	0.07491	4.99E+16	3.22E+16	3.2E+19	0.11606	1.99267	597.801	69383.1
228.7	0.07471	5.01E+16	3.24E+16	3.2E+19	0.11601	1.99791	599.372	69533.7
229	0.07452	5.03E+16	3.26E+16	3.3E+19	0.11596	2.00315	600.946	69684.7
229.3	0.07432	5.05E+16	3.28E+16	3.3E+19	0.11591	2.0084	602.521	69836.1
229.6	0.07413	5.07E+16	3.3E+16	3.3E+19	0.11586	2.01366	604.099	69987.9
229.9	0.07394	5.09E+16	3.32E+16	3.3E+19	0.1158	2.01893	605.679	70140.1
230.2	0.07374	5.11E+16	3.34E+16	3.3E+19	0.11575	2.0242	607.26	70292.7
230.5	0.07355	5.13E+16	3.36E+16	3.4E+19	0.1157	2.02948	608.844	70445.7
230.8	0.07336	5.15E+16	3.38E+16	3.4E+19	0.11565	2.03477	610.43	70599.1
231.1	0.07317	5.17E+16	3.4E+16	3.4E+19	0.11561	2.04006	612.018	70752.9
231.4	0.07298	5.19E+16	3.42E+16	3.4E+19	0.11556	2.04536	613.608	70907.1
231.7	0.07279	5.21E+16	3.44E+16	3.4E+19	0.11551	2.05067	615.2	71061.7
232	0.0726	5.23E+16	3.46E+16	3.5E+19	0.11546	2.05598	616.794	71216.7

232.3	0.07242	5.25E+16	3.48E+16	3.5E+19	0.11542	2.0613	618.39	71372.1
232.6	0.07223	5.27E+16	3.5E+16	3.5E+19	0.11537	2.06663	619.989	71527.9
232.9	0.07204	5.29E+16	3.52E+16	3.5E+19	0.11532	2.07196	621.589	71684.1
233.2	0.07186	5.31E+16	3.54E+16	3.5E+19	0.11528	2.0773	623.191	71840.7
233.5	0.07167	5.33E+16	3.56E+16	3.6E+19	0.11523	2.08265	624.796	71997.7
233.8	0.07149	5.35E+16	3.58E+16	3.6E+19	0.11519	2.08801	626.402	72155.1
234.1	0.07131	5.37E+16	3.6E+16	3.6E+19	0.11515	2.09337	628.011	72312.9
234.4	0.07112	5.39E+16	3.62E+16	3.6E+19	0.1151	2.09874	629.621	72471.1
234.7	0.07094	5.42E+16	3.64E+16	3.6E+19	0.11506	2.10411	631.234	72629.7
235	0.07076	5.44E+16	3.66E+16	3.7E+19	0.11502	2.1095	632.849	72788.7
235.3	0.07058	5.46E+16	3.68E+16	3.7E+19	0.11498	2.11489	634.466	72948.2
235.6	0.0704	5.48E+16	3.7E+16	3.7E+19	0.11493	2.12028	636.084	73108
235.9	0.07022	5.5E+16	3.72E+16	3.7E+19	0.11489	2.12568	637.705	73268.3
236.2	0.07005	5.52E+16	3.75E+16	3.7E+19	0.11485	2.13109	639.328	73428.9
236.5	0.06987	5.54E+16	3.77E+16	3.8E+19	0.11481	2.13651	640.953	73590
236.8	0.06969	5.56E+16	3.79E+16	3.8E+19	0.11477	2.14194	642.581	73751.5
237.1	0.06951	5.58E+16	3.81E+16	3.8E+19	0.11473	2.14737	644.21	73913.4
237.4	0.06934	5.6E+16	3.83E+16	3.8E+19	0.1147	2.1528	645.841	74075.7
237.7	0.06916	5.63E+16	3.85E+16	3.9E+19	0.11466	2.15825	647.474	74238.4
238	0.06899	5.65E+16	3.87E+16	3.9E+19	0.11462	2.1637	649.11	74401.5
238.3	0.06882	5.67E+16	3.89E+16	3.9E+19	0.11458	2.16916	650.747	74565
238.6	0.06864	5.69E+16	3.92E+16	3.9E+19	0.11455	2.17462	652.387	74728.9
238.9	0.06847	5.71E+16	3.94E+16	3.9E+19	0.11451	2.18009	654.028	74893.3
239.2	0.0683	5.73E+16	3.96E+16	4E+19	0.11448	2.18557	655.672	75058.1
239.5	0.06813	5.75E+16	3.98E+16	4E+19	0.11444	2.19106	657.318	75223.2
239.8	0.06796	5.78E+16	4E+16	4E+19	0.1144	2.19655	658.965	75388.8
240.1	0.06779	5.8E+16	4.02E+16	4E+19	0.11437	2.20205	660.615	75554.9
240.4	0.06762	5.82E+16	4.05E+16	4E+19	0.11434	2.20756	662.267	75721.3
240.7	0.06745	5.84E+16	4.07E+16	4.1E+19	0.1143	2.21307	663.921	75888.1
241	0.06728	5.86E+16	4.09E+16	4.1E+19	0.11427	2.21859	665.577	76055.4
241.3	0.06712	5.89E+16	4.11E+16	4.1E+19	0.11424	2.22412	667.235	76223.1
241.6	0.06695	5.91E+16	4.13E+16	4.1E+19	0.1142	2.22965	668.895	76391.1
241.9	0.06678	5.93E+16	4.15E+16	4.2E+19	0.11417	2.23519	670.557	76559.7
242.2	0.06662	5.95E+16	4.18E+16	4.2E+19	0.11414	2.24074	672.222	76728.6
242.5	0.06645	5.97E+16	4.2E+16	4.2E+19	0.11411	2.24629	673.888	76897.9
242.8	0.06629	6E+16	4.22E+16	4.2E+19	0.11408	2.25185	675.556	77067.7
243.1	0.06613	6.02E+16	4.24E+16	4.2E+19	0.11405	2.25742	677.227	77237.9
243.4	0.06596	6.04E+16	4.27E+16	4.3E+19	0.11402	2.263	678.899	77408.5
243.7	0.0658	6.06E+16	4.29E+16	4.3E+19	0.11399	2.26858	680.574	77579.5
244	0.06564	6.08E+16	4.31E+16	4.3E+19	0.11396	2.27417	682.251	77751
244.3	0.06548	6.11E+16	4.33E+16	4.3E+19	0.11393	2.27976	683.929	77922.8
244.6	0.06532	6.13E+16	4.36E+16	4.4E+19	0.11391	2.28537	685.61	78095.1
244.9	0.06516	6.15E+16	4.38E+16	4.4E+19	0.11388	2.29098	687.293	78267.9
245.2	0.065	6.18E+16	4.4E+16	4.4E+19	0.11385	2.29659	688.978	78441
245.5	0.06484	6.2E+16	4.42E+16	4.4E+19	0.11382	2.30222	690.665	78614.6
245.8	0.06468	6.22E+16	4.45E+16	4.4E+19	0.1138	2.30785	692.354	78788.6
246.1	0.06452	6.24E+16	4.47E+16	4.5E+19	0.11377	2.31348	694.045	78963
246.4	0.06437	6.27E+16	4.49E+16	4.5E+19	0.11375	2.31913	695.738	79137.8

246.7	0.06421	6.29E+16	4.51E+16	4.5E+19	0.11372	2.32478	697.433	79313.1
247	0.06405	6.31E+16	4.54E+16	4.5E+19	0.1137	2.33043	699.13	79488.8
247.3	0.0639	6.34E+16	4.56E+16	4.6E+19	0.11367	2.3361	700.83	79664.9
247.6	0.06374	6.36E+16	4.58E+16	4.6E+19	0.11365	2.34177	702.531	79841.5
247.9	0.06359	6.38E+16	4.61E+16	4.6E+19	0.11362	2.34745	704.234	80018.4
248.2	0.06344	6.4E+16	4.63E+16	4.6E+19	0.1136	2.35313	705.94	80195.8
248.5	0.06328	6.43E+16	4.65E+16	4.7E+19	0.11358	2.35883	707.648	80373.7
248.8	0.06313	6.45E+16	4.68E+16	4.7E+19	0.11356	2.36452	709.357	80551.9
249.1	0.06298	6.47E+16	4.7E+16	4.7E+19	0.11353	2.37023	711.069	80730.6
249.4	0.06283	6.5E+16	4.72E+16	4.7E+19	0.11351	2.37594	712.783	80909.8
249.7	0.06268	6.52E+16	4.75E+16	4.7E+19	0.11349	2.38166	714.498	81089.3
250	0.06253	6.54E+16	4.77E+16	4.8E+19	0.11347	2.38739	716.216	81269.3
250.3	0.06238	6.57E+16	4.79E+16	4.8E+19	0.11345	2.39312	717.936	81449.7
250.6	0.06223	6.59E+16	4.82E+16	4.8E+19	0.11343	2.39886	719.658	81630.6
250.9	0.06208	6.62E+16	4.84E+16	4.8E+19	0.11341	2.40461	721.382	81811.9
251.2	0.06193	6.64E+16	4.87E+16	4.9E+19	0.11339	2.41036	723.109	81993.6
251.5	0.06178	6.66E+16	4.89E+16	4.9E+19	0.11337	2.41612	724.837	82175.8
251.8	0.06163	6.69E+16	4.91E+16	4.9E+19	0.11335	2.42189	726.567	82358.4
252.1	0.06149	6.71E+16	4.94E+16	4.9E+19	0.11333	2.42766	728.299	82541.4
Column 9 sum: Pressure at core-mantle boundary (MPa)								18.4122

Moments of inertia were calculated for six models with different interior structures using the standard formula for spherical shells. The first model is fully-differentiated, with a silicate outer core and metallic inner core; the last is homogenous throughout and represents the highest possible value of I for Enceladus. The remaining models represent intermediate degrees of differentiation.

Table C2. Moments of inertia; note the range, with the highest possible value being 31.57% greater than the one for the model used throughout the text (in italics).

Mantle ρ	Outer core radius	Outer core ρ	Inner core radius	Inner core ρ	Moment (x 10^{24} kgm^2)
1000	*161.8*	*3000*	*63.3*	*8000*	*2.08509*
1000	161.8	3300	N/A	N/A	2.13346
1000	169.5	3000	N/A	N/A	2.17497
1000	178.9	2700	N/A	N/A	2.22814
1000	232	1780	N/A	N/A	2.58451
1000	252.1	1608	N/A	N/A	2.74325

Triple Points of Water

Table C3. Equilibrium triple points of water and ice (Eisenberg and Kauzmann, 1969)

Phases	Pressure (MPa)	Temperature (°C)
Ice I – liquid – vapor	6.1×10^{-4}	0.01
Ice I – liquid – Ice III	207	-22.0
Ice I – Ice II – Ice III	213	-34.7
Ice II – Ice III – Ice V	344	-24.3
Ice III – liquid – Ice V	346	-17.0
Ice V – liquid – Ice VI	626	0.16
Ice VI – liquid – Ice VII	2,200	81.6
Ice VI – Ice VII – Ice VIII	2,100	~5

1 bar = 100 kPa; 1 kbar = 100 Mpa

Amorphous ice, as produced by the destruction of crystalline ice by charged-particle radiation, can also be produced by condensation of water vapor onto a clean solid surface at temperatures similar to those found at the surface of Enceladus (Franks, 1974). However, amorphous or glassy ice is unstable and anneals irreversibly to the metastable form ice Ic at temperatures as low as 135K, and further heating in the range of 160 – 210K invariably (and irreversibly) produces ice Ih (idem). Ice Ic is isomorphous with diamond and differs only slightly in density (~0.93 vs. ~0.92) from the hexagonal form Ih which is isomorphous with tridymite (Eisenberg and Kauzmann, 1969).

APPENDIX D

REFERENCE GRID CONSTRUCTION

Reference Grid Construction

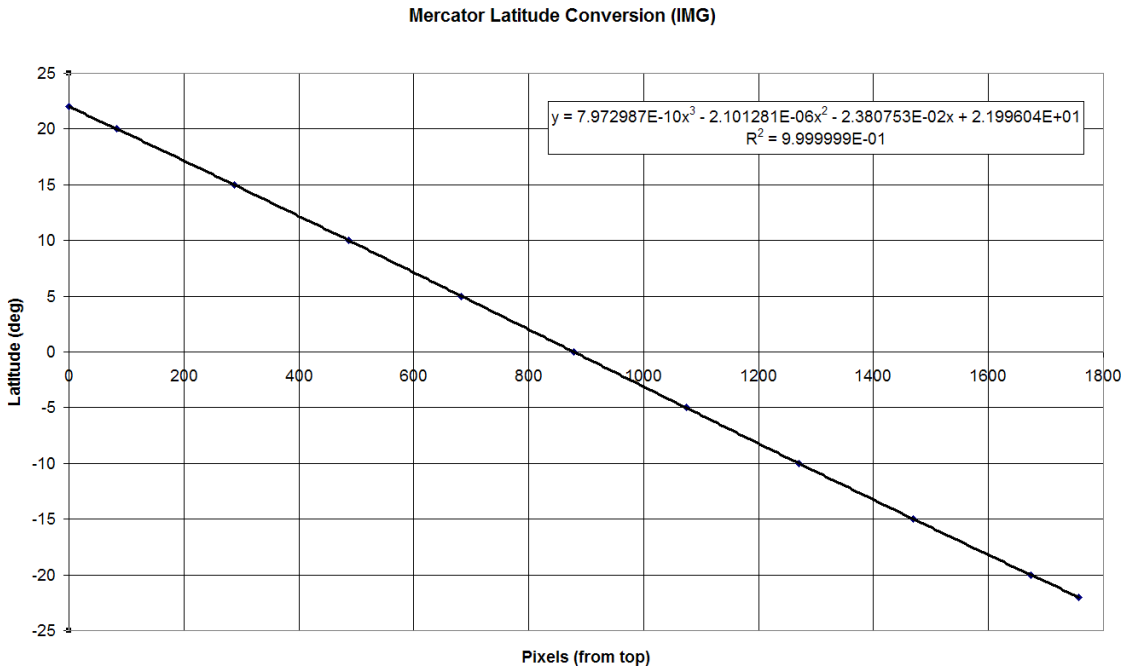


Figure D1. Plot of inverse formula for calculating Mercator latitude as a function of pixel coordinates for the unannotated DLR base images. Note the R^2 value.

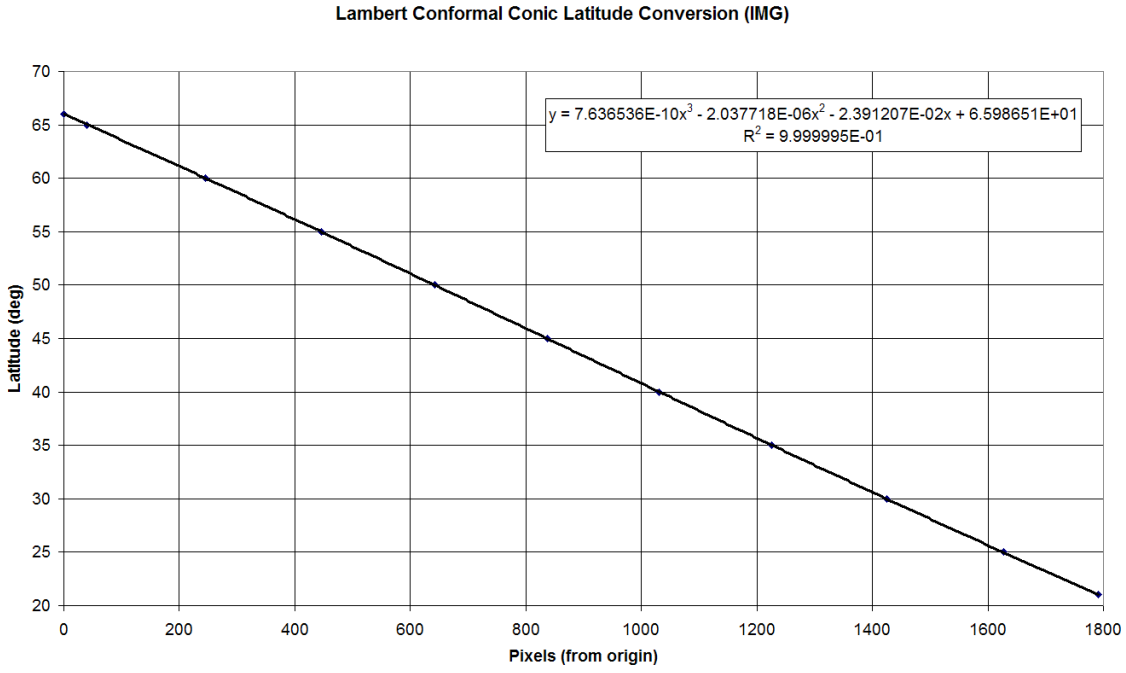


Figure D2. Plot of inverse formula for calculating Lambert conformal conic latitude as a function of pixel coordinates for the unannotated DLR base images. Note the R^2 value.

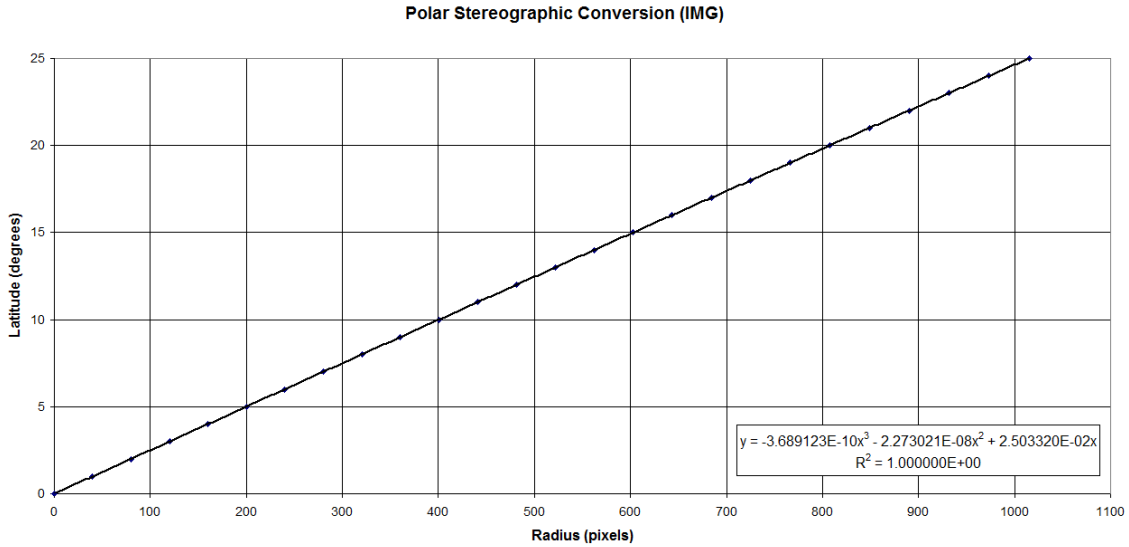


Figure D3. Plot of inverse formula for calculating Polar stereographic latitude as a function of pixel coordinates for the unannotated DLR base images. Note the R^2 value.

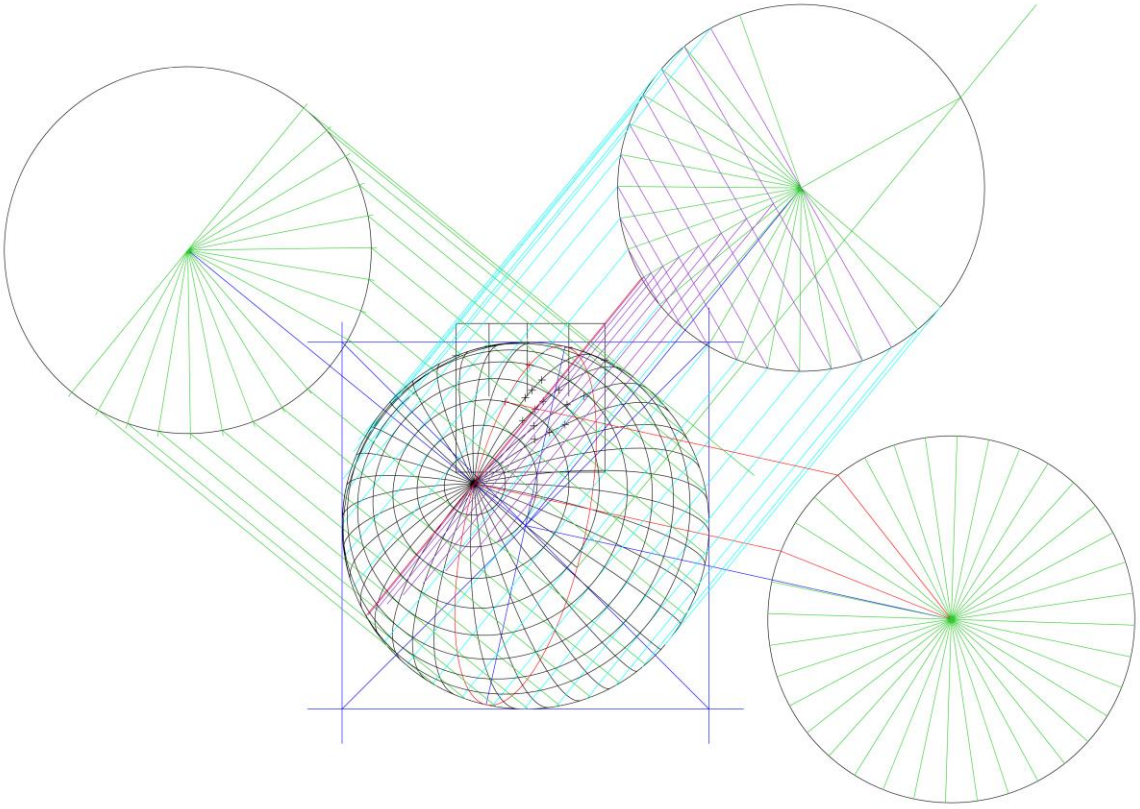


Figure D4. Partial construction setup in CAD to create the rotated, tilted 10° x 10° orthographic grid overlay for Figure 7 (the small black square). The small crosses are lat-long control points.

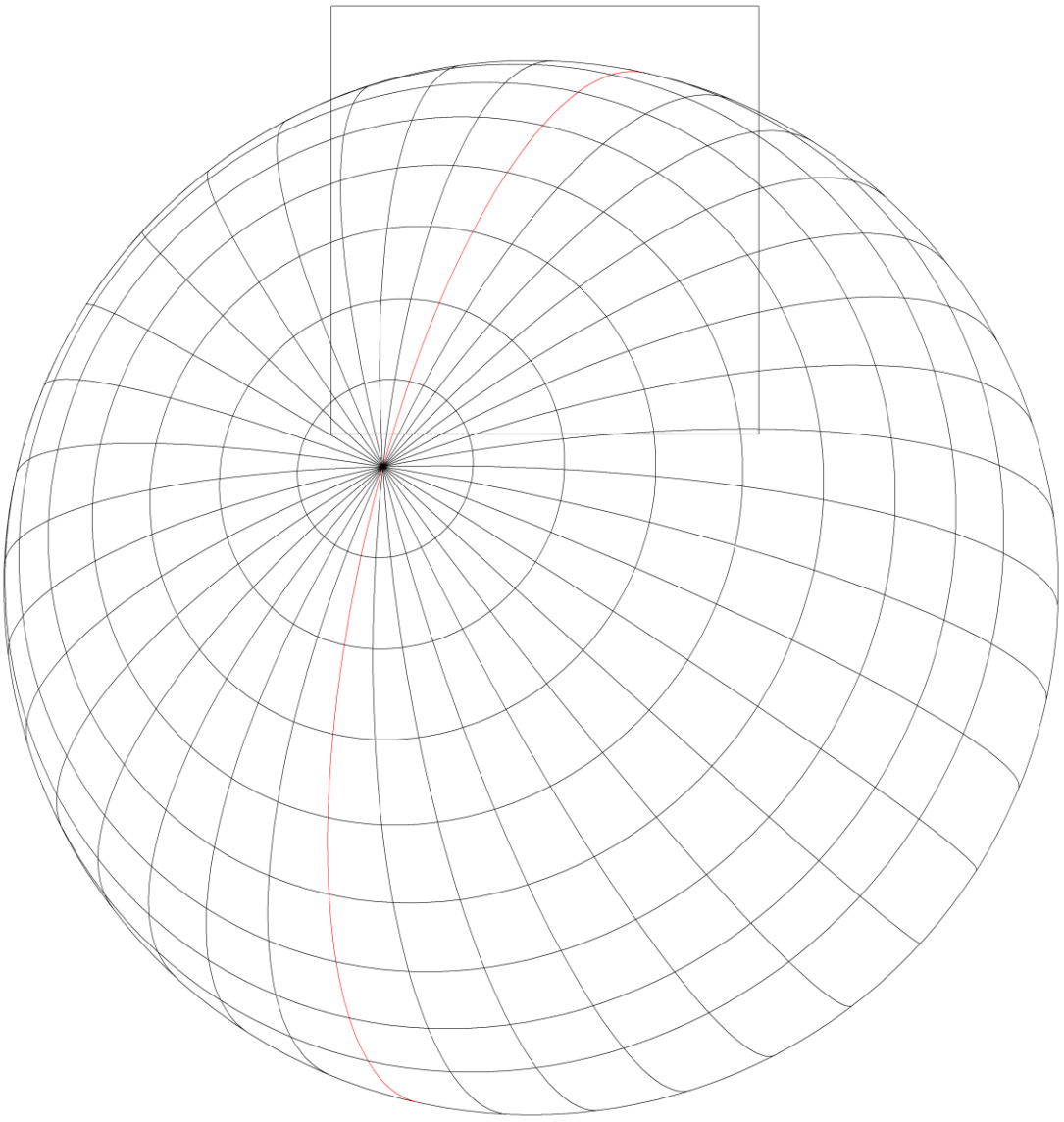


Figure D5. Figure D4 with extraneous construction lines removed. The remainder of the orthographic grid outside the square, shown here for context, was also removed. The prime meridian is already marked in red, but the rest of the grid was subsequently changed to yellow for better contrast against the base image (N00103768). After rasterization, the final grid (within the square) was saved as a PNG file to support the addition of the transparent overlay indicating the counted region shown in Figure 7. As indicated in Figure D4, despite its 3-D appearance, this figure was actually created in a 2-D workspace; construction of tilted and rotated grids by this method is a complex and error-prone procedure and should be avoided if possible.

APPENDIX E

CRATER COUNTING DATA

Crater Counting Data

Locations, general information and summary data for the crater counted regions are presented below, followed by the actual counts. As stated previously, zero longitude for synchronous satellites is defined as the center of the sub-planetary hemisphere, and counts westward from 0-360° (except for the Moon, which like Earth counts 0-180° east and west of the prime meridian). Hence, the counted Ali Baba zone (for example) is defined by the following points: 70N 40W, 70N 350W, 40N 350W, 40N 40W. Areas can be calculated from the simplified 10° x 10° grid shown below.

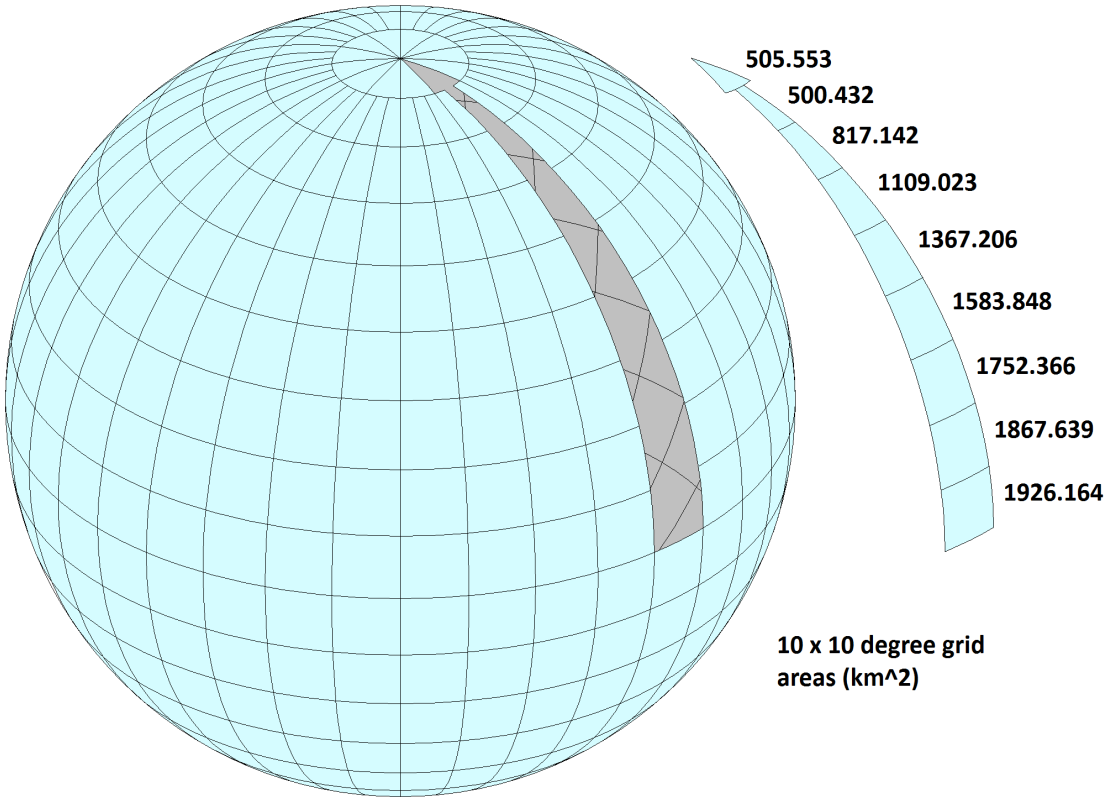


Figure E1. 10 degree reference grid used to calculate areas

The regions were selected based on the criteria that they were geologically contiguous, reasonably distant from each other, and had been imaged at sufficiently high resolution for practical counting down to at least 1 km. Craters were counted and sized using the count tool and ruler tool in Adobe® Photoshop CS3 Extended according to the guidelines presented in NASA TM-79730 (Arvidson et al., 1978). Measurements were taken in pixels and converted to meters. In the case of the Ali Baba image, which was not reprojected, crater diameters were measured along the longest apparent axis since virtually all craters are round when formed (Melosh, 1989). Bin sizes were allocated using the rule $D \rightarrow \sqrt{2}\, D$ with the smallest bin starting at 1km. The lower limit of 1km was chosen for two reasons: first, it is a recommended bin limit, and second, the scale of the mosaics means that including a bin smaller than 1km would mean attempting to size between features between 6 and 9 pixels across, a possibly error-prone procedure. However, the lower resolution of the Ali Baba image meant exactly that – counting craters between 5 and 7 pixels across. Despite the potential for (probably systematic) errors in the lower bins, it was felt that a count of this region was worth the effort; as mentioned previously, the data reduction procedure used in crater counting is inherently resistant to such effects and the results bear this out (that if sufficient care is taken, even small craters can be counted with reasonable accuracy). Unfortunately, the measured diameters for Ali Baba and Aladdin, the only IAU-ratified objects within the counted area, did not match the published values, which are approximately 25% larger. The reference grid fitted to the base image was checked for

errors and agreed with the angular resolution calculated from the range to target (31,856 km) to 7.5%. It was decided that applying a correction factor to all the craters counted in this region based on the published sizes for Ali Baba and Aladdin would perhaps be disingenuous with respect to the remainder of the data, and in any case when it was tried out of curiosity, the graphical results were indistinguishable from the raw version. The source of this systematic error remains unknown. In total, 1,255 craters were measured for all areas combined (some "Bin 0" and "Bin -1" craters were counted for Epimetheus but not used in the analysis due to doubts about the accuracy and the absence of equivalent data for Enceladus).

Table E1. Bin sizes; bin 11 was not used (see above). The very large impact that covers almost the entire southern hemisphere of Epimetheus would have occupied bin 14 (90.5 – 128 km).

Bin #	***D* -> √2 *D* (km)**
1	1 – 1.4
2	1.4 – 2.0
3	2.0 – 2.8
4	2.8 – 4.0
5	4.0 – 5.6
6	5.6 – 8.0
7	8.0 – 11.0
8	11.0 – 16.0
9	16.0 – 22.0
10	22.0 – 32.0
11	32.0 – 45.0

While the largest crater on Enceladus is less than 40 km in diameter, the count for Epimetheus revealed the presence of a probable impact feature almost 100 km across; the bin for this crater is not shown in the table.

Note that the linear distortion of the mosaics reaches a maximum of only ~5% at the extreme lateral limits of the Mercator projections; given the pixel size limits for each bin and the areas selected for counting, applying a correction for this distortion would be both unnecessary and impractical.

Table E2. Summary data from crater counts. Key to locations: 1 = Ali Baba, 2 = Aziz, 3 = Dalilah, 4 = Ebony, 5 = Fitnah, 6 = Zumurrud, 7 = Epimetheus (* Total for Epimetheus includes a single crater in bin 13, omitted here for clarity. The quoted surface area is approximately that of a complete hemisphere, using the geometric mean radius).

Location	**1**	**2**	**3**	**4**	**5**	**6**	**7**
A (km^2)	16,467	3,620	2,734	7,588	2,734	14,260	20,774
Bin 1	87	22	35	3	25	76	27
Bin 2	110	35	42	0	28	130	17
Bin 3	64	21	19	4	15	92	16
Bin 4	61	12	13	2	14	48	18
Bin 5	32	7	4	0	14	15	36
Bin 6	18	4	3	0	6	10	21
Bin 7	11	3	2	1	1	5	6
Bin 8	4	0	2	0	0	4	1
Bin 9	0	0	0	0	0	1	4
Bin 10	2	0	0	0	0	0	1
Total	389	104	120	10	103	381	148*

Table E3. Angular extent of crater counted regions.

	Latitude	Longitude
Ali Baba	40° - 70° N	320° - 010° W
Aziz	10° - 30° N	340° - 350° W
Dalilah	40° - 50° N	220° - 240° W
Ebony	0° - 20° N	270° - 290° W
Fitnah	40° - 50° N	290° - 310° W
Zumurrud	0° - 40° S	170° - 190° W
Epimetheus	≈ Southern hemisphere	

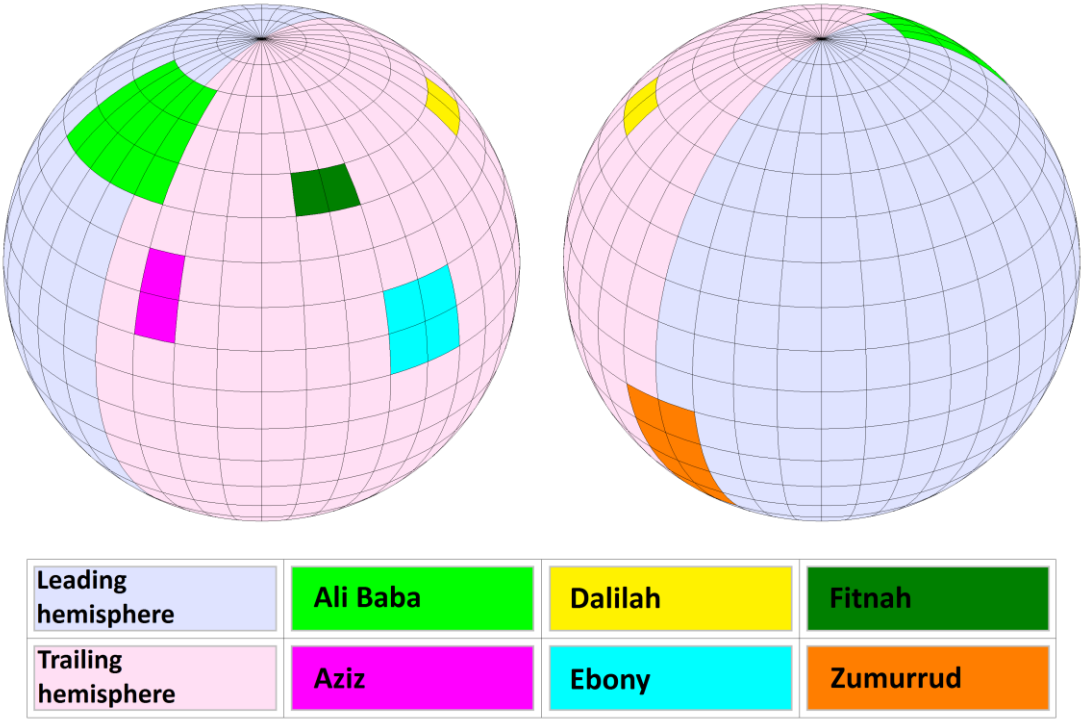


Figure E2. Spatial distribution of counted regions with respect to leading/trailing hemispheres; North is up and the sub-Saturn hemisphere is on the left. Note that the selected areas are not evenly distributed, due to the uneven resolution of the DLR mosaics, the predominance of nearly craterless ridged plains on the leading hemisphere, and the paucity of craters toward the active south polar terrain. Colors in this diagram follow those used in the cumulative-frequency and R-plots.

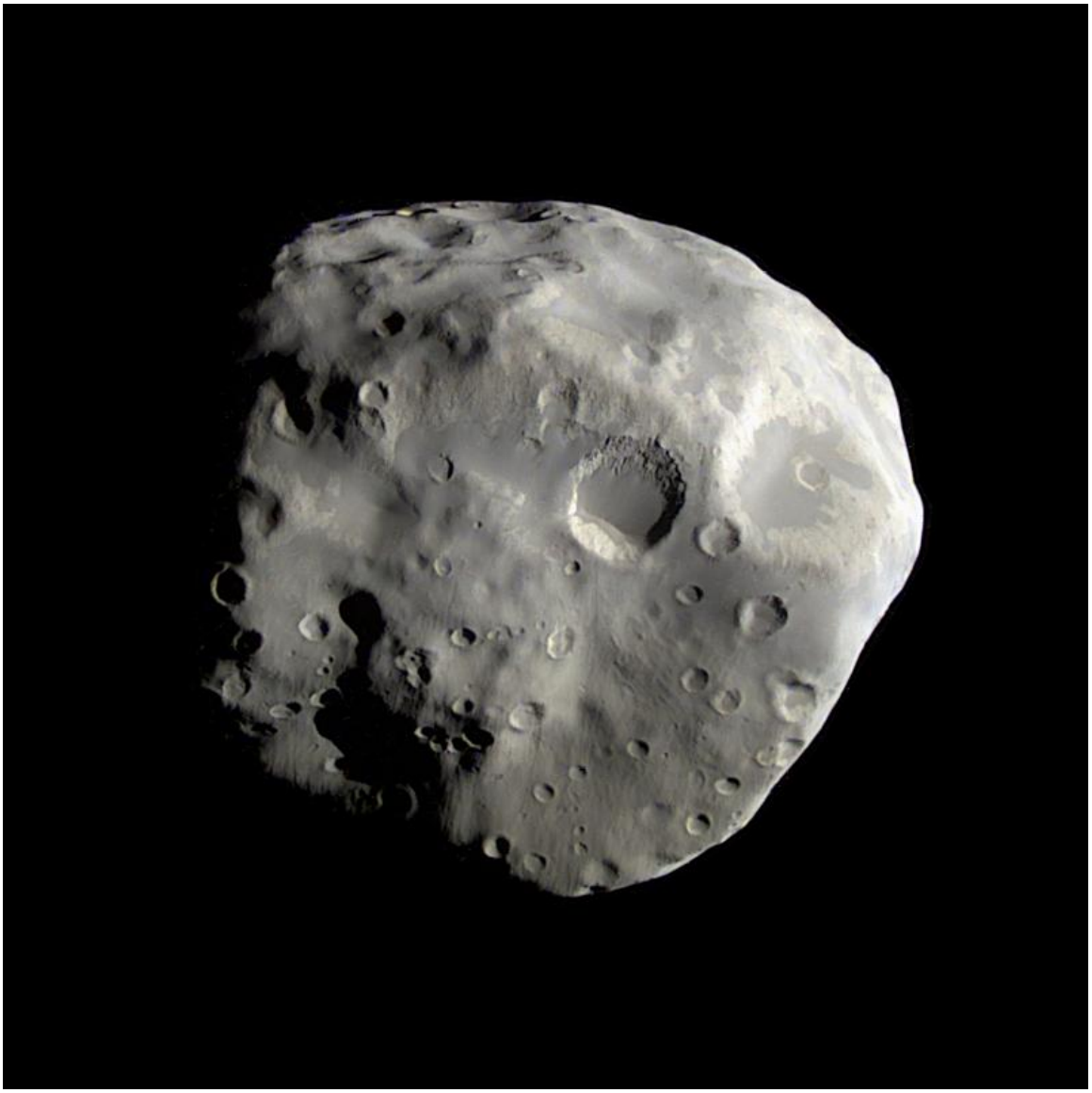


Figure E3. An 800 x 800 pixel crop from PIA09813, the enhanced-color image of Epimetheus used for crater counting; range is ~37,400 km, scale = 224 m / pixel. Note the relative absence of very small craters, and the ponding of dark, bluish-grey material in low-lying areas. This is a good example of downslope movement of material even in an extremely low gravity field. The protrusion (casting a shadow) at the 7 o'clock position is interpreted as the central peak of a very large impact, almost the diameter of the entire body. Courtesy NASA/JPL/Space Science Institute.

The formula for R in tables E11 – E17 is given by (Arvidson et al., 1978)

$$R = \overline{D}^{3} (n / A) (D_b - D_a)$$

Where $\overline{D}$ = geometric mean of the craters in a particular bin, n = number of craters counted per bin, A = area over which the count was performed, and D_b and D_a are the upper and lower bin limits. Note that R is dimensionless. In tables E4 – E10, alternating color blocks in the first column represent bins.

Table E4. Crater counts for the Ali Baba region. A = 16,467 km^2.

d (pix)	d (km)	log (d)	n	n/A	log (n/A)
168	31.92	1.504063	1	6.07E-05	-4.21661
155	29.45	1.469085	2	0.000121	-3.91558
78	14.82	1.170848	3	0.000182	-3.73949
75	14.25	1.153815	4	0.000243	-3.61455
64	12.16	1.084934	5	0.000304	-3.51764
60	11.4	1.056905	6	0.000364	-3.43846
53	10.07	1.003029	7	0.000425	-3.37152
52	9.88	0.994757	8	0.000486	-3.31352
52	9.88	0.994757	9	0.000547	-3.26237
50	9.5	0.977724	10	0.000607	-3.21661
49	9.31	0.96895	11	0.000668	-3.17522
49	9.31	0.96895	12	0.000729	-3.13743
48	9.12	0.959995	13	0.000789	-3.10267
47	8.93	0.950851	14	0.00085	-3.07049
45	8.55	0.931966	15	0.000911	-3.04052
43	8.17	0.912222	16	0.000972	-3.01249
43	8.17	0.912222	17	0.001032	-2.98617
42	7.98	0.902003	18	0.001093	-2.96134
41	7.79	0.891537	19	0.001154	-2.93786
41	7.79	0.891537	20	0.001215	-2.91558
41	7.79	0.891537	21	0.001275	-2.8944
41	7.79	0.891537	22	0.001336	-2.87419
40	7.6	0.880814	23	0.001397	-2.85489
39	7.41	0.869818	24	0.001457	-2.8364
38	7.22	0.858537	25	0.001518	-2.81867
36	6.84	0.835056	26	0.001579	-2.80164
35	6.65	0.822822	27	0.00164	-2.78525
35	6.65	0.822822	28	0.0017	-2.76946
34	6.46	0.810233	29	0.001761	-2.75422
34	6.46	0.810233	30	0.001822	-2.73949
33	6.27	0.797268	31	0.001883	-2.72525
32	6.08	0.783904	32	0.001943	-2.71146
31	5.89	0.770115	33	0.002004	-2.6981
31	5.89	0.770115	34	0.002065	-2.68514
31	5.89	0.770115	35	0.002125	-2.67255
29	5.51	0.741152	36	0.002186	-2.66031
29	5.51	0.741152	37	0.002247	-2.64841

29	5.51	0.741152	38	0.002308	-2.63683
28	5.32	0.725912	39	0.002368	-2.62555
28	5.32	0.725912	40	0.002429	-2.61455
27	5.13	0.710117	41	0.00249	-2.60383
27	5.13	0.710117	42	0.002551	-2.59337
27	5.13	0.710117	43	0.002611	-2.58315
27	5.13	0.710117	44	0.002672	-2.57316
26	4.94	0.693727	45	0.002733	-2.5634
26	4.94	0.693727	46	0.002793	-2.55386
26	4.94	0.693727	47	0.002854	-2.54452
26	4.94	0.693727	48	0.002915	-2.53537
26	4.94	0.693727	49	0.002976	-2.52642
25	4.75	0.676694	50	0.003036	-2.51764
25	4.75	0.676694	51	0.003097	-2.50904
25	4.75	0.676694	52	0.003158	-2.50061
25	4.75	0.676694	53	0.003219	-2.49234
24	4.56	0.658965	54	0.003279	-2.48422
24	4.56	0.658965	55	0.00334	-2.47625
24	4.56	0.658965	56	0.003401	-2.46843
23	4.37	0.640481	57	0.003461	-2.46074
23	4.37	0.640481	58	0.003522	-2.45319
23	4.37	0.640481	59	0.003583	-2.44576
23	4.37	0.640481	60	0.003644	-2.43846
23	4.37	0.640481	61	0.003704	-2.43128
23	4.37	0.640481	62	0.003765	-2.42422
22	4.18	0.621176	63	0.003826	-2.41727
22	4.18	0.621176	64	0.003887	-2.41043
22	4.18	0.621176	65	0.003947	-2.4037
22	4.18	0.621176	66	0.004008	-2.39707
22	4.18	0.621176	67	0.004069	-2.39054
21	3.99	0.600973	68	0.004129	-2.38411
21	3.99	0.600973	69	0.00419	-2.37777
21	3.99	0.600973	70	0.004251	-2.37152
21	3.99	0.600973	71	0.004312	-2.36536
21	3.99	0.600973	72	0.004372	-2.35928
21	3.99	0.600973	73	0.004433	-2.35329
20	3.8	0.579784	74	0.004494	-2.34738
20	3.8	0.579784	75	0.004555	-2.34155
20	3.8	0.579784	76	0.004615	-2.3358
20	3.8	0.579784	77	0.004676	-2.33012
20	3.8	0.579784	78	0.004737	-2.32452
20	3.8	0.579784	79	0.004797	-2.31899
20	3.8	0.579784	80	0.004858	-2.31352
20	3.8	0.579784	81	0.004919	-2.30813
19	3.61	0.557507	82	0.00498	-2.3028
19	3.61	0.557507	83	0.00504	-2.29754

19	3.61	0.557507	84	0.005101	-2.29234
19	3.61	0.557507	85	0.005162	-2.2872
19	3.61	0.557507	86	0.005223	-2.28212
19	3.61	0.557507	87	0.005283	-2.2771
18	3.42	0.534026	88	0.005344	-2.27213
18	3.42	0.534026	89	0.005405	-2.26722
18	3.42	0.534026	90	0.005465	-2.26237
18	3.42	0.534026	91	0.005526	-2.25757
18	3.42	0.534026	92	0.005587	-2.25283
18	3.42	0.534026	93	0.005648	-2.24813
17	3.23	0.509203	94	0.005708	-2.24349
17	3.23	0.509203	95	0.005769	-2.23889
17	3.23	0.509203	96	0.00583	-2.23434
17	3.23	0.509203	97	0.005891	-2.22984
17	3.23	0.509203	98	0.005951	-2.22539
17	3.23	0.509203	99	0.006012	-2.22098
17	3.23	0.509203	100	0.006073	-2.21661
17	3.23	0.509203	101	0.006133	-2.21229
17	3.23	0.509203	102	0.006194	-2.20801
17	3.23	0.509203	103	0.006255	-2.20378
17	3.23	0.509203	104	0.006316	-2.19958
17	3.23	0.509203	105	0.006376	-2.19543
17	3.23	0.509203	106	0.006437	-2.19131
16	3.04	0.482874	107	0.006498	-2.18723
16	3.04	0.482874	108	0.006559	-2.18319
16	3.04	0.482874	109	0.006619	-2.17919
16	3.04	0.482874	110	0.00668	-2.17522
16	3.04	0.482874	111	0.006741	-2.17129
16	3.04	0.482874	112	0.006801	-2.1674
16	3.04	0.482874	113	0.006862	-2.16354
16	3.04	0.482874	114	0.006923	-2.15971
16	3.04	0.482874	115	0.006984	-2.15592
16	3.04	0.482874	116	0.007044	-2.15216
15	2.85	0.454845	117	0.007105	-2.14843
15	2.85	0.454845	118	0.007166	-2.14473
15	2.85	0.454845	119	0.007227	-2.14107
15	2.85	0.454845	120	0.007287	-2.13743
15	2.85	0.454845	121	0.007348	-2.13383
15	2.85	0.454845	122	0.007409	-2.13025
15	2.85	0.454845	123	0.007469	-2.12671
15	2.85	0.454845	124	0.00753	-2.12319
15	2.85	0.454845	125	0.007591	-2.1197
15	2.85	0.454845	126	0.007652	-2.11624
15	2.85	0.454845	127	0.007712	-2.11281
15	2.85	0.454845	128	0.007773	-2.1094
14	2.66	0.424882	129	0.007834	-2.10602

14	2.66	0.424882	130	0.007895	-2.10267
14	2.66	0.424882	131	0.007955	-2.09934
14	2.66	0.424882	132	0.008016	-2.09604
14	2.66	0.424882	133	0.008077	-2.09276
14	2.66	0.424882	134	0.008137	-2.08951
14	2.66	0.424882	135	0.008198	-2.08628
14	2.66	0.424882	136	0.008259	-2.08308
14	2.66	0.424882	137	0.00832	-2.07989
14	2.66	0.424882	138	0.00838	-2.07674
14	2.66	0.424882	139	0.008441	-2.0736
14	2.66	0.424882	140	0.008502	-2.07049
14	2.66	0.424882	141	0.008563	-2.0674
14	2.66	0.424882	142	0.008623	-2.06433
14	2.66	0.424882	143	0.008684	-2.06128
13	2.47	0.392697	144	0.008745	-2.05825
13	2.47	0.392697	145	0.008805	-2.05525
13	2.47	0.392697	146	0.008866	-2.05226
13	2.47	0.392697	147	0.008927	-2.0493
13	2.47	0.392697	148	0.008988	-2.04635
13	2.47	0.392697	149	0.009048	-2.04343
13	2.47	0.392697	150	0.009109	-2.04052
13	2.47	0.392697	151	0.00917	-2.03764
13	2.47	0.392697	152	0.009231	-2.03477
13	2.47	0.392697	153	0.009291	-2.03192
13	2.47	0.392697	154	0.009352	-2.02909
13	2.47	0.392697	155	0.009413	-2.02628
13	2.47	0.392697	156	0.009473	-2.02349
12	2.28	0.357935	157	0.009534	-2.02071
12	2.28	0.357935	158	0.009595	-2.01796
12	2.28	0.357935	159	0.009656	-2.01522
12	2.28	0.357935	160	0.009716	-2.01249
12	2.28	0.357935	161	0.009777	-2.00979
12	2.28	0.357935	162	0.009838	-2.0071
12	2.28	0.357935	163	0.009899	-2.00443
12	2.28	0.357935	164	0.009959	-2.00177
12	2.28	0.357935	165	0.01002	-1.99913
12	2.28	0.357935	166	0.010081	-1.99651
12	2.28	0.357935	167	0.010141	-1.9939
12	2.28	0.357935	168	0.010202	-1.99131
12	2.28	0.357935	169	0.010263	-1.98873
12	2.28	0.357935	170	0.010324	-1.98617
12	2.28	0.357935	171	0.010384	-1.98362
12	2.28	0.357935	172	0.010445	-1.98109
12	2.28	0.357935	173	0.010506	-1.97857
11	2.09	0.320146	174	0.010567	-1.97607
11	2.09	0.320146	175	0.010627	-1.97358

11	2.09	0.320146	176	0.010688	-1.9711
11	2.09	0.320146	177	0.010749	-1.96864
11	2.09	0.320146	178	0.010809	-1.96619
11	2.09	0.320146	179	0.01087	-1.96376
11	2.09	0.320146	180	0.010931	-1.96134
11	2.09	0.320146	181	0.010992	-1.95894
11	2.09	0.320146	182	0.011052	-1.95654
11	2.09	0.320146	183	0.011113	-1.95416
11	2.09	0.320146	184	0.011174	-1.9518
11	2.09	0.320146	185	0.011235	-1.94944
11	2.09	0.320146	186	0.011295	-1.9471
11	2.09	0.320146	187	0.011356	-1.94477
11	2.09	0.320146	188	0.011417	-1.94246
11	2.09	0.320146	189	0.011478	-1.94015
11	2.09	0.320146	190	0.011538	-1.93786
11	2.09	0.320146	191	0.011599	-1.93558
11	2.09	0.320146	192	0.01166	-1.93331
10	1.9	0.278754	193	0.01172	-1.93106
10	1.9	0.278754	194	0.011781	-1.92881
10	1.9	0.278754	195	0.011842	-1.92658
10	1.9	0.278754	196	0.011903	-1.92436
10	1.9	0.278754	197	0.011963	-1.92215
10	1.9	0.278754	198	0.012024	-1.91995
10	1.9	0.278754	199	0.012085	-1.91776
10	1.9	0.278754	200	0.012146	-1.91558
10	1.9	0.278754	201	0.012206	-1.91342
10	1.9	0.278754	202	0.012267	-1.91126
10	1.9	0.278754	203	0.012328	-1.90912
10	1.9	0.278754	204	0.012388	-1.90698
10	1.9	0.278754	205	0.012449	-1.90486
10	1.9	0.278754	206	0.01251	-1.90275
10	1.9	0.278754	207	0.012571	-1.90064
10	1.9	0.278754	208	0.012631	-1.89855
10	1.9	0.278754	209	0.012692	-1.89647
10	1.9	0.278754	210	0.012753	-1.8944
10	1.9	0.278754	211	0.012814	-1.89233
10	1.9	0.278754	212	0.012874	-1.89028
10	1.9	0.278754	213	0.012935	-1.88823
10	1.9	0.278754	214	0.012996	-1.8862
10	1.9	0.278754	215	0.013056	-1.88418
10	1.9	0.278754	216	0.013117	-1.88216
10	1.9	0.278754	217	0.013178	-1.88015
10	1.9	0.278754	218	0.013239	-1.87816
10	1.9	0.278754	219	0.013299	-1.87617
10	1.9	0.278754	220	0.01336	-1.87419
10	1.9	0.278754	221	0.013421	-1.87222

10	1.9	0.278754	222	0.013482	-1.87026
10	1.9	0.278754	223	0.013542	-1.86831
9	1.71	0.232996	224	0.013603	-1.86637
9	1.71	0.232996	225	0.013664	-1.86443
9	1.71	0.232996	226	0.013724	-1.86251
9	1.71	0.232996	227	0.013785	-1.86059
9	1.71	0.232996	228	0.013846	-1.85868
9	1.71	0.232996	229	0.013907	-1.85678
9	1.71	0.232996	230	0.013967	-1.85489
9	1.71	0.232996	231	0.014028	-1.853
9	1.71	0.232996	232	0.014089	-1.85113
9	1.71	0.232996	233	0.01415	-1.84926
9	1.71	0.232996	234	0.01421	-1.8474
9	1.71	0.232996	235	0.014271	-1.84555
9	1.71	0.232996	236	0.014332	-1.8437
9	1.71	0.232996	237	0.014392	-1.84187
9	1.71	0.232996	238	0.014453	-1.84004
9	1.71	0.232996	239	0.014514	-1.83822
9	1.71	0.232996	240	0.014575	-1.8364
9	1.71	0.232996	241	0.014635	-1.8346
9	1.71	0.232996	242	0.014696	-1.8328
9	1.71	0.232996	243	0.014757	-1.83101
9	1.71	0.232996	244	0.014818	-1.82922
9	1.71	0.232996	245	0.014878	-1.82745
9	1.71	0.232996	246	0.014939	-1.82568
9	1.71	0.232996	247	0.015	-1.82392
9	1.71	0.232996	248	0.01506	-1.82216
9	1.71	0.232996	249	0.015121	-1.82042
9	1.71	0.232996	250	0.015182	-1.81867
9	1.71	0.232996	251	0.015243	-1.81694
9	1.71	0.232996	252	0.015303	-1.81521
9	1.71	0.232996	253	0.015364	-1.81349
9	1.71	0.232996	254	0.015425	-1.81178
8	1.52	0.181844	255	0.015486	-1.81007
8	1.52	0.181844	256	0.015546	-1.80837
8	1.52	0.181844	257	0.015607	-1.80668
8	1.52	0.181844	258	0.015668	-1.80499
8	1.52	0.181844	259	0.015728	-1.80331
8	1.52	0.181844	260	0.015789	-1.80164
8	1.52	0.181844	261	0.01585	-1.79997
8	1.52	0.181844	262	0.015911	-1.79831
8	1.52	0.181844	263	0.015971	-1.79666
8	1.52	0.181844	264	0.016032	-1.79501
8	1.52	0.181844	265	0.016093	-1.79337
8	1.52	0.181844	266	0.016154	-1.79173
8	1.52	0.181844	267	0.016214	-1.7901

8	1.52	0.181844	268	0.016275	-1.78848
8	1.52	0.181844	269	0.016336	-1.78686
8	1.52	0.181844	270	0.016396	-1.78525
8	1.52	0.181844	271	0.016457	-1.78365
8	1.52	0.181844	272	0.016518	-1.78205
8	1.52	0.181844	273	0.016579	-1.78045
8	1.52	0.181844	274	0.016639	-1.77886
8	1.52	0.181844	275	0.0167	-1.77728
8	1.52	0.181844	276	0.016761	-1.77571
8	1.52	0.181844	277	0.016822	-1.77413
8	1.52	0.181844	278	0.016882	-1.77257
8	1.52	0.181844	279	0.016943	-1.77101
8	1.52	0.181844	280	0.017004	-1.76946
8	1.52	0.181844	281	0.017064	-1.76791
8	1.52	0.181844	282	0.017125	-1.76637
8	1.52	0.181844	283	0.017186	-1.76483
8	1.52	0.181844	284	0.017247	-1.7633
8	1.52	0.181844	285	0.017307	-1.76177
8	1.52	0.181844	286	0.017368	-1.76025
8	1.52	0.181844	287	0.017429	-1.75873
8	1.52	0.181844	288	0.01749	-1.75722
8	1.52	0.181844	289	0.01755	-1.75572
8	1.52	0.181844	290	0.017611	-1.75422
8	1.52	0.181844	291	0.017672	-1.75272
8	1.52	0.181844	292	0.017732	-1.75123
8	1.52	0.181844	293	0.017793	-1.74975
8	1.52	0.181844	294	0.017854	-1.74827
8	1.52	0.181844	295	0.017915	-1.74679
8	1.52	0.181844	296	0.017975	-1.74532
8	1.52	0.181844	297	0.018036	-1.74386
8	1.52	0.181844	298	0.018097	-1.7424
8	1.52	0.181844	299	0.018158	-1.74094
8	1.52	0.181844	300	0.018218	-1.73949
8	1.52	0.181844	301	0.018279	-1.73805
8	1.52	0.181844	302	0.01834	-1.73661
7	1.33	0.123852	303	0.0184	-1.73517
7	1.33	0.123852	304	0.018461	-1.73374
7	1.33	0.123852	305	0.018522	-1.73231
7	1.33	0.123852	306	0.018583	-1.73089
7	1.33	0.123852	307	0.018643	-1.72948
7	1.33	0.123852	308	0.018704	-1.72806
7	1.33	0.123852	309	0.018765	-1.72666
7	1.33	0.123852	310	0.018826	-1.72525
7	1.33	0.123852	311	0.018886	-1.72385
7	1.33	0.123852	312	0.018947	-1.72246
7	1.33	0.123852	313	0.019008	-1.72107

7	1.33	0.123852	314	0.019068	-1.71968
7	1.33	0.123852	315	0.019129	-1.7183
7	1.33	0.123852	316	0.01919	-1.71693
7	1.33	0.123852	317	0.019251	-1.71556
7	1.33	0.123852	318	0.019311	-1.71419
7	1.33	0.123852	319	0.019372	-1.71282
7	1.33	0.123852	320	0.019433	-1.71146
7	1.33	0.123852	321	0.019494	-1.71011
7	1.33	0.123852	322	0.019554	-1.70876
7	1.33	0.123852	323	0.019615	-1.70741
7	1.33	0.123852	324	0.019676	-1.70607
7	1.33	0.123852	325	0.019736	-1.70473
7	1.33	0.123852	326	0.019797	-1.7034
7	1.33	0.123852	327	0.019858	-1.70207
7	1.33	0.123852	328	0.019919	-1.70074
7	1.33	0.123852	329	0.019979	-1.69942
7	1.33	0.123852	330	0.02004	-1.6981
7	1.33	0.123852	331	0.020101	-1.69679
7	1.33	0.123852	332	0.020162	-1.69548
7	1.33	0.123852	333	0.020222	-1.69417
7	1.33	0.123852	334	0.020283	-1.69287
7	1.33	0.123852	335	0.020344	-1.69157
7	1.33	0.123852	336	0.020404	-1.69028
7	1.33	0.123852	337	0.020465	-1.68898
7	1.33	0.123852	338	0.020526	-1.6877
7	1.33	0.123852	339	0.020587	-1.68641
7	1.33	0.123852	340	0.020647	-1.68514
7	1.33	0.123852	341	0.020708	-1.68386
7	1.33	0.123852	342	0.020769	-1.68259
7	1.33	0.123852	343	0.02083	-1.68132
7	1.33	0.123852	344	0.02089	-1.68006
7	1.33	0.123852	345	0.020951	-1.6788
7	1.33	0.123852	346	0.021012	-1.67754
7	1.33	0.123852	347	0.021072	-1.67629
7	1.33	0.123852	348	0.021133	-1.67504
7	1.33	0.123852	349	0.021194	-1.67379
7	1.33	0.123852	350	0.021255	-1.67255
7	1.33	0.123852	351	0.021315	-1.67131
6	1.14	0.056905	352	0.021376	-1.67007
6	1.14	0.056905	353	0.021437	-1.66884
6	1.14	0.056905	354	0.021498	-1.66761
6	1.14	0.056905	355	0.021558	-1.66639
6	1.14	0.056905	356	0.021619	-1.66516
6	1.14	0.056905	357	0.02168	-1.66395
6	1.14	0.056905	358	0.02174	-1.66273
6	1.14	0.056905	359	0.021801	-1.66152

6	1.14	0.056905	360	0.021862	-1.66031
6	1.14	0.056905	361	0.021923	-1.65911
6	1.14	0.056905	362	0.021983	-1.65791
6	1.14	0.056905	363	0.022044	-1.65671
6	1.14	0.056905	364	0.022105	-1.65551
6	1.14	0.056905	365	0.022166	-1.65432
6	1.14	0.056905	366	0.022226	-1.65313
6	1.14	0.056905	367	0.022287	-1.65195
6	1.14	0.056905	368	0.022348	-1.65077
6	1.14	0.056905	369	0.022408	-1.64959
6	1.14	0.056905	370	0.022469	-1.64841
6	1.14	0.056905	371	0.02253	-1.64724
6	1.14	0.056905	372	0.022591	-1.64607
6	1.14	0.056905	373	0.022651	-1.64491
6	1.14	0.056905	374	0.022712	-1.64374
6	1.14	0.056905	375	0.022773	-1.64258
6	1.14	0.056905	376	0.022834	-1.64143
6	1.14	0.056905	377	0.022894	-1.64027
6	1.14	0.056905	378	0.022955	-1.63912
6	1.14	0.056905	379	0.023016	-1.63798
6	1.14	0.056905	380	0.023076	-1.63683
6	1.14	0.056905	381	0.023137	-1.63569
6	1.14	0.056905	382	0.023198	-1.63455
6	1.14	0.056905	383	0.023259	-1.63342
6	1.14	0.056905	384	0.023319	-1.63228
6	1.14	0.056905	385	0.02338	-1.63115
6	1.14	0.056905	386	0.023441	-1.63003
6	1.14	0.056905	387	0.023502	-1.6289
6	1.14	0.056905	388	0.023562	-1.62778
6	1.14	0.056905	389	0.023623	-1.62666

Table E5. Crater counts for the Aziz region. A = 3,620 km^2.

d (pix)	d (km)	log (d)	n	n/A	log (n/A)
102	11.118	1.046027	1	0.000276	-3.55871
79	8.611	0.935054	2	0.000552	-3.25768
79	8.611	0.935054	3	0.000829	-3.08159
72	7.848	0.894759	4	0.001105	-2.95665
67	7.303	0.863501	5	0.001381	-2.85974
58	6.322	0.800854	6	0.001657	-2.78056
55	5.995	0.777789	7	0.001934	-2.71361
48	5.232	0.718668	8	0.00221	-2.65562
45	4.905	0.690639	9	0.002486	-2.60447
44	4.796	0.680879	10	0.002762	-2.55871
44	4.796	0.680879	11	0.003039	-2.51732
43	4.687	0.670895	12	0.003315	-2.47953

37	4.033	0.605628	13	0.003591	-2.44477
37	4.033	0.605628	14	0.003867	-2.41258
35	3.815	0.581495	15	0.004144	-2.38262
34	3.706	0.568905	16	0.00442	-2.35459
33	3.597	0.55594	17	0.004696	-2.32826
32	3.488	0.542576	18	0.004972	-2.30344
31	3.379	0.528788	19	0.005249	-2.27995
30	3.27	0.514548	20	0.005525	-2.25768
30	3.27	0.514548	21	0.005801	-2.23649
29	3.161	0.499824	22	0.006077	-2.21629
29	3.161	0.499824	23	0.006354	-2.19698
28	3.052	0.484585	24	0.00663	-2.1785
27	2.943	0.46879	25	0.006906	-2.16077
26	2.834	0.4524	26	0.007182	-2.14374
25	2.725	0.435367	27	0.007459	-2.12734
25	2.725	0.435367	28	0.007735	-2.11155
24	2.616	0.417638	29	0.008011	-2.09631
24	2.616	0.417638	30	0.008287	-2.08159
22	2.398	0.379849	31	0.008564	-2.06735
22	2.398	0.379849	32	0.00884	-2.05356
22	2.398	0.379849	33	0.009116	-2.04019
22	2.398	0.379849	34	0.009392	-2.02723
22	2.398	0.379849	35	0.009669	-2.01464
21	2.289	0.359646	36	0.009945	-2.00241
21	2.289	0.359646	37	0.010221	-1.99051
21	2.289	0.359646	38	0.010497	-1.97892
20	2.18	0.338456	39	0.010773	-1.96764
20	2.18	0.338456	40	0.01105	-1.95665
20	2.18	0.338456	41	0.011326	-1.94592
20	2.18	0.338456	42	0.011602	-1.93546
20	2.18	0.338456	43	0.011878	-1.92524
19	2.071	0.31618	44	0.012155	-1.91526
19	2.071	0.31618	45	0.012431	-1.9055
19	2.071	0.31618	46	0.012707	-1.89595
19	2.071	0.31618	47	0.012983	-1.88661
18	1.962	0.292699	48	0.01326	-1.87747
18	1.962	0.292699	49	0.013536	-1.86851
18	1.962	0.292699	50	0.013812	-1.85974
18	1.962	0.292699	51	0.014088	-1.85114
17	1.853	0.267875	52	0.014365	-1.84271
17	1.853	0.267875	53	0.014641	-1.83443
17	1.853	0.267875	54	0.014917	-1.82631
17	1.853	0.267875	55	0.015193	-1.81835
17	1.853	0.267875	56	0.01547	-1.81052
16	1.744	0.241546	57	0.015746	-1.80283
16	1.744	0.241546	58	0.016022	-1.79528

16	1.744	0.241546	59	0.016298	-1.78786
16	1.744	0.241546	60	0.016575	-1.78056
16	1.744	0.241546	61	0.016851	-1.77338
16	1.744	0.241546	62	0.017127	-1.76632
16	1.744	0.241546	63	0.017403	-1.75937
15	1.635	0.213518	64	0.01768	-1.75253
15	1.635	0.213518	65	0.017956	-1.7458
15	1.635	0.213518	66	0.018232	-1.73916
14	1.526	0.183555	67	0.018508	-1.73263
14	1.526	0.183555	68	0.018785	-1.7262
14	1.526	0.183555	69	0.019061	-1.71986
14	1.526	0.183555	70	0.019337	-1.71361
14	1.526	0.183555	71	0.019613	-1.70745
14	1.526	0.183555	72	0.01989	-1.70138
14	1.526	0.183555	73	0.020166	-1.69539
13	1.417	0.15137	74	0.020442	-1.68948
13	1.417	0.15137	75	0.020718	-1.68365
13	1.417	0.15137	76	0.020994	-1.67789
13	1.417	0.15137	77	0.021271	-1.67222
13	1.417	0.15137	78	0.021547	-1.66661
13	1.417	0.15137	79	0.021823	-1.66108
13	1.417	0.15137	80	0.022099	-1.65562
13	1.417	0.15137	81	0.022376	-1.65022
13	1.417	0.15137	82	0.022652	-1.64489
12	1.308	0.116608	83	0.022928	-1.63963
12	1.308	0.116608	84	0.023204	-1.63443
12	1.308	0.116608	85	0.023481	-1.62929
12	1.308	0.116608	86	0.023757	-1.62421
12	1.308	0.116608	87	0.024033	-1.61919
12	1.308	0.116608	88	0.024309	-1.61423
12	1.308	0.116608	89	0.024586	-1.60932
12	1.308	0.116608	90	0.024862	-1.60447
12	1.308	0.116608	91	0.025138	-1.59967
11	1.199	0.078819	92	0.025414	-1.59492
11	1.199	0.078819	93	0.025691	-1.59023
11	1.199	0.078819	94	0.025967	-1.58558
11	1.199	0.078819	95	0.026243	-1.58098
11	1.199	0.078819	96	0.026519	-1.57644
11	1.199	0.078819	97	0.026796	-1.57194
10	1.09	0.037426	98	0.027072	-1.56748
10	1.09	0.037426	99	0.027348	-1.56307
10	1.09	0.037426	100	0.027624	-1.55871
10	1.09	0.037426	101	0.027901	-1.55439
10	1.09	0.037426	102	0.028177	-1.55011
10	1.09	0.037426	103	0.028453	-1.54587
10	1.09	0.037426	104	0.028729	-1.54168

Table E6. Crater counts for the Dalilah region. A = 2,734 km^2.

d (pix)	d (km)	log (d)	n	n/A	log (n/A)
130	14.69	1.167022	1	0.000366	-3.4368
115	12.995	1.113776	2	0.000732	-3.13577
93	10.509	1.021561	3	0.001097	-2.95968
85	9.605	0.982497	4	0.001463	-2.83474
67	7.571	0.879153	5	0.001829	-2.73783
59	6.667	0.82393	6	0.002195	-2.65865
54	6.102	0.785472	7	0.00256	-2.5917
45	5.085	0.706291	8	0.002926	-2.53371
42	4.746	0.676328	9	0.003292	-2.48256
41	4.633	0.665862	10	0.003658	-2.4368
38	4.294	0.632862	11	0.004023	-2.39541
33	3.729	0.571592	12	0.004389	-2.35762
33	3.729	0.571592	13	0.004755	-2.32286
32	3.616	0.558228	14	0.005121	-2.29067
32	3.616	0.558228	15	0.005486	-2.26071
31	3.503	0.54444	16	0.005852	-2.23268
29	3.277	0.515476	17	0.006218	-2.20635
29	3.277	0.515476	18	0.006584	-2.18153
29	3.277	0.515476	19	0.00695	-2.15804
28	3.164	0.500236	20	0.007315	-2.13577
28	3.164	0.500236	21	0.007681	-2.11458
27	3.051	0.484442	22	0.008047	-2.09438
27	3.051	0.484442	23	0.008413	-2.07507
26	2.938	0.468052	24	0.008778	-2.05659
25	2.825	0.451018	25	0.009144	-2.03886
25	2.825	0.451018	26	0.00951	-2.02183
24	2.712	0.43329	27	0.009876	-2.00543
23	2.599	0.414806	28	0.010241	-1.98964
22	2.486	0.395501	29	0.010607	-1.9744
22	2.486	0.395501	30	0.010973	-1.95968
22	2.486	0.395501	31	0.011339	-1.94544
21	2.373	0.375298	32	0.011704	-1.93165
21	2.373	0.375298	33	0.01207	-1.91828
21	2.373	0.375298	34	0.012436	-1.90532
20	2.26	0.354108	35	0.012802	-1.89273
20	2.26	0.354108	36	0.013168	-1.8805
20	2.26	0.354108	37	0.013533	-1.8686
19	2.147	0.331832	38	0.013899	-1.85701
19	2.147	0.331832	39	0.014265	-1.84573
19	2.147	0.331832	40	0.014631	-1.83474
18	2.034	0.308351	41	0.014996	-1.82401
18	2.034	0.308351	42	0.015362	-1.81355
18	2.034	0.308351	43	0.015728	-1.80333

17	1.921	0.283527	44	0.016094	-1.79335
17	1.921	0.283527	45	0.016459	-1.78359
17	1.921	0.283527	46	0.016825	-1.77404
17	1.921	0.283527	47	0.017191	-1.7647
17	1.921	0.283527	48	0.017557	-1.75556
16	1.808	0.257198	49	0.017922	-1.7466
16	1.808	0.257198	50	0.018288	-1.73783
16	1.808	0.257198	51	0.018654	-1.72923
16	1.808	0.257198	52	0.01902	-1.7208
15	1.695	0.22917	53	0.019386	-1.71252
15	1.695	0.22917	54	0.019751	-1.7044
15	1.695	0.22917	55	0.020117	-1.69644
15	1.695	0.22917	56	0.020483	-1.68861
15	1.695	0.22917	57	0.020849	-1.68092
15	1.695	0.22917	58	0.021214	-1.67337
15	1.695	0.22917	59	0.02158	-1.66595
14	1.582	0.199206	60	0.021946	-1.65865
14	1.582	0.199206	61	0.022312	-1.65147
14	1.582	0.199206	62	0.022677	-1.64441
14	1.582	0.199206	63	0.023043	-1.63746
14	1.582	0.199206	64	0.023409	-1.63062
14	1.582	0.199206	65	0.023775	-1.62389
14	1.582	0.199206	66	0.02414	-1.61725
14	1.582	0.199206	67	0.024506	-1.61072
13	1.469	0.167022	68	0.024872	-1.60429
13	1.469	0.167022	69	0.025238	-1.59795
13	1.469	0.167022	70	0.025604	-1.5917
13	1.469	0.167022	71	0.025969	-1.58554
13	1.469	0.167022	72	0.026335	-1.57947
13	1.469	0.167022	73	0.026701	-1.57348
13	1.469	0.167022	74	0.027067	-1.56757
13	1.469	0.167022	75	0.027432	-1.56174
13	1.469	0.167022	76	0.027798	-1.55598
13	1.469	0.167022	77	0.028164	-1.55031
13	1.469	0.167022	78	0.02853	-1.5447
13	1.469	0.167022	79	0.028895	-1.53917
13	1.469	0.167022	80	0.029261	-1.53371
13	1.469	0.167022	81	0.029627	-1.52831
13	1.469	0.167022	82	0.029993	-1.52298
13	1.469	0.167022	83	0.030358	-1.51772
13	1.469	0.167022	84	0.030724	-1.51252
13	1.469	0.167022	85	0.03109	-1.50738
12	1.356	0.13226	86	0.031456	-1.5023
12	1.356	0.13226	87	0.031822	-1.49728
12	1.356	0.13226	88	0.032187	-1.49232
12	1.356	0.13226	89	0.032553	-1.48741

12	1.356	0.13226	90	0.032919	-1.48256
12	1.356	0.13226	91	0.033285	-1.47776
12	1.356	0.13226	92	0.03365	-1.47301
12	1.356	0.13226	93	0.034016	-1.46832
12	1.356	0.13226	94	0.034382	-1.46367
12	1.356	0.13226	95	0.034748	-1.45907
12	1.356	0.13226	96	0.035113	-1.45453
12	1.356	0.13226	97	0.035479	-1.45003
11	1.243	0.094471	98	0.035845	-1.44557
11	1.243	0.094471	99	0.036211	-1.44116
11	1.243	0.094471	100	0.036576	-1.4368
11	1.243	0.094471	101	0.036942	-1.43248
11	1.243	0.094471	102	0.037308	-1.4282
11	1.243	0.094471	103	0.037674	-1.42396
11	1.243	0.094471	104	0.03804	-1.41977
11	1.243	0.094471	105	0.038405	-1.41561
10	1.13	0.053078	106	0.038771	-1.41149
10	1.13	0.053078	107	0.039137	-1.40741
10	1.13	0.053078	108	0.039503	-1.40337
10	1.13	0.053078	109	0.039868	-1.39937
10	1.13	0.053078	110	0.040234	-1.39541
10	1.13	0.053078	111	0.0406	-1.39148
10	1.13	0.053078	112	0.040966	-1.38758
10	1.13	0.053078	113	0.041331	-1.38372
10	1.13	0.053078	114	0.041697	-1.37989
10	1.13	0.053078	115	0.042063	-1.3761
10	1.13	0.053078	116	0.042429	-1.37234
10	1.13	0.053078	117	0.042794	-1.36861
9	1.017	0.007321	118	0.04316	-1.36492
9	1.017	0.007321	119	0.043526	-1.36125
9	1.017	0.007321	120	0.043892	-1.35762

Table E7. Crater counts for the Ebony region. A = 7,588 km^2.

d (pix)	d (km)	log (d)	n	n/A	log (n/A)
96	10.56	1.023664	1	0.000132	-3.88013
33	3.63	0.559907	2	0.000264	-3.5791
27	2.97	0.472756	3	0.000395	-3.40301
21	2.31	0.363612	4	0.000527	-3.27807
20	2.2	0.342423	5	0.000659	-3.18116
20	2.2	0.342423	6	0.000791	-3.10198
19	2.09	0.320146	7	0.000923	-3.03503
11	1.21	0.082785	8	0.001054	-2.97704
11	1.21	0.082785	9	0.001186	-2.92588
10	1.1	0.041393	10	0.001318	-2.88013

Table E8. Crater counts for the Fitnah region. A = 2,734 km^2.

d (pix)	d (km)	log (d)	n	n/A	log (n/A)
71	8.023	0.904337	1	0.000366	-3.4368
65	7.345	0.865992	2	0.000732	-3.13577
58	6.554	0.816506	3	0.001097	-2.95968
58	6.554	0.816506	4	0.001463	-2.83474
54	6.102	0.785472	5	0.001829	-2.73783
53	5.989	0.777354	6	0.002195	-2.65865
51	5.763	0.760649	7	0.00256	-2.5917
50	5.65	0.752048	8	0.002926	-2.53371
47	5.311	0.725176	9	0.003292	-2.48256
46	5.198	0.715836	10	0.003658	-2.4368
46	5.198	0.715836	11	0.004023	-2.39541
43	4.859	0.686547	12	0.004389	-2.35762
42	4.746	0.676328	13	0.004755	-2.32286
42	4.746	0.676328	14	0.005121	-2.29067
41	4.633	0.665862	15	0.005486	-2.26071
40	4.52	0.655138	16	0.005852	-2.23268
39	4.407	0.644143	17	0.006218	-2.20635
39	4.407	0.644143	18	0.006584	-2.18153
39	4.407	0.644143	19	0.00695	-2.15804
37	4.181	0.62128	20	0.007315	-2.13577
36	4.068	0.609381	21	0.007681	-2.11458
35	3.955	0.597146	22	0.008047	-2.09438
35	3.955	0.597146	23	0.008413	-2.07507
33	3.729	0.571592	24	0.008778	-2.05659
33	3.729	0.571592	25	0.009144	-2.03886
33	3.729	0.571592	26	0.00951	-2.02183
32	3.616	0.558228	27	0.009876	-2.00543
31	3.503	0.54444	28	0.010241	-1.98964
31	3.503	0.54444	29	0.010607	-1.9744
31	3.503	0.54444	30	0.010973	-1.95968
28	3.164	0.500236	31	0.011339	-1.94544
28	3.164	0.500236	32	0.011704	-1.93165
26	2.938	0.468052	33	0.01207	-1.91828
26	2.938	0.468052	34	0.012436	-1.90532
26	2.938	0.468052	35	0.012802	-1.89273
25	2.825	0.451018	36	0.013168	-1.8805
24	2.712	0.43329	37	0.013533	-1.8686
22	2.486	0.395501	38	0.013899	-1.85701
22	2.486	0.395501	39	0.014265	-1.84573
20	2.26	0.354108	40	0.014631	-1.83474
20	2.26	0.354108	41	0.014996	-1.82401
20	2.26	0.354108	42	0.015362	-1.81355
20	2.26	0.354108	43	0.015728	-1.80333

19	2.147	0.331832	44	0.016094	-1.79335
19	2.147	0.331832	45	0.016459	-1.78359
19	2.147	0.331832	46	0.016825	-1.77404
18	2.034	0.308351	47	0.017191	-1.7647
18	2.034	0.308351	48	0.017557	-1.75556
18	2.034	0.308351	49	0.017922	-1.7466
18	2.034	0.308351	50	0.018288	-1.73783
17	1.921	0.283527	51	0.018654	-1.72923
17	1.921	0.283527	52	0.01902	-1.7208
17	1.921	0.283527	53	0.019386	-1.71252
16	1.808	0.257198	54	0.019751	-1.7044
15	1.695	0.22917	55	0.020117	-1.69644
15	1.695	0.22917	56	0.020483	-1.68861
15	1.695	0.22917	57	0.020849	-1.68092
15	1.695	0.22917	58	0.021214	-1.67337
15	1.695	0.22917	59	0.02158	-1.66595
15	1.695	0.22917	60	0.021946	-1.65865
14	1.582	0.199206	61	0.022312	-1.65147
14	1.582	0.199206	62	0.022677	-1.64441
14	1.582	0.199206	63	0.023043	-1.63746
14	1.582	0.199206	64	0.023409	-1.63062
14	1.582	0.199206	65	0.023775	-1.62389
14	1.582	0.199206	66	0.02414	-1.61725
14	1.582	0.199206	67	0.024506	-1.61072
14	1.582	0.199206	68	0.024872	-1.60429
14	1.582	0.199206	69	0.025238	-1.59795
13	1.469	0.167022	70	0.025604	-1.5917
13	1.469	0.167022	71	0.025969	-1.58554
13	1.469	0.167022	72	0.026335	-1.57947
13	1.469	0.167022	73	0.026701	-1.57348
13	1.469	0.167022	74	0.027067	-1.56757
13	1.469	0.167022	75	0.027432	-1.56174
13	1.469	0.167022	76	0.027798	-1.55598
13	1.469	0.167022	77	0.028164	-1.55031
13	1.469	0.167022	78	0.02853	-1.5447
12	1.356	0.13226	79	0.028895	-1.53917
12	1.356	0.13226	80	0.029261	-1.53371
12	1.356	0.13226	81	0.029627	-1.52831
12	1.356	0.13226	82	0.029993	-1.52298
12	1.356	0.13226	83	0.030358	-1.51772
12	1.356	0.13226	84	0.030724	-1.51252
12	1.356	0.13226	85	0.03109	-1.50738
12	1.356	0.13226	86	0.031456	-1.5023
12	1.356	0.13226	87	0.031822	-1.49728
12	1.356	0.13226	88	0.032187	-1.49232
11	1.243	0.094471	89	0.032553	-1.48741

11	1.243	0.094471	90	0.032919	-1.48256
11	1.243	0.094471	91	0.033285	-1.47776
11	1.243	0.094471	92	0.03365	-1.47301
11	1.243	0.094471	93	0.034016	-1.46832
11	1.243	0.094471	94	0.034382	-1.46367
10	1.13	0.053078	95	0.034748	-1.45907
10	1.13	0.053078	96	0.035113	-1.45453
9	1.017	0.007321	97	0.035479	-1.45003
9	1.017	0.007321	98	0.035845	-1.44557
9	1.017	0.007321	99	0.036211	-1.44116
9	1.017	0.007321	100	0.036576	-1.4368
9	1.017	0.007321	101	0.036942	-1.43248
9	1.017	0.007321	102	0.037308	-1.4282
9	1.017	0.007321	103	0.037674	-1.42396

Table E9. Crater counts for the Zumurrud region. A = 14,260 km^2.

d (pix)	d (km)	log (d)	n	n/A	log (n/A)
186	20.646	1.314836	1	7.01E-05	-4.15412
126	13.86	1.141763	2	0.00014	-3.85309
126	13.86	1.141763	3	0.00021	-3.677
120	13.32	1.124504	4	0.000281	-3.55206
107	11.877	1.074707	5	0.000351	-3.45515
83	9.213	0.964401	6	0.000421	-3.37597
82	9.102	0.959137	7	0.000491	-3.30902
79	8.69	0.93902	8	0.000561	-3.25103
78	8.58	0.933487	9	0.000631	-3.19988
76	8.36	0.922206	10	0.000701	-3.15412
72	7.92	0.898725	11	0.000771	-3.11273
69	7.59	0.880242	12	0.000842	-3.07494
65	7.215	0.858236	13	0.000912	-3.04018
64	7.04	0.847573	14	0.000982	-3.00799
62	6.82	0.833784	15	0.001052	-2.97803
62	6.82	0.833784	16	0.001122	-2.95
60	6.66	0.823474	17	0.001192	-2.92367
54	5.94	0.773786	18	0.001262	-2.89885
53	5.83	0.765669	19	0.001332	-2.87537
52	5.72	0.757396	20	0.001403	-2.85309
51	5.61	0.748963	21	0.001473	-2.8319
50	5.5	0.740363	22	0.001543	-2.8117
49	5.439	0.735519	23	0.001613	-2.79239
49	5.39	0.731589	24	0.001683	-2.77391
47	5.17	0.713491	25	0.001753	-2.75618
47	5.17	0.713491	26	0.001823	-2.73915
46	5.106	0.708081	27	0.001893	-2.72276
45	4.995	0.698535	28	0.001964	-2.70696
43	4.773	0.678791	29	0.002034	-2.69172

42	4.62	0.664642	30	0.002104	-2.677
41	4.551	0.658107	31	0.002174	-2.66276
41	4.51	0.654177	32	0.002244	-2.64897
41	4.51	0.654177	33	0.002314	-2.63561
40	4.4	0.643453	34	0.002384	-2.62264
37	4.07	0.609594	35	0.002454	-2.61005
36	3.996	0.601625	36	0.002525	-2.59782
36	3.996	0.601625	37	0.002595	-2.58592
36	3.996	0.601625	38	0.002665	-2.57434
36	3.96	0.597695	39	0.002735	-2.56305
35	3.885	0.589391	40	0.002805	-2.55206
35	3.85	0.585461	41	0.002875	-2.54134
34	3.774	0.576802	42	0.002945	-2.53087
34	3.74	0.572872	43	0.003015	-2.52065
33	3.63	0.559907	44	0.003086	-2.51067
32	3.552	0.550473	45	0.003156	-2.50091
32	3.552	0.550473	46	0.003226	-2.49136
32	3.52	0.546543	47	0.003296	-2.48202
32	3.52	0.546543	48	0.003366	-2.47288
31	3.441	0.536685	49	0.003436	-2.46392
31	3.441	0.536685	50	0.003506	-2.45515
31	3.441	0.536685	51	0.003576	-2.44655
31	3.441	0.536685	52	0.003647	-2.43812
31	3.441	0.536685	53	0.003717	-2.42984
31	3.41	0.532754	54	0.003787	-2.42173
31	3.41	0.532754	55	0.003857	-2.41376
30	3.33	0.522444	56	0.003927	-2.40593
30	3.33	0.522444	57	0.003997	-2.39824
30	3.3	0.518514	58	0.004067	-2.39069
30	3.3	0.518514	59	0.004137	-2.38327
30	3.3	0.518514	60	0.004208	-2.37597
29	3.219	0.507721	61	0.004278	-2.36879
29	3.219	0.507721	62	0.004348	-2.36173
29	3.19	0.503791	63	0.004418	-2.35478
29	3.19	0.503791	64	0.004488	-2.34794
29	3.19	0.503791	65	0.004558	-2.34121
28	3.108	0.492481	66	0.004628	-2.33458
28	3.08	0.488551	67	0.004698	-2.32804
27	2.997	0.476687	68	0.004769	-2.32161
27	2.997	0.476687	69	0.004839	-2.31527
27	2.997	0.476687	70	0.004909	-2.30902
27	2.97	0.472756	71	0.004979	-2.30286
27	2.97	0.472756	72	0.005049	-2.29679
27	2.97	0.472756	73	0.005119	-2.2908
27	2.97	0.472756	74	0.005189	-2.28489
27	2.97	0.472756	75	0.005259	-2.27906
26	2.886	0.460296	76	0.00533	-2.27331
26	2.886	0.460296	77	0.0054	-2.26763

26	2.886	0.460296	78	0.00547	-2.26202
26	2.86	0.456366	79	0.00554	-2.25649
26	2.86	0.456366	80	0.00561	-2.25103
26	2.86	0.456366	81	0.00568	-2.24563
26	2.86	0.456366	82	0.00575	-2.24031
26	2.86	0.456366	83	0.00582	-2.23504
25	2.775	0.443263	84	0.005891	-2.22984
25	2.775	0.443263	85	0.005961	-2.2247
25	2.775	0.443263	86	0.006031	-2.21962
25	2.775	0.443263	87	0.006101	-2.2146
25	2.75	0.439333	88	0.006171	-2.20964
25	2.75	0.439333	89	0.006241	-2.20473
25	2.75	0.439333	90	0.006311	-2.19988
25	2.75	0.439333	91	0.006381	-2.19508
24	2.664	0.425534	92	0.006452	-2.19033
24	2.664	0.425534	93	0.006522	-2.18564
24	2.64	0.421604	94	0.006592	-2.18099
23	2.553	0.407051	95	0.006662	-2.1764
23	2.553	0.407051	96	0.006732	-2.17185
23	2.53	0.403121	97	0.006802	-2.16735
23	2.53	0.403121	98	0.006872	-2.16289
23	2.53	0.403121	99	0.006942	-2.15848
23	2.53	0.403121	100	0.007013	-2.15412
22	2.442	0.387746	101	0.007083	-2.1498
22	2.442	0.387746	102	0.007153	-2.14552
22	2.442	0.387746	103	0.007223	-2.14128
22	2.442	0.387746	104	0.007293	-2.13709
22	2.442	0.387746	105	0.007363	-2.13293
22	2.442	0.387746	106	0.007433	-2.12881
22	2.42	0.383815	107	0.007504	-2.12474
22	2.42	0.383815	108	0.007574	-2.1207
22	2.42	0.383815	109	0.007644	-2.11669
22	2.42	0.383815	110	0.007714	-2.11273
22	2.42	0.383815	111	0.007784	-2.1088
22	2.42	0.383815	112	0.007854	-2.1049
22	2.42	0.383815	113	0.007924	-2.10104
22	2.42	0.383815	114	0.007994	-2.09721
22	2.42	0.383815	115	0.008065	-2.09342
22	2.42	0.383815	116	0.008135	-2.08966
22	2.42	0.383815	117	0.008205	-2.08593
21	2.331	0.367542	118	0.008275	-2.08224
21	2.331	0.367542	119	0.008345	-2.07857
21	2.331	0.367542	120	0.008415	-2.07494
21	2.331	0.367542	121	0.008485	-2.07133
21	2.331	0.367542	122	0.008555	-2.06776
21	2.331	0.367542	123	0.008626	-2.06421
21	2.331	0.367542	124	0.008696	-2.0607
21	2.331	0.367542	125	0.008766	-2.05721

21	2.331	0.367542	126	0.008836	-2.05375
21	2.331	0.367542	127	0.008906	-2.05032
21	2.31	0.363612	128	0.008976	-2.04691
21	2.31	0.363612	129	0.009046	-2.04353
21	2.31	0.363612	130	0.009116	-2.04018
21	2.31	0.363612	131	0.009187	-2.03685
21	2.31	0.363612	132	0.009257	-2.03355
21	2.31	0.363612	133	0.009327	-2.03027
21	2.31	0.363612	134	0.009397	-2.02701
21	2.31	0.363612	135	0.009467	-2.02379
21	2.31	0.363612	136	0.009537	-2.02058
21	2.31	0.363612	137	0.009607	-2.0174
21	2.31	0.363612	138	0.009677	-2.01424
21	2.31	0.363612	139	0.009748	-2.0111
21	2.31	0.363612	140	0.009818	-2.00799
20	2.22	0.346353	141	0.009888	-2.0049
20	2.22	0.346353	142	0.009958	-2.00183
20	2.22	0.346353	143	0.010028	-1.99878
20	2.22	0.346353	144	0.010098	-1.99576
20	2.22	0.346353	145	0.010168	-1.99275
20	2.22	0.346353	146	0.010238	-1.98977
20	2.22	0.346353	147	0.010309	-1.9868
20	2.22	0.346353	148	0.010379	-1.98386
20	2.22	0.346353	149	0.010449	-1.98093
20	2.22	0.346353	150	0.010519	-1.97803
20	2.2	0.342423	151	0.010589	-1.97514
20	2.2	0.342423	152	0.010659	-1.97228
20	2.2	0.342423	153	0.010729	-1.96943
20	2.2	0.342423	154	0.010799	-1.9666
19	2.109	0.324077	155	0.01087	-1.96379
19	2.109	0.324077	156	0.01094	-1.96099
19	2.109	0.324077	157	0.01101	-1.95822
19	2.109	0.324077	158	0.01108	-1.95546
19	2.109	0.324077	159	0.01115	-1.95272
19	2.109	0.324077	160	0.01122	-1.95
19	2.109	0.324077	161	0.01129	-1.94729
19	2.109	0.324077	162	0.01136	-1.9446
19	2.109	0.324077	163	0.011431	-1.94193
19	2.109	0.324077	164	0.011501	-1.93928
19	2.09	0.320146	165	0.011571	-1.93664
19	2.09	0.320146	166	0.011641	-1.93401
19	2.09	0.320146	167	0.011711	-1.9314
19	2.09	0.320146	168	0.011781	-1.92881
19	2.09	0.320146	169	0.011851	-1.92623
19	2.09	0.320146	170	0.011921	-1.92367
19	2.09	0.320146	171	0.011992	-1.92112
19	2.09	0.320146	172	0.012062	-1.91859
19	2.09	0.320146	173	0.012132	-1.91607

19	2.09	0.320146	174	0.012202	-1.91357
19	2.09	0.320146	175	0.012272	-1.91108
18	1.998	0.300595	176	0.012342	-1.90861
18	1.998	0.300595	177	0.012412	-1.90615
18	1.998	0.300595	178	0.012482	-1.9037
18	1.998	0.300595	179	0.012553	-1.90127
18	1.998	0.300595	180	0.012623	-1.89885
18	1.998	0.300595	181	0.012693	-1.89644
18	1.998	0.300595	182	0.012763	-1.89405
18	1.998	0.300595	183	0.012833	-1.89167
18	1.998	0.300595	184	0.012903	-1.8893
18	1.998	0.300595	185	0.012973	-1.88695
18	1.998	0.300595	186	0.013043	-1.88461
18	1.998	0.300595	187	0.013114	-1.88228
18	1.998	0.300595	188	0.013184	-1.87996
18	1.998	0.300595	189	0.013254	-1.87766
18	1.98	0.296665	190	0.013324	-1.87537
18	1.98	0.296665	191	0.013394	-1.87309
18	1.98	0.296665	192	0.013464	-1.87082
18	1.98	0.296665	193	0.013534	-1.86856
18	1.98	0.296665	194	0.013604	-1.86632
18	1.98	0.296665	195	0.013675	-1.86408
17	1.887	0.275772	196	0.013745	-1.86186
17	1.887	0.275772	197	0.013815	-1.85965
17	1.887	0.275772	198	0.013885	-1.85745
17	1.887	0.275772	199	0.013955	-1.85527
17	1.887	0.275772	200	0.014025	-1.85309
17	1.887	0.275772	201	0.014095	-1.85092
17	1.887	0.275772	202	0.014165	-1.84877
17	1.887	0.275772	203	0.014236	-1.84662
17	1.887	0.275772	204	0.014306	-1.84449
17	1.887	0.275772	205	0.014376	-1.84237
17	1.87	0.271842	206	0.014446	-1.84025
17	1.87	0.271842	207	0.014516	-1.83815
17	1.87	0.271842	208	0.014586	-1.83606
17	1.87	0.271842	209	0.014656	-1.83397
17	1.87	0.271842	210	0.014727	-1.8319
17	1.87	0.271842	211	0.014797	-1.82984
17	1.87	0.271842	212	0.014867	-1.82778
17	1.87	0.271842	213	0.014937	-1.82574
16	1.776	0.249443	214	0.015007	-1.82371
16	1.776	0.249443	215	0.015077	-1.82168
16	1.776	0.249443	216	0.015147	-1.81967
16	1.776	0.249443	217	0.015217	-1.81766
16	1.776	0.249443	218	0.015288	-1.81566
16	1.776	0.249443	219	0.015358	-1.81368
16	1.776	0.249443	220	0.015428	-1.8117
16	1.776	0.249443	221	0.015498	-1.80973

16	1.776	0.249443	222	0.015568	-1.80777
16	1.776	0.249443	223	0.015638	-1.80581
16	1.776	0.249443	224	0.015708	-1.80387
16	1.776	0.249443	225	0.015778	-1.80194
16	1.776	0.249443	226	0.015849	-1.80001
16	1.776	0.249443	227	0.015919	-1.79809
16	1.776	0.249443	228	0.015989	-1.79618
16	1.776	0.249443	229	0.016059	-1.79428
16	1.76	0.245513	230	0.016129	-1.79239
16	1.76	0.245513	231	0.016199	-1.79051
16	1.76	0.245513	232	0.016269	-1.78863
16	1.76	0.245513	233	0.016339	-1.78676
16	1.76	0.245513	234	0.01641	-1.7849
16	1.76	0.245513	235	0.01648	-1.78305
15	1.665	0.221414	236	0.01655	-1.78121
15	1.665	0.221414	237	0.01662	-1.77937
15	1.665	0.221414	238	0.01669	-1.77754
15	1.665	0.221414	239	0.01676	-1.77572
15	1.665	0.221414	240	0.01683	-1.77391
15	1.665	0.221414	241	0.0169	-1.7721
15	1.665	0.221414	242	0.016971	-1.7703
15	1.665	0.221414	243	0.017041	-1.76851
15	1.665	0.221414	244	0.017111	-1.76673
15	1.665	0.221414	245	0.017181	-1.76495
15	1.665	0.221414	246	0.017251	-1.76318
15	1.665	0.221414	247	0.017321	-1.76142
15	1.665	0.221414	248	0.017391	-1.75967
15	1.665	0.221414	249	0.017461	-1.75792
15	1.665	0.221414	250	0.017532	-1.75618
15	1.665	0.221414	251	0.017602	-1.75445
15	1.665	0.221414	252	0.017672	-1.75272
15	1.665	0.221414	253	0.017742	-1.751
15	1.665	0.221414	254	0.017812	-1.74929
15	1.665	0.221414	255	0.017882	-1.74758
15	1.65	0.217484	256	0.017952	-1.74588
15	1.65	0.217484	257	0.018022	-1.74419
15	1.65	0.217484	258	0.018093	-1.7425
15	1.65	0.217484	259	0.018163	-1.74082
15	1.65	0.217484	260	0.018233	-1.73915
15	1.65	0.217484	261	0.018303	-1.73748
15	1.65	0.217484	262	0.018373	-1.73582
14	1.554	0.191451	263	0.018443	-1.73416
14	1.554	0.191451	264	0.018513	-1.73252
14	1.554	0.191451	265	0.018583	-1.73087
14	1.554	0.191451	266	0.018654	-1.72924
14	1.554	0.191451	267	0.018724	-1.72761
14	1.554	0.191451	268	0.018794	-1.72598
14	1.554	0.191451	269	0.018864	-1.72437

14	1.554	0.191451	270	0.018934	-1.72276
14	1.554	0.191451	271	0.019004	-1.72115
14	1.54	0.187521	272	0.019074	-1.71955
14	1.54	0.187521	273	0.019144	-1.71796
14	1.54	0.187521	274	0.019215	-1.71637
14	1.54	0.187521	275	0.019285	-1.71479
14	1.54	0.187521	276	0.019355	-1.71321
14	1.54	0.187521	277	0.019425	-1.71164
14	1.54	0.187521	278	0.019495	-1.71007
14	1.54	0.187521	279	0.019565	-1.70852
13	1.443	0.159266	280	0.019635	-1.70696
13	1.443	0.159266	281	0.019705	-1.70541
13	1.443	0.159266	282	0.019776	-1.70387
13	1.443	0.159266	283	0.019846	-1.70233
13	1.443	0.159266	284	0.019916	-1.7008
13	1.443	0.159266	285	0.019986	-1.69927
13	1.443	0.159266	286	0.020056	-1.69775
13	1.443	0.159266	287	0.020126	-1.69624
13	1.443	0.159266	288	0.020196	-1.69473
13	1.443	0.159266	289	0.020266	-1.69322
13	1.443	0.159266	290	0.020337	-1.69172
13	1.443	0.159266	291	0.020407	-1.69023
13	1.443	0.159266	292	0.020477	-1.68874
13	1.443	0.159266	293	0.020547	-1.68725
13	1.443	0.159266	294	0.020617	-1.68577
13	1.443	0.159266	295	0.020687	-1.6843
13	1.43	0.155336	296	0.020757	-1.68283
13	1.43	0.155336	297	0.020827	-1.68136
13	1.43	0.155336	298	0.020898	-1.6799
13	1.43	0.155336	299	0.020968	-1.67845
13	1.43	0.155336	300	0.021038	-1.677
13	1.43	0.155336	301	0.021108	-1.67555
13	1.43	0.155336	302	0.021178	-1.67411
13	1.43	0.155336	303	0.021248	-1.67268
13	1.43	0.155336	304	0.021318	-1.67125
13	1.43	0.155336	305	0.021388	-1.66982
12	1.332	0.124504	306	0.021459	-1.6684
12	1.332	0.124504	307	0.021529	-1.66698
12	1.332	0.124504	308	0.021599	-1.66557
12	1.332	0.124504	309	0.021669	-1.66416
12	1.332	0.124504	310	0.021739	-1.66276
12	1.332	0.124504	311	0.021809	-1.66136
12	1.332	0.124504	312	0.021879	-1.65996
12	1.332	0.124504	313	0.02195	-1.65858
12	1.332	0.124504	314	0.02202	-1.65719
12	1.332	0.124504	315	0.02209	-1.65581
12	1.332	0.124504	316	0.02216	-1.65443
12	1.332	0.124504	317	0.02223	-1.65306

12	1.332	0.124504	318	0.0223	-1.65169
12	1.32	0.120574	319	0.02237	-1.65033
12	1.32	0.120574	320	0.02244	-1.64897
12	1.32	0.120574	321	0.022511	-1.64761
12	1.32	0.120574	322	0.022581	-1.64626
12	1.32	0.120574	323	0.022651	-1.64492
12	1.32	0.120574	324	0.022721	-1.64357
12	1.32	0.120574	325	0.022791	-1.64224
12	1.32	0.120574	326	0.022861	-1.6409
12	1.32	0.120574	327	0.022931	-1.63957
12	1.32	0.120574	328	0.023001	-1.63825
12	1.32	0.120574	329	0.023072	-1.63692
12	1.32	0.120574	330	0.023142	-1.63561
12	1.32	0.120574	331	0.023212	-1.63429
12	1.32	0.120574	332	0.023282	-1.63298
11	1.221	0.086716	333	0.023352	-1.63168
11	1.221	0.086716	334	0.023422	-1.63037
11	1.221	0.086716	335	0.023492	-1.62907
11	1.221	0.086716	336	0.023562	-1.62778
11	1.221	0.086716	337	0.023633	-1.62649
11	1.221	0.086716	338	0.023703	-1.6252
11	1.221	0.086716	339	0.023773	-1.62392
11	1.221	0.086716	340	0.023843	-1.62264
11	1.221	0.086716	341	0.023913	-1.62137
11	1.221	0.086716	342	0.023983	-1.62009
11	1.221	0.086716	343	0.024053	-1.61883
11	1.221	0.086716	344	0.024123	-1.61756
11	1.221	0.086716	345	0.024194	-1.6163
11	1.221	0.086716	346	0.024264	-1.61504
11	1.221	0.086716	347	0.024334	-1.61379
11	1.221	0.086716	348	0.024404	-1.61254
11	1.21	0.082785	349	0.024474	-1.61129
11	1.21	0.082785	350	0.024544	-1.61005
11	1.21	0.082785	351	0.024614	-1.60881
11	1.21	0.082785	352	0.024684	-1.60758
11	1.21	0.082785	353	0.024755	-1.60634
11	1.21	0.082785	354	0.024825	-1.60512
11	1.21	0.082785	355	0.024895	-1.60389
11	1.21	0.082785	356	0.024965	-1.60267
11	1.21	0.082785	357	0.025035	-1.60145
11	1.21	0.082785	358	0.025105	-1.60024
11	1.21	0.082785	359	0.025175	-1.59903
10	1.11	0.045323	360	0.025245	-1.59782
10	1.11	0.045323	361	0.025316	-1.59661
10	1.11	0.045323	362	0.025386	-1.59541
10	1.11	0.045323	363	0.025456	-1.59421
10	1.11	0.045323	364	0.025526	-1.59302
10	1.11	0.045323	365	0.025596	-1.59183

10	1.11	0.045323	366	0.025666	-1.59064
10	1.11	0.045323	367	0.025736	-1.58945
10	1.11	0.045323	368	0.025806	-1.58827
10	1.11	0.045323	369	0.025877	-1.58709
10	1.11	0.045323	370	0.025947	-1.58592
10	1.11	0.045323	371	0.026017	-1.58475
10	1.11	0.045323	372	0.026087	-1.58358
10	1.11	0.045323	373	0.026157	-1.58241
10	1.11	0.045323	374	0.026227	-1.58125
10	1.1	0.041393	375	0.026297	-1.58009
10	1.1	0.041393	376	0.026367	-1.57893
10	1.1	0.041393	377	0.026438	-1.57778
10	1.1	0.041393	378	0.026508	-1.57663
10	1.1	0.041393	379	0.026578	-1.57548
10	1.1	0.041393	380	0.026648	-1.57434
10	1.1	0.041393	381	0.026718	-1.57319

Table E10. Crater counts for Epimetheus. A = 20,774 km^2.

d (pix)	d (km)	log (d)	n	n/A	log (n/A)
445	99.68	1.998608	1	4.81E-05	-4.31752
142	31.808	1.502536	2	9.63E-05	-4.01649
92	20.608	1.314036	3	0.000144	-3.8404
86	19.264	1.284746	4	0.000193	-3.71546
77	17.248	1.236739	5	0.000241	-3.61855
73	16.352	1.213571	6	0.000289	-3.53937
69	15.456	1.189097	7	0.000337	-3.47242
49	10.976	1.040444	8	0.000385	-3.41443
44	9.856	0.993701	9	0.000433	-3.36328
42	9.408	0.973497	10	0.000481	-3.31752
41	9.184	0.963032	11	0.00053	-3.27613
41	9.184	0.963032	12	0.000578	-3.23834
39	8.736	0.941313	13	0.000626	-3.20358
35	7.84	0.894316	14	0.000674	-3.17139
34	7.616	0.881727	15	0.000722	-3.14143
34	7.616	0.881727	16	0.00077	-3.1134
33	7.392	0.868762	17	0.000818	-3.08707
33	7.392	0.868762	18	0.000866	-3.06225
32	7.168	0.855398	19	0.000915	-3.03877
32	7.168	0.855398	20	0.000963	-3.01649
31	6.944	0.84161	21	0.001011	-2.9953
30	6.72	0.827369	22	0.001059	-2.9751
30	6.72	0.827369	23	0.001107	-2.95579
29	6.496	0.812646	24	0.001155	-2.93731
29	6.496	0.812646	25	0.001203	-2.91958
28	6.272	0.797406	26	0.001252	-2.90255
27	6.048	0.781612	27	0.0013	-2.88616

27	6.048	0.781612	28	0.001348	-2.87036
27	6.048	0.781612	29	0.001396	-2.85512
27	6.048	0.781612	30	0.001444	-2.8404
27	6.048	0.781612	31	0.001492	-2.82616
27	6.048	0.781612	32	0.00154	-2.81237
26	5.824	0.765221	33	0.001589	-2.79901
26	5.824	0.765221	34	0.001637	-2.78604
25	5.6	0.748188	35	0.001685	-2.77345
25	5.6	0.748188	36	0.001733	-2.76122
25	5.6	0.748188	37	0.001781	-2.74932
24	5.376	0.730459	38	0.001829	-2.73774
24	5.376	0.730459	39	0.001877	-2.72646
24	5.376	0.730459	40	0.001925	-2.71546
24	5.376	0.730459	41	0.001974	-2.70474
24	5.376	0.730459	42	0.002022	-2.69427
23	5.152	0.711976	43	0.00207	-2.68405
23	5.152	0.711976	44	0.002118	-2.67407
23	5.152	0.711976	45	0.002166	-2.66431
23	5.152	0.711976	46	0.002214	-2.65476
23	5.152	0.711976	47	0.002262	-2.64542
23	5.152	0.711976	48	0.002311	-2.63628
23	5.152	0.711976	49	0.002359	-2.62732
23	5.152	0.711976	50	0.002407	-2.61855
23	5.152	0.711976	51	0.002455	-2.60995
22	4.928	0.692671	52	0.002503	-2.60152
22	4.928	0.692671	53	0.002551	-2.59324
21	4.704	0.672467	54	0.002599	-2.58513
21	4.704	0.672467	55	0.002648	-2.57716
21	4.704	0.672467	56	0.002696	-2.56933
21	4.704	0.672467	57	0.002744	-2.56165
20	4.48	0.651278	58	0.002792	-2.55409
20	4.48	0.651278	59	0.00284	-2.54667
20	4.48	0.651278	60	0.002888	-2.53937
20	4.48	0.651278	61	0.002936	-2.53219
19	4.256	0.629002	62	0.002984	-2.52513
19	4.256	0.629002	63	0.003033	-2.51818
19	4.256	0.629002	64	0.003081	-2.51134
18	4.032	0.605521	65	0.003129	-2.50461
18	4.032	0.605521	66	0.003177	-2.49798
18	4.032	0.605521	67	0.003225	-2.49145
18	4.032	0.605521	68	0.003273	-2.48501
18	4.032	0.605521	69	0.003321	-2.47867
18	4.032	0.605521	70	0.00337	-2.47242
17	3.808	0.580697	71	0.003418	-2.46626
17	3.808	0.580697	72	0.003466	-2.46019
17	3.808	0.580697	73	0.003514	-2.4542
17	3.808	0.580697	74	0.003562	-2.44829
17	3.808	0.580697	75	0.00361	-2.44246

16	3.584	0.554368	76	0.003658	-2.43671
16	3.584	0.554368	77	0.003707	-2.43103
16	3.584	0.554368	78	0.003755	-2.42543
15	3.36	0.526339	79	0.003803	-2.41989
15	3.36	0.526339	80	0.003851	-2.41443
15	3.36	0.526339	81	0.003899	-2.40904
15	3.36	0.526339	82	0.003947	-2.40371
15	3.36	0.526339	83	0.003995	-2.39844
14	3.136	0.496376	84	0.004044	-2.39324
14	3.136	0.496376	85	0.004092	-2.3881
13	2.912	0.464191	86	0.00414	-2.38302
13	2.912	0.464191	87	0.004188	-2.378
13	2.912	0.464191	88	0.004236	-2.37304
12	2.688	0.429429	89	0.004284	-2.36813
12	2.688	0.429429	90	0.004332	-2.36328
12	2.688	0.429429	91	0.00438	-2.35848
12	2.688	0.429429	92	0.004429	-2.35373
12	2.688	0.429429	93	0.004477	-2.34904
12	2.688	0.429429	94	0.004525	-2.34439
11	2.464	0.391641	95	0.004573	-2.3398
10	2.24	0.350248	96	0.004621	-2.33525
10	2.24	0.350248	97	0.004669	-2.33075
10	2.24	0.350248	98	0.004717	-2.32629
9	2.016	0.304491	99	0.004766	-2.32188
9	2.016	0.304491	100	0.004814	-2.31752
9	2.016	0.304491	101	0.004862	-2.3132
9	2.016	0.304491	102	0.00491	-2.30892
9	2.016	0.304491	103	0.004958	-2.30468
9	2.016	0.304491	104	0.005006	-2.30049
8	1.792	0.253338	105	0.005054	-2.29633
8	1.792	0.253338	106	0.005103	-2.29221
8	1.792	0.253338	107	0.005151	-2.28814
8	1.792	0.253338	108	0.005199	-2.2841
8	1.792	0.253338	109	0.005247	-2.28009
8	1.792	0.253338	110	0.005295	-2.27613
7	1.568	0.195346	111	0.005343	-2.2722
7	1.568	0.195346	112	0.005391	-2.2683
7	1.568	0.195346	113	0.005439	-2.26444
7	1.568	0.195346	114	0.005488	-2.26062
7	1.568	0.195346	115	0.005536	-2.25682
7	1.568	0.195346	116	0.005584	-2.25306
7	1.568	0.195346	117	0.005632	-2.24933
7	1.568	0.195346	118	0.00568	-2.24564
7	1.568	0.195346	119	0.005728	-2.24197
7	1.568	0.195346	120	0.005776	-2.23834
7	1.568	0.195346	121	0.005825	-2.23473
6	1.344	0.128399	122	0.005873	-2.23116
6	1.344	0.128399	123	0.005921	-2.22762

6	1.344	0.128399	124	0.005969	-2.2241
6	1.344	0.128399	125	0.006017	-2.22061
6	1.344	0.128399	126	0.006065	-2.21715
6	1.344	0.128399	127	0.006113	-2.21372
6	1.344	0.128399	128	0.006162	-2.21031
6	1.344	0.128399	129	0.00621	-2.20693
6	1.344	0.128399	130	0.006258	-2.20358
6	1.344	0.128399	131	0.006306	-2.20025
6	1.344	0.128399	132	0.006354	-2.19695
6	1.344	0.128399	133	0.006402	-2.19367
5	1.12	0.049218	134	0.00645	-2.19042
5	1.12	0.049218	135	0.006499	-2.18719
5	1.12	0.049218	136	0.006547	-2.18398
5	1.12	0.049218	137	0.006595	-2.1808
5	1.12	0.049218	138	0.006643	-2.17764
5	1.12	0.049218	139	0.006691	-2.17451
5	1.12	0.049218	140	0.006739	-2.17139
5	1.12	0.049218	141	0.006787	-2.1683
5	1.12	0.049218	142	0.006835	-2.16523
5	1.12	0.049218	143	0.006884	-2.16218
5	1.12	0.049218	144	0.006932	-2.15916
5	1.12	0.049218	145	0.00698	-2.15615
5	1.12	0.049218	146	0.007028	-2.15317
5	1.12	0.049218	147	0.007076	-2.1502
5	1.12	0.049218	148	0.007124	-2.14726

Table E11. Relative frequency distribution summary for Ali Baba.

bin	Upper (km)	Lower (km)	geomean	n	R	log geomean	bin width	log R
1	1.4142	1	1.2434	87	0.02452	0.094611	0.414214	-1.61049
2	2	1.4142	1.6733	110	0.053426	0.22357	0.585786	-1.27225
3	2.8284	2	2.3414	64	0.060216	0.369468	0.828427	-1.22028
4	4	2.8284	3.3088	61	0.114539	0.519669	1.171573	-0.94105
5	5.6569	4	4.7372	32	0.124689	0.675526	1.656854	-0.90417
6	8	5.6569	6.8742	18	0.15154	0.837222	2.343146	-0.81947
7	11.314	8	9.1496	11	0.154408	0.961402	3.313708	-0.81133
8	16	11.314	13.081	4	0.091957	1.116625	4.686292	-1.03641
10	32	22.627	30.66	2	0.296055	1.486574	9.372583	-0.52863

Table E12. Relative frequency distribution summary for Aziz.

bin	Upper (km)	Lower (km)	geomean	n	R	log geomean	bin width	log R
1	1.4142	1	1.2053	22	0.025693	0.081108	0.414214	-1.59019
2	2	1.4142	1.6267	35	0.071044	0.211303	0.585786	-1.14847
3	2.8284	2	2.3114	21	0.086468	0.363866	0.828427	-1.06314

4	4	2.8284	3.2937	12	0.101102	0.517685	1.171573	-0.99524
5	5.6569	4	4.6121	7	0.114499	0.663899	1.656854	-0.9412
6	8	5.6569	6.8269	4	0.150048	0.834226	2.343146	-0.82377
7	11.314	8	9.3766	3	0.206173	0.972045	3.313708	-0.68577

Table E13. Relative frequency distribution summary for Dalilah.

bin	Upper (km)	Lower (km)	geomean	n	R	log geomean	bin width	log R
1	1.4142	1	1.2183	35	0.055891	0.085765	0.414214	-1.25266
2	2	1.4142	1.6005	42	0.107516	0.204254	0.585786	-0.96853
3	2.8284	2	2.3486	19	0.108676	0.370811	0.828427	-0.96387
4	4	2.8284	3.3277	13	0.149561	0.522148	1.171573	-0.82518
5	5.6569	4	4.681	4	0.09057	0.670336	1.656854	-1.04302
6	8	5.6569	6.7533	3	0.144238	0.829519	2.343146	-0.84092
7	11.314	8	10.047	2	0.223875	1.002029	3.313708	-0.64999
8	16	11.314	13.817	2	0.411718	1.140399	4.686292	-0.3854

Table E14. Relative frequency distribution summary for Ebony.

bin	Upper (km)	Lower (km)	geomean	n	R	log geomean	bin width	log R
1	1.4142	1	1.1722	3	0.001537	0.068988	0.414214	-2.81327
3	2.8284	2	2.1986	4	0.006763	0.342151	0.828427	-2.16987
4	4	2.8284	3.2835	2	0.007964	0.516332	1.171573	-2.09887
7	11.314	8	10.56	1	0.046833	1.023664	3.313708	-1.32945

Table E15. Relative frequency distribution summary for Fitnah.

bin	Upper (km)	Lower (km)	geomean	n	R	log geomean	bin width	log R
1	1.4142	1	1.2075	25	0.038863	0.081873	0.414214	-1.41046
2	2	1.4142	1.6084	28	0.072742	0.206388	0.585786	-1.13822
3	2.8284	2	2.2631	15	0.076766	0.35471	0.828427	-1.11483
4	4	2.8284	3.4363	14	0.177348	0.536089	1.171573	-0.75117
5	5.6569	4	4.7177	14	0.324511	0.673728	1.656854	-0.48877
6	8	5.6569	6.3642	6	0.241431	0.803747	2.343146	-0.61721
7	11.314	8	8.023	1	0.057003	0.904337	3.313708	-1.2441

Table E16. Relative frequency distribution summary for Zumurrud.

bin	Upper (km)	Lower (km)	geomean	n	R	log geomean	bin width	log R
1	1.4142	1	1.2204	76	0.023387	0.086504	0.414214	-1.63102
2	2	1.4142	1.6911	130	0.075259	0.228157	0.585786	-1.12344
3	2.8284	2	2.325	92	0.097872	0.366415	0.828427	-1.00934

4	4	2.8284	3.2852	48	0.101866	0.516558	1.171573	-0.99197
5	5.6569	4	4.9	15	0.074693	0.690198	1.656854	-1.12672
6	8	5.6569	6.7184	10	0.090757	0.827267	2.343146	-1.04212
7	11.314	8	8.7831	5	0.071695	0.94365	3.313708	-1.14451
8	16	11.314	13.203	4	0.137773	1.120684	4.686292	-0.86084
9	22.627	16	20.646	1	0.09312	1.314836	6.627417	-1.03096

Table E17. Relative frequency distribution summary for Epimetheus.

bin	Upper (km)	Lower (km)	geomean	n	R	log geomean	bin width	log R
1	1.4142	1	1.2145	27	0.005621	0.08441	0.414214	-2.25015
2	2	1.4142	1.6437	17	0.006203	0.215814	0.585786	-2.20737
3	2.8284	2	2.3194	16	0.0116	0.365369	0.828427	-1.93555
4	4	2.8284	3.4074	18	0.029258	0.532423	1.171573	-1.53375
5	5.6569	4	4.794	36	0.115236	0.680697	1.656854	-0.93841
6	8	5.6569	6.6253	21	0.12546	0.821202	2.343146	-0.90149
7	11.314	8	9.5317	6	0.075479	0.97917	3.313708	-1.12217
8	16	11.314	15.456	1	0.037926	1.189097	4.686292	-1.42106
9	22.627	16	18.292	4	0.177834	1.262273	6.627417	-0.74999
10	32	22.627	31.808	1	0.165284	1.502536	9.372583	-0.78177
13	90.51	64	99.68	1	1.798455	1.998608	26.50967	0.2549

The nature of impact cratering and the data reduction process used for crater counting makes it a suitable procedure to compare bodies of differing sizes as well as regions of different areas (Arvidson et al., 1978; Melosh, 1989), so despite the size difference between Enceladus and Epimetheus, the deficit in small craters on the latter can be regarded as a true observation rather than an artifact of the sampling method. No doubt crater counts on other nearby bodies in the Saturn system (Tethys, Dione and Rhea, for example) would prove helpful in understanding this effect. The reader may also wish to draw their own conclusions by comparing Figure E3 to Figures 5 and 11 for a more graphic representation of the extreme differences in surface morphology that can occur between objects in similar orbits (specifically, Epimetheus and Hyperion).

APPENDIX F

NAMED FEATURES ON ENCELADUS

Named Features on Enceladus

The International Astronomical Union (IAU) is the body charged with ratifying names of objects and feature on those objects throughout the solar system. While most of the planets known from antiquity, and their moons, bear names derived from Greco-Roman myth and legend, the supply of such names is not limitless and it became apparent sometime after the discovery of Uranus in the late 18th century that alternate sources would eventually have to be employed. For example, satellites of Uranus bear the names of characters from Shakespeare's plays (notably *A Midsummer Night's Dream* and *The Tempest*), and *The Rape of the Lock* by Alexander Pope. Features on Enceladus are named after characters and places in Sir Richard Francis Burton's 10-volume translation of *The Book of the Thousand Nights and a Night* (1885), hence the Arabic theme which the reader will have noted throughout this thesis.

Relatively few features on Enceladus are named, and those only belong to five of the more than fifty available classes: craters, dorsa, fossa, planitia and sulci. They are listed in abbreviated form in the following tables (minus the approval status and derivation within the source). The USGS maintains a website in collaboration with the IAU devoted to planetary nomenclature; the URL for Enceladus' table of contents is <http://planetarynames.wr.usgs.gov/jsp/FeatureTypes2.jsp?system=Saturn&body=Enceladus&systemID=6&bodyID=3&sort=AName&show=Fname&show=Lat&show=Long&show=Diam&show=Stat&show=Orig>. This Appendix is best used in conjunction with the annotated photomosaics in Plate 1.

Table F1. Craters.

Name	Center Latitude	Center Longitude	Diameter (km)
Ahmad	58.76	311.57	18.7
Al-Bakbuk	5.65	191.19	9.0
Al-Fakik	35.54	307.3	16.5
Al-Haddar	50.54	200.64	14.0
Al-Kuz	-18.66	178.23	9.3
Al-Mustazi	-20.86	202.04	10.3
Aladdin	60.69	26.66	37.4
Ali Baba	55.11	22.34	39.2
Ayyub	38.44	295.67	18.0
Aziz	16.73	348.84	11.0
Behram	-15.41	181.02	13.7
Dalilah	51.89	248.54	16.0
Duban	58.38	282.91	19.0
Dunyazad	41.9	200.62	30.9
Fitnah	45.06	290.63	16.5
Ghanim	38.45	281.5	13.9
Gharib	81.12	241.15	26.0
Hassan	-31.31	188.47	14.5
Jansha	-30.36	156.87	9.8
Julnar	52.79	350.0	19.0
Khusrau	-3.77	185.47	12.3
Marjanah	38.24	303.81	14.5
Musa	72.42	17.58	25.0
Omar	17.66	273.93	12.0
Otbah	-39.8	159.51	9.4
Peri-Banu	62.0	322.91	18.0
Rayya	-32.45	178.41	9.0
Salih	-5.29	4.67	4.0
Samad	60.3	4.48	16.3
Shahrazad	47.3	199.73	20.0
Shahryar	58.32	227.5	24.0
Shakashik	-17.27	180.82	8.5
Sharrkan	16.07	302.21	3.7
Shirin	-1.9	172.44	8.7
Sindbad	67.0	212.07	29.1
Zumurrud	-21.9	181.57	21.0

Table F2. Dorsa (ridge); length refers to greatest dimension. The dorsa are the only significant positive-relief features on Enceladus other than crater rims.

Name	Center Latitude	Center Longitude	Length (km)
Cufa Dorsa	3.19	286.17	90.0
Ebony Dorsum	5.74	280.54	70.0

Table F3. Fossae (long, narrow depression).

Name	Center Latitude	Center Longitude	Length (km)
Anbar Fossa	-8.76	323.32	165.0
Bassorah Fossa	39.8	19.9	75.0
Daryabar Fossa	9.65	5.42	200.0
Isbanir Fossa	11.3	358.26	170.0
Khorasan Fossa	-19.0	236.87	290.0

Table F4. Planitia (low plains); diameter refers to greatest extent as these features are not circular.

Name	Center Latitude	Center Longitude	Diameter (km)
Diyar Planitia	-13.4	251.95	325.0
Sarandib Planitia	10.23	311.82	165.0

Table F5. Sulci (subparallel furrows and ridges); Lengths are approximate.

Name	Center Latitude	Center Longitude	Length (km)
Alexandria Sulcus	-75.63	137.56	111.0
Baghdad Sulcus	-86.91	230.54	176.0
Cairo Sulcus	-81.62	154.48	165.0
Camphor Sulcus	-70.78	149.4	77.0
Cashmere Sulci	-52.07	296.06	260.0
Damascus Sulcus	-80.59	285.87	125.0
Hamah Sulci	27.26	306.0	164.0
Harran Sulci	26.39	245.93	291.0
Labtayt Sulci	-27.69	286.08	162.0
Láhej Sulci	-10.89	302.0	150.0
Mosul Sulci	-58.1	336.73	60.0
Samarkand Sulci	30.0	327.5	360.0

APPENDIX G

ADDITIONAL STRUCTURAL INTERPRETATIONS

Additional Structural Interpretations

A man-made analog for a basin structurally similar to the SPT in that it is pinned around its entire periphery are the subsidence craters produced by deep underground nuclear tests, where the detonation occurs at a sufficient depth to prevent the blast breaching the surface. A spherical volume of rock surrounding the device is vaporized, effectively removing support from the overburden, and a more or less cylindrical column of shattered strata collapses into the void thus created. An example of the morphology of such a deep detonation is shown below.



Figure G1. ~330m diameter subsidence crater at Yucca Flat, NV (date and identity of test unknown). Note the relatively intact interior surface, surrounded by many concentric extensional fractures. Google Earth image.

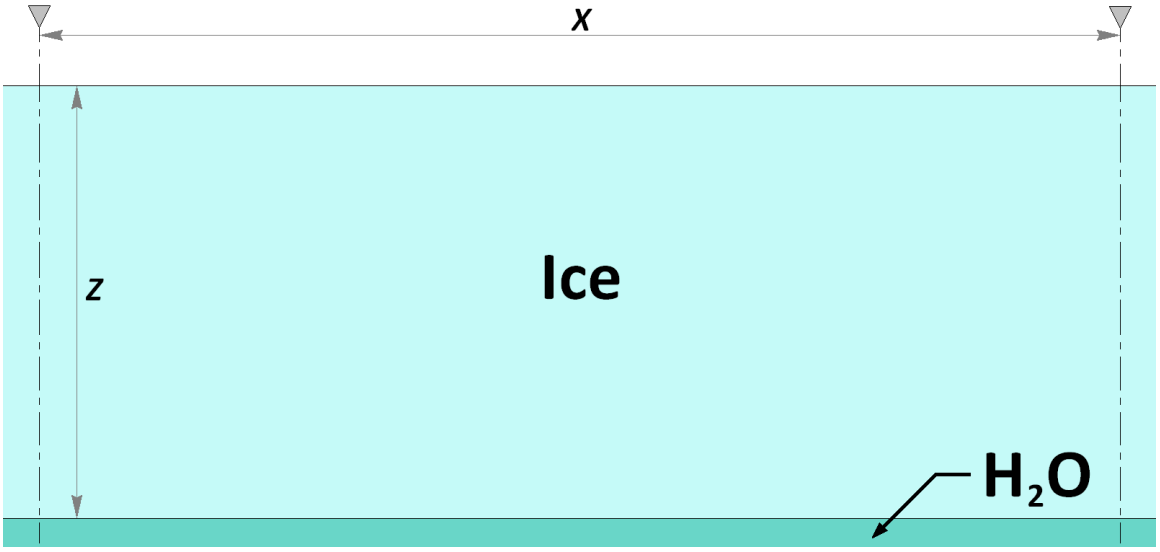


Figure G2. A schematic cross-section through an icy crust of constant thickness *Z* overlying a liquid water mantle, pinned at both ends over a distance *X* (as shown in Figures 30 and 31).

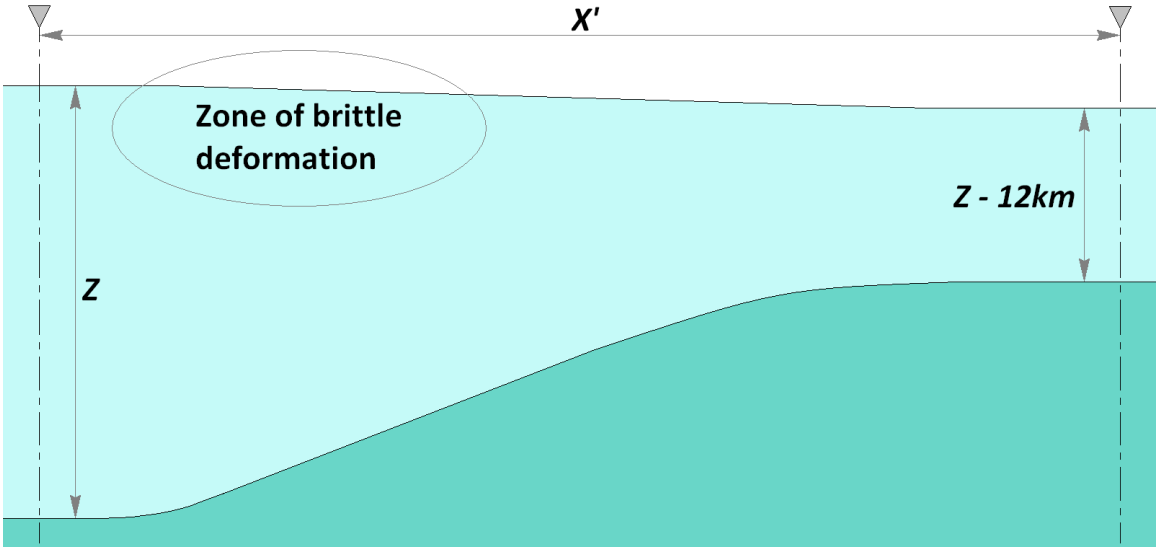


Figure G3. To achieve 1 km of subsidence using the density values given in the text, the crust must be thinned by ~12 km, regardless of its initial thickness. The percentage of extension over *X'* depends on the nature of the hinge zone; the shorter the hinge, the greater the extension. If 1 km of subsidence was accommodated over 10 km of deformation, the extension would be ~0.5%. The true value would likely be much less. On thickening and re-equilibration, *X'* would be shortened to approximately *X*.

It is probably reasonable to infer a detachment zone fairly close to the surface, as depicted in Figure 33, for at least four reasons:

1. The outermost layers of Enceladus' regolith have probably been recycled through the E-ring and are therefore unlikely to be even close to solid ice
2. Some evidence of stratigraphic layering is visible in the tilted blocks that form the extensional architecture bordering the SPT (though the geological significance of these layers is unknown), and density variations in loosely consolidated particulate ice would create inherent zones of weakness (as seen in terrestrial snow pack)
3. The topography across Cashmere Sulci at the location shown in Figure 32 is suggestive of the presence of both synthetic and antithetic faults, which are consistent with a listric normal fault-style detachment
4. If the extensional terrain at the border of the SPT represented domino-style faulted blocks that penetrated the full thickness of the crust, venting should be observed along the faults from the subsurface liquid layer, but geyser activity is confined to the central part of the SPT, presumably where the ice is very thin due to high heat flow

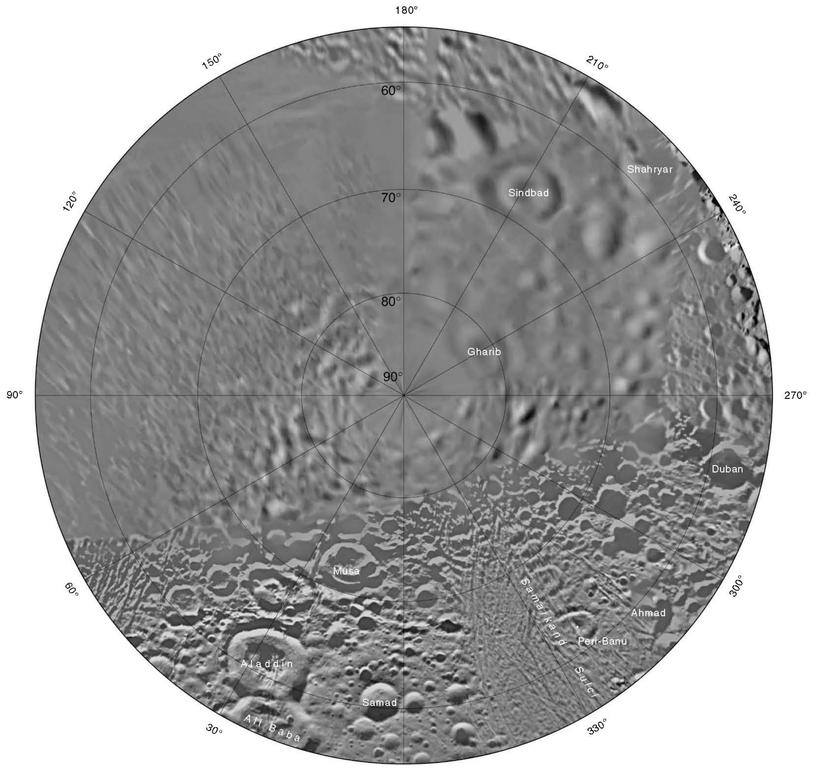
The exact nature, and especially the subsurface geometry, of the normal faults surrounding the SPT is debatable, as there are numerous different configurations that can produce similar topography (e.g. Hatcher, 1995, p. 264, Figure 13-19), and it is entirely possible, if not likely, that the boundary of the SPT is not uniform along its

entire length of over 1,000 km with respect to fault geometry. With the impending Saturnian vernal equinox and the consequent passage of the south polar regions of Enceladus into several years of night, opportunities for high-resolution imagery of these features, especially on the under-represented leading hemisphere, may well prove elusive (or nonexistent) for the foreseeable future.

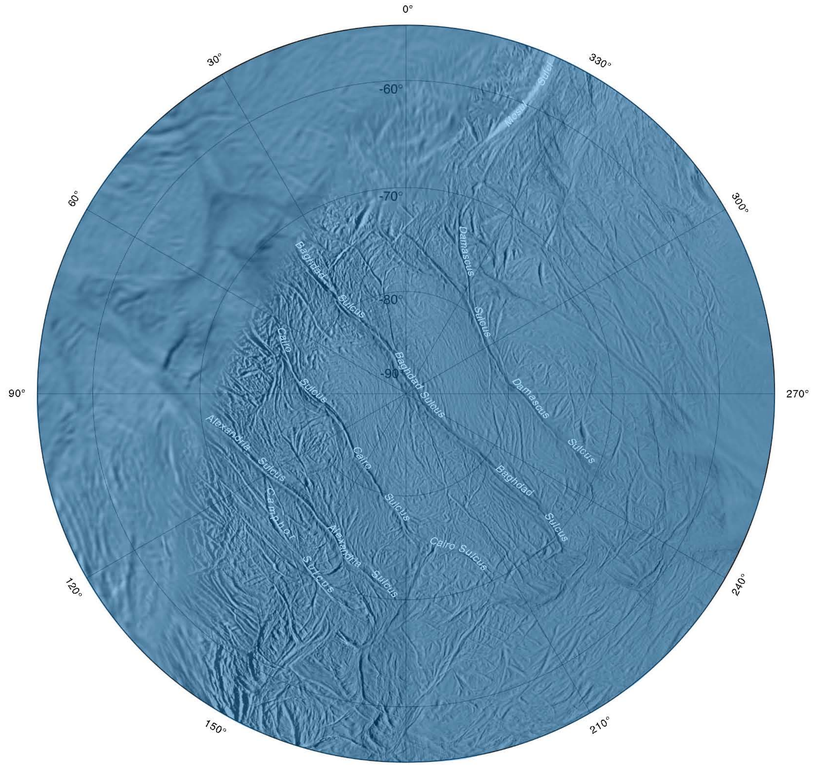
PLATE 1

South Polar Terrain (SPT)

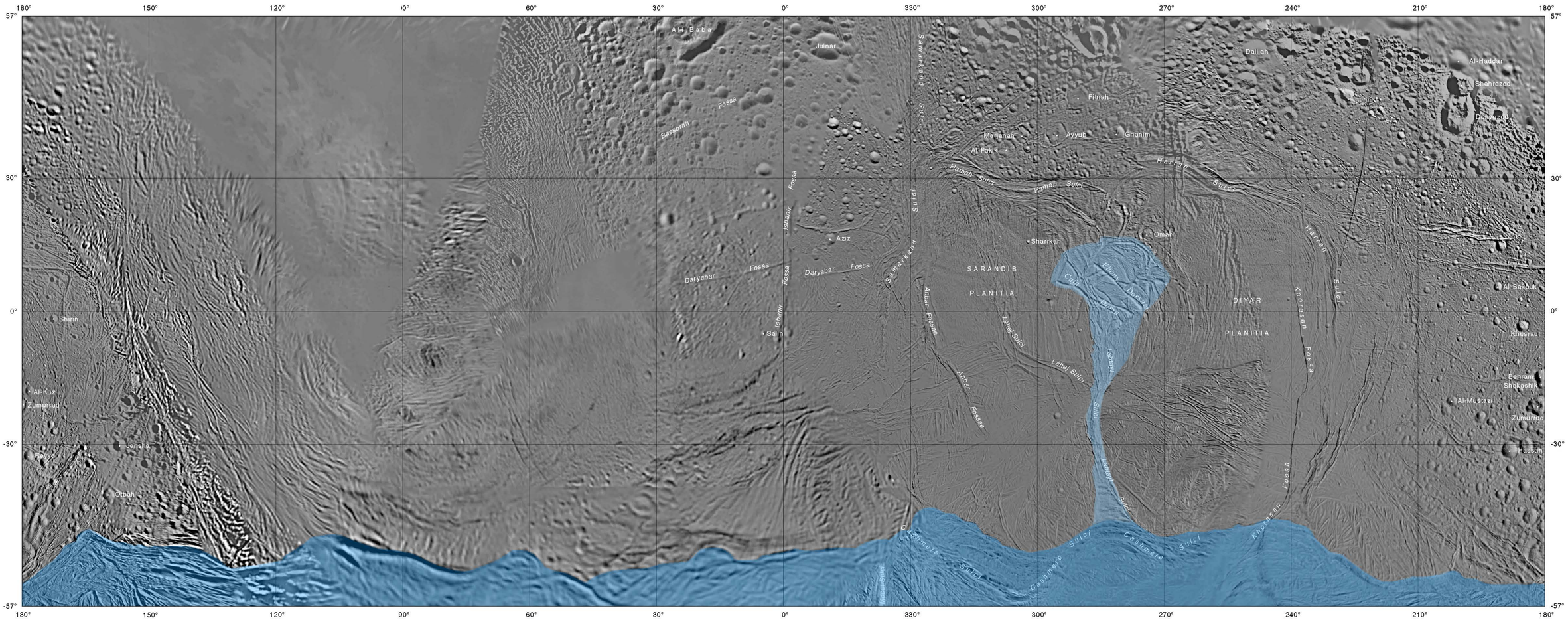
Ancestral Antapical Venting System (AAVS)



North Pole



South Pole



ENCELADUS

Image mosaic provided by the Cassini imaging team; modified and with additions by the author

(For more information about Enceladus imagery, see Th. Roatsch, M. Wählisch, B. Giese, A. Hoffmeister, K.-D. Matz, F. Scholten, R. Wagner, G. Neukum, P. Helfenstein, and C. Porco, High Resolution Enceladus Atlas derived from Cassini-ISS Images, submitted to Planetary and Space Sciences, 2006.)

PLATE 2
South pole of Enceladus
Stereographic Projection
Base Image: PIA11126
Courtesy NASA/JPL/Space Science Institute
Overlays by the author

South polar terrain (SPT)

Ancestral Antapical Venting System (AAVS)

0°

-30°

-60°

90°

270°

180°